

ABSTRACT

QUAYYUM, SHAHRIAR. Advanced Finite Element Analyses of Moment Resisting Connections for Improving Seismic Performance and Exploring Effects of Residual Stress and Fire Damage. (Under the direction of Dr. Tasnim Hassan).

This dissertation research deals with rigorous finite element (FE) analysis and experimental investigation for exploring failure mechanisms of welded steel moment connections (WSMCs) and developing seismic performance enhancement techniques for moment resisting steel buildings. Two types of moment resisting connections in steel buildings were studied, viz. eight bolt stiffened extended end-plate (8ES) connection and welded unreinforced flange bolted/welded web (WUF-B/WUF-W) connection. The AISC prequalified eight bolt stiffened extended end plate (8ES) connection showed good performance in energy dissipation and ductility in many experimental studies under seismic loading. However, fracture of beam flange or stiffener or weld between beam flange/end plate and stiffener, leading to early strength degradation or brittle failure of the connection has also been observed. Hence, the 8ES connection was analyzed using advanced nonlinear finite element (FE) modeling to explore these failure responses. Based on the simulation responses, seismic performance enhancement techniques were developed and analytically evaluated. The modified 8ES connection has been experimentally validated to demonstrate excellent seismic performance.

The aftermath of the 1994 Northridge Earthquake led to significant modifications in the design of moment resisting connections. Although the post-Northridge modified connections showed improved performance in terms of ductility and energy dissipation capacity, low-cycle fatigue failures have been repeatedly observed at the weld toe or access hole of the welded unreinforced flange bolted web (WUF-B) connections. Weld induced residual stresses are considered to be one of the leading contributors to the low-cycle fatigue failures observed in the post-Northridge connections. An experimental study was performed on WUF-B connection to study the influence of welding procedure on the failure mechanism of the connections. Two specimens of WUF-B connections were tested under constant amplitude cyclic loading history and accumulation of axial strain near the welded joint was

observed for both the specimens. However, the rate and magnitude of strain accumulation was different for different welding sequence and hence, the fatigue lives of the specimens were different. Two specimens used in the experimental investigation were simulated, using advanced thermo-mechanical finite element modeling techniques. Numerical techniques, incorporating the W-shape manufacturing processes and real time weld sequences, were developed for simulating initial and welding residual stresses. The analysis model was validated based on the measured temperature history during welding and strain data from the experimental study, and initial residual stress data from literature. The simulation responses of the WUF-W connection demonstrated that under low-cycle fatigue loading despite the welding residual stress relaxation, the axial strain at the weld toe continued to grow with cycle (strain ratcheting) to induce brittle fracture similar to what was observed in the experiments. The critical locations of high stress and strain concentrations are also depicted by the simulated contour plots. These novel numerical techniques can be implemented to optimize weld sequence and heat treatment techniques for enhancing seismic or fatigue life of beam-column connections.

Finally, implications of fire damage to moment resisting steel building under seismic loading have been explored. It is not known how a rehabilitated fire damaged building would behave under a seismic event. Properties of structural steel become heterogeneous because of different peak temperature exposure at different locations of the building. Depending on the rate of cooling or water quenching steel properties will have a much wider range compared to those before fire exposure. Finite element analysis was performed to shed light on the performance of the fire damaged building under simulated seismic loading. The seismic analysis results demonstrated that the lateral drift demands were significantly influenced by the post-fire strength degradation and heterogeneity of structural steel. It was observed that nearly all of the earthquake-induced lateral displacement occurs at the story level where the fire exposed compartments are located. This may lead to single story mechanism commonly known as soft story mechanism at the fire exposed story level which may lead to catastrophic failure of the structure.

© Copyright 2014 Shahriar Quayyum

All Rights Reserved

Advanced Finite Element Analyses of Moment Resisting Connections for Improving Seismic Performance and Exploring Effects of Residual Stress and Fire Damage

by
Shahriar Quayyum

A dissertation submitted to the Graduate Faculty of
North Carolina State University
in partial fulfillment of the
requirements for the degree of
Doctor of Philosophy

Civil Engineering

Raleigh, North Carolina

2014

APPROVED BY:

Dr. Tasnim Hassan
Committee Chair

Dr. Jim Nau

Dr. Mervyn Kowalsky

Dr. Gracious Ngaile

DEDICATION

To my lovely wife Simia,

Very happy son Aariz

and

Loving Parents

BIOGRAPHY

Shahriar Quayyum was born in Dhaka, Bangladesh on April 26, 1983. He received a BSc in Civil Engineering from Bangladesh University of Engineering and Technology (BUET), Dhaka, Bangladesh in 2006. After graduating from BUET, he joined as a lecturer at Presidency University in Bangladesh, where he taught theoretical courses in Civil Engineering at the undergraduate level. He worked at Presidency University for two years, and in 2009 he pursued a Master's degree in Civil Engineering from the University of British Columbia, BC, Canada. During the Master's degree, his research focus was on bond behavior of fiber reinforced polymer reinforcing bars in concrete. He graduated from the University of British Columbia in 2010 and started his PhD in Civil Engineering at North Carolina State University, NC, USA. His PhD research work focused on the seismic performance enhancement of steel moment resisting connections, residual stress and fire damage analysis of steel buildings.

ACKNOWLEDGEMENTS

The author wishes to convey his profound gratitude to the almighty for allowing him to bring this effort to fruition. The study was undertaken under the supervision of Dr. Tasnim Hassan, Professor, Department of Civil, Construction and Environmental Engineering, North Carolina State University, Raleigh, NC. His systematic guidance and constant persuasion has immensely helped the author throughout this work. The author sincerely acknowledges his heartiest gratitude and indebtedness to him for his superior technical expertise and solutions to many projects and computer-related problems. The author is thankful to his doctoral committee members Dr. Jim Nau, Dr. Mervyn Kowalsky and Dr. Gracious Ngaile for their encouragement, insightful comments, and time throughout this research.

The author also pays his deepest homage to his parents, whom he believes to be cardinal source of inspiration for all his achievement.

The author would like to acknowledge his research partner Machel Morrison for his theoretical and experimental inputs which helped author during his dissertation research. The contribution provided by Machel Morrison and Doug schweizer in experimental validation of the concept developed in study is greatly acknowledged. In addition, the author would like to thank all his colleagues, namely Nazrul Islam, Patrick Graham Pritchard, Raashed Ahmed, Paul Barret for sharing their knowledge and ideas during the course of the research.

Finally, the author would like to take the opportunity to thank his spouse Simia Madhuchhanda for being by his side all the time and act as a cradle of motivation for everything.

TABLE OF CONTENTS

LIST OF SYMBOLS	ix
LIST OF TABLES	xii
LIST OF FIGURES	xiii
CHAPTER 1: INTRODUCTION	1
1. Background and Motivation	1
2. Scope and Organization.....	4
3. References.....	7
CHAPTER 2: AN IMPROVED UNSTIFFENED 8 BOLT EXTENDED END PLATE MOMENT CONNECTION FOR SPECIAL AND INTERMEDIATE MOMENT FRAMES, PART I: NUMERICAL MODELING AND MODIFIED DESIGN DEVELOPMENT	11
Abstract	11
1. Introduction.....	12
2. Finite Element Modeling of Extended End Plate Connection.....	17
2.1. Finite Element Discretization	18
2.2. Material Models	20
2.3. Loads and Boundary Conditions.....	24
3. Validation of Finite Element Model.....	25
4. Finite Element Analysis of Extended End Plate Connections.....	27
4.1. Eight Bolt Stiffened Extended End Plate Connection (8ES).....	28
4.2. Eight Bolt Unstiffened Extended End Plate Connection (8E).....	31
4.3. Four Bolt Wide Unstiffened Extended End Plate Connection (4W)	34
4.4. Eight Bolt Unstiffened Modified Extended End Plate Connection (8EM).....	37
5. Further Development of the Modified Design of Extended End Plate Connection.....	43
6. Conclusions.....	55
7. References.....	56

CHAPTER 3: AN IMPROVED UNSTIFFENED 8 BOLT EXTENDED END PLATE MOMENT CONNECTION FOR SPECIAL AND INTERMEDIATE MOMENT FRAMES, PART II: EXPERIMENTAL VALIDATION AND ADDRESSING FURTHER DEVELOPMENT..... 63

Abstract	63
1. Introduction.....	64
2. Review of Proposed Novel Performance Enhancing Techniques	65
3. Connection Design and Experimental Setup	67
4. Instrumentation	70
5. Test Results.....	71
5.1. Global Response of Modified BEEP Connection.....	71
5.2. Plastic Hinge Formation in Modified BEEP Connection.....	72
5.3. Bolt Response in Modified BEEP Connection.....	76
5.4. Failure Mechanism.....	76
6. Post-Test FEA and Discussion.....	78
7. Further Development of Modified BEEP Connection	82
7.1. Future Work on Web Stiffener.....	83
7.2. Design Development.....	84
8. Conclusions.....	84
9. References.....	85

CHAPTER 4: INFLUENCE OF WELD SEQUENCE ON THE SEISMIC RESPONSE OF MOMENT RESISTING CONNECTIONS..... 88

Abstract	88
1. Introduction.....	89
2. Cyclic Testing of WSMCs.....	91
2.1. Welding Procedure and Welding Details	92
2.2. Test Setup	97
2.3. Loading History	98
3. Cyclic Response of WUF-B Connections	100
3.1. Global Response	100

3.2. Local Response	104
4. Conclusions.....	110
5. References.....	111

CHAPTER 5: SIMULATION OF INITIAL RESIDUAL STRESSES IN HOT-ROLLED WIDE FLANGE SHAPES..... 116

Abstract	116
1. Introduction.....	116
2. Manufacturing Process of Structural Shapes and Formation of Initial Residual Stresses	119
3. Finite Element Modeling of the Cooling Process	121
3.1. Thermal Analysis	122
3.2. Residual Stress Analysis	127
4. Results and Discussion	130
5. Influence of IRS on Buckling Response of Wide Flange Steel Columns	133
6. Conclusions.....	141
7. References.....	142

CHAPTER 6: INFLUENCE OF WELDING ON THE SEISMIC PERFORMANCE OF MOMENT RESISTING CONNECTION 147

Abstract	147
1. Introduction.....	148
2. Numerical Scheme for Weld Residual Stress Simulation	150
3. Thermal Analysis	153
4. Residual Stress Analysis.....	162
5. Influence of Initial Residual Stresses	172
6. Effect of Residual Stresses on the Seismic Performance of WSMCs.....	174
7. Post Weld Heat Treatment of WSMCs	188
8. Conclusions.....	196
9. References.....	198

CHAPTER 7: SEISMIC PERFORMANCE OF A FIRE DAMAGED MOMENT RESISTING FRAME	208
.....	208
Abstract	208
1. Introduction.....	208
2. Post-Fire Mechanical Properties of Steel	212
3. Seismic Analysis of Moment Resisting Frames with Fire Damage.....	214
3.1. Finite Element Modeling.....	215
3.2. Distortion Analysis of a Single Story Moment Resisting Frame during Fire	
.....	216
3.3. Seismic Response of Fire Damaged Moment Resisting Frames	225
3.4. Seismic Response of an Exterior WUF-W Connection with Fire Damage	232
4. Conclusions.....	237
5. References.....	238
CHAPTER 8: CONCLUSIONS AND RECOMMENDATIONS.....	243
1. Conclusions.....	243
2. Recommendations for Future Works	245
2.1. Modified Extended End Plate Connection with Extended Shear Tab	246
2.2. Further Study on Seismic Analysis of WSMCs with Residual Stresses	246
2.3. Fire Damage Analysis with Water Quenched Structural Steel.....	247
2.4. Simulation with Advanced Constitutive Models	247

LIST OF SYMBOLS

d_b	Bolt diameter
E	Elastic modulus
σ_0	Initial size of the yield surface
C_i	Kinematic hardening parameter
γ_i	Kinematic hardening parameter
$\underline{\sigma}$	Stress tensor
$\underline{\alpha}$	Current center of the yield surface in the total stress space
\underline{s}	Deviatoric stress tensor
\underline{a}	Current yield surface center in the deviatoric space
R	Isotropic hardening variable
p	Accumulated plastic strain
Q	Size of the plastic strain surface
σ_x	Axial stress
ε_x	Axial strain
M	Moment at the centerline of the column
θ	Interstory drift angle
θ_b	Beam rotation
θ_{pz}	Panel zone rotation
θ_c	Column rotation
θ_{ep}	End plate rotation
N	Number of loading cycles
T	Temperature
T_P	Peak Temperature
t_h	Hold time at peak temperature
ω	Distance along the width of the beam flange from the centerline of the web
δ	Distance along the length of the beam flange from the weld toe
k	Thermal conductivity
Q	Generated heat energy
ρ	Density
c_p	Specific heat
α	Coefficient of thermal expansion
ν	Poisson's ratio

t	Time
ε	Mechanical strain
$x, y,$	Cartesian coordinates
h	Surface coefficient of heat transfer
n	Coordinate normal to surface
T_{atm}	Atmospheric temperature
$\{T\}$	Vector of nodal temperatures
$[C]$	Heat-capacity matrix
$\{K\}$	Heat conductivity matrix
$\{Q\}$	Vector of heat energy
$d\varepsilon^p$	Plastic strain increment
$d\lambda$	Plastic multiplier
dp	Equivalent plastic strain increment
$d\varepsilon$	Total strain increment
$d\varepsilon^e$	Elastic strain increment
$d\varepsilon^T$	Thermal strain increment
$\{d\sigma\}$	Stress increment matrix
$[D]$	Consistent tangent modulus matrix
$\{d\varepsilon\}$	Strain increment matrix
$[C^{th}]$	Thermal stiffness matrix
$\{dT\}$	Temperature increment matrix
ΔT	Temperature difference
σ_{Rx}	Longitudinal residual stress
U_x	Displacement in the x direction
U_y	Displacement in y direction
U_z	Displacement in z direction
R_x	Rotation about x axis
R_y	Rotation about y axis
R_z	Rotation about z axis
η	Arc efficiency
U	Arc voltage
I	Arc current
Q_s	Surface heat flux

Q_b	Body heat flux
q_s	Specific surface heat flux
q_b	Specific body heat flux
J_2	Second invariant
\underline{a}_i	Decomposed deviator of back stress
σ_i	Initial yield stress as a function of T, T_c
σ_{xm}	Mean axial stress
ε_{zm}	Mean axial strain
ε_{za}	Axial strain amplitude
σ_{ORT}	Initial yield stress at room temperature
T_c	Conditioning temperature

LIST OF TABLES

CHAPTER 2: AN IMPROVED UNSTIFFENED 8 BOLT EXTENDED END PLATE MOMENT CONNECTION FOR SPECIAL AND INTERMEDIATE MOMENT FRAMES, PART I: NUMERICAL MODELING AND MODIFIED DESIGN DEVELOPMENT

Table 1	Nonlinear kinematic hardening parameters for different steel materials ...	21
---------	----------------------------------------------------------------------------	----

CHAPTER 4: INFLUENCE OF WELD SEQUENCE ON THE SEISMIC RESPONSE OF MOMENT RESISTING

Table 1	Details of weld sequence for specimen MC1	94
Table 2	Details of weld sequence for specimen MC2	96

CHAPTER 5: SIMULATION OF INITIAL RESIDUAL STRESSES IN HOT-ROLLED WIDE FLANGE SHAPES

Table 1	Width-thickness ratio for different column sections	137
---------	-----------------------------------------------------------	-----

LIST OF FIGURES

CHAPTER 1: INTRODUCTION

Figure 1 Beam-column connection fractures during the 1994 Northridge earthquake [1].....	1
------------------------------------------------------------------------------------------	---

CHAPTER 2: AN IMPROVED UNSTIFFENED 8 BOLT EXTENDED END PLATE MOMENT CONNECTION FOR SPECIAL AND INTERMEDIATE MOMENT FRAMES, PART I: NUMERICAL MODELING AND MODIFIED DESIGN DEVELOPMENT

Figure 1 Different configurations of extended end plate moment connections	13
Figure 2 Finite element mesh of an eight bolt stiffened extended end plate connection	19
Figure 3 Experimental and simulated response of strain controlled hysteresis loop with Chaboche model parameters. (a) ASTM A572 Gr.50 steel; (b) ASTM A36 steel; (c) ASTM A992 steel	22
Figure 4 Monotonic stress-strain curves for bolt and weld materials. (a) ASTM A490 bolt; (b) E70 weld	23
Figure 5 (a) A typical experimental setup for seismic testing of moment connections [31]; (b) SAC loading protocol [14]	24
Figure 6 Comparison between experimental and simulated moment-rotation response of eight bolt stiffened extended end plate connection (8ES-1.25-1.75-30) tested by Sumner <i>et al.</i> [10]	26
Figure 7 Comparison of experimental and simulated deformed shape for 8ES-1.25-1.75-30 specimen of Sumner <i>et al.</i> [10] showing formation of plastic hinge at the base of the stiffener	26
Figure 8 Eight bolt stiffened extended end plate connection (8ES). (a) FE mesh; (b) Equivalent plastic strain contour showing formation of plastic hinge after cyclic loading upto 6% interstory drift angle	28
Figure 9 Cyclic response of 8ES configuration of connection. (a) Moment-rotation hysteresis response for cyclic loading upto 6% interstory drift angle; (b) Contribution of different components of the connection in the total rotation.....	29
Figure 10 Bolt strains for 8ES configuration during loading cycles at the top flange of the beam	30

Figure 11 Eight bolt unstiffened extended end plate connection (8E). (a) FE mesh; (b) Equivalent plastic strain contour showing formation of plastic hinge after cyclic loading upto 6% interstory drift angle	32
Figure 12 Axial strain profile along the width of beam flange at the weld toe for 8E configuration of the connection	32
Figure 13 Bolt strains for 8E configuration during loading cycles at the top flange of the beam	33
Figure 14 Four bolt wide unstiffened extended end plate connection (4W). (a) FE mesh; (b) Equivalent plastic strain contour showing bolt failure and high weld strain at 3% interstory drift angle	35
Figure 15 (a) Equivalent plastic strain contour of end plate at the end of 3% interstory drift angle; (b) Moment-rotation hysteresis response of 4W connection	35
Figure 16 Bolt strains for 4W configuration during loading cycles at the top flange of the beam	36
Figure 17 Axial strain profile along the width of beam flange at the weld toe for 4W configuration of the connection	37
Figure 18 (a) Proposed bolt rearrangement in a hexagonal pattern; (b) FE mesh with the modified bolt arrangement for 8EM configuration of the connection; (c) Equivalent plastic strain contour of 8EM configuration of the connection showing formation of plastic hinge	38
Figure 19 Cyclic response of 8EM configuration of connection. (a) Moment-rotation hysteresis response for cyclic loading upto 6% interstory drift angle; (b) Contribution of different components of the connection in the total rotation.....	39
Figure 20 Bolt strains for 8EM configuration during loading cycles at the top flange of the beam	41
Figure 21 Moment-rotation envelopes of the extended end plate connections for different bolt arrangements	42
Figure 22 Axial strain profile along the width of the beam bottom flange for different arrangements of the bolts. (a) At weld toe during loading cycles at 4% interstory drift angle; (b) At plastic hinge location during loading cycles at 6% interstory drift angle	43
Figure 23 Participation of end plate and panel zone in the total rotation capacity at 6% interstory drift angle for different configurations of bolt. (a) End plate; (b) Panel zone	44

Figure 24 8EM configuration of the connection with W30×148 beam section. (a) Equivalent plastic strain contour showing formation of plastic hinge; (b) Axial strain profile along the width of the beam flange for loading cycles upto 6% interstory drift angle	45
Figure 25 Heat treatment of modified extended end plate connection for seismic performance enhancement	46
Figure 26 (a) Monotonic stress-strain response for unheat treated and heat treated ASTM A992 specimens; (b) Experimental and simulated response of strain controlled hysteresis loop with Chaboche parameters for heat treated ASTM A992 steel	47
Figure 27 Cyclic response of 8EMH configuration of the connection with W30×148 beam section. (a) Equivalent plastic strain contour showing formation of plastic hinge in the heat treated region of the beam flanges; (b) Moment-rotation response upto 6% interstory drift angle	47
Figure 28 Cyclic response of the connection for 8EMH configuration of the bolts. (a) Axial strain profile along the beam flange at the weld toe; (b) Participation of different components of the connection in the total rotation capacity of the connection.....	49
Figure 29 Bolt strains for 8EMH configuration of the connection with W30×148 beam section	50
Figure 30 Local buckling of beam web and flanges at different loading cycles for 8EMH configuration of the connection with W30×148 beam section	51
Figure 31 (a) Modified extended end plate connection (8EMH-W) with heat treatment and web stiffener; (b) Formation of plastic hinge in the heat treated region of beam flanges under simulated seismic loading with 8EMH-W configuration of the connection	52
Figure 32 Cyclic response of 8EMH-W configuration of the connection upto 6% interstory drift angle. (a) Moment-rotation hysteresis response; (b) Axial strain profile along beam flange at the weld toe	53
Figure 33 Bolt strains for 8EMH-W configuration of the connection with W30×148 beam section	54
Figure 34 Moment-rotation envelopes of different configurations of the extended end plate connections. (a) W30×148 beam section; (b) W30×99 beam section	55

CHAPTER 3: AN IMPROVED 8 BOLT EXTENDED END PLATE MOMENT CONNECTION FOR SPECIAL AND INTERMEDIATE MOMENT FRAMES: PART II. EXPERIMENTAL VALIDATION AND ADDRESSING FURTHER DEVELOPMENT

Figure 1 Sketch of Modified BEEP Connection	66
Figure 2 Engineering stress-strain response of A992 and heat-treated A992 steel	66
Figure 3 HBS 4 Test setup. (a) Sketch of test setup, (b) photograph showing test setup	67
Figure 4 HBS 4 connection details. (a) Elevation of connection, (b) photograph of HBS 4 connection prior to testing, (c) section A-A showing connection of beam web and webstiffeners to endplate, (d) elevation of end plate showing modified bolt arrangement	68
Figure 5 Heat-treatment setup. (a) Photograph showing electric surface heating pads during installation on a beam flange, (b) photograph showing insulation of beam flange for well controlled heating and cooling	69
Figure 6 Instrumentation of HBS 4. (a) LED markers placed on beam top flange, beam web and webstiffeners, (b) LED markers placed on the sides of beam top and bottom flange, beam web and webstiffeners	71
Figure 7 Experimental response of HBS 4. (a) Moment rotation hysteresis response, (b) total rotation contributions	72
Figure 8 Plastic rotation contributions by components of HBS 4. (a) Total connection plastic rotation, (b) panel zone shear plastic rotation, (c) column flexural plastic rotation, and (d) beam plastic rotation	73
Figure 9 Recorded longitudinal strains along the center of top flange of the beam from HBS 4	74
Figure 10 Progression of yielding and plastic hinge formation in HBS 4. (a) 1% drift, (b) 2% drift, (c) 3% drift, and (d) 4% drift	74
Figure 11 Measured flexural strains from strain gages placed on the bottom flange of HBS 4. Strains are shown from the beginning of test to the second cycle of 3% drift	75
Figure 12 Recorded axial bolt strain vs column centerline moment	77
Figure 13 Local buckling failure of HBS 4. (a) Post test photograph showing flange and web local buckling, (b) photograph showing fracture of beam flange in the crest of flange buckle	78

Figure 14 Validation of post-test FEA of HBS 4. (a) FEA discretization including initial distortion of web stiffener plates, (b) comparison between FEA prediction and the recorded moment-rotation response, (c) photograph of HBS 4 during loading cycles at 6% drift, (d) FEA prediction of deformation at 6% drift, (e) comparison between FEA predictions and recorded top flange vertical displacements during various stages of loading history, (f) photograph of HBS 4 top flange during loading at 4% drift	80
Figure 15 Post-test FEA simulation results showing the effect of initial web stiffener plate distortion. (a) Moment-rotation envelop, (b) plastic equivalent strain prediction at 5% drift for HBS 4 (post-test simulation with initial web stiffener distortion), (c) plastic equivalent strain prediction at 5% drift for HBS 4 (pre-test simulation without initial web stiffener distortion)	81

CHAPTER 4: INFLUENCE OF WELD SEQUENCE ON THE SEISMIC RESPONSE OF MOMENT RESISTING CONNECTIONS

Figure 1 Sketch of the full-scale exterior WUF-B connection tested in this study	92
Figure 2 Sketch of weld sequences at the beam top and bottom flange for specimen MC1 showing number of welding passes in order of completion	93
Figure 3 Sketch of weld sequences at the beam top and bottom flanges for specimen MC2 showing number of welding passes in order of completion	95
Figure 4 Schematic of the test setup used for cyclic testing of WUF-B Connections	98
Figure 5 (a) SAC loading protocol [35], (b) non-standard loading history prescribed in the experiments	99
Figure 6 Response of specimen MC1. (a) moment-rotation hysteresis response, (b) rupture in the beam top flange	101
Figure 7 Response of specimen MC2. (a) moment-rotation hysteresis response, (b) cracks in the reinforcing fillet weld of bottom beam flange	102
Figure 8 Response of specimen MC2. (a) rupture of the top flange initiated at the flattened portion of the weld access hole, (b) cracks in the weld-base metal interface of top beam flange	103
Figure 9 Mean axial strain and amplitude plotted against number of loading cycles recorded at the top flange (inside surface) of the connections	105

Figure 10 Mean axial strain and amplitude plotted against number of loading cycles recorded at the beam bottom flange (inside surface) of the connections	106
Figure 11 Mean axial strain and amplitude plotted against number of loading cycles recorded at the beam bottom flange (outside surface) of the connections	108
Figure 12 Mean axial strain and amplitude plotted against number of loading cycles recorded at the column flange of the connections	109

CHAPTER 5: SIMULATION OF INITIAL RESIDUAL STRESSES IN HOT-ROLLED WIDE FLANGE SHAPES

Figure 1 Schematic diagram showing the manufacturing process of structural steel shapes [26].....	120
Figure 2 (a) Beam blank continuous caster mold, (b) cross-sectional view of beam blank, (c) cross-sectional view of finished product after hot-rolling	121
Figure 3 Finite element mesh for thermal finite element analysis of W36×150 shape	122
Figure 4 Material coefficients of structural steel as a function of temperature used in thermal finite element analysis. (a) Specific heat [32], (b) thermal conductivity [32], (c) heat transfer coefficient [33], (d) enthalpy [34]	124
Figure 5 Contour showing temperature distribution (in °K) during the cooling process of hot rolled W36×150 section from initial 1300°C reheat temperature. (a) after 15 minutes, (b) 30 minutes, (c) 45 minutes	125
Figure 6 (a) Cooling curves at three different locations over the cross section of a W36×150 section, (b) temperature difference as a function of cooling time over the cross section of a W36×150 section	126
Figure 7 (a) Poisson’s ratio [37] and (b) thermal expansion coefficient [38] of structural steel plotted as a function of temperature	128
Figure 8 (a) Monotonic stress-strain response of ASTM A36 steel at different temperatures, (b) monotonic stress-strain response of ASTM A992 steel at different temperatures [36].....	129
Figure 9 Contour showing longitudinal stress distribution during the cooling process of hot rolled W36×150 section. (a) after 15 minutes, (b) 1 hour, (c) 2 hours ...	130
Figure 10 Residual stress analysis results for a W36×150 section. (a), (b) Measured [3] and simulated longitudinal residual stresses at the centerline along the beam	

length, (c) simulated longitudinal residual stress distribution along the length of beam, (d) simulated longitudinal residual stresses plotted against cooling time at different locations of the beam section	132
Figure 11 Measured [1] and simulated longitudinal residual stresses at the centerline along the beam length for a W14×43 section	133
Figure 12 Measured [20] and simulated longitudinal residual stresses at the centerline along the beam length for a W16×50 section	134
Figure 13 Measured [20] and simulated longitudinal residual stresses at the centerline along the beam length for a W27×102 section	134
Figure 14 (a) Equivalent plastic strain contour of W12×87 column under axial compression, (b) simulated and experimental [12] axial load-displacement response, (c) simulated and experimental [12] out-of-plane deflection response	135
Figure 15 (a) Finite element mesh used in the cyclic response evaluation of wide flange column sections, (b) displacement-based simulated earthquake loading history [42]	136
Figure 16 Cyclic response of W24×131 column without considering IRS. (a) Equivalent plastic strain contour, and (b) moment-rotation hysteresis response at the end of 6% interstory drift angle	138
Figure 17 Cyclic response of W24×131 column considering IRS. (a) Equivalent plastic strain contour, and (b) moment-rotation hysteresis response at the end of 6% interstory drift angle	139
Figure 18 Moment-rotation envelope showing peak moment at each loading cycle for different column sections with and without IRS. (a) W14×132, (b) W24×131, (c) W24×250, (d) W36×230	140

CHAPTER 6: INFLUENCE OF WELDING ON THE SEISMIC PERFORMANCE OF MOMENT RESISTING CONNECTION

Figure 1 Steps performed in the thermo-mechanical analysis of WUF-W connection	151
Figure 2 Finite element mesh of WUF-W connection used in the study	152
Figure 3 Material coefficients of structural steel as a function of temperature used in thermal analysis. (a) Specific heat [55], (b) thermal conductivity [55], (c) heat transfer coefficient [20], (d) enthalpy [56]	154

Figure 4 Element birth and death technique in the FE simulation of welding process	155
Figure 5 Illustration of moving temperature (in Kelvin) field during the final welding pass in the top flange of a welded steel moment connection (a-e) and cooling (f)	156
Figure 6 Sketch of weld sequences in beam top and bottom flanges for specimen MC1 showing number of welding passes in order of completion	157
Figure 7 Sketch of weld sequences in beam top and bottom flanges for specimen MC2 showing number of welding passes in order of completion	158
Figure 8 Measured and simulated temperature profiles at the beam top flange for the two specimens. (a) Specimen MC1, (b) specimen MC2	159
Figure 9 Simulated temperature profiles at the top and bottom flange of the beam showing variation for two different welding sequences. (a) Top flange, (b) bottom flange	160
Figure 10 Temperature distribution (in Kelvin) at the end of weld passes 1 and 2 of welding sequence A at the beam bottom flange of specimen MC1 showing nonuniform temperature on both sides of the beam web	161
Figure 11 Temperature distribution (in Kelvin) at the end of weld passes 1 and 2 of welding sequence B at the beam bottom flange of specimen MC2 showing uniform temperature on both sides of the beam web	161
Figure 12 Monotonic tension test response of ASTM A992 steel at different temperatures [57]. (a) Monotonic stress-strain response, (b) initial yield stress plotted as a function of temperature, (c) elastic modulus plotted against temperature	163
Figure 13 (a) Poisson's ratio [59] and (b) thermal expansion coefficient of structural steel plotted as a function of temperature [60]	164
Figure 14 (a) Stress-strain response of ASTM A992 coupons conditioned at different peak temperatures [62], (b) temperature dependent yield stress of ASTM A992 for five temperature levels to account for the material heterogeneity	165
Figure 15 Residual stress distribution (in Pa) for specimen MC1. (a) Longitudinal direction, (b) transverse direction	167
Figure 16 Residual stress distribution (in Pa) for specimen MC2. (a) Longitudinal direction, (b) transverse direction	167

Figure 17 Welding induced residual stress distribution in the beam top flange of specimen MC1. (a) Across width, (b) across length	168
Figure 18 Welding induced residual stress distribution in the beam bottom flange of specimen MC1 for weld sequence A. (a) Across width, (b) across length	169
Figure 19 Welding induced residual stress distribution in the beam top flange of specimen MC2. (a) Across width, (b) across length	170
Figure 20 Welding induced residual stress distribution in the beam bottom flange of specimen MC2 for weld sequence B. (a) Across width, (b) across length	171
Figure 21 Welding induced residual stress distribution across the width of beam flange near weld toe for the two specimens. (a) Top flange, (b) bottom flange	171
Figure 22 Residual stress distribution along the length of the beam for specimen MC1 showing the influence of initial residual stresses. (a) Beam top flange, (b) beam bottom flange	173
Figure 23 (a) SAC loading protocol [70], (b) non-standard constant amplitude loading history prescribed in this study	175
Figure 24 Experimental and simulated response of strain controlled hysteresis loop for ASTM A992 steel with Chaboche parameters	177
Figure 25 Plastic strain contour in axial direction showing accumulation of strains near weld toe and weld access hole in presence of residual stresses	178
Figure 26 Low-cycle fatigue response of the connection for specimen MC1. (a) Axial mean strain and amplitude plotted against number of loading cycles, (b) axial stress-strain hysteresis cycles showing ratcheting	179
Figure 27 Low-cycle fatigue response of the connection for specimen MC2. (a) Axial mean strain and amplitude plotted against number of loading cycles, (b) axial stress-strain hysteresis cycles showing ratcheting	179
Figure 28 Low-cycle fatigue response of the connection at the beam bottom flange for specimen MC1. (a) Axial mean strain, and (b) strain amplitude plotted against number of loading cycles at different locations across the width near weld toe; (c) axial mean strain and (d) strain amplitude across the length	181
Figure 29 (a) Axial mean stress plotted against number of loading cycles for specimen MC1 at different locations across the width of near weld toe showing stress relaxation, (d) axial mean strain and amplitude near the top and bottom beam flange weld access hole for specimen MC1	183

Figure 30 Axial mean stress and strain, and von-Mises mean stress plotted against number of loading cycles at the top flange for specimen MC1. (a) 25 mm from weld toe, (b) 190 mm from weld toe	184
Figure 31 Comparison of stress-strain response at the beam top flange for the two specimens. (a) Stress-strain hysteresis response, (b) axial mean strain and amplitude plotted against number of loading cycles	185
Figure 32 Comparison of stress-strain response at the beam bottom flange for the two specimens with different weld sequences. (a) Stress-strain hysteresis response, (b) axial mean strain and amplitude plotted against number of loading cycles	186
Figure 33 Axial mean strain and amplitude plotted against number of loading cycles at different locations of the beam flanges showing influence of weld sequence	187
Figure 34 A schematic of the time-temperature curve for the post weld heat treatment specified by AWS D1.1 [79]	189
Figure 35 Post weld heat treatment cases investigated in the study	190
Figure 36 Residual stress contours showing distribution of residual stresses after PWHT for the six cases under investigation for specimen MC1	192
Figure 37 Residual stress distribution in the beam top flange for specimen MC1 showing effect of post weld heat treatment (Case-VI). (a) Across the width of the flange near the weld toe, (b) along the length of the beam	193
Figure 38 Residual stress distribution in the beam bottom flange for specimen MC1 with weld sequence A showing effect of post weld heat treatment (Case-VI). (a) Across the width of the flange near the weld toe, (b) along the length of the beam	194
Figure 39 Axial strain mean and amplitude plotted against number of loading cycles at (a) beam top flange near weld toe, (b) bottom flange near weld toe, (c) around weld access hole near beam top flange of the connection for specimen MC1 showing influence of PWHT (Case-VI)	195

CHAPTER 7: SEISMIC PERFORMANCE OF A FIRE DAMAGED MOMENT RESISTING FRAME

Figure 1 Monotonic stress-strain response of ASTM A992 steel heated at different peak temperatures followed by air cooling [29]	213
---------------------------------------------------------------------------------------------------------------------------------------	-----

Figure 2 (a) A schematic of the special moment frame used in this study (adapted from Adan [31]), (b) finite element mesh developed for the frame analysis	214
Figure 3 Displacement based simulated earthquake loading history [30]	216
Figure 4 (a) Time-temperature curves to represent a fire scenario, (b) monotonic stress-strain response of ASTM A992 steel at elevated temperatures [37].....	218
Figure 5 Finite element mesh developed for thermo-mechanical analysis of a single story two bay moment frame	219
Figure 6 Response of a single story frame with fire in a single compartment. (a) Temperature distribution (in Kelvin) at the end of peak temperature exposure (50 minutes), (b) vertical deflection (in meter), and (c) out-of-plane deflection (in meter) at the end of the cooling phase	220
Figure 7 Response of a single story frame with fire in both compartments. (a) Temperature distribution (in Kelvin) at the end of peak temperature exposure (50 minutes), (b) vertical deflection (in meter), and (c) out-of-plane deflection (in meter) at the end of the cooling phase	221
Figure 8 Stress (in Pa) in longitudinal direction of a single story frame with fire in a single compartment. (a) At the end of peak temperature exposure (50 minutes), (b) at the end of the cooling phase.....	223
Figure 9 (a) Stress in longitudinal direction, and (b) out-of-plane deformation at three different locations across the beam cross section along the centerline of the beam length.....	224
Figure 10 Cyclic response of the frame at room temperature. (a) Equivalent plastic strain contour of the frame at 6% interstory drift angle, (b) base shear plotted against interstory drift angle showing hysteresis response of the frame, (c) equivalent plastic strain contour of the exterior (left), and (d) interior connection at the 3 rd level at 6% interstory drift angle	226
Figure 11 Displacement contours (in meter) of the frame at room temperature at 6% interstory drift angle. (a) Lateral displacement, (b) out-of-plane displacement	227
Figure 12 Hysteresis response of the frame for different fire cases	228
Figure 13 Comparison of frame responses at room temperature and different fire cases. (a) Peak positive and negative lateral forces at each loading cycle plotted against interstory drift angle, (b) interstory drift angles at each story level.....	229

Figure 14 Formation of plastic hinge in the interior column at the 2 nd level. (a) Fire Case-III, (b) Fire Case-IV	229
Figure 15 Out-of-plane displacement contours (in meter) of the frame for different fire cases	231
Figure 16 (a) Reference special moment frame showing an exterior WUF-W connection taken for the study, (b) finite element mesh of the external WUF-W connection	233
Figure 17 Response of WUF-W connection at room temperature under simulated seismic loading history. (a) Equivalent plastic strain contour showing formation of plastic hinges, (b) moment-rotation hysteresis response	234
Figure 18 (a) Temperature distribution (in Kelvin) at the peak temperature level of fire exposure in the WUF-W connection, (b) equivalent plastic strain contour of fire damaged WUF-W connection showing formation of plastic hinges	235
Figure 19 (a) Moment-rotation hysteresis response of WUF-W connection with fire damage under simulated seismic loading history, (b) comparison of moment-rotation envelopes showing peak positive and negative moments at each loading cycle	236

CHAPTER 1: INTRODUCTION

1. Background and Motivation

Before the 1994 Northridge Earthquake, welded unreinforced flange bolted web (WUF-B) moment connections were used extensively in the construction of multistory buildings in North America and it was anticipated that under seismic loading, damage would be limited to ductile yielding of members or connection. The Northridge Earthquake in 1994 challenged the connections in meeting seismic demands. During the Northridge Earthquake many steel buildings were extensively damaged at the WUF-B connections and several exhibited brittle fractures [1-4]. These brittle fractures were observed at the weld between the bottom beam flange and the column flange as shown in Figure 1(a). In some cases, the cracks continued through the column flange right above the weld as shown in Figure 1(b). Interestingly, the same types of brittle connection failures were observed during the Kobe Earthquake exactly one year after the Northridge Earthquake.



(a) Fracture at fused zone



(b) Fracture through column flange

Figure 1 Beam-column connection fractures during the 1994 Northridge earthquake [1].

Many failure mechanisms were observed, and many were addressed through research over the last two decades. The lack of ductility displayed in the pre-Northridge welded steel moment connections (WSMCs) prompted research by the Federal Emergency Management

Agency (FEMA) as well as the SAC Joint Venture, a partnership between the Structural Engineers Association of California (SEAOC), the Applied Technology Council (ATC), and the California Universities for Research in Earthquake Engineering (CUREE). Weld-base metal mismatch, base metal and weld metal toughnesses, backing bar, fillet weld reinforcement, residual stress, continuity plates, panel zone, reduced beam section, weld access hole, and column flange through-thickness fractures have all been investigated and modifications were made in the existing design of moment connections [1-2, 4-11].

Based on a decade of research activities, deformation based performance requirements for WSMCs in steel moment frame was developed [1, 12]. These requirements are specified in the 2010 AISC Seismic Provisions for structural steel buildings [12]. According to these provisions, beam-to-column moment connections in special moment frames (SMFs) are required to sustain a total interstorey drift angle of $\pm 4\%$ without significant loss of strength. Significant loss of strength is defined to occur when the flexural resistance of the connection drops below 80% of the nominal plastic moment capacity of the beam. These interstorey drift angle requirements include both elastic and inelastic components of frame deformation. In order to fulfill this performance criteria, many modifications were made in the pre-Northridge connection to enhance the connection's ductility and energy dissipation capacity, and the seismic performance of the modified connections were tested under standard seismic loading protocol [13-19]. Based on the results of these experimental studies, AISC 358-10 Standards approved five moment connections for special and intermediate moment frames (SMF and IMFs) [20] application. These are reduced beam section (RBS) moment connection, bolted stiffened and unstiffened extended end-plate moment connection, bolted flange-plate (BFP) moment connection, welded unreinforced flange welded web (WUF-W) moment connection, and Kaiser bolted bracket (KBB) moment connection. Recently, Side Plate and ConX connections are prequalified for SMF and IMFs.

The design modifications to the pre-Northridge connections showed significant improvement in the ductility and energy dissipation capacity of welded steel moment frames; however, the fundamental reasons for the brittle failures at the local level were not uncovered. As a result, some of the prequalified moment connections often suffered localized

fractures. Testing of post-Northridge welded steel moment connections have shown that localized low-cycle fatigue cracks may initiate near the welds [6-7, 21-23]. Research by the European community has also demonstrated localized low-cycle fatigue fractures and concluded that an exhaustive understanding of the low-cycle fatigue strength of steel members and joints is required [23]. Further, several researchers found that under constant, small amplitude tests where the beam doesn't develop its full plastic moment capacity, the connection is susceptible to brittle fractures near the weld metal and heat affected zone [24]. Brittle fractures were also observed in connections with strong panel zones prior to the development of the plastic moment in the beam [25].

Some of the European tests have demonstrated problems with the RBS beam column connection which is the most widely used post-Northridge connection in USA. Failures have been observed in the welds due to high stress concentrations, thus RBS is not considered as an acceptable solution in Europe [23]. The RBS moment connection also results in lower stiffness and lower capacity of the beam. This could lead to selecting larger members, thus higher material costs. In addition, the resistance to lateral and torsional stability of RBS are reduced compared to the WSMC beam. As a result, special attention must be paid to lateral bracing of the flanges at the reduced beam section. The extended end-plate connection for smaller size beam sections showed significant seismic performance improvement, but for larger size beam sections the connection requires an end-plate stiffener. The stiffener induces high stress concentration at the base of the stiffener which may lead to premature failure of the beam flanges and stiffener welds [27-29].

Thus based on the observations made from the literature it is apparent that some of the post-Northridge connections may still be exposed to brittle failure because of low-cycle fatigue mechanism, and lateral or torsional buckling before reaching the interstory drift $\pm 4\%$ without significant loss of strength [6, 18]. While many design procedures can predict the performance of a global structural parameter under prescribed load conditions, those same procedures do not attempt to correlate these quantities with local responses. This is not a shortcoming of the current guidelines and design procedures; however it is a limitation on the knowledge on local failure mechanisms. Hence it is essential that the cause and mechanism

of local failure of welded steel moment frames be understood to effectively and reliably meet the seismic demands. In order to fully understand the connection failure mechanisms, localized failure mechanisms should be studied along with global failure mechanisms, which is the subject of this study.

This study implemented advanced finite element analysis techniques and experimental study to analyze and understand the local and global failure mechanisms of welded steel moment connections. The finite element models were validated against experimental results prior to analyzing the failure mechanisms. The failure mechanism of two prequalified moment connections such as eight bolt stiffened extended end plate (8ES) and welded unreinforced flange welded web (WUF-W) moment connection were studied through finite element analysis. Seismic performance of welded unreinforced flange bolted web (WUF-B) connection was investigated through experimental study. The outcome of the study demonstrated the influence of various parameters in influencing the failure mode of the connections. Some of these parameters are not accounted for in the design of moment resisting buildings. Based on analysis results of the force transfer and failure mechanism of the 8ES connection, techniques to enhance its seismic performance are developed and the modified connection is validated through experimental investigation. The influence of residual stress are investigated through complex thermo-mechanical finite element analysis and validated against experimental responses of WUF-B connections. Analysis responses demonstrated that the fire damages in steel buildings may result in soft story mechanism towards collapse of the building. These results are presented in three parts: i) seismic performance enhancement of extended end-plate moment connection via detailed investigation of local and global response of the connection, ii) effect of residual stresses on the localized failure of WUF-B and WUF-W connections, iii) effect of fire induced material heterogeneity on the seismic performance of welded steel moment frame.

2. Scope and Organization

This dissertation deals with rigorous finite element (FE) analysis and experimental investigation for exploring failure mechanisms of welded steel moment connections

(WSMCs) and developing seismic performance enhancement techniques for moment resisting steel buildings. The findings of this study are presented through the six chapters written in journal paper format. Chapter 1 is the current chapter introducing the dissertation. Chapters 2 to 7 are the six journal papers describing the various findings in detail. Chapter 8 is the concluding chapter discussing recommendations for future research.

Chapter 2 is a journal paper to be submitted to the Engineering Structures on the development of a modified design of extended end plate moment connection to enhance the seismic performance. The AISC prequalified eight bolt stiffened extended end plate connection has been investigated in detail by using finite element modeling techniques. Firstly, the finite element models were validated against experimental results from the literature, and afterwards, the seismic performance of the connection with design modifications was studied. The goal of this study was to eliminate the necessity of end plate stiffener with an optimized bolt arrangement that ensures even distribution of bolt forces. Based on global and local responses of all the connections studied, a modified design of extended end plate connection was proposed which consists of a hexagonal pattern of bolt arrangement, heat treatment of the beam flanges near the welded joint and inclusion of a stiffener plate at the web of the beam near connection region. The study discussed sequentially the development of the proposed modified design and shows comparison of the performance of the different connections.

The modified design of extended end plate connection developed in Chapter 2 has been experimentally validated through full scale cyclic testing of the connection under simulated seismic loading history which is presented in Chapter 3. The experiment was conducted at the Constructed Facilities Laboratory (CFL) by the graduate students, Machel Morrison and Doug Schweizer. My contributions in the experimental study were through the pre and post-test analyses. This is a journal paper to be submitted to the Engineering Structures. This chapter gives detail of the experimental setup of the connection and the results obtained from the experiments, which demonstrated excellent performance under seismic loading. The post-test analysis simulated the seismic performance of the connection considering the initial imperfections and actual loading.

Chapter 4 is a journal paper to be submitted to the Journal of Structural Engineering on the experimental investigation of the influence of welding sequence on the seismic response of the WUF-B connection. This study was motivated by the low-cycle fatigue cracks at the weld toe that was observed in the cyclic testing of post-Northridge connections which was attributed to the residual stresses induced by welding near the welded region. This study takes into account two exterior sub-assemblages of WUF-B moment connections having different sequence of welding for connecting the beam flange to the column flange. The objective was to investigate the effect of welding procedure on the localized low-cycle fatigue failure mechanism of the connections especially the local strain responses. The results demonstrates the influence of weld sequence on the strain responses near the welded joint and weld access hole and thereby influence the crack initiation life.

Chapters 5 and 6 are the continuation of the Chapter 4 study and demonstrate the influence of initial and welding residual stresses on the seismic response of moment resisting connections. These studies dealt with complex finite element modeling of moment resisting connections. Chapter 5 deals with the development of advanced numerical technique to simulate the residual stresses in the wide flange shapes and will be submitted to the Journal of Structural Engineering. This chapter describes the detail of the modeling feature for the heat transfer analysis followed by a thermo-mechanical analysis to simulate the initial residual stresses. The residual stress measurements obtained from the finite element simulation were validated against experimental data from the literature. An example was presented on the application of the numerical simulation technique on the influence of initial residual stresses on the seismic performance of wide flange steel columns. The results of the analysis demonstrated the vulnerability of the steel columns with initial residual stresses.

Chapter 6 deals with the understanding of the residual stresses and their influence on the localized failure mechanism of welded steel moment resisting connections. This study developed a numerical technique based on sequentially coupled transient nonlinear thermo-mechanical analysis to simulate the welding residual stresses and their influence on localized fatigue responses. The finite element simulation technique was validated against the experimental temperature and strain measurements. The simulated response of residual

stresses showed development of very high residual stresses close to the weld region. The welding induced residual stresses together with the initial residual stresses in wide flange shapes were included for the seismic analysis of moment resisting connections, which demonstrated the influence of the residual stresses on the low-cycle fatigue failure mechanism of the connections. The results of the finite element investigation also explain the variability of the low-cycle fatigue failure response for different weld sequences. Finally, a method to reduce the magnitude of the residual stresses has been proposed based on the concept of post weld heat treatment which showed improved performance under seismic type of loading. Chapter 6 on the welding residual stress will be submitted to the Journal of Constructional Steel Research.

Chapter 7 is a journal paper to be submitted to the Journal of Constructional Steel Research on the seismic performance assessment of fire damaged steel moment resisting frames. The objective of the study was to investigate how a fire damaged steel building will respond under a seismic event if it is rehabilitated for continued service. The post-fire material strength degradation and material heterogeneity was considered to account for the damage caused by fire. A three story reference steel moment resisting frame was modeled by using finite element software ANSYS and its performance was investigated under different fire scenarios where different compartments at different stories were exposed to fire. The results of the fire exposed structures are compared to that of the structure at ambient temperature. Moreover, to characterize the influence of the fire damage on the seismic response of an isolated connection, an exterior beam-column connection was analyzed under different fire scenarios. The results of the study demonstrate the vulnerability of fire damaged steel buildings during seismic events.

3. References

- [1] FEMA-350. Recommendation and seismic design criteria for new steel moment-frame buildings. Prepared by the SAC Joint Venture for the Federal Emergency Management Agency, Washington, DC, 2000.

- [2] FEMA-353. Recommended specifications and quality assurance guidelines for steel moment- frame construction for seismic applications. Prepared by the SAC Joint Venture for the Federal Emergency Management Agency, Washington, DC, 2000.
- [3] FEMA-355B. State of the art report on welding and inspection. Prepared by the SAC Joint Venture for the Federal Emergency Management Agency, Washington, DC, 2000.
- [4] FEMA-355D. State of the art report on connection performance. Prepared by the SAC Joint Venture for the Federal Emergency Management Agency, Washington, DC, 2000.
- [5] Nakashima M, Suita K, Marisako K, Maruoka Y. Tests of welded beam-column subassemblies. I. Global behavior. *Journal of Structural Engineering* 1998;124:1236-1244.
- [6] SAC/BD-99/23. Failure analysis of welded beam to column connections. by Barsom, JM, Pellegrino JV.
- [7] Uang CM, Yu QS, Noel S, Gross J. Cyclic testing of steel moment connections rehabilitated with RBS or welded haunch. *Journal of Structural Engineering* 2000;126:57-68.
- [8] Stojadinovic B, Goel SC, Lee KH, Margarian AG, Choi JH. Parametric tests on unreinforced steel moment connections. *Journal of Structural Engineering* 2000;126:40-49.
- [9] SAC/BD-00/01. Parametric tests on unreinforced connections. by Lee KH, Stojadinovic B, Goel SC, Margarian AG, Choi J, Wongkaew A, Reyher BP, Lee DY.
- [10] SAC/BD-00/24. Development and evaluation of improved details for ductile welded unreinforced flange connections. by Ricles JM, Mao C, Lu LW, Fisher JW.

- [11] Lee D, Cotton SC, Hajjar JF, Dexter RJ. Cyclic behavior of steel moment-resisting connections reinforced by alternative column stiffener details, I. Connection performance and continuity plate detailing. *Engineering Journal* 2005;4th Quarter:189-213.
- [12] AISC (2010a). Seismic provisions for structural steel buildings. American Institute of Steel Construction 341, AISC 341-10.
- [13] Tsai KC, Popov EP. Cyclic behavior of end-plate moment connections. *Journal of Structural Engineering* 1990;116(11):2917-2930.
- [14] Roeder CW, Douglas AF. Experimental results for seismic resistant steel moment frame connections. *Journal of Structural Engineering* 1996;122(6):581-588.
- [15] Engelhardt MD, Winneberger T, Zekany AJ, Polyraj TJ. Experimental investigation of dogbone moment connections. *Engineering Journal* 1998;35:128-139.
- [16] Adey BT, Grondin GY, Cheng JJR. Cyclic loading of end plate moment connections. *Canadian Journal of Civil Engineering* 2000;27:683-701.
- [17] Popov EP, Takhirov SM. Bolted large seismic steel beam-to-column connections part 1: experimental study. *Engineering Structures* 2002;24:1523-1534.
- [18] Ricles JM, Fisher JW, Lu LW, Kaufmann EJ. Development of improved welded moment connections for earthquake-resistant design. *Journal of Constructional Steel Research* 2002;58:565-604.
- [19] Sumner EA, Murray TM. Behavior of extended end-plate moment connections subject to cyclic loading. *Journal of Structural Engineering* 2002;128(4):501-508.
- [20] AISC (2010b). Prequalified connections for special and intermediate steel moment frames for seismic applications. American Institute of Steel Construction 358, AISC 358-10.

- [21] Stojadinovic B, Goel SC, Lee KH, Margarian AG, Choi JH. Parametric tests on unreinforced steel moment connections. *Journal of Structural Engineering* 2000;126:40-49.
- [22] Suita K, Nakashima M, Morisako K. Tests of welded beam-column subassemblies II: Detailed behavior. *Journal of Structural Engineering* 1998;124(11):1245-1252.
- [23] Mazzolani FM. (Editor). *Moment resistant connections of steel frames in seismic areas: design and reliability*. E&FN Spon, 2000.
- [24] Castiglioni CA. Effects of the loading history on the local buckling behavior and failure mode of welded beam-to-column joints in moment-resisting steel frames. *Journal of Engineering Mechanics* 2005;131:568-585.
- [25] Han SW, Kwon GU, Moon KH. Cyclic behavior of post-Northridge WUF-B connections. *Journal of Constructional Steel Research* 2009;63(3):365-374.
- [26] Rodgers JE, Stephen AM. Effects of connection fractures on global behavior of steel moment frames subjected to earthquakes. *Journal of Structural Engineering* 2006;132(1):78-88.
- [27] Shi G, Shi Y, Wang Y. Behavior of end-plate moment connections under earthquake loading. *Engineering structures* 2007;29(5):703-716.
- [28] Guo B, Gu Q, Liu F. Experimental behavior of stiffened and unstiffened end-plate connections under cyclic loading. *Journal of Structural Engineering* 2006;132(9):1352-1357.
- [29] Ghobarah A, Osman A, Korol RM. Behavior of extended end-plate connections under cyclic loading. *Engineering Structures* 1990;12(1):15-27.

**CHAPTER 2: AN IMPROVED UNSTIFFENED 8 BOLT EXTENDED
END PLATE MOMENT CONNECTION FOR SPECIAL AND
INTERMEDIATE MOMENT FRAMES
PART I: NUMERICAL MODELING AND MODIFIED DESIGN
DEVELOPMENT**

Abstract

Eight bolt stiffened extended (8ES) end plate connection is one of the prequalified connections proposed by AISC 358 Standards for special moment frames (SMFs) in seismic regions. In 8ES connection, a gusset plate is welded between the end plate and the beam flanges to strengthen the extended portion of the end plate. In addition to increasing the flexural strength, it helps in forming plastic hinge away from the connection region as well as distributing the flange forces evenly to the connecting bolts. In experimental studies, this connection showed good performance in energy dissipation and ductility in many cases, whereas premature fracture of beam flange or stiffener or weld between beam flange/end plate and stiffener, leading to a brittle mode of failure of the connection have also been observed due to high stress concentration. The study reported herein performed detailed finite element analysis to understand the failure mechanism of the eight bolt unstiffened/stiffened extended end plate moment connections, and thereby develop a modified design of eight bolt extended end plate connection. In the modified design, the end plate stiffeners were excluded from the connection to eliminate the stress concentration associated with the stiffener, and the bolts were rearranged into a hexagonal pattern to ensure uniform distribution of bolt forces. It was observed that the hexagonal rearrangement of the bolts improves connection performance, but does not necessarily ensure formation of plastic hinge away from the connection region for different beam sections. However, with a recent idea of heat treating the beam flanges integrated into the connection design ensures formation of the plastic hinge at the desired location regardless of the size of the beam. The modified design with the new bolt pattern and heat treatment showed improvement in the seismic

response of the connection in terms of ductility and energy dissipation capacity. However, in terms of strength degradation, no noticeable improvement was observed because of the lateral instability of the connection. To delay the onset of strength degradation for the modified connection, the web of the beam was strengthened by a stiffener to reinforce the connection region. It was observed that the modified connection was able to sustain 6% interstory drift angle without losing significant strength and also, exhibited very good ductility and energy dissipation capacity under simulated seismic loading. Overall, the seismic resilience of the extended end plate connection has been improved with the proposed design. The novel connection design has been validated through full scale experimental testing of extended end plate moment connections and has demonstrated excellent performance under simulated seismic loading, which will be presented in a separate study.

Keywords: Extended end plate connection, Seismic performance, Hexagonal bolt arrangement, Heat treated beam section, Beam web stiffener

1. Introduction

Before the 1994 Northridge Earthquake, welded unreinforced flange bolted web (WUF-B) moment connections were used extensively in the construction of steel buildings in North America. However, during the 1994 Northridge Earthquake many steel buildings were seriously damaged at the WUF-B connections and several exhibited brittle failures [1]. Since then a considerable research activities have been performed to find alternatives to the WUF-B moment connections [1-8]. Based on a decade of research activities after the 1994 Northridge earthquake, five moment resisting connections were prequalified by AISC 358 Standards for special (SMFs) and intermediate (IMFs) moment frames [9]. One of these five prequalified connections is extended end plate connection which is the subject of this study. In extended end plate connections, a steel plate is shop welded to the end of a beam which is then field bolted to the connecting member. These connections are primarily used to connect a beam to a column or to splice two beams together. The end plate is extended beyond the beam flanges such that the bolts can be positioned outside the flanges on the extended part of

the end plate. Extended end plate connection can be stiffened or unstiffened. The stiffened configuration has a gusset plate (stiffener) welded to the outside of the beam flange and to the end plate. The stiffener is aligned with the web of the connecting beam to strengthen the extended portion of the end plate. Extended end plate moment connections are further classified based on the number and arrangement of the bolts. The two most common types of the extended end plate connections prequalified by the AISC 358 Standards are four bolt extended unstiffened and eight bolt extended stiffened end plate connections (Figure 1a, b). The prequalification of these connections emanated from the study of Sumner and co-workers [10-13], where they performed experimental investigation of the connections under simulated seismic loading recommended by the Protocol for Fabrication, Inspection, Testing, and Documentation of Beam-column Connection Tests and Other Experimental Specimens [14]. The study reported herein dealt with the eight bolt configuration of the extended end plate connection.

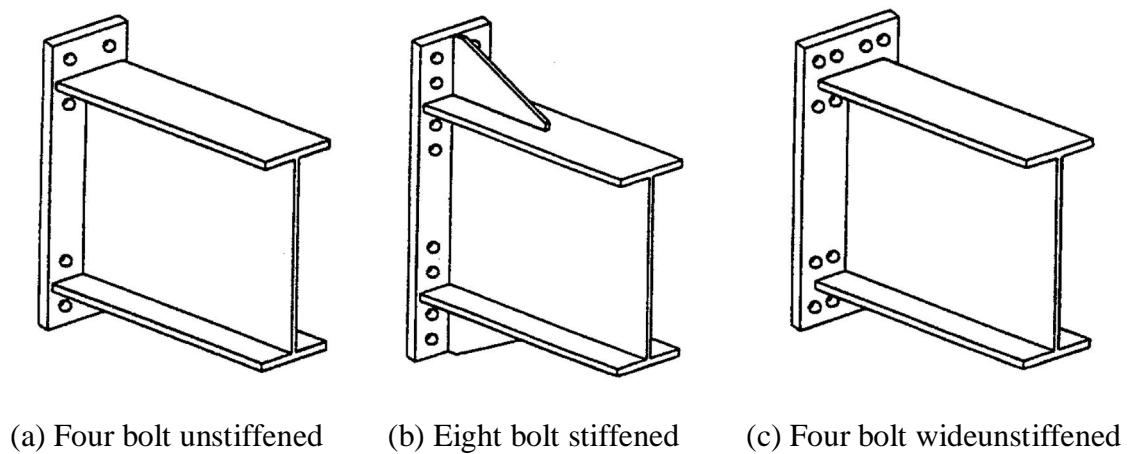


Figure 1 Different configurations of extended end plate moment connections.

The eight bolt configuration of the extended end plate connection is prequalified with a stiffener welded between the end plate and the beam flanges commonly referred to as eight bolt stiffened extended end plate connection or 8ES connection. The stiffener is usually provided to strengthen the extended portion of the end plate. In addition to enhancing the

flexural strength, it helps in forming plastic hinge away from the connection region as well as ensure uniform distribution of bolt forces. In many experimental studies, stiffened connections showed good performance in energy dissipation and ductility [10-13, 15-23] which demonstrated the applicability of the connection for seismic application. However, there have been some experimental studies where undesirable mode of failure was observed which was associated with the presence of the stiffener in the extended portion of the end plate. In the studies by Ghobarah *et al.* [17], Korol *et al.* [16] and Guo *et al.* [24] crack was observed at the toe of the weld between the beam and the end plate stiffener at large inelastic loading cycles which was attributed to the stress concentration induced by the stiffener. In the experiments performed by Adey *et al.* [13], the end plate ruptured around the beam flange and stiffener. They also observed pullout of the stiffener in some of their experiments. Shi *et al.* [25] observed fracture and buckling of the end plate stiffener during cyclic testing of extended end plate connections. The observations made in these studies led to the notion that the end plate stiffener imposes a high stress concentration at the interface between the stiffener and the beam flange or end plate. As a result, the inelastic actions are localized at these locations which may lead to fracture of beam flange, end plate or stiffener, fracture of the welds between the stiffener and beam flange/end plate and local buckling of the stiffener. In addition to the unfavorable failure modes caused by the stiffener, a portion of the stiffened end plate may extend above the finished floor requiring a larger column closer and reduced useable floor area [26]. Moreover, the cost of construction increases due to the weld works required for attaching the stiffener to beam flange and end plate. These shortcomings of the 8ES connection induced by the presence of the stiffener motivate further investigation for improving the resilience of the connection by removing the end plate stiffener.

In the works of Sumner and co-workers [10], a different configuration of the eight bolt extended end plate connection was investigated, where four bolts were arranged in a single row at each of the beam flanges eliminating the necessity of end plate stiffener as shown in Figure 1c. In their experiments, this type of connection was referred to as four bolt wide unstiffened extended end plate connection or 4W connection. In the experiments, the 4W connection exhibited non-ductile behavior due to an uneven distribution of flange forces to

the connecting bolts, which disqualified this connection for seismic applications. The uneven distribution of the flange force between the bolts generated an unfavorable load path where the flange forces attempted to reach only the interior bolts, hence the interior bolts ruptured leading to tearing of end plate. The observations made from this study led to the conclusion that bolt arrangement can be a critical parameter in the flange force distribution as well as overall performance of the connection. Not much literature is available on the study of bolt arrangement on the seismic performance of extended end plate moment connection. Borgsmiller *et al.* [27] and Meng [28] showed that the connection geometry greatly influences the load path to the bolts and for some configurations, half of the bolts are ineffective in carrying load at all. Mays [29] performed parametric studies on the effect of the pitch distances between the bolt and the beam flange and also, between bolt columns for four bolt wide unstiffened extended end plate moment connection. It was observed that when the outer bolts remained at least 6.35 mm inside the beam flange tip, all the bolts performed effectively in distributing the flange forces. When the distance between the beam flange tip and bolt increased, an unfavorable load path was generated with very high strains in the inner bolts leading to bolt rupture type of failure. Adey *et al.* [21-23] observed greater flexibility and energy dissipation capacity of both four bolt and eight bolt extended end plate connections with and without stiffeners, when the distance between the bolt and beam flange was increased from $2d_b$ to $3d_b$ (d_b -bolt diameter). They also noticed that with increase in the pitch distance, the web to flange junction remained remote from the bolts which reduced the stresses at the web to flange junction. This could be beneficial because of the lack of fusion that may result when weld access holes are not used may not be detrimental to the behavior of the end plate connection. Gerami *et al.* [30] noticed an increased participation in the connection's components when the pitch distance was increased between the bolt and the beam flange. They also observed change in the failure mode based on the arrangement of the bolts for T-stub connection. These observations from the literature demonstrated that to get a better ductility and energy dissipation from the connection, it is important to generate a favorable load path so that the flange forces can be distributed evenly to the connecting bolts.

This study is motivated by these two findings from the literature-one is the problems associated with the presence of the stiffener and the other is the influence of bolt arrangement on the performance of the connection. In this study an attempt has been made to design an eight bolt extended end plate connection without end plate stiffener to eliminate the stress concentration, while the bolts have been rearranged to generate a favorable loading path through even distribution of bolt forces. A detailed finite element analysis was performed on extended end plate moment connections to understand the failure mechanisms for different types of bolt arrangement and thereby, a hexagonal pattern of bolt arrangement has been proposed such that all the bolts remain effective in distributing the flange forces equally. Although the hexagonal bolt arrangement alone showed improved performance of the connection for smaller size beam sections, it was observed that for larger size beam sections plastic hinge forms very close to the connection region leading to very high strain demands on the welds. Hence, a recent idea of heat treating the beam flanges proposed by Morrison *et al.* [31] was implemented to ensure formation of plastic hinge at a desired location by weakening the material strength. The modified bolt arrangement with heat treatment eliminates the necessity of using end plate stiffener, and is applicable to all the beam sections available. This connection showed improved performance in ductility and energy dissipation capacity compared to the 8ES connection. Nonetheless, the strength degradation started almost at the same interstory drift level for both the 8ES and modified connection due to the lateral instability of the connection as a result of reduced strength of the material. This indicates that the performance can be further improved if the onset of strength degradation can be delayed which was necessitated by the local buckling of the beam flanges and web. Therefore, the web of the beam was strengthened by welding a stiffener extended from the end plate to the end of the heat treated region to reinforce the connection region. The modified connection with heat treatment and web stiffener showed significant improvement in the seismic response of the connection, especially the strength degradation was significantly delayed because of the presence of web stiffener.

It must be mentioned here that during the course of developing the modified design of extended end plate connection in this study, Kiamanesh *et al.* [32] investigated a circular type

of bolt arrangement for extended end plate connection which is very similar to the type of bolt arrangement proposed in this study. The circular bolt arrangement was proposed to reduce the hysteresis pinching observed in extended end plate connection with rectangular bolt pattern without end plate stiffener. It was shown that the circular bolt pattern reduces hysteresis pinching noticeably for end plate connections with large bolts and thick end plates, whereas for connections with small bolts and thin end plates, the influence of circular bolt arrangement was insignificant. Although this study showed the promise of circular bolt pattern on the cyclic response of extended end plate connections, the necessity of modified bolt arrangement has not been addressed with proper comparison with the prequalified connection, where an end plate stiffener is used to strengthen the extended portion of the end plate. Moreover, the influence of circular bolt arrangement on the plastic hinge formation as well as the applicability of the circular bolt pattern based on the size of the beam section has not been addressed which should be a particular concern while designing a special moment frame for seismic application. The study reported herein addresses the necessity for developing the modified bolt arrangement with particular attention to the bolt force distribution, plastic hinge formation, energy dissipation, and ductility of the connection. Further, the applicability of the modified design for different beam sections available has been explained.

2. Finite Element Modeling of Extended End plate Connection

It has been shown that finite element methods can be used to predict the behavior of extended end plate connections reasonably [28-30, 33-39]. However, to capture the behavior of the extended end plate connection, it is important to model each individual component and their interaction precisely. In this study advanced finite element modeling technique has been employed to model each component of the connection and their interaction accurately. A brief description of the finite element modeling scheme adopted in this study is presented next.

2.1. Finite Element Discretization

Three dimensional nonlinear finite element models were developed for extended end plate connections by using the finite element analysis software ANSYS. Both geometric and material nonlinearities were incorporated in the finite element models. The beams and columns were modeled and discretized by eight noded solid brick elements (SOLID 185). This type of solid element is well suited for modeling 3D solid structures which can be defined by eight nodes having three degrees of freedom at each node. The modeling of bolt and end plate is very critical for accurate prediction of extended end plate connection's behavior because the rigid body motion in extended end plate connection is solely constrained by the contact between the bolt and the end plate. In order to precisely model the bolts and their interaction with the end plate, the solid bolt model was adopted in the finite element simulation. Although there are other bolt models available in the literature such as coupled bolt model, spider bolt model and no-bolt model, the solid bolt model is the most realistic finite element model since it considers the influence of the bolt stiffness on simulation, and has the provision of applying bolt pretension and generating contact between the bolt and the flanges [40]. The end plate and the bolt were discretized by twenty noded solid brick elements (SOLID 186) which exhibits quadratic displacement behavior. The interaction between the end plate and column flange, bolt head and end plate, bolt nut and column flange, and bolt shank and circular holes in the end plate and column flange are intricate and the modeling of these interactions is one of the important features in the finite element modeling. These interactions in the finite element modeling were defined by incorporating small sliding contact surfaces. Surface-to-surface contact elements (CONTA 174) and target elements (TARGE 170) were used to generate the contact regions. The contact elements themselves overlaid the solid elements describing the boundary of a deformable body and were potentially in contact with the target surface defined by TARGE170. This target surface is discretized by a set of target segment elements (TARGE170) and is paired with its associated contact surface via a shared real constant set. A penetration tolerance factor was applied in the direction of the surface normal to determine if penetration compatibility is satisfied. The amount of penetration between contact and

target surfaces depends on the normal stiffness. Higher stiffness values decrease the amount of penetration/slip, but can lead to ill-conditioning of the global stiffness matrix and to convergence difficulties. Lower stiffness values can lead to a certain amount of penetration/slip and produce an inaccurate solution. In the finite element modeling of the extended end plate connection, frictional contact was generated by using penalty stiffness with the penalty value of 0.1 so that the penetration/slip is acceptably small, but the problem is well-behaved in terms of convergence. In static analysis, rigid body motion will be an issue if the body is not sufficiently constrained. Since in extended end plate connection, the rigid body motion will be constrained by only the presence of contact, it was ensured that the contact pairs are in contact in the initial geometry i.e. the model was built in such a way that initially the contact pairs are just touching. This was accomplished through the use of the coefficients of initial contact closure and contact surface offset.

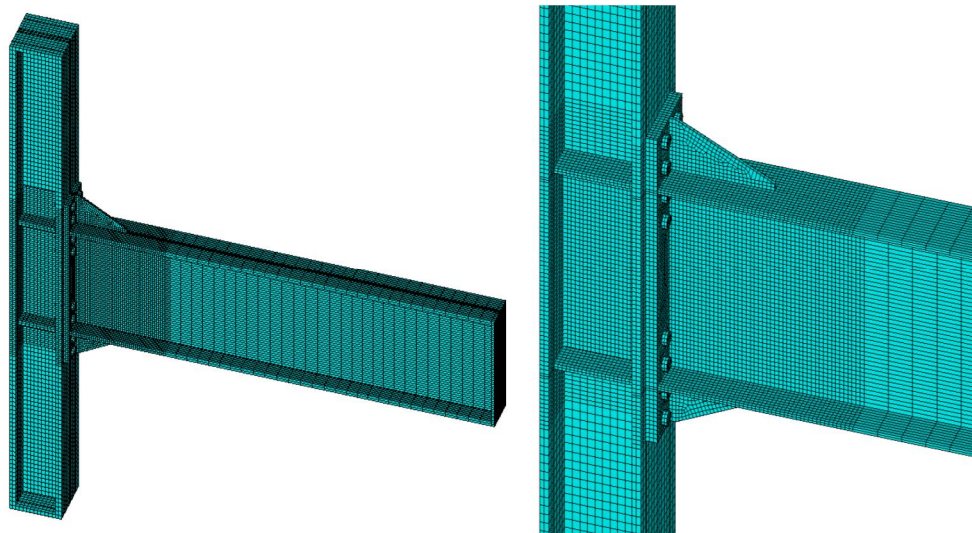


Figure 2 Finite element mesh of an eight bolt stiffened extended end plate connection.

Pretension in bolts and other structural components often have significant effect on deflections and stresses and hence, in the finite element modeling, it is essential to include

the effect of bolt pretensioning. For the finite element modeling of extended end plate connection, bolt pretension was modeled by using two ANSYS features, the PRETS179 pretension element and the PSMESH pretension meshing command. The pretension load was applied as specified by the AISC LRFD Specification [41]. A finer mesh was considered along the beam and column length in the vicinity of the beam-to-column connection, and also in the column panel zone where majority of the inelastic action occurs. The bolts and end plate was also discretized with finer mesh for accurate prediction of the connection behavior. The other regions of the connection will remain elastic and hence, coarser mesh was used in those places to reduce the computational time and cost. The mesh density was finalized based on a convergence study which gave a finite element model of extended end plate connection with 50569 elements and 71913 nodes. Figure 2 shows an example of the finite element mesh generated for an eight bolt stiffened extended end plate connection.

2.2. Material Models

The prediction of experimental responses of moment connections using finite element simulation is highly sensitive to the material models adopted and the parameters of the adopted material models, especially under cyclic loading. In the literature, most of the works related to the finite element modeling and analysis of extended end plate connection used either bilinear or multilinear kinematic hardening material model in the finite element simulation of the cyclic behavior of moment connections [29-30, 38-39]. Although both bilinear and multilinear material models obey von-Mises yield criterion and include Bauschinger effect, both the models are incapable of simulating ratcheting or shakedown, which is essential for cyclic response simulation of moment connections. Both multilinear and bilinear material models have a linear kinematic hardening rule and hence, are not sufficient for simulating ratcheting or shakedown. To simulate ratcheting and shakedown in a FE simulation, a metal plasticity model is required with a nonlinear kinematic hardening rule. Nonlinear kinematic hardening implies a shift (or movement) of the yield surface along a nonlinear path. The Chaboche material model [42], available in ANSYS Mechanical software, offers such a nonlinear kinematic hardening rule. Since this study deals with cyclic

response simulation of extended end plate connections, the advanced nonlinear kinematic hardening model of Chaboche [42] has been adopted in this study to define the material characteristics. A brief description of the Chaboche [42] model is given below to demonstrate different features of the model.

Table 1 Nonlinear kinematic hardening parameters for different steel materials.

Parameters	ASTM A36	ASTM A572 Gr.50	ASTM A992	ASTM A490	Heat treated ASTM A992
E (MPa)	186861	191505	199948	199948	199948
σ_0 (MPa)	261.5	251.7	238.6	777.7	193.74
C_1 (MPa)	119996.4	125415.7	383336.8	204615.8	1015116
C_2 (MPa)	10873.1	28868.4	280782.1	152250.1	145075.9
C_3 (MPa)	537.8	2675.2	50780	101318.5	59398.9
C_4 (MPa)	68.9	144.8	1958.3	32219.2	372.2
γ_1	1036	4585	21081.2	4143	60464.5
γ_2	129	324	6256.2	285	5253.1
γ_3	5	42	515	107	619
γ_4	0	0	13.2	0	9.8

The yield criterion:

$$J_2(\underline{\sigma} - \underline{\alpha}) = \left[\frac{3}{2} (\underline{s} - \underline{a}) \cdot (\underline{s} - \underline{a}) \right]^{1/2} = \sigma_0 + R(p, q), \quad (1)$$

where $\underline{\sigma}$ is the stress tensor, $\underline{\alpha}$ is the current center of the yield surface in the total stress space, \underline{s} is the deviatoric stress tensor, \underline{a} is the current yield surface center in the deviatoric space, σ_0 is the initial size of the yield surface, and R represents the isotropic hardening variable as a function of the accumulated plastic strain p and the size of the plastic strain surface q . The rate-independent plastic strain increment will be calculated using the associated flow rule:

$$d\underline{\varepsilon}^p = d\lambda \frac{\partial J_2}{\partial \underline{\sigma}} = \frac{3}{2} dp \frac{\underline{s} - \underline{a}}{\sigma_0 + R} \quad (2)$$

The superimposed kinematic hardening rule is given by:

$$d\mathbf{a} = \sum_{i=1}^4 d\mathbf{a}_i \quad (3)$$

$$d\mathbf{a}_i = \frac{2}{3} C_i d\mathbf{\underline{\epsilon}}^p - \gamma_i \mathbf{a}_i d\mathbf{p} \quad (4)$$

Each of the superposed kinematic hardening rules has a strain hardening term (1st term in Eq. 4) and a dynamic recovery term (2nd term in Eq. 4). These are important modeling features for simulating cyclic responses of materials.

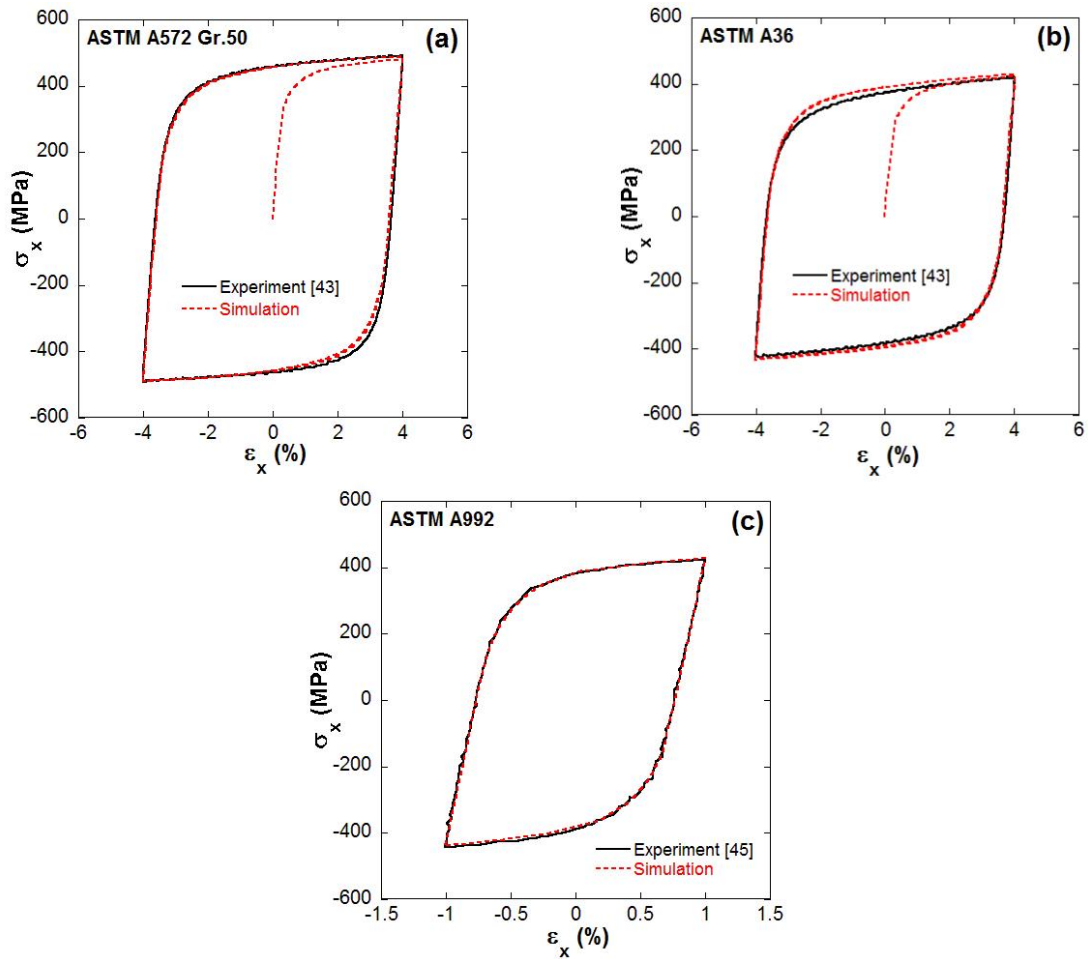


Figure 3 Experimental and simulated response of strain controlled hysteresis loop with Chaboche model parameters. (a) ASTM A572 Gr.50 steel; (b) ASTM A36 steel; (c) ASTM A992 steel.

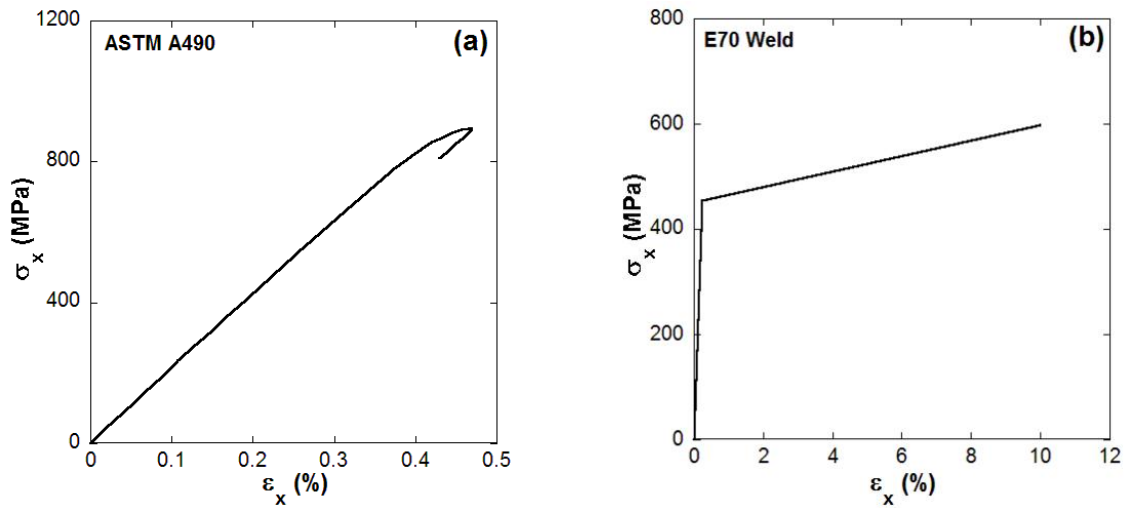


Figure 4 Monotonic stress-strain curves for bolt and weld materials. (a) ASTM A490 bolt; (b) E70 weld [2].

In the finite element modeling of the extended end plate connection, ASTM A992 and A570 Gr.50 steels were used as the beam and column materials, whereas ASTM A36 was used as the end plate material. Bolts were modeled as ASTM A490/A325 bolts. Use of Chaboche model to simulate the material responses requires that the stable hysteresis loop of the cyclic stress–strain response be known. In this case, stable hysteresis loops were obtained from single amplitude strain controlled cyclic test of ASTM A992, ASTM A572 Gr.50 and ASTM A36 steel coupons [43-44]. Chaboche parameters were determined from the up going strain controlled experiment of ASTM A992, ASTM A572 Gr.50 and ASTM A36 steels. The nonlinear kinematic hardening parameters (shown in Table 1) were determined by using a genetic algorithm based optimization method. Simulations were made at the material level with obtained parameters for validation. As shown in Figure 3, the simulated responses harmonized very well with the experimental responses. The connection between the beam flanges and end plate was modeled with groove welds using the flux core arc welding procedure with E70TG-K2 electrodes. The material properties of E70 weld metal was obtained from FEMA-355B [2] and it was implemented in the FE simulation through bilinear

material model as shown Figure 4b. For determining the material properties of ASTM A490 bolts, uniaxial test was performed on ASTM A490 bolts, and Chaboche model parameters (shown in Table 1) were obtained through fitting the monotonic stress-strain curve (Figure 4a) by using genetic algorithm based optimization method.

2.3. Loads and Boundary Conditions

In the finite element modeling of the extended end plate moment connection, the boundary conditions were applied such that it mimics the boundary conditions applied in the experimental setup for conventional seismic testing of moment connections. A typical experimental setup for full scale seismic testing of an exterior beam-column assembly used by Morrison *et al.* [31] is shown in Figure 5a and this configuration of the experimental setup was adopted for the finite element analysis of extended end plate connections. In the finite element modeling, the nodes at the two ends of the column were hinged i.e. x, y and z-direction of the nodal displacements were zeroed.

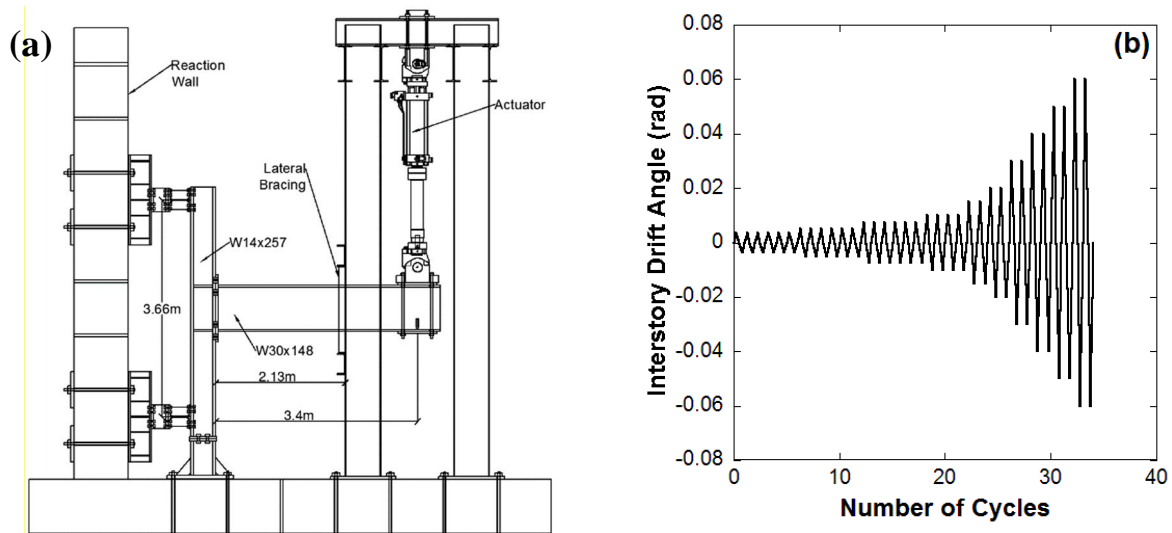


Figure 5 (a) A typical experimental setup for seismic testing of moment connections [31];
(b) SAC loading protocol [14].

Lateral supports were simulated as lateral restraint with z-direction nodal translation zeroed at their point of contact with the beam. Vertical displacement was applied at all the central nodes located on the stiffener plate at the free end of the beam so as to simulate the displacement controlled actuator loading during the actual test. All beam-column assembly was analyzed with a displacement-based artificial loading protocol offered by SAC/BD-97/02 [14]. The displacement based time history was based on the SAC Test Protocol and consisted of imposing a series of prescribed quasi-static cyclic displacements to the end of the beam [14]. The prescribed displacements included six cycles of 0.375, 0.5 and 0.75% interstory drift, followed by four cycles of 1% interstory drift and two cycles each of 1.5, 2, 3, 4, 5, 6% and so forth interstory drift [14]. A schematic of the loading protocol is shown in Figure 5b.

3. Validation of Finite Element Model

The first step of the finite element analysis was to validate the precision of the finite element model in predicting the cyclic response of extended end plate moment connections. This was achieved by comparing finite element analysis (FEA) results against experimental responses. In this study, the finite element model was validated against the experimental response of the eight bolt stiffened extended end plate connection (8ES-1.25-1.75-30) of Sumner *et al.* [10]. Figure 6 shows comparison of simulated and experimental moment-rotation response of 8ES-1.25-1.75-30 specimen tested by Sumner *et al.* [10]. It was observed that the simulated hysteresis loop shapes accorded very well with the experimental hysteresis loop shapes. The peak moments in each cycle and the initiation of strength degradation in the experimental responses was captured precisely in the finite element simulation. The global and local buckling phenomena observed in the experiments were also simulated very well by the finite element model as shown in Figure 7, where the simulated deformed shape of the specimen is compared with the experimental deformed shape showing plastic hinge formation at the base of the stiffener at the end of loading cycles corresponding to 6% interstory drift angle. The resemblance of the simulated responses with those of the

experimental responses validates the adequacy of the developed finite element model for predicting the seismic response of extended end plate moment connections.

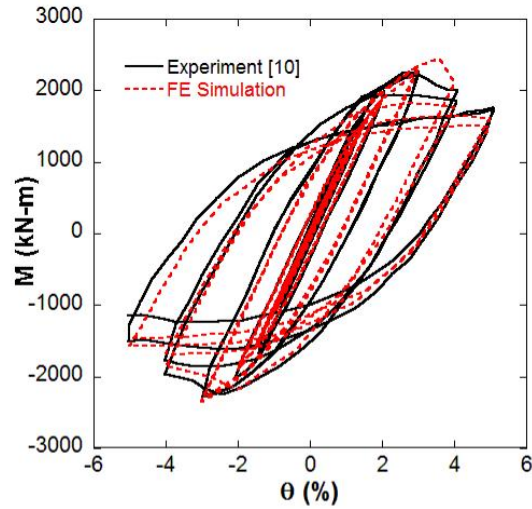


Figure 6 Comparison between experimental and simulated moment-rotation response of eight bolt stiffened extended end plate connection (8ES-1.25-1.75-30) tested by Sumner *et al.* [10].

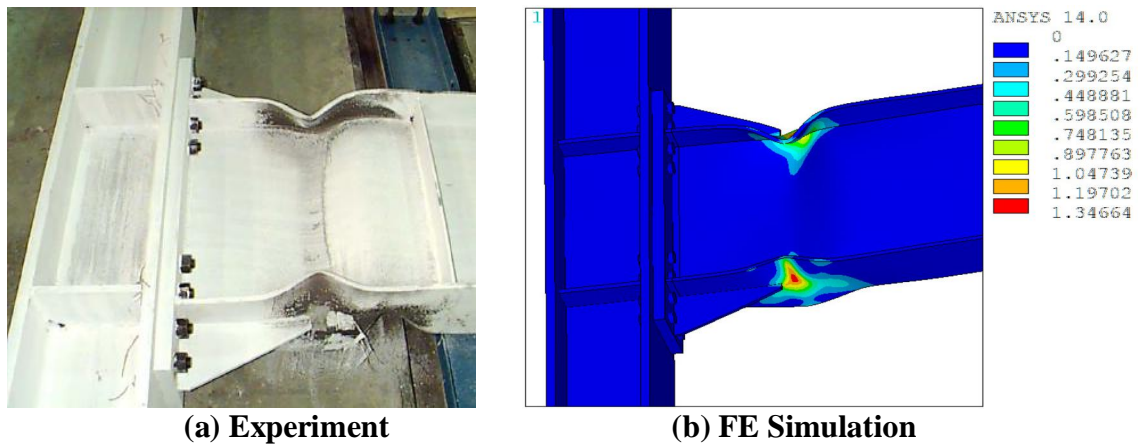


Figure 7 Comparison of experimental and simulated deformed shape for 8ES-1.25-1.75-30 specimen of Sumner *et al.* [10] showing formation of plastic hinge at the base of the stiffener.

4. Finite Element Analysis of Extended End plate Connections

In this part of the study, detailed finite element analysis was performed on eight bolt extended end plate connections with different bolt arrangements in order to investigate the failure mechanisms involved and come up with an optimized bolt arrangement which does not require end plate stiffener, yet improves the seismic performance of the connection. An exterior sub-assembly was chosen consisting of a W14×193 (ASTM A992) column with a single W30×99 (ASTM A992) beam attached to the flange. This is the connection setup that was used by Sumner *et al.* [10] as discussed in the validation part of the study, except the fact that in the experiments, the beam and column material was ASTM A572 Gr.50. The beam-to-column connection was designed to develop 110% of the nominal plastic moment capacity of the beam as recommended by AISC 358 Standard [9]. The following four types of connection configurations were considered consisting of eight bolts at each flange with different arrangements of bolts.

- i. Eight bolt stiffened connection (8ES): four rows of two bolts at each flange, two rows above and two rows below the flange with end plate stiffener (Sumner *et al.* [10]).
- ii. Eight bolt unstiffened connection (8E): four rows of two bolts at each flange, two rows above and two rows below the flange without end plate stiffener.
- iii. Four bolt wide unstiffened connection (4W): two rows of four bolts at each flange, one row above and one row below the flange without end plate stiffener (Sumner *et al.* [10]).
- iv. Modified eight bolt unstiffened connection (8EM): four rows of two bolts at each flange, two rows above and two rows below the flange without end plate stiffener with hexagonal bolt pattern.

The end plate material used was ASTM A36 which was bolted to the column flange with ASTM A490/A325 bolts. The bolts were given a pretension as specified in the AISC LRFD specification [41]. The column was reinforced with 19.05 mm continuity plates and a 9.525 mm doubler plate. Lateral supports were provided for the beam at a distance of 1.25 m, 2.46 m and 5.72 m from the centerline of the column [10]. No lateral supports were provided for the column. The loading was applied to the beam at a distance of 6.13 m from the centerline

of the column. All the connections were analyzed under displacement controlled cyclic loading in accordance with the SAC loading protocol [14] as shown in Figure 5b. The results of the finite element analysis on the above mentioned four types of connection configurations are presented next.

4.1. Eight Bolt Stiffened Extended End plate Connection (8ES)

The conventional eight bolt stiffened extended end plate connection (8ES) was designed according to the AISC [9] design requirements for SMFs in the regions of moderate to high seismicity. The connection had an end plate thickness of 44.45 mm (ASTM A36) which was bolted to the column flange with 31.75 mm diameter ASTM A490 bolts. The bolts were arranged in four rows of two bolts at each flange, two rows above and two rows below the flange. There was a 12.7 mm thick end plate stiffener placed at the extended portion of the end plate which was welded to the end plate and the beam flange. The material properties used for end plate stiffener was ASTM A36. The finite element model was developed mimicking the test configuration of Sumner *et al.* [10] which was then subjected to simulated earthquake loading history upto 6% interstory drift angle to evaluate its seismic performance.

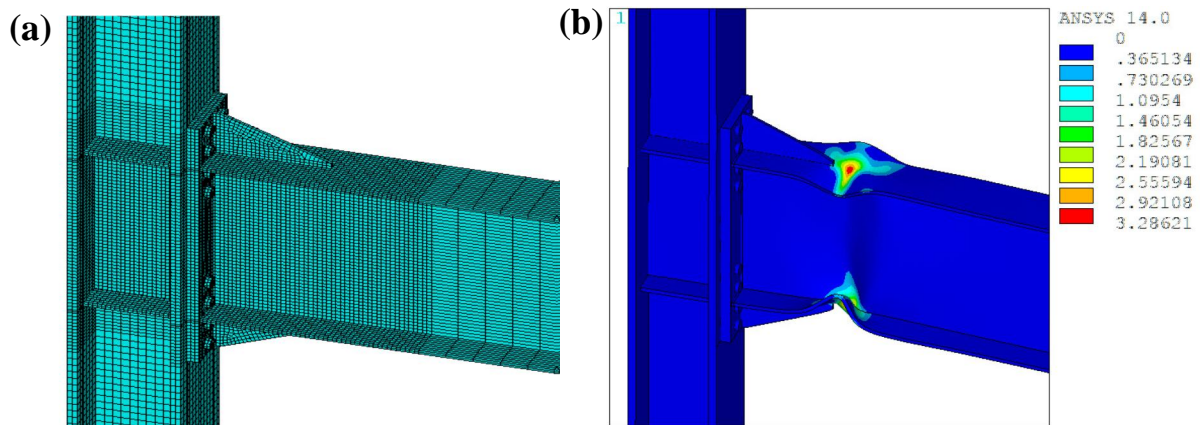


Figure 8 Eight bolt stiffened extended end plate connection (8ES). (a) FE mesh; (b) Equivalent plastic strain contour showing formation of plastic hinge after cyclic loading upto 6% interstory drift angle.

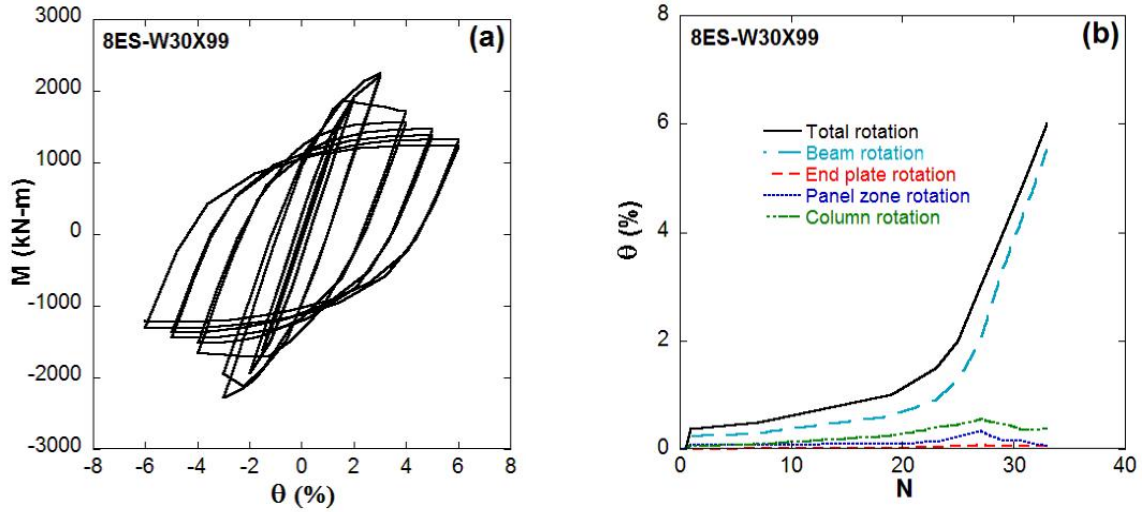


Figure 9 Cyclic response of 8ES configuration of connection. (a) Moment-rotation hysteresis response for cyclic loading up to 6% interstory drift angle; (b) Contribution of different components of the connection in the total rotation.

The finite element mesh of the connection is shown in Figure 8a. In the discussion, this configuration of the connection has been denoted as 8ES followed by the beam size analyzed. The connection showed ductile behavior by forming plastic hinge at a distance of 492 mm away from the face of the column which was at the base of the end plate stiffener as can be seen in Figure 8b. The moment-rotation plot of the connection (shown in Figure 9a) showed initiation of strength degradation in the 2nd cycle of 3% interstory drift angle which became significant (30%) during loading cycles for 4% interstory drift angle. As the loading cycles progressed, the strength of the connection dropped by 40% at 6% interstory drift angle, because of the instability created due to the lateral buckling of the beam. The contributions of the beam, panel zone, column and end plate to the maximum interstory drift angle of 6% were: $\theta_b=5.51\%$, $\theta_{pz}=0.07\%$, $\theta_c=0.37\%$, $\theta_{ep}=0.05\%$ (shown in Figure 9b). It was obvious that beam played the most dominant role in carrying most of the rotation capacity of the connection by forming plastic hinge away from the face of the column. The participation of the other components of the connection such as end plate, column and panel zone was

negligible in comparison to beam, especially the end plate's contribution in the rotation capacity of the connection was minimal. This was expected as the connection was designed for 110% of the nominal plastic moment capacity of the beam and the presence of end plate stiffener made the connection more rigid which attenuated the participation of the end plate.

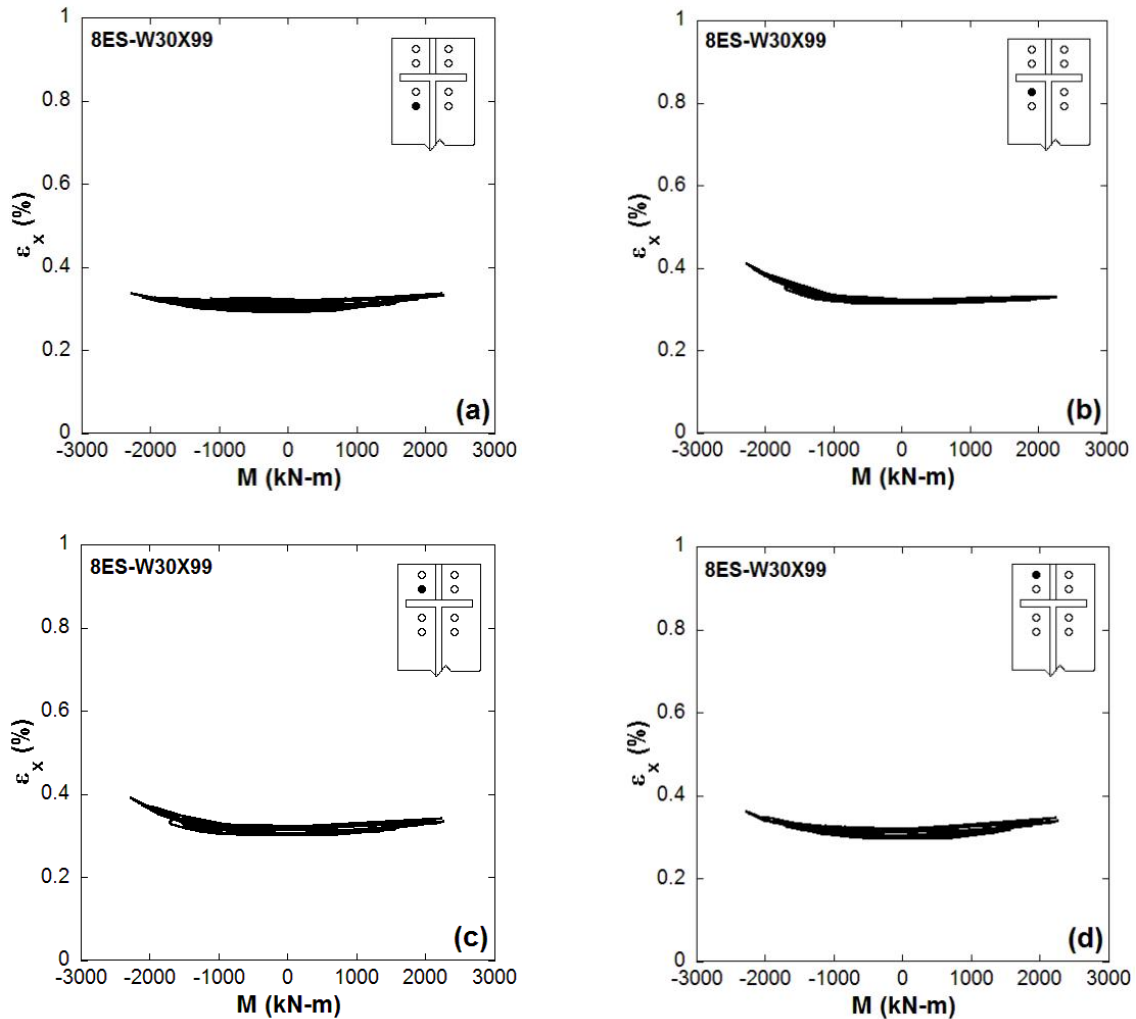


Figure 10 Bolt strains for 8ES configuration during loading cycles at the top flange of the beam.

It is to be noted here that the contributions from panel zone, column and end plate in the rotation capacity of the connection started to decrease when the beam started to buckle

locally, indicating an increase in the beam's participation in the rotation capacity of the connection. The bolt strains were in the elastic range and a gradual decrease in the bolt strains was observed during cycling (Figure 10). The bolt strains cycled within the pretension strain range and it was noticeable that the bolt strains in the outer and inner bolts for both top and bottom rows of bolts at each flange was uniform. This was achieved through the presence of the end plate stiffener which generated a favorable load path for the flanges to distribute the forces to the bolts evenly. Throughout the loading cycles, the axial strains in both the top and bottom flange groove weld never crossed 1% which shows lower strain demands on the welds of the beam. The axial strain profile along the width of the beam bottom flange at the weld toe is shown in Figure 22a for loading cycle at the end of 4% interstory drift angle.

4.2. Eight Bolt Unstiffened Extended End plate Connection (8E)

For the sake of comparison, the end plate stiffener in 8ES connection was removed and the connection was analyzed under simulated earthquake loading history to understand the influence of the stiffener on the performance of the connection. In the discussion, this configuration of the connection has been denoted as 8E followed by the beam size analyzed. The finite element mesh and the equivalent plastic strain contour for 8E configuration of the connection are shown in Figure 11. The 8E configuration also showed global and local buckling of the beam flanges leading to formation of plastic hinge (Figure 11b), but unlike 8ES connection, the plastic hinge formed close to the column (100 mm) as a result of the removal of end plate stiffener. Consequently, the axial strains at the toe of the weld was much higher compared to the 8ES configuration. The weld strain profile shown in Figure 12 showed that the axial strain reached 5% during loading cycles at 5% interstory drift angle leading to around 8% strain in the bottom beam flange weld during 6% interstory drift angle. This imposes a large strain demand on the weld, which might lead to brittle weld failure of the connection. Moreover, two bolt inner rows are relatively closer to the beam flanges compared to the outer rows of bolts, and since the end plate stiffener has been removed, the strain distribution in the bolts was not uniform unlike 8ES configuration of the connection.

As shown in Figure 13, the inner bolt strains were much higher than the strains in the outer bolts indicating an uneven distribution of the flange forces to the bolts.

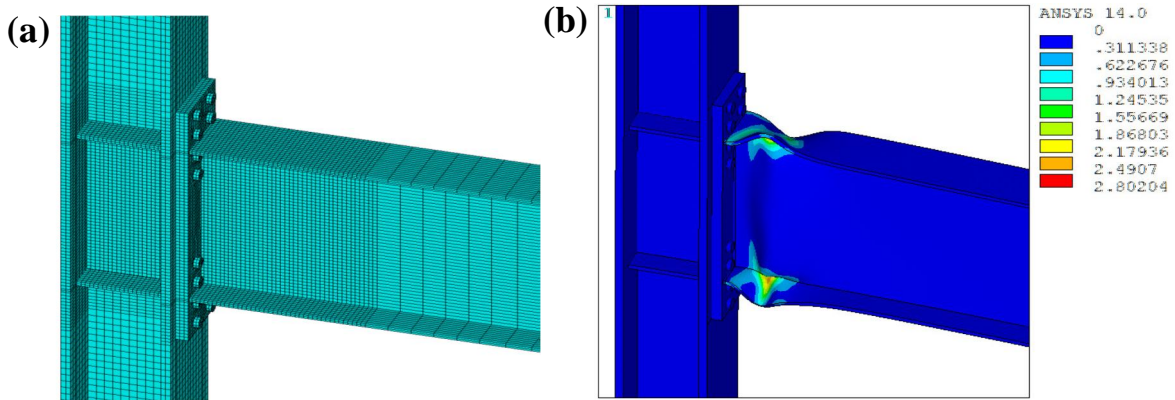


Figure 11 Eight bolt unstiffened extended end plate connection (8E). (a) FE mesh; (b) Equivalent plastic strain contour showing formation of plastic hinge after cyclic loading upto 6% interstory drift angle.

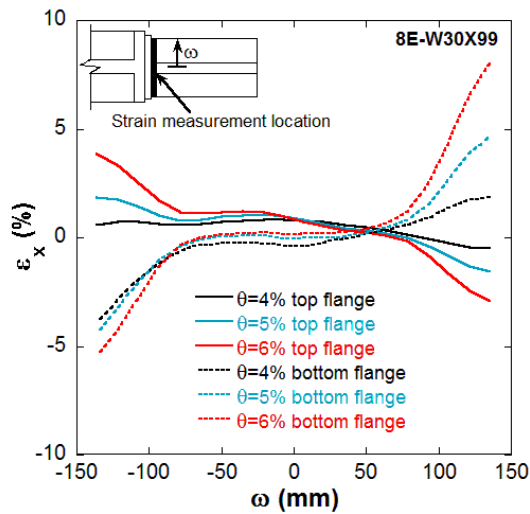


Figure 12 Axial strain profile along the width of beam flange at the weld toe for 8E configuration of the connection.

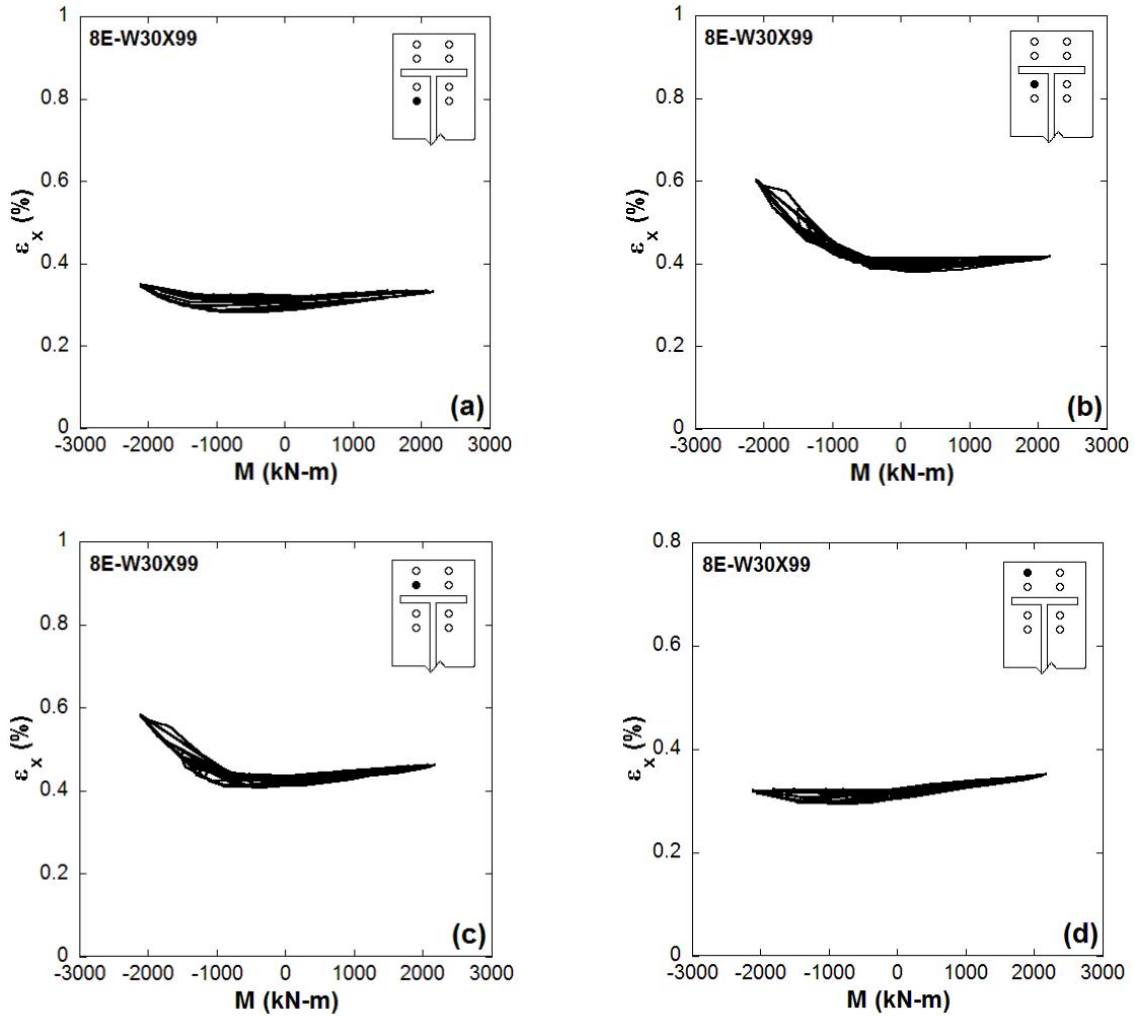


Figure 13 Bolt strains for 8E configuration during loading cycles at the top flange of the beam.

In other words, the outer bolts were not as effective as the inner bolts in carrying the flange forces. However, the strains in both the inner and outer bolts were in the elastic range during the loading cycles. For outer bolts, the strain in the bolts cycled within the pretension strain range with a gradual decrease in the bolt strain during cycling. On the other hand, for inner bolts, the bolt strains were observed to cycle from the initial pretension strain up to strains of approximately 40% above the pretension strain. The finite element analysis results

of the 8E configuration of the connection revealed the consequence of removal of end plate stiffener which showed uneven bolt force distribution and high strain demands on the weld, which may lead to brittle failure of the connection.

4.3. Four Bolt Wide Unstiffened Extended End plate Connection (4W)

Similar to 8ES and 8E configuration of the connection, the four bolt wide unstiffened extended end plate connection (4W) utilizes eight bolts at each flange for connecting the beam to the column, but the bolts are arranged in two rows instead of four rows unlike 8ES and 8E connections. Each row has four bolts, one row above and one row below each flange of the beam. This configuration of the connection is particularly suitable for wide flange W shapes since it requires a larger width of the end plate compared to 8E and 8ES connection. On the contrary, arranging bolts in single row reduces the depth of the end plate. As already mentioned, this type of connection configuration was tested by Sumner *et al.* [10], and the connection developed unfavorable loading path which led to non-ductile failure of the connection through interior bolt rupture and end plate tearing. Figure 14 shows the FE mesh developed in this study for 4W connection and the equivalent plastic strain contour of 4W connection when subjected to the simulated earthquake loading history. The connection was not able to sustain more than 3% interstory drift angle and the bolt strains became so high that the finite element model suffered numerical instability. Initial yielding of the specimen was observed during loading cycles at 1% interstory drift angle in the beam flanges close to the weld. During load cycles for 2% interstory drift angle, additional yielding of the beam flanges was observed with small amount of yielding of beam web, panel zone and end plate. During cycling in 3% interstory drift angle, severe yielding of the beam flanges was observed close to the welds. At this point, the panel zone and end plate have yielded significantly. At the last cycle of 3% interstory drift angle, the two inner bolts in the inside face of the beam bottom flange showed very high strains which might lead to rupture of the bolts (Figure 14b). The same bolts ruptured in the tests performed by Sumner *et al.* [10]. In the test, the end plate tearing was observed very close to the weld region of the beam flanges. In the FE simulation, very high strain was observed at the same location which shows sign of possible failure of

end plate at that location. Figure 16 shows the equivalent plastic strain contour plots of end plate at 3% interstory drift angle.

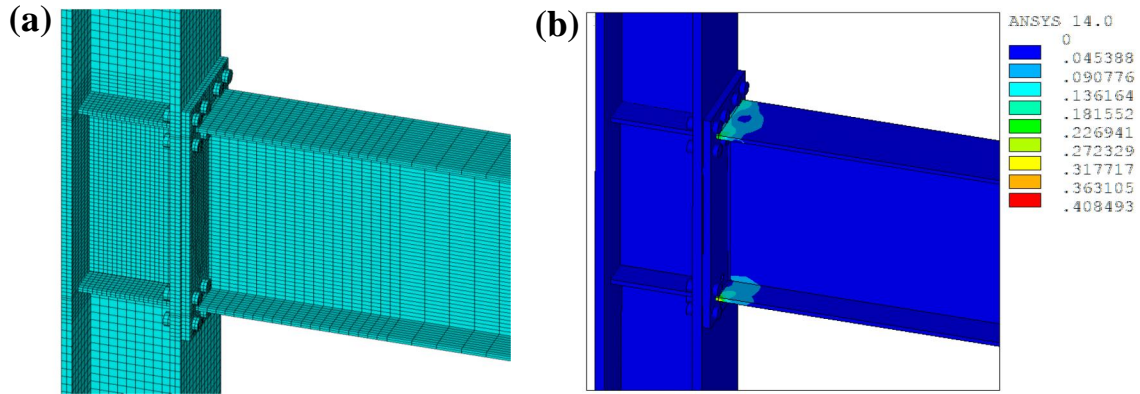


Figure 14 Four bolt wide unstiffened extended end plate connection (4W). (a) FE mesh; (b) Equivalent plastic strain contour showing bolt failure and high weld strain at 3% interstory drift angle.

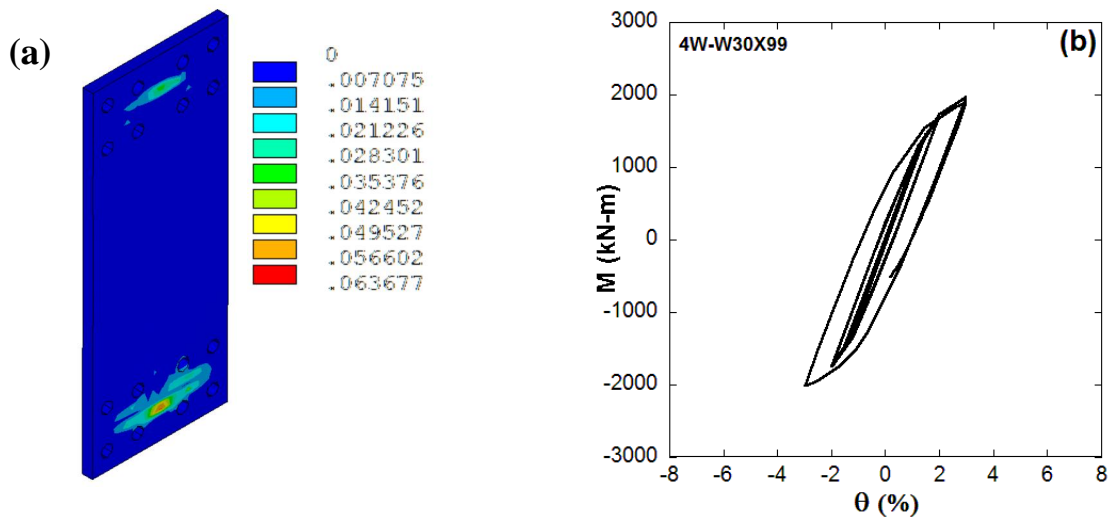


Figure 15 (a) Equivalent plastic strain contour of end plate at the end of 3% interstory drift angle; (b) Moment-rotation hysteresis response of 4W connection.

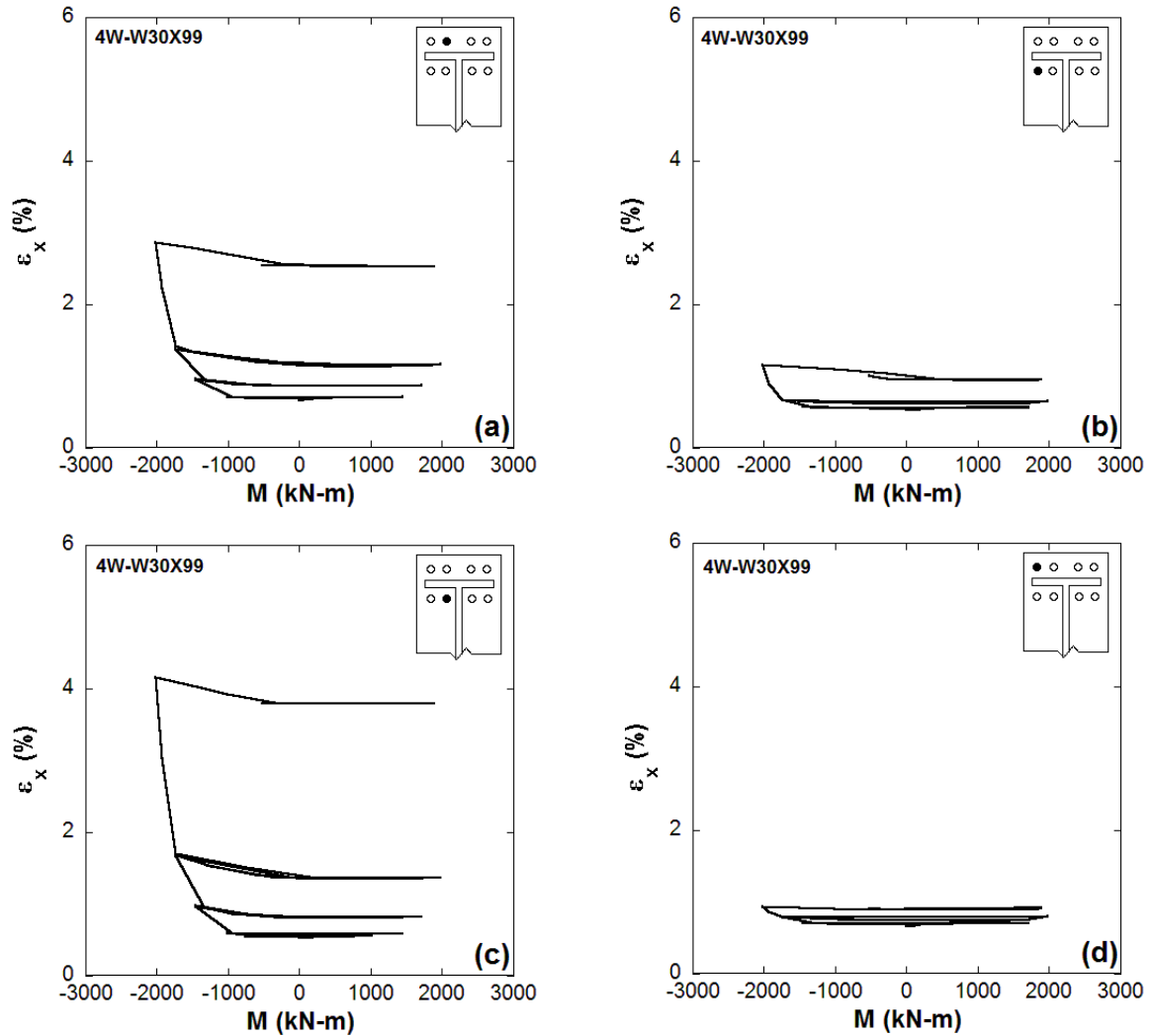


Figure 16 Bolt strains for 4W configuration during loading cycles at the top flange of the beam.

It is quite apparent that end plate had yielded significantly close to the beam flanges which might lead to tearing of the end plate. There was no reduction in the strength of the connection upto 3% interstory drift angle (Figure 16b) since it did not show any sign of local flange or web buckling. The bolts strain plots in Figure 16 show that the outside bolts in a row was not as effective as the inside bolts i.e. the flange forces were not distributed to all the bolts uniformly. The inside bolts on both the outer and inner rows showed very high strains

compared to the outside bolt strains. This uneven distribution of the flange forces to the connecting bolts generated an unfavorable loading path which may lead to premature bolt rupture and end plate tearing although a considerable amount of energy can be dissipated. In addition to high strains in the bolts and the end plate, the beam flanges yielded significantly very close to the groove weld, and once the bolt in the bottom flange experienced very high strains during the 2nd cycle of 3% interstory drift angle, there is a sudden jump in the axial strains (around 10% at the bottom flange as shown in Figure 17) at the weld toe which may lead to brittle weld failure of the connection. It is apparent that the 4W configuration of the connection is not suitable for seismic application because of the unfavorable load path generated during cyclic loading leading to premature bolt rupture, end plate tearing and very high weld strain demand.

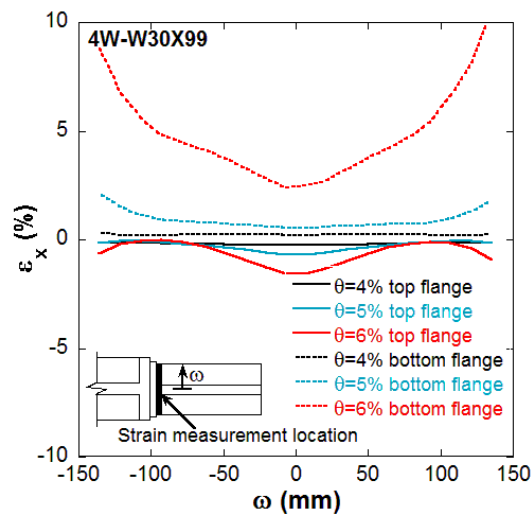


Figure 17 Axial strain profile along the width of beam flange at the weld toe for 4W configuration of the connection.

4.4. Eight Bolt Unstiffened Modified Extended End plate Connection (8EM)

From the finite element response and discussion in the preceding sections, it is quite obvious that 8E and 4W configurations of extended end plate connections showed unfavorable seismic behavior which is not suitable for SMFs. The distribution of flange

forces was uneven in the connecting bolts, the weld showed higher strain demands, and considerable amount of yielding of the end plate was observed. These shortcomings of the connections necessitate the importance of end plate stiffener in the conventional design of eight bolt stiffened extended end plate connections. However, as observed in some previous studies, the presence of the stiffener can degrade performance of the connection and result in a non-desirable failure mode such as buckling and fracture of the triangular stiffener, fracture of the beam flanges, and fracture of the weld between the stiffener and beam flange/end plate [16, 18, 21, 24-25]. In addition to producing undesirable failure modes, the inclusion of the end plate stiffener reduces the usable floor area as well as increases the construction cost because of the CJP groove weld that is required to attach the stiffener to the beam flanges and end plate.

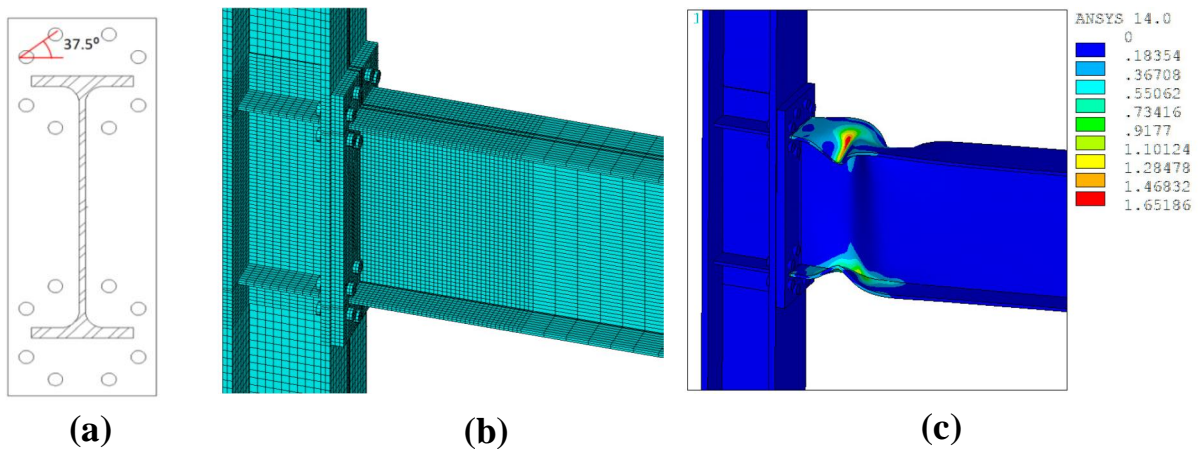


Figure 18 (a) Proposed bolt rearrangement in a hexagonal pattern; (b) FE mesh with the modified bolt arrangement for 8EM configuration of the connection; (c) Equivalent plastic strain contour of 8EM configuration of the connection showing formation of plastic hinge.

To eliminate the uncertainty associated with the triangular stiffeners and to allow for an equal distribution of demands in the bolts, a connection with a hexagonal-type bolt pattern was proposed in this study. This pattern was adjusted to allow for a balanced demand distribution amongst the bolts without the need for a triangular stiffener. Through finite element analysis utilizing trial and error convergence until optimized performance was

found, an angle of 37.5° between the top and bottom layers of bolts was found (See Figure 18a). This angle allows equal participation amongst the bolts without the need of a triangular stiffener. The eight bolt extended end plate connection with this modified configuration of the bolt was analyzed under the simulated earthquake loading history to investigate its seismic performance and compare with the response of the stiffened connection. The FE mesh and the equivalent plastic strain contour of the connection is shown in Figure 18 which shows ductile behavior of the connection by formation of plastic hinge at a distance of 286 mm away from the face of the column. The connection showed almost the same response as the stiffened connection. The moment-rotation plot of the connection (shown in Figure 19a) showed initiation of strength degradation in the 2nd cycle of 4% interstory drift angle which became significant (34%) during loading cycles for 5% interstory drift angle. As the loading cycles progressed, the strength of the connection dropped by 56% at 6% interstory drift angle, because of the instability created due to the lateral buckling of the beam.

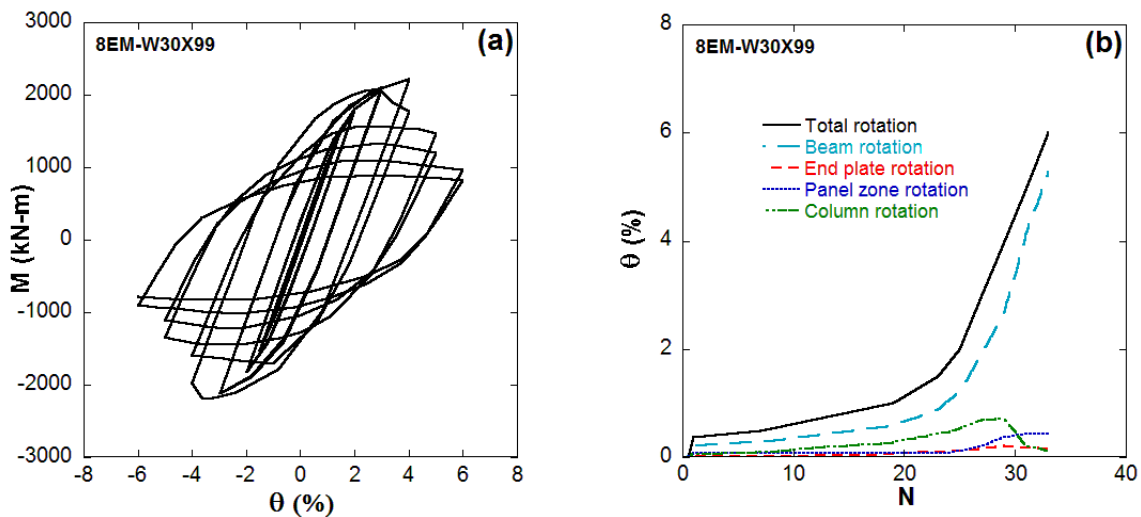


Figure 19 Cyclic response of 8EM configuration of connection. (a) Moment-rotation hysteresis response for cyclic loading up to 6% interstory drift angle; (b) Contribution of different components of the connection in the total rotation.

The contributions of the beam, panel zone, column and end plate to the maximum interstory drift angle of 6% were: $\theta_b=5.55\%$, $\theta_{pz}=0.26\%$, $\theta_c=0.1\%$, $\theta_{ep}=0.08\%$ (shown in Figure 19b). This is almost similar type of response that was observed for 8ES connection. The beam took most of the inelastic action where more than 90% of the rotation capacity came from the beam itself. On the other hand, the participation of the end plate and panel zone increased in comparison to 8ES connection. It is to be noted here that the contributions from panel-zone, column and end plate in the rotation capacity of the connection started to decrease when the beam started to buckle locally, indicating an increase in the beam's participation in the rotation capacity of the connection.

Moving on to the bolt strains, the hexagonal pattern of bolt arrangement was successful in distributing the flange forces uniformly to the connecting bolts. As seen in Figure 20, the strains in all the connecting bolts showed similar trend during the loading cycles. The bolt strains remained in the elastic range and the strains cycled within the pretension strain range with a gradual decrease of pretension strain with progression of loading cycles. For 8E and 4W configurations of the connections, the weld strain demand increased significantly due to the absence of the end plate stiffener. However, for 8EM configuration of the connection, the weld strain remained less than 2% during the loading cycles. The axial strain profile along the width of the beam bottom flange at the weld toe for 8EM configuration of the connection is shown in Figure 22a for loading cycles up to 4% interstory drift angle which shows lower strain demands on the welds unlike 8E or 4W connections. After 4% interstory drift angle, the beam experienced local buckling which reduced the strain demand at the weld toe.

A comparison of the moment-rotation envelopes of the extended end plate connections analyzed is presented in Figure 21. It can be observed that the connection with the modified bolt arrangement showed better performance than the other configurations of the connection in terms of strength degradation and energy dissipation. For 8EM configuration, the connection started to lose strength after 4% interstory drift angle, whereas the connection with stiffener (8ES) started to lose strength after 3% interstory drift angle. The 8E and 4W connections also showed good performance in terms of strength degradation, but they suffered with higher weld strains and non-uniform bolt strains which eventually made their

performance undesirable for seismic application. Upto 5% interstory drift angle, 8ES, 8E and 8EM showed similar strength; however, the degradation of 8EM was higher than the others for loading at 6% interstory drift angle.

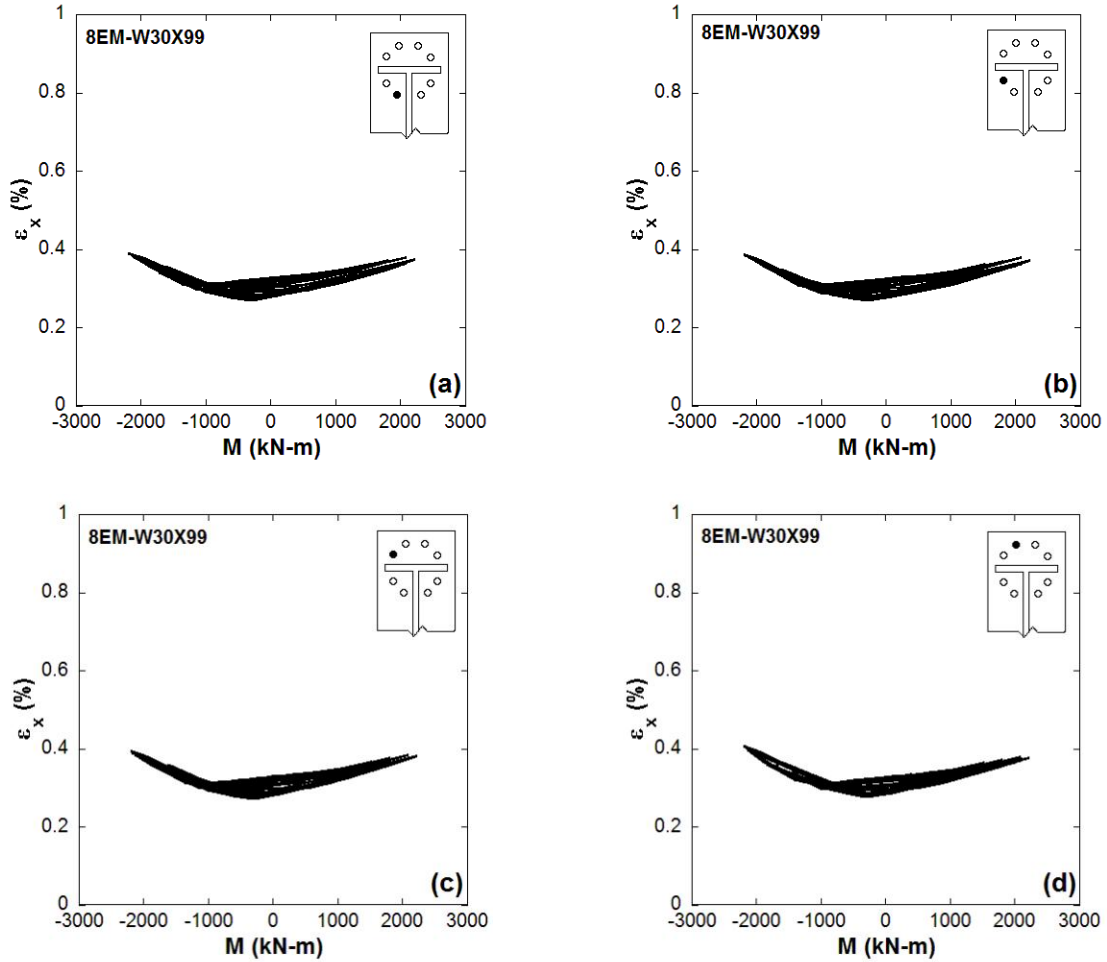


Figure 20 Bolt strains for 8EM configuration during loading cycles at the top flange of the beam.

Figure 22b shows the axial strain profile along the width of beam bottom flange at the location of plastic hinge for different configurations of the connection at the end of loading cycles for 6% interstory drift angle. It is clearly visible that for 8ES configuration, there is a

significant increase in the strain demand near the center of the beam flange at the plastic hinge location as a result of high stress concentration due to the presence of end plate stiffener. This higher demand on the beam flanges were attenuated for 8EM configuration by removing the stiffener which reduced the strain demand to 23% from 57% for 8ES connection. This will allow the connection to sustain more story drift levels without fracture of the flange. On the contrary, the maximum strain demand at the weld toe for both 8ES and 8EM configuration of the connection was low compared to the other configuration of the connection (Figure 22a). In addition, the 8EM configuration increased the contributions of end plate and panel-zone in the total rotation capacity of the connection compared to 8ES configuration as shown in Figure 23. This will help in dissipating more energy.

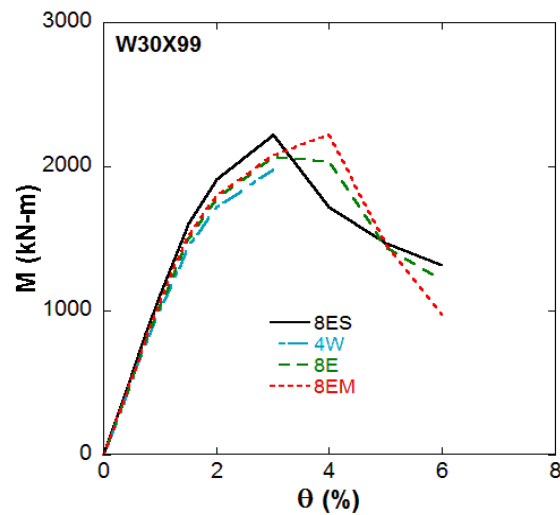


Figure 21 Moment-rotation envelopes of the extended end plate connections for different bolt arrangements.

To conclude, the modified bolt arrangement can be a viable alternative to the conventional eight bolt stiffened extended end plate connection which eliminates the stress concentration on the beam flanges producing better seismic response than the stiffened connection. Moreover, it ensures better utilization of the floor space and reduces the overall

construction cost by excluding the weld works for the end plate stiffeners. However, the analysis results presented to this point was based on only one size of the beam (W30×99) that was used by Sumner *et al.* [10]. More analyses with different sizes of the beam need to be investigated to generalize the use of the hexagonal pattern of the bolt. The analysis results presented hitherto manifests that the stiffener in the eight bolt stiffened extended end plate connection can be removed with proper arrangement of the bolts to generate a favorable loading path so that the flange forces are distributed evenly to all the connecting bolts, thereby ensuring a ductile mode of failure through inelastic buckling of the beam.

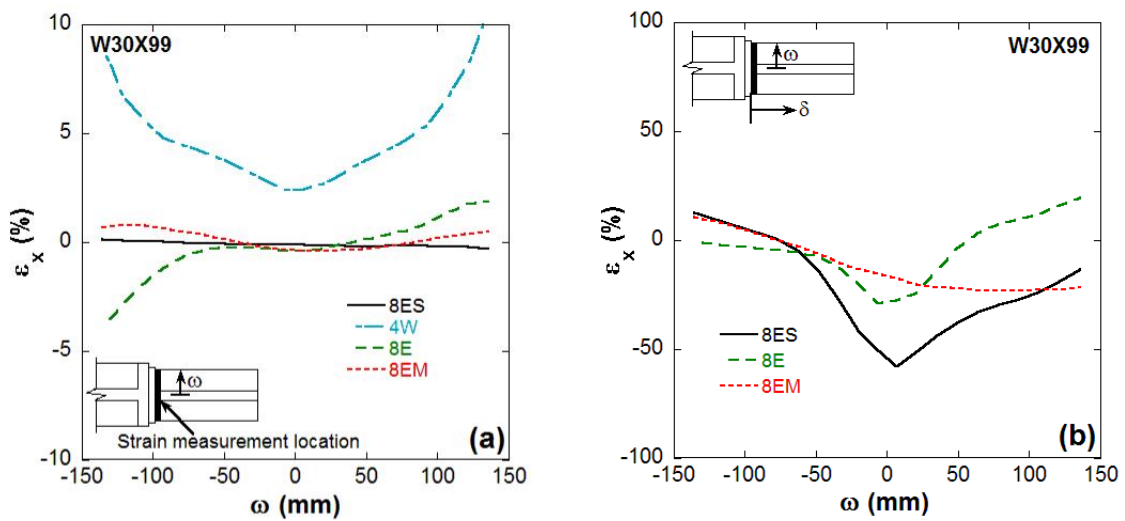


Figure 22 Axial strain profile along the width of the beam bottom flange for different arrangements of the bolts. (a) At weld toe during loading cycles at 4% interstory drift angle; (b) At plastic hinge location during loading cycles at 6% interstory drift angle.

5. Further Development of the Modified Design for Extended End plate Connection

In order to investigate the applicability of the modified bolt arrangement for larger beam section, finite element analysis was performed on eight bolt extended end plate connection with modified bolt arrangement, where a W30×148 beam section was connected to a W14×257 column section. The connection was designed for 110% plastic moment capacity

of the beam. The stiffener, bolt and end plate were designed based on the requirements of AISC [45] for seismic application. The beam, column material used was ASTM A992 and the end plate material used was ASTM A36. The design required an end plate thickness of around 47.625 mm which was bolted to the flange of the column with 38.1 mm diameter A490 bolts. The bolts were given a pretension of 658 kN as specified in the AISC LRFD specification. The column was reinforced with 25.4 mm continuity plates and a 25.4 mm doubler plate. This connection was analyzed under the simulated seismic loading as shown in Figure 5.

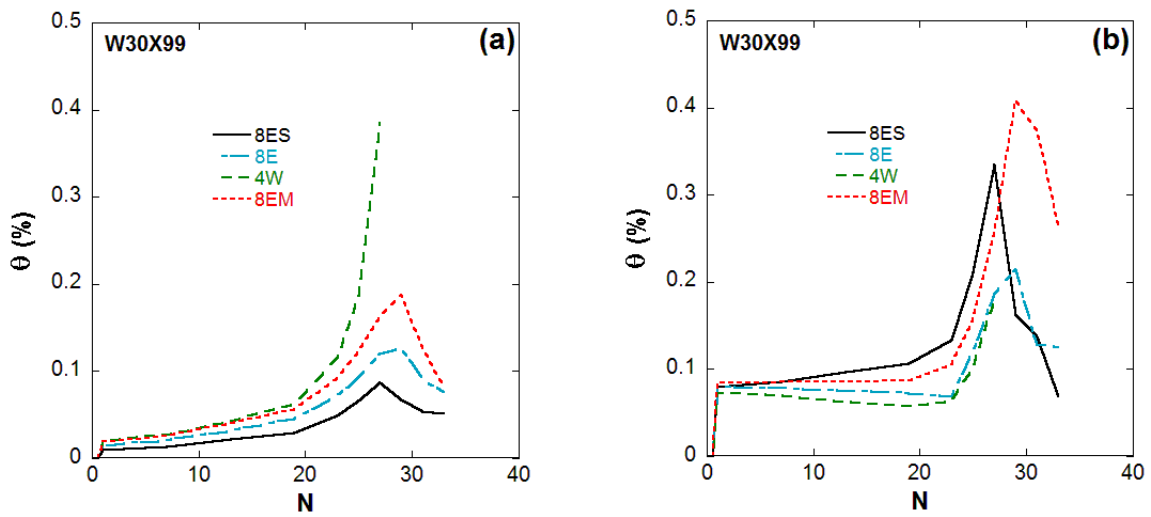


Figure 23 Participation of end plate and panel zone in the total rotation capacity at 6% interstory drift angle for different configurations of bolt. (a) End plate; (b) Panel zone.

The equivalent plastic strain contour and the moment-rotation response for the eight bolt modified extended end plate connection (8EM) with W30×148 beam section is shown in Figure 24a. The connection showed local and global buckling of the beam flanges and web leading to formation of plastic hinge at a distance of 145 mm away from the end plate. As expected the bolt forces were uniformly distributed as a result of the modified bolt arrangement. However, since the plastic hinge formed very close to the weld connection, the

strain demand on the welds of beam flanges were very high. It was observed that the maximum weld strain was around 5% for loading cycles at 4% interstory drift angle which crossed 10% for loading cycles at 5% and 6% interstory drift angles. Hence, this configuration of the connection might show undesirable mode of brittle failure at the weld between the end plate and the beam flanges.

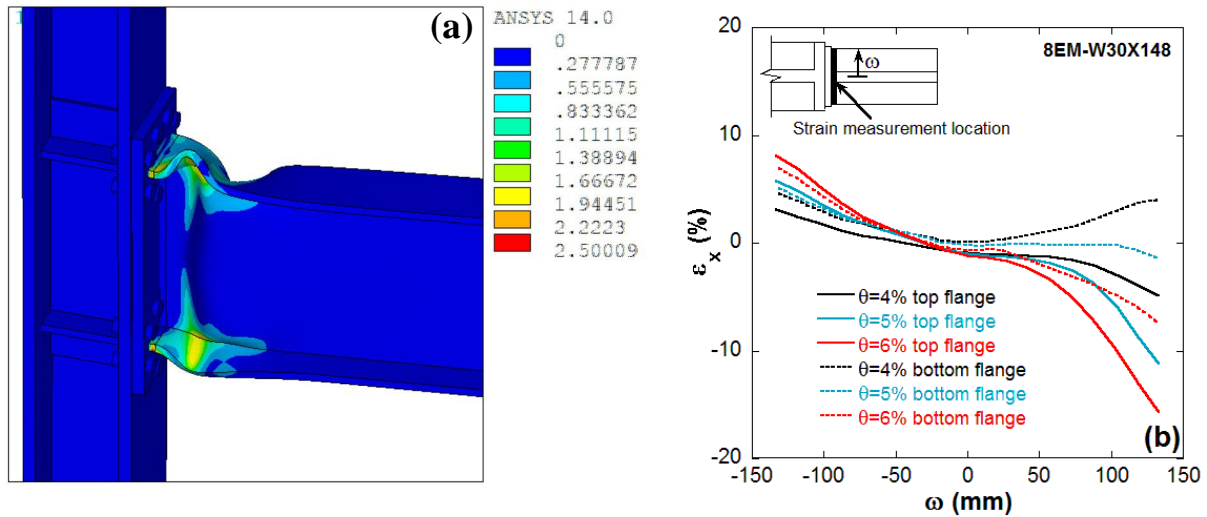
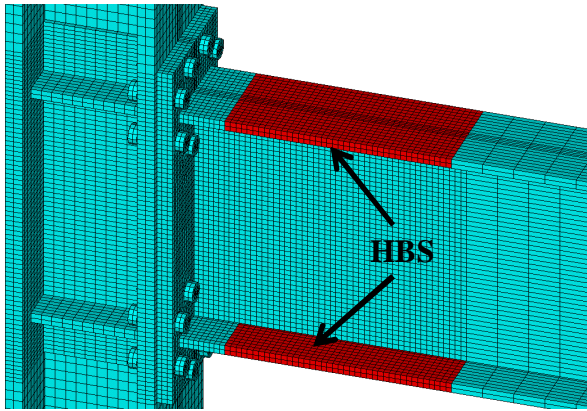


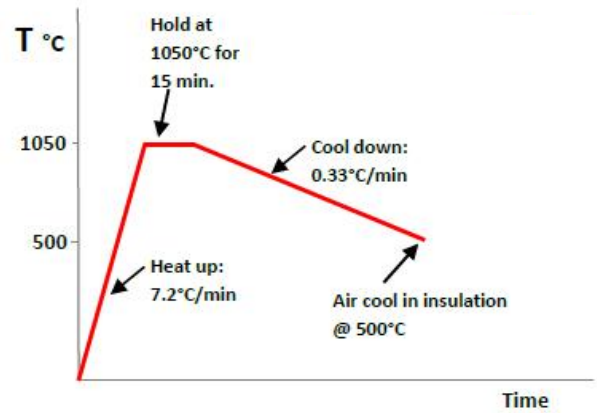
Figure 24 8EM configuration of the connection with W30×148 beam section. (a) Equivalent plastic strain contour showing formation of plastic hinge; (b) Axial strain profile along the width of the beam flange for loading cycles upto 6% interstory drift angle.

From the results of the analysis, it is apparent that for larger size beam sections, the rearrangement of the bolts in hexagonal pattern alone may not be sufficient to ensure ductile mode of failure. Hence, the flanges of the beam section were heat treated at a specific distance away from the face of the column to reduce the strength of the beam. This innovative seismic performance enhancement technique (known as heat treated beam section or HBS) has been developed by Morrison *et al.* [31] and it has been implemented for welded unreinforced flange welded web (WUF-W) moment resisting connection successfully as a part of the NEES (Network for Earthquake Engineering Simulation) project. In this type of connection, the flanges of the beam near the connection region are heat treated (highlighted

red in Figure 25a) to a peak temperature (T_p) of 1050°C; maintain the peak temperature for 15 minutes (t_h) before slow air cooling as shown in Figure 25b. For detail of the heat treatment technique and the seismic performance of WUF-W connections with heat treated beam section (HBS), the readers are referred to Morrison *et al.* [31]. However, it was shown that the heat treatment reduced the strength of steel in the heat treated areas of the flange and consequently, under seismic loading plastic hinge developed at the heat treated region of the beam flanges and required ductility capacity of connections was achieved.



(a) Exterior connection with heat treated section



(b) Heat treatment temperature

Figure 25 Heat treatment of modified extended end plate connection for seismic performance enhancement.

During heat treating the beam flanges, it was observed that the temperature was not uniform in the HBS region. The temperature was relatively uniform in the center of the HBS region (1050°C), whereas at the edges of the HBS region the temperature was found to be around 850°C. On the other hand, just outside of the HBS region, the temperature was found to be in the range of 500-600°C. A study by Morrison [46] on the seismic response simulation of WUF-W HBS connections showed that the response of the connection during inelastic loading cycles do not show significant difference whether temperature non-uniformity in the HBS region is considered or not. Similar observations were made in this study. Material tests results [47] also showed that the stress-strain response of ASTM A992

steel upto 600°C is very close to the stress-strain response at room temperature. Hence, instead of taking multiple material properties of ASTM A992 steel for the HBS region, material properties of ASTM A992 steel at 1050°C was used for HBS region, whereas room temperature ASTM steel properties were used for the rest of the connection region and other components of the connection. This reduces the material parameters to be determined for each temperature range as well as the complexity of the model. The readers are referred to [47] for detailed material response of ASTM A992 at different heat treatment temperature.

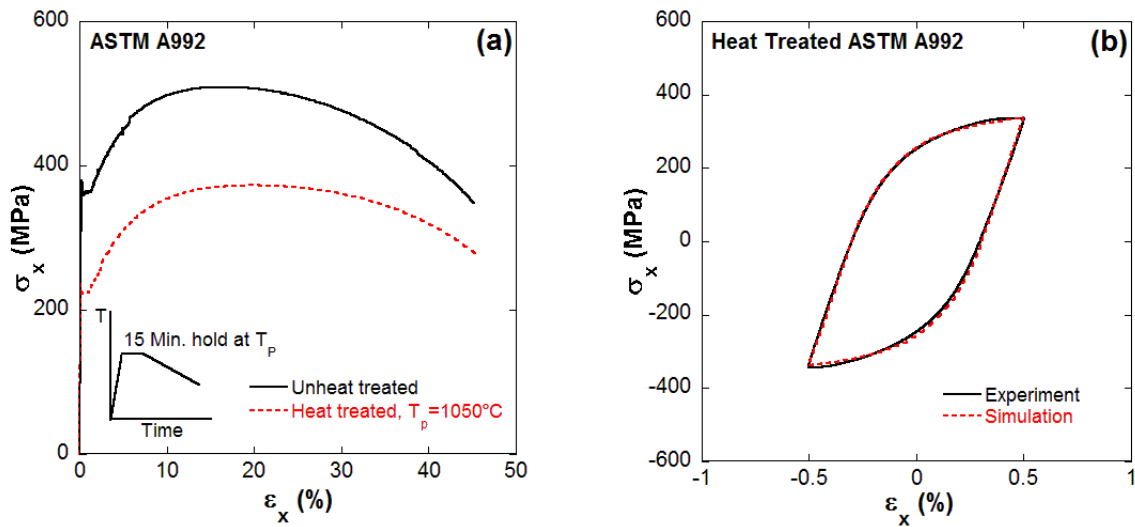


Figure 26 (a) Monotonic stress-strain response for unheat treated and heat treated ASTM A992 specimens; (b) Experimental and simulated response of strain controlled hysteresis loop with Chaboche parameters for heat treated ASTM A992 steel.

To implement heat treated beam flange in the finite element modeling, the heat treated material properties of ASTM A992 steel was incorporated in the specified location of the beam flanges. For determining material properties for heat treated ASTM A992 steel, a set of monotonic tension and cyclic tests of beam flange steel coupons (ASTM A992), heat treated by 1050°C with a 15 minutes hold were conducted. The stress-strain response from one set of the monotonic tension tests are shown in Figure 26a. It was observed that with heat treatment both the yield and ultimate stresses of the beam steel decreased by downward shift of the

stress-strain curves. The reduction in yield stress by heat treatment with maximum temperature 1050°C was about 40%. It is also important to note in Figure 26a that the elastic modulus of the beam flange steel was not altered much by the heat treatment process. For Chaboche model parameter determination for heat treated ASTM A992 steel (see Table 1), the upgoing curve of the stable hysteresis loop obtained from single amplitude, strain-controlled cycle was fitted. Simulations were made at the material level with obtained parameters for validation and as shown in Figure 26b, the simulated responses matched very well with the experimental responses.

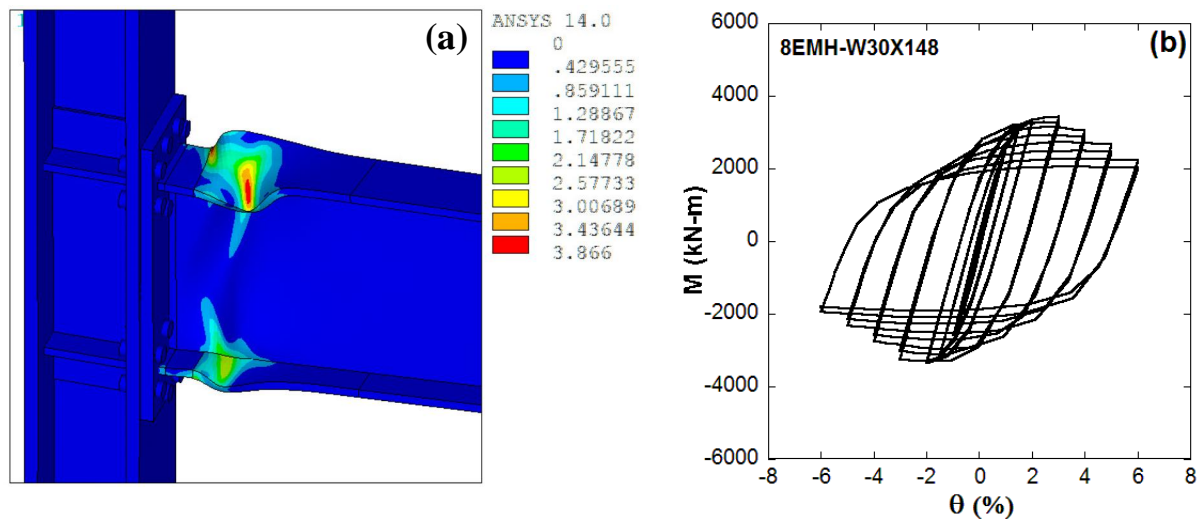


Figure 27 Cyclic response of 8EMH configuration of the connection with W30×148 beam section. (a) Equivalent plastic strain contour showing formation of plastic hinge in the heat treated region of the beam flanges; (b) Moment-rotation response upto 6% interstory drift angle.

Once the material properties were determined, the 8EM connection was analyzed under the simulated seismic loading with heat treated beam flanges. This configuration of the connection has been denoted as 8EMH connection. The heat treatment was performed at a distance of 127 mm away for the end plate for a length of 635 mm along the beam length.

The equivalent plastic strain contour along with the moment-rotation response of the connection is shown in Figure 27. It can be observed that the plastic hinge formed right at the heat treated beam flanges. The connection's strength was lowered because of the heat treatment which reduced the strength of the material. The strength of the connection started to degrade at loading cycles for 4% interstory drift angle, where significant buckling of the beam flanges were observed in addition to small web buckling. For loading cycles at 5% and 6% interstory drift angles, severe buckling of the beam flanges and web led to lateral torsional buckling of the beam and the strength of the connection deteriorated by around 40% at the end of 6% interstory drift angle. Most of the inelastic action occurred on the beam flanges in heat treated region. In the total rotation capacity, beam played the most dominant role as anticipated with small contributions from the end plate and panel zone as shown in Figure 28b. It is very interesting to note here that the heat treatment reduced the strain demand on the weld significantly.

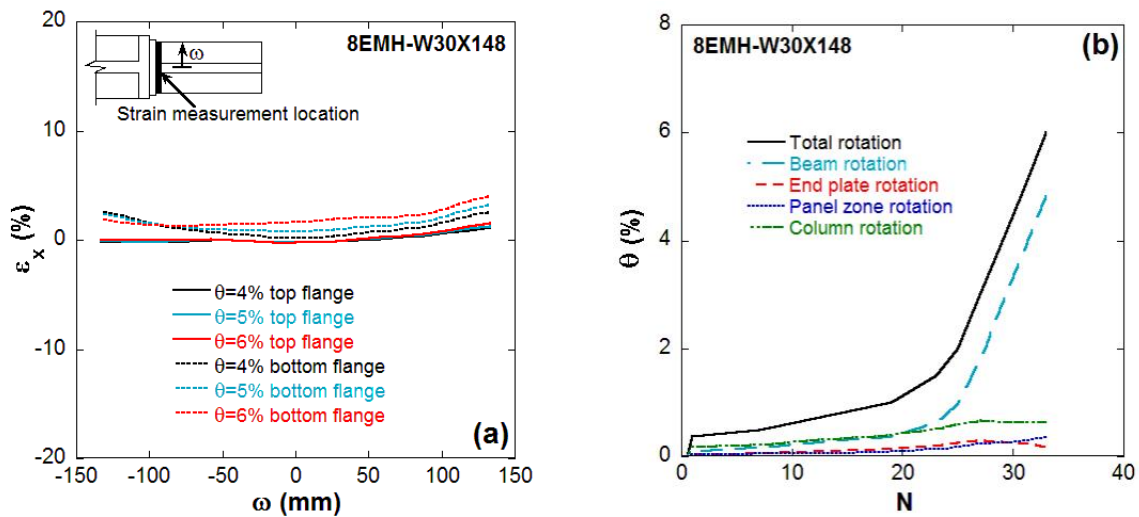


Figure 28 Cyclic response of the connection for 8EMH configuration of the bolts. (a) Axial strain profile along the beam flange at the weld toe; (b) Participation of different components of the connection in the total rotation capacity of the connection.

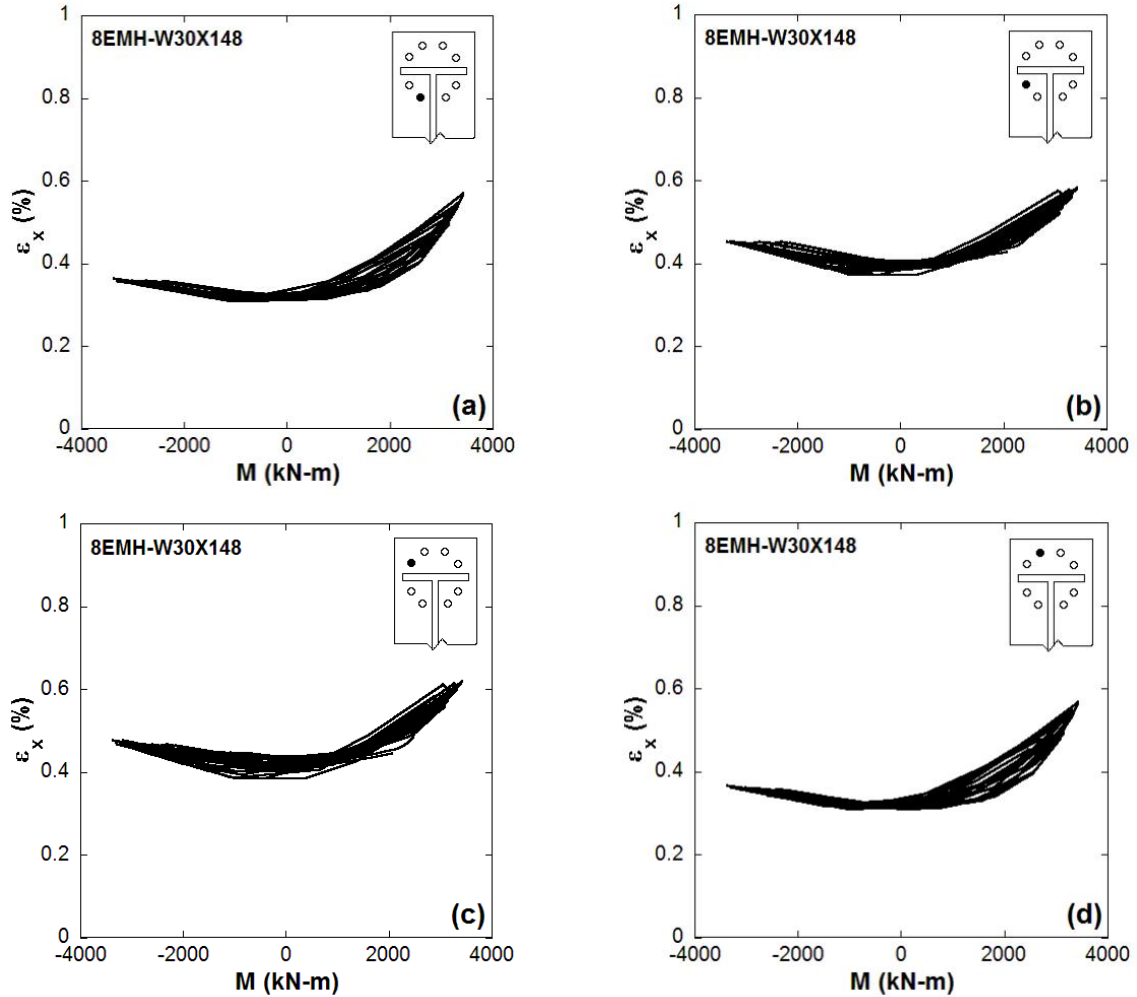


Figure 29 Bolt strains for 8EMH configuration of the connection with W30×148 beam section.

The axial strains at the weld toe never crossed 2% upto interstorey drift angle of 6% as shown in Figure 28a. Moreover, both the outside and inside bolts showed equal and similar pattern of strains indicating a better distribution of flange forces to the connecting bolts (Figure 29). Overall, the required ductility and the energy dissipation capacity of the connection was achieved. A comparison of the moment-rotation envelope of the peak moments in each loading cycle for 8ES and 8EMH connection (Figure 34a) showed that the strength degradation for 8ES connection was very steep compared to 8EMH connection,

which indicates a more ductile and stable response of the connection for 8EMH configuration. Since the plastic hinge location with the modified bolt arrangement varies with the size of the beam section, heat treatment of the beam flanges ensures formation of plastic hinge at a specified location regardless of the size of the beam. In this way the proposed modified connection design with hexagonal bolt arrangement and HBS can be implemented as a unified design for all the beam sections available in the AISC LRFD design manual. Although 8EMH connection showed improvement in the ductility and energy dissipation capacity of the connection compared to 8ES connection, no significant improvement was observed in terms of strength degradation. As can be noticed from Figure 34b that for both the 8ES and 8EMH connections, the strength degradation initiated at the same interstory drift angle, although the strength degradation was much slower for 8EMH connection compared to 8ES connection. Hence, the strength degradation mechanism of the connection was investigated to study whether the seismic performance of the modified connection can be further improved by delaying the onset of strength degradation. The local flange and web buckling were plotted for each cycle of loading to explore the mechanism involved in strength degradation. The local buckling modes during the onset of strength degradation are shown in Figure 30.

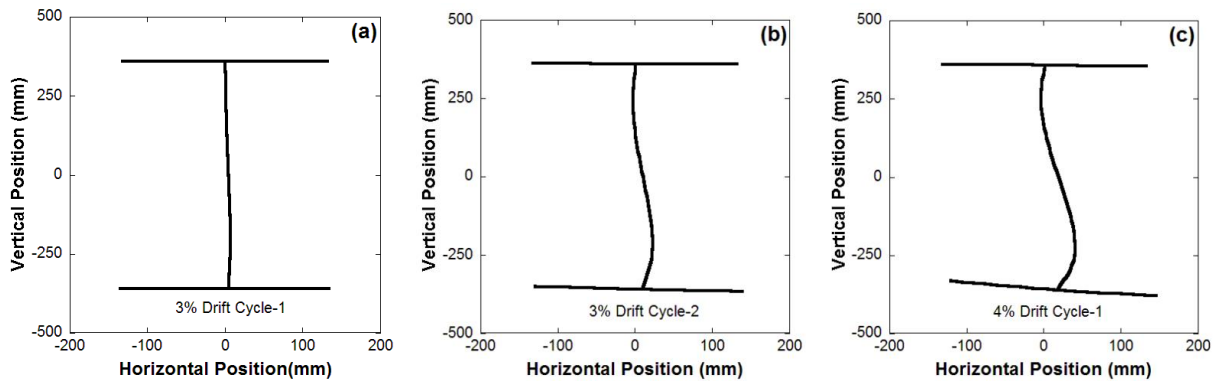


Figure 30 Local buckling of beam web and flanges at different loading cycles for 8EMH configuration of the connection with W30×148 beam section.

It was observed that beam web started to buckle at the first cycle of 3% story drift followed by beam flange buckling, but no strength degradation was observed. At the second cycle of 3% storey drift, the web of the beam started to twist which initiated lateral-torsional buckling of the beam and this in turn initiated strength degradation of the connection. As the load amplitude was further increased, the lateral torsional buckling became more pronounced and strength degradation increased significantly. Similar observations were also made by [16, 18, 48-52] where they observed that strength degradation is caused by either lateral buckling or lateral torsional buckling of the beam. Since lateral torsional buckling for the 8EMH connection under consideration was initiated by the web buckling of the beam, incorporating a web stiffener may delay the strength degradation of the connection by delaying the initiation of web buckling as well as lateral torsional buckling.

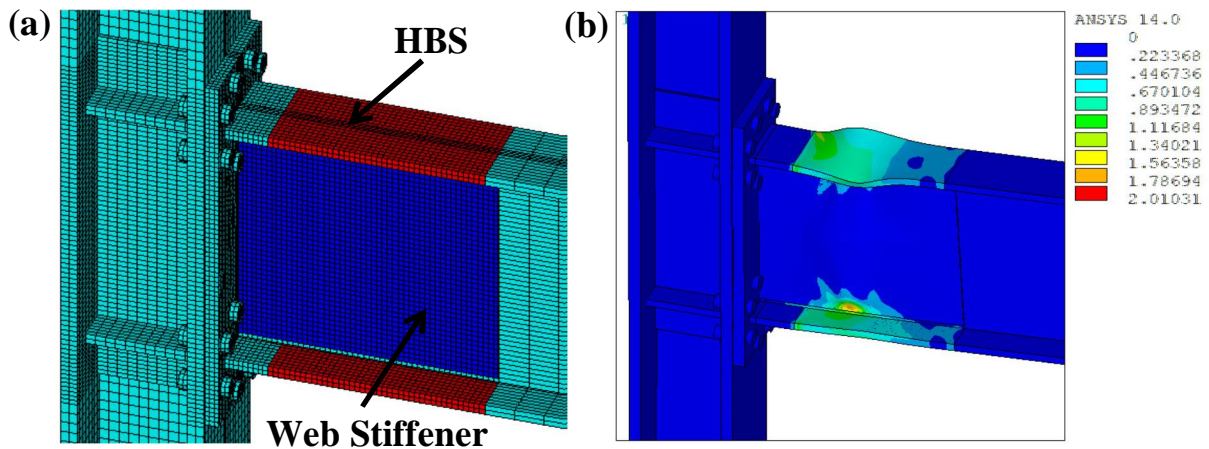


Figure 31 (a) Modified extended end plate connection (8EMH-W) with heat treatment and web stiffener; (b) Formation of plastic hinge in the heat treated region of beam flanges under simulated seismic loading with 8EMH-W configuration of the connection.

A finite element analysis was performed on the 8EMH connection by incorporating a web stiffener on each side of the beam web. This connection configuration is denoted as 8EMH-W. The web stiffener consisted of a 6.35 mm thick plate welded to the beam web and extending from the face of the end plate to the end of the heat treated region as shown in

Figure 31a. It was observed from the analysis responses that the plastic hinge still formed at the heat treated beam flanges (Figure 31b) and there was no noticeable strength degradation upto 6% interstory drift angle (Figure 32a). The axial strain at the weld toe was less than 2% during the loading cycles (Figure 32b) since most of the inelastic action was taking place at the heat treated beam region. Moreover, the connecting bolts were equally effective in distributing the flange forces as a result of the modified bolt arrangement (Figure 33).

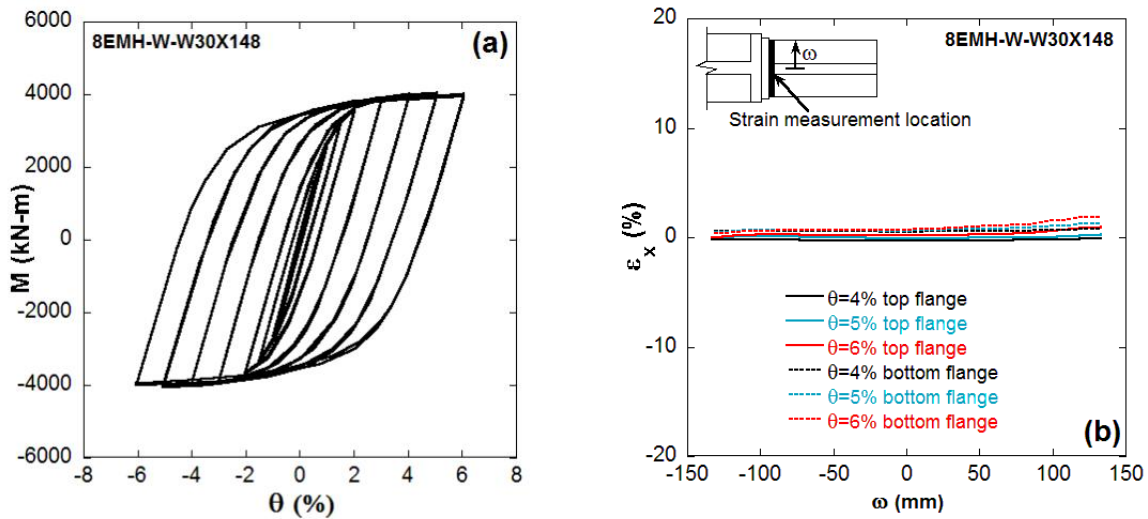


Figure 32 Cyclic response of 8EMH-W configuration of the connection upto 6% interstory drift angle. (a) Moment-rotation hysteresis response; (b) Axial strain profile along beam flange at the weld toe.

A comparison of the moment-rotation envelope of the 8ES, 8EMH and 8EMH-W connection with W30×148 beam section is shown in Figure 34a. It is evident that 8EMH-W connection shows a marked improvement in the ductility and energy dissipation capacity compared to the 8ES and 8EMH connections. However, the peak strength of the connection was lower than the 8ES connection because of the reduced strength of the material due to heat treatment, whereas the peak strength of the connection is higher compared to the 8EMH connection because of the presence of the web stiffener.

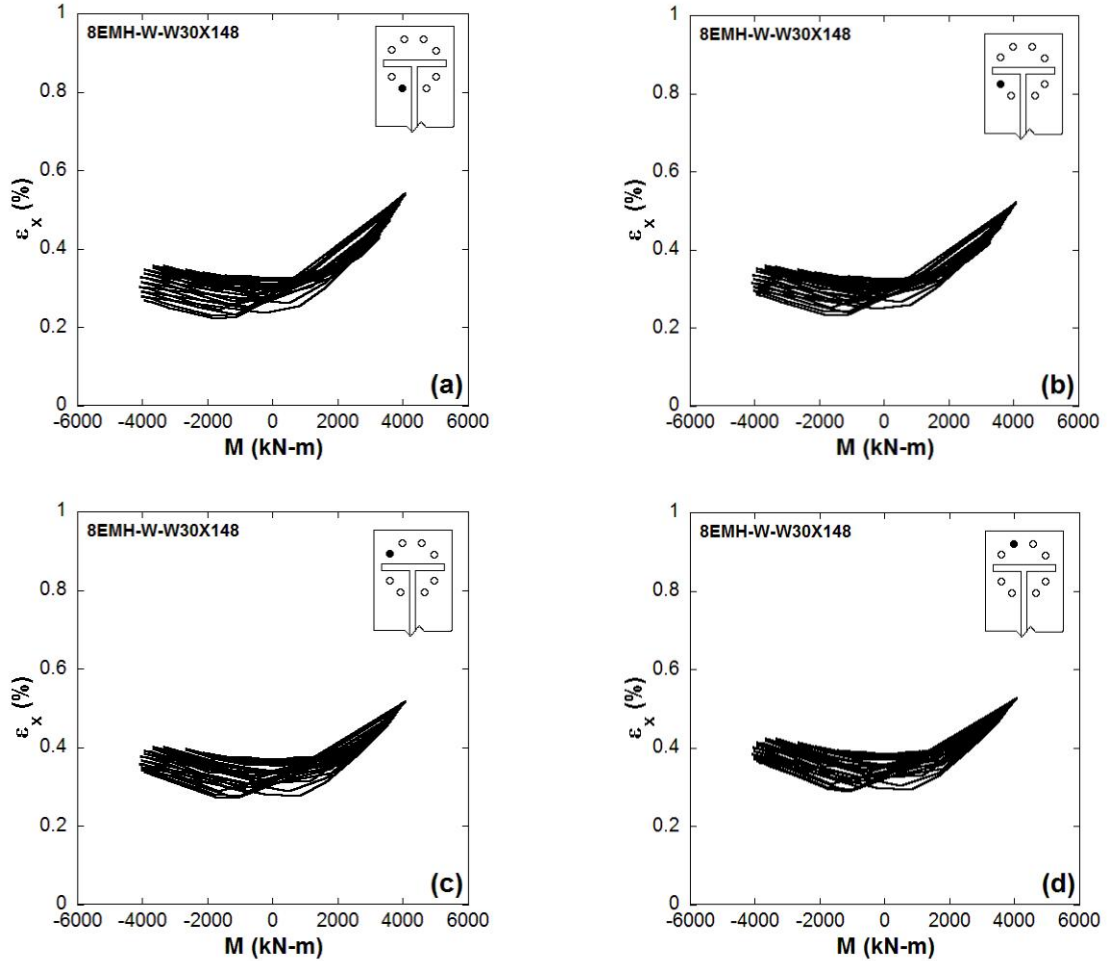


Figure 33 Bolt strains for 8EMH-W configuration of the connection with W30×148 beam section.

The modified design of the extended end plate connection with heat treatment and web stiffener was also investigated for W30×99 beam section (Figure 34b) and similar observations were made where 8EMH-W connection showed no significant degradation in strength upto 6% interstory drift angle, still plastic hinge formed at the heat treated region of the beam flanges. Based on the observations from the finite element investigation performed in this study, it is apparent that the proposed design of extended end plate connection with hexagonal bolt arrangement, heat treated beam section and web stiffener can improve the

seismic resilience of the extended end plate connection significantly compared to the existing extended end plate connection. The novel connection design has been experimentally validated and will be presented in a separate study.

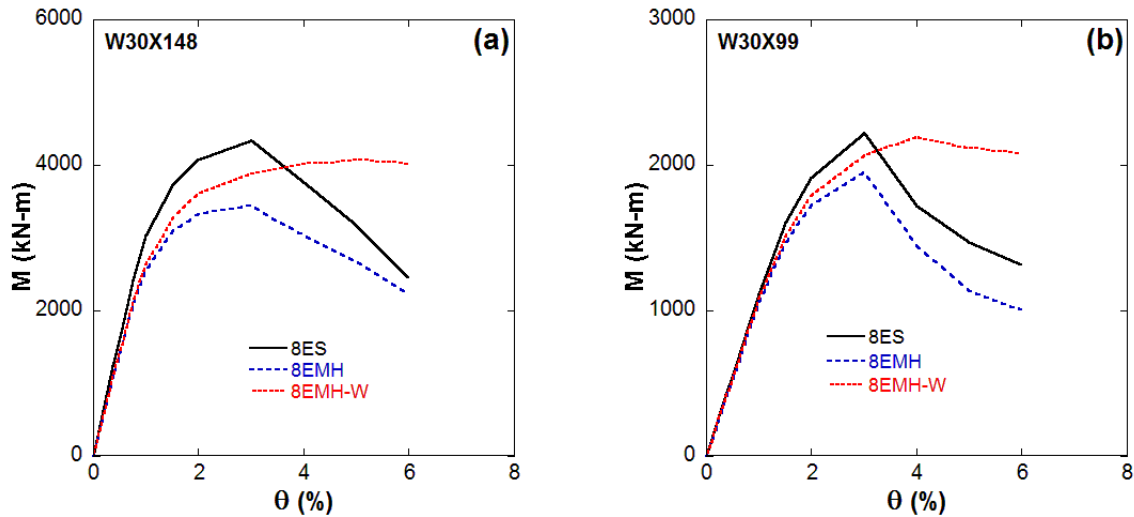


Figure 34 Moment-rotation envelopes of different configurations of the extended end plate connections. (a) W30×148 beam section; (b) W30×99 beam section.

6. Conclusions

The stiffeners in the eight bolt stiffened extended end plate connection causes dispraging failure mechanisms due high stress concentration. In addition to the stress concentration, the stiffeners reduce the usable floor area as well as increase cost of construction for the weld works associated with the stiffener. This study proposed a modified design of extended end plate moment connection without end plate stiffeners based on a detailed finite element study. The modified design consists of rearranging the bolts into a hexagonal pattern to distribute the flange forces evenly to the connecting bolts, heat treating the beam flanges to ensure formation of plastic hinge away from the connection region, and welding stiffeners on both the sides of the beam web to delay the onset of strength degradation. The performance of the proposed connection has been evaluated under simulated seismic loading and

compared with the stiffened connection. The connection showed significant improvement over the existing connection in terms of strength, ductility and energy dissipation capacity. To conclude, the modified design of extended end plate connection demonstrates a great potential to be used as a viable alternative to the conventional stiffened extended end plate connection where the uncertainty and unfavorable failure mechanisms associated with the end plate stiffener can be eliminated. The novel connection design has been validated through full scale experimental testing of extended end plate moment connections and has demonstrated excellent performance under simulated seismic loading, which will be presented in a separate study.

7. References

- [1] FEMA-350. Recommendation and seismic design criteria for new steel moment-frame buildings. Prepared by the SAC Joint Venture for the Federal Emergency Management Agency, Washington, DC, 2000.

- [2] FEMA-353. Recommended specifications and quality assurance guidelines for steel moment- frame construction for seismic applications. Prepared by the SAC Joint Venture for the Federal Emergency Management Agency, Washington, DC, 2000.

- [3] FEMA-355B. State of the art report on welding and inspection. Prepared by the SAC Joint Venture for the Federal Emergency Management Agency, Washington, DC, 2000.

- [4] FEMA-355D. State of the art report on connection performance. Prepared by the SAC Joint Venture for the Federal Emergency Management Agency, Washington, DC, 2000.

- [5] Stojadinovic B, Goel SC, Lee KH, Margarian AG, Choi JH. Parametric tests on unreinforced steel moment connections. *Journal of Structural Engineering* 2000;126:40-49.

- [6] SAC/BD-00/01. Parametric tests on unreinforced connections. by Lee, K.H., Stojandinovic, B., Goel, S.C., Margarian, A.G., Choi, J., Wongkaew, A., Reyher, B.P., and Lee, D.-Y.
- [7] SAC/BD-00/24. Development and evaluation of improved details for ductile welded unreinforced flange connections. by Ricles, J.M., Mao, C., Lu, L.-W., Fisher, J.W.
- [8] Lee D, Cotton SC, Hajjar JF, Dexter RJ. Cyclic behavior of steel moment-resisting connections reinforced by alternative column stiffener details, I. Connection performance and continuity plate detailing. *Engineering Journal* 2005;4th Quarter:189-213.
- [9] AISC (2010a). Prequalified connections for special and intermediate steel moment frames for seismic applications. *American Institute of Steel Construction* 358, AISC 358-10.
- [10] Sumner EA, Mays TW, Murray TM. Cyclic testing of bolted moment end-plate connections. Research Report No. CE/VPI-ST-00/03, SAC Report No. SAC/BD-00/21, submitted to the SAC Joint Venture, 2000, 327 pages.
- [11] Sumner EA, Murray TM. Experimental investigation of four bolts wide extended end-plate moment connections. Research Report No. CE/VPI-ST- 01/15, submitted to Star Building Systems, Inc., Oklahoma City, Oklahoma, 2001a, 114 pages.
- [12] Sumner EA, Murray TM. Experimental investigation of the mre 1/2 end-plate moment connection. Research Report No. CE/VPI-ST-01/14, submitted to Metal Building Manufacturers Association, Cleveland, Ohio, 2001b, 91 pages.
- [13] Sumner EA, Murray TM. Behavior of extended end-plate moment connections subject to cyclic loading. *Journal of Structural Engineering* 2002;128(4):501-508.

- [14] SAC/BD-97/02. Protocol for fabrication, inspection, testing and documentation of beam-column connection tests and other experimental specimens. by Clark, P., Frank, K., Krawinkler, H., and Shaw, R.
- [15] Tsai KC, Popov EP. Cyclic behavior of end-plate moment connections. *Journal of Structural Engineering* 1990;116(11):2917-2930.
- [16] Korol RM, Ghobarah A, Osman A. Extended end-plate connections under cyclic loading: behavior and design. *Journal of Constructional Steel Research* 1990;16(4):253-279.
- [17] Ghobarah A, Korol RM, Osman A. Cyclic behavior of extended end-plate joints. *Journal of Structural Engineering* 1992;118(5):1333-1353.
- [18] Ghobarah A, Osman A, Korol RM. Behavior of extended end-plate connections under cyclic loading. *Engineering Structures* 1990;12:15-26.
- [19] Castellani A, Castiglioni CA, Chesi C, Plumier A. A European research program on the cyclic behavior of welded beam to column connections. *Proceedings of the NEHRP Conference and Workshop on Research on the Northridge, California Earthquake of January 17, 1994, National Earthquake Hazards Reduction Program* 1998;Vol. III-B:510-517.
- [20] Coons RG. Seismic design and database of end plate and t-stub connections. M.S. Thesis, University of Washington, Seattle, Washington, 1999.
- [21] Adey BT, Grondin GY, Cheng JJR. Cyclic loading of end plate moment connections. *Canadian Journal of Civil Engineering* 2000;27:683-701.

- [22] Adey BT, Grondin GY, Cheng JJR. Extended end plate moment connections under cyclic loading. Structural Engineering Report No. 216, Department of Civil and Environmental Engineering, University of Alberta, Alberta, Canada, 1997.
- [23] Adey BT, Grondin GY, Cheng JJR. Extended end plate moment connections under cyclic loading. Journal of Constructional Steel Research 1998;46(1-3),Paper No. 133.
- [24] Guo B, Gu Q, Liu F. Experimental behavior of stiffened and unstiffened end-plate connections under cyclic loading. Journal of Structural Engineering 2006;132(9):1352-1357.
- [25] Shi G, Shi Y, Wang Y. Behavior of end-plate moment connections under earthquake loading. Engineering Structures 2007;29:703-716.
- [26] Murray TM, Kukreti AR. Design of 8-bolt stiffened moment end plates. Engineering Journal 1988;2nd Quarter:45-52.
- [27] Borgsmiller JT, Sumner EA, Murray TM. Tests of multi-row moment end-plate connections having large inner pitch distances. Research Report No. CE/VPI-ST-95/01, submitted to Kawada Industries, Costa Mesa, California, 1995.
- [28] Meng RL. Design of moment end-plate connections for seismic loading. Ph.D. Dissertation, Virginia Polytechnic Institute and State University, Virginia Polytechnic Institute and State University, Blacksburg, VA, 1996.
- [29] Mays TW. Application of the finite element method to the seismic design and analysis of large moment end-plate connections. Ph.D. Dissertation, Virginia Polytechnic Institute and State University, Blacksburg, VA, 2000.

- [30] Gerami M, Saberi H, Saberi V, Daryan AS. Cyclic behavior of bolted connections with different arrangement of bolts. *Journal of Constructional Steel Research* 2011;67:690-705.
- [31] Morrison M, Schweizer D, Hassan T. An innovative seismic performance enhancement technique for steel building moment resisting connections. Submitted to *Journal of Constructional Steel Research* 2014.
- [32] Kiamanesh R, Abolmaali A, Razavi M. Effect of circular bolt pattern on behavior of extended end-plate connection. *Journal of Structural Engineering* 2012; 139(11):1833-1841.
- [33] Bahaari MR, Sherbourne AN. Computer modeling of an extended end-plate bolted connection. *Computers and Structures* 1994;52:879-893.
- [34] Choi CK, Chung GT. Refined three-dimensional finite element model for end-plate connection. *Journal of Structural Engineering* 1996;122(11):1307-1316.
- [35] Bose B, Wang ZM, Sarkar S. Finite-element analysis of unstiffened flush end-plate bolted joints. *Journal of Structural Engineering* 1997;123:1614-1621.
- [36] Bursi OS, Jaspart JP. Basic issues in the finite element simulation of extended end plate connections. *Computers and Structures* 1998;69(3):361-382.
- [37] Maggi YI, Goncalves RM, Leon RT, Ribeiro LFL. Parametric analysis of steel bolted end plate connections using finite element modeling. *Journal of Constructional Steel Research* 2005;61:689-708.
- [38] Díaz C, Victoria M, Martí P, Querin OM. FE model of beam-to-column extended end-plate joints. *Journal of Constructional Steel Research* 2011;67(10):1578-1590.

- [39] Lim C, Choi W, Sumner EA. Low cycle fatigue life prediction using a four-bolt extended unstiffened end plate moment connection. *Engineering Structures* 2012;41:373-384.
- [40] Kim J, Yoon JC, Kang BS. Finite element analysis and modeling of structure with bolted joints. *Applied Mathematical Modeling* 2007;31:895-911.
- [41] AISC (2006). *Manual of steel construction load and resistance factor design*. 13th ed. Chicago, IL.
- [42] Chaboche JL. Constitutive equations for cyclic plasticity and cyclic viscoplasticity. *International Journal of Plasticity* 1989;5(3):247-302.
- [43] Kaufmann EJ, Metrovich BR, Pense AW. Characterization of cyclic inelastic strain behavior on properties of A572 Gr. 50 and A913 Gr. 50 rolled sections. ATLSS Report No. 01-13, Lehigh University, 2001.
- [44] Royster PB. Localized low cycle fatigue failure of welded steel moment connections. MS Thesis, North Carolina State University, Raleigh, NC, 2007.
- [45] AISC (2010b). *Seismic provisions for structural steel buildings*. American Institute of Steel Construction 341, AISC 341-10.
- [46] Morrison M. An innovative seismic performance enhancement techniques for welded steel moment connections. PhD Dissertation Research, North Carolina State University, Raleigh, NC, 2014.
- [47] Schweizer DQ. Experimental investigation of innovative seismic performance enhancement techniques for steel building beam to column moment connections. MS Thesis, North Carolina State University, Raleigh, NC, 2013.

- [48] Ellison MS, Corona E. Buckling of T-beams under cyclic bending. *International Journal of Mechanical Sciences* 1998;40(9):835-855.
- [49] Stojadinovic B. Stability and low-cycle fatigue limits of moment connection rotation capacity. *Engineering Structures* 2003;25:691-700.
- [50] Nakashima M, Liu D, Kanao I. Lateral–torsional and local instability of steel beams subjected to large cyclic loading. *International Journal Steel Structures* 2003;3(3):179-189.
- [51] Yin S, Corona E, Ellison MS. Degradation and buckling of I-beams under cyclic pure bending. *Journal of Engineering Mechanics* 2004;130(7):809-817.
- [52] Okazaki T, Liu D, Nakashima M, Engelhardt MD. Stability requirements for beams in seismic steel moment frames. *Journal of Structural Engineering* 2006;132(9):1334-1342.

**CHAPTER 3: AN IMPROVED UNSTIFFENED 8 BOLT EXTENDED
END PLATE MOMENT CONNECTION FOR SPECIAL AND
INTERMEDIATE MOMENT FRAMES
PART II: EXPERIMENTAL VALIDATION AND ADDRESSING
FURTHER DEVELOPMENT**

Abstract

Extended end plate (EEP) moment resisting connections provide the advantage of eliminating field welding and by virtue of this, facilitate fast field erection of building frames. Currently, EEP connections have been prequalified for use in the 2010ANSI/AISC 358 standard. For seismic applications rolled wide flange sections with a depth greater than 24" necessitate the use of a stiffened 8 bolt configuration. In this connection the stiffener serves the purpose of strengthening the end plate, distributing flange forces uniformly amongst the bolt group and promoting the formation of a plastic hinge away from the welds connecting the beam flange to the end plate. The study reported herein proposes an unstiffened 8 bolted end plate connection in which the bolt arrangement is modified so as to promote uniform distribution of flange force among the bolt group and plastic hinge formation is promoted by reducing the strength of steel over specified regions of the beam flanges by exposing the regions to high temperatures followed by slow cooling. Finally, strength degradation due to local web and flange buckling in the plastic hinge region is delayed via the addition of a web stiffener. Development of the proposed connection through detailed finite element studies was presented in part 1 of the study. Here, the results of full scale testing are presented and analyzed to demonstrate the seismic performance of the proposed connection. Connection behavior is further analyzed through post experiment finite element analysis. Future analytical as well as experimental needs for further development of the proposed connection are discussed.

Keywords: Steel moment connection, Extended end plate connection, Seismic performance enhancement, Beam plastic hinge, Reduced beam section

1. Introduction

In bolted extended end plate moment connections (BEEP) a steel plate is shop welded to the end of a beam which is then field bolted to the connecting members. Though shop fabrication of BEEP connections may be more costly than field welded connections, they offer the advantage of eliminating the difficulties associated with field welding and may provide rapid erection of moment frames [1]. Simulated seismic testing of BEEP connections have also shown them to be capable of providing significant ductility and seismic resilience and as a result, BEEP connections have prequalified for use in special moment frames (SMF) in the 2010ANSI/AISC 358 [2] prequalified connections for special and intermediate moment frames for seismic applications. The 2010ANSI/AISC 358 prequalifies 3 types of BEEP connections, the four bolt unstiffened, four bolt stiffened and the eight bolt stiffened extended end plate connections. In the stiffened connections a gusset plate is welded to the extended portion of the end plate and to the outer surface of the beam flange. This stiffener has been found to strengthen and stiffen the extended portion of the end plate usually resulting in thinner end plates in current design practice [3]. The stiffener also promotes yielding and plastic hinge formation at the base of the stiffener away from the beam flange to end plate CJP welds [4]. Investigations on 8 bolted and 4 bolted stiffened extended end plate connections [5-7] have shown ductile performance and good energy dissipation. However, in other studies [7-11] premature failure of the weld between the beam flange and the stiffener or fractures initiating at beam flange to end plate CJP welds followed by gross section fractures of the stiffener have been observed. In one study [12] fracture was reported to have initiated at the toe of the weld between the end-plate stiffener and the beam flange and was attributed to the stress concentration in this region. This stress concentration results from the geometric discontinuity introduced by the stiffener and may be exacerbated by the presence of weld defects some of which may not be detected by welding inspection practice [13]. Careful detailing, fabrication and inspection of stiffened BEEP connections may reduce the

likelihood of failures arising from the stress concentration induced by the flange stiffener, however the seismic performance uncertainty and added complexity to design, fabrication and inspection associated with stiffened BEEP connections has motivated the development of an 8 bolt unstiffened extended end plate connection in which 3 novel seismic performance enhancing techniques have been introduced. This connection was developed through detailed finite element simulations in a companion paper by Quayyum and Hassan [14]. In that paper, the 8 bolted extended end plate moment connection was studied in detail to assess the influence of the flange stiffeners, bolt arrangement, plastic hinge formation and other parameters on connection behavior and ductility. The study presented herein describes the results of full scale testing of the connection proposed by Quayyum and Hassan [14]. Experimental development as well as measured global and local experimental responses will be discussed. Connection performance is further analyzed through post-test finite element simulations; also, analytical as well as experimental needs for further development of this connection will be addressed.

2. Review of Proposed Novel Performance Enhancing Techniques

In the companion paper by Quayyum and Hassan [14] details of the conceptual and finite element development of the proposed modified 8 bolt extended end plate connection are presented, however they are briefly summarized here as follows. The first of the 3 performance enhancing modifications is the removal of the end plate stiffener and rearrangement of the bolts in a hexagonal pattern as shown in Figure 1 and Figure 4d. Finite element analysis (FEA) showed that the end plate stiffener creates a stress concentration at the toe of the weld between the stiffener and the beam flange. To avoid this stress concentration the stiffener was removed, however in order to ensure uniform bolt force distribution rearrangement of the bolt group was necessary. The proposed hexagonal pattern was found to be effective in promoting uniform force distribution amongst the bolt group reducing the likelihood of non-ductile failure modes such as bolt rupture and end plate fractures. Such failures were observed in 8 bolt-4 wide unstiffened extended end plate connections tested by Sumner *et al.* [7].

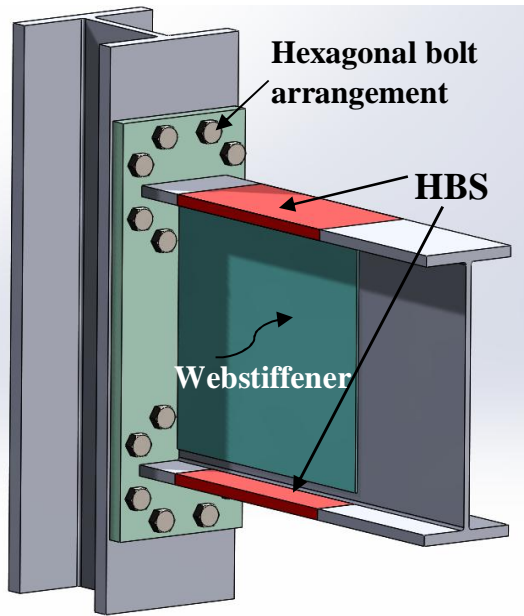


Figure 1 Sketch of Modified BEEP Connection.

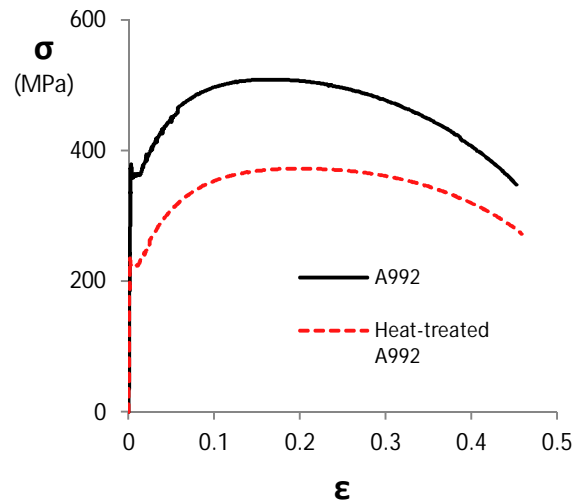


Figure 2 Engineering stress-strain response of A992 and heat-treated A992 steel.

To further enhance performance, high temperature heat treatment of the beam flanges was added to the proposed connection. This heat treatment involves subjecting selected regions of the beam flange to high temperatures followed by slow cooling and by so doing reduces the strength of steel in the heat-treated beam section (HBS). Details of the heat treatment and its effect upon a wide range of material properties are presented elsewhere [15] however, the uniaxial stress strain response comparison of an ASTM A992 steel coupon before and after heat treatment is shown in Figure 2. As can be seen from this figure the yield and tensile strength of the material is reduced by 38% and 25% respectively while the elastic modulus and ductility remain unaffected. This reduction in strength promotes yielding and plastic hinging within the HBS in a manner similar to the reduced beam section (RBS). However, a connection modified with the HBS does not sacrifice elastic stiffness or buckling resistance as does the RBS. The HBS technique was previously validated on welded flange-welded web (all welded) moment connections by Morrison *et al.* [15].

Finally, a technique for delaying the onset of strength degradation was included in the proposed connection. This technique involves welding a steel plate to the beam web and end plate in the expected plastic hinge region which stiffens the beam web and delays the onset of web local buckling. In the companion study web local buckling was observed to be the first mode of instability that eventually led to lateral torsional buckling and strength degradation. The addition of the proposed “web stiffener” was found to be effective in delaying the onset and slowing the rate of strength degradation [14]. The connection which was proposed in the companion paper was called 8EMH-W [14], however the testing of this connection was included as a part of a broad experimental program in which the test specimen was assigned the name HBS 4 and will be referred to as such in the following.

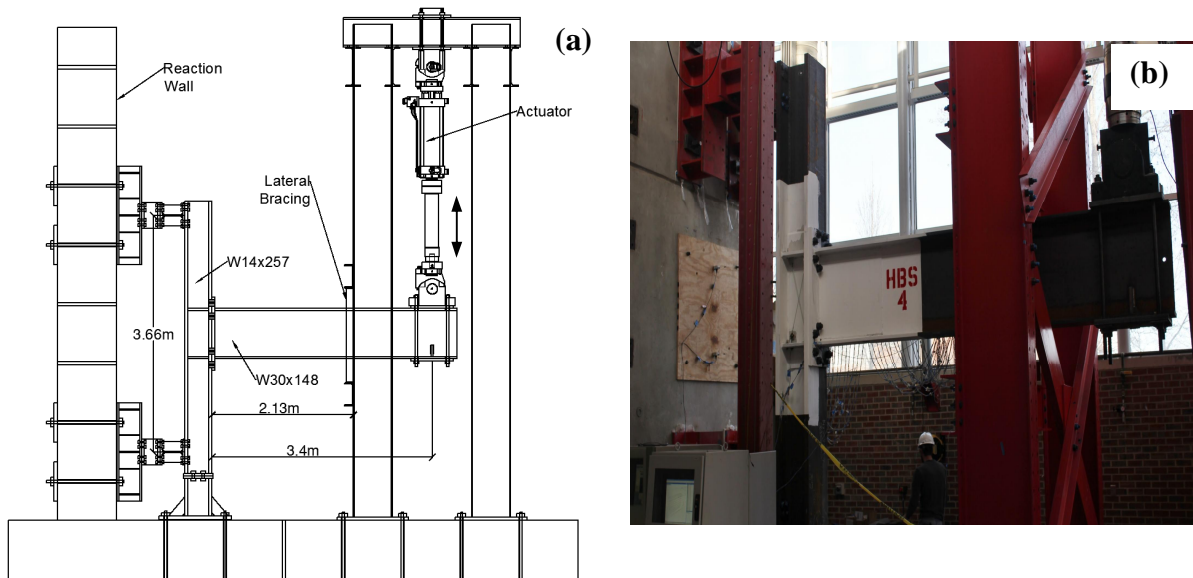


Figure 3 HBS 4 Test setup. (a) Sketch of test setup, (b) photograph showing test setup.

3. Connection Design and Experimental Setup

One large scale specimen (HBS 4) was tested to evaluate all three performance enhancing modifications. The test setup and details of the test specimen are shown in Figures 3 and 4. The connection was fabricated by an AISC certified commercial fabricator. All welds were made in the fabrication shop in the down hand position and welding was accomplished using

gas shielded metal arc welding (GMAW) with E71T-1C-H8 electrodes (Lincoln ultra core 71C) which is specified to meet all the requirements of AWS D1.8. The beam flange was welded to the end plate with complete joint penetration welds (CJP) similar to the AWS prequalified TC-U4b-GF weld. These welds were made without an access hole and backing bar, however an 8 mm (5/16 inch) backing fillet weld was provided.

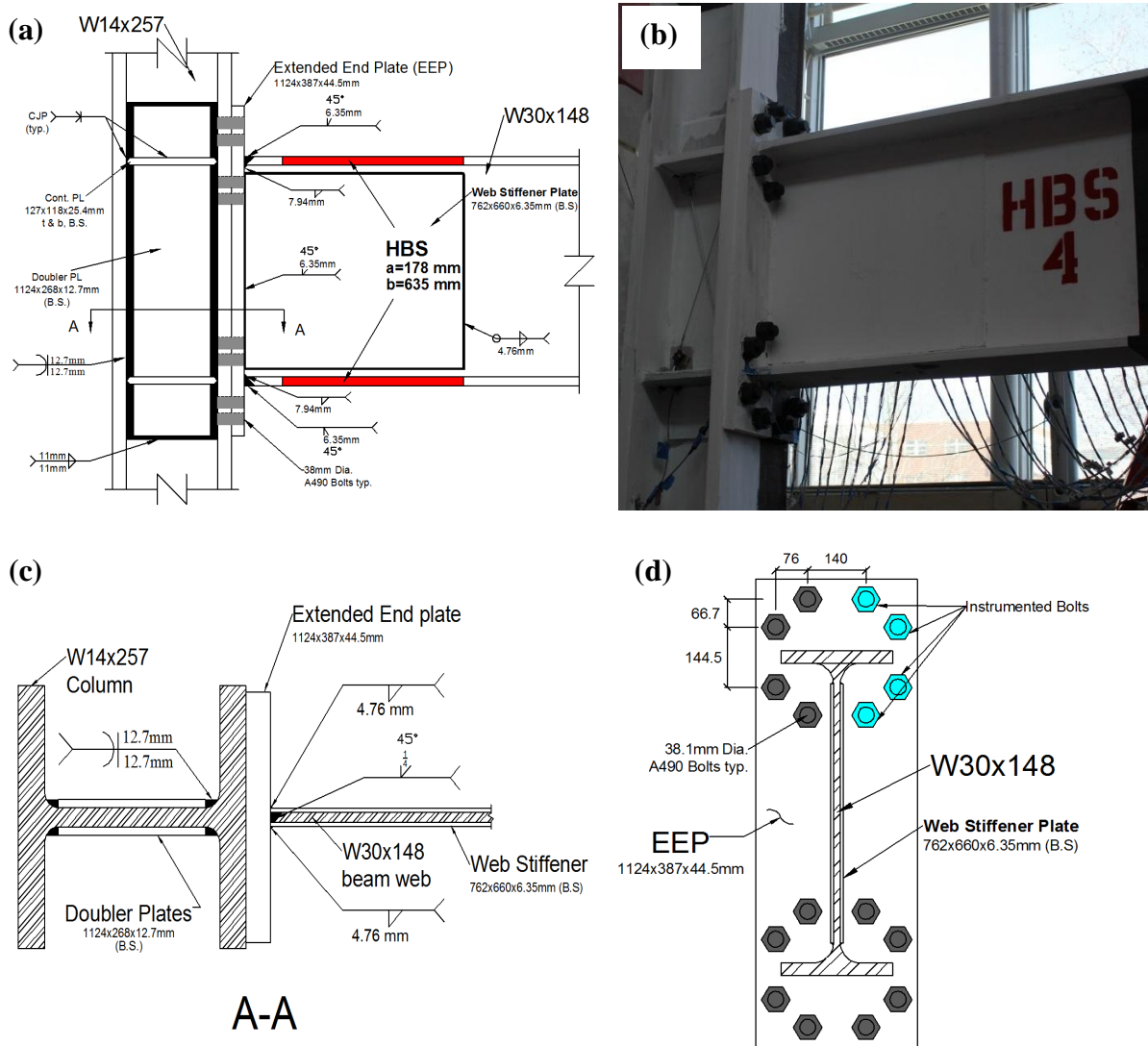


Figure 4 HBS 4 connection details. (a) Elevation of connection, (b) photograph of HBS 4 connection prior to testing, (c) section A-A showing connection of beam web and web stiffeners to end plate, (d) elevation of end plate showing modified bolt arrangement.

This weld detail is similar to that used in other BEEP studies [3] and results in a small region of the CJP weld (directly above the beam web) that is uninspected. The beam web was welded using a CJP weld, which was used in lieu of fillet welds to facilitate the fit up and welding of the web stiffeners as shown in Figures 4a and 4c. As may be inferred from Figure 4c the web stiffener plate adjacent to the root of the bevel was used as a backer for the beam web CJP weld. Fillet welds were used to connect the web stiffeners to the end plate and to the beam web as shown in Figure 4a. These welds resulted in distortion of the web stiffener plates which adversely affected their effectiveness in delaying the onset and retarding the progression of local buckling as will be discussed later. Finally, the column was reinforced with two-12.7 mm (1/2 inch) doubler plates which were designed to promote strong panel zone behavior in order to ensure that most of the inelastic action was confined to the beam.

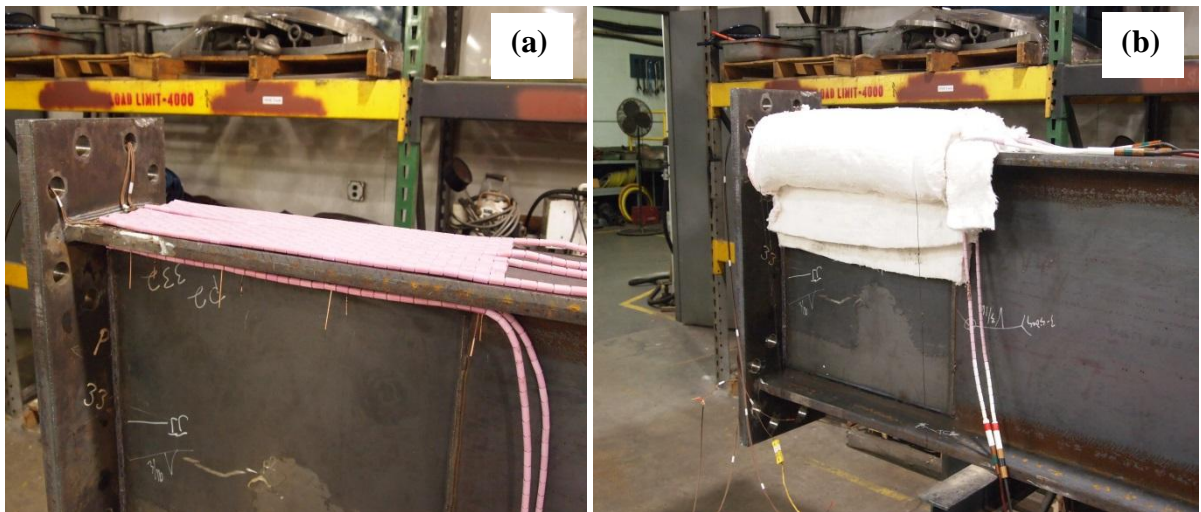


Figure 5 Heat-treatment setup. (a) Photograph showing electric surface heating pads during installation on a beam flange, (b) photograph showing insulation of beam flange for well controlled heating and cooling.

Upon completion of fabrication, selected regions of the beam flanges were heat treated. The locations of the heat treated regions are shown in Figure 4a and were decided upon numerically through finite element simulations [14-15]. Heat treatment was performed using electrical resistance ceramic mat heating pads as shown in Figure 5a. Heating pads were

sized according to the required dimensions of the HBS and were installed on the inner and outer surface of the beam flanges. The heating pads were connected to a power supply and type K thermocouples were used to monitor temperatures and provide continuous feed back to the power supply. Two (2) layers of 50 mm (2 inch) high density ceramic fiber insulation blankets were wrapped around the beam flanges as shown in Figure 5b to provide well controlled heating and cooling. More details about the heat treatment setup and procedure are provided in Morrison *et al.* [15]. The assembly of the beam and column was made with the column in the vertical “upright” position. Bolts were installed and ‘tightened’ using the turn-of-nut method. The turn-of-nut procedure was first verified by tightening bolts from the same batch of those used in the test specimen in a Skidmore Wilhelm bolt tension calibrator to the minimum pretension specified by the AISC LRFD Specification [16].

4. Instrumentation

The test specimen was equipped with strain gauges along the beam flanges to monitor longitudinal flange strains at various locations including the beam flange to end plate weld toe and HBS region. Bolt response was of particular interest; as such, 4 of the 16 bolts were instrumented by installing a strain gauge in the center of the unthreaded portion of the bolt shank. The instrumented bolts are highlighted in blue in Figure 4d. String and linear potentiometers were used to monitor displacements in the column, beam and panel zone. A calibrated load cell in the hydraulic actuator provided readings of force response during the experiment. All specimens were painted with hydrated lime prior to testing to visually indicate regions of yielding. The Optotrak Certus HD three-dimensional (3D) position system produced by Northern Digital Incorporated was used to capture the positions of markers placed along the beam flanges and web as shown in Figures 6a and 6b. Two Optotrak cameras were used which were able to capture the motion of markers placed on the top and sides of the beam top flange, the beam web and the side of the beam bottom flange. Position time history data obtained from this system was post processed to calculate displacements and strains in areas of interest. The Optotrak system provides the advantage of being able to

record large cyclic inelastic strains while electrical resistance strain gages may either exhibit gradual strain drift or fail to remain adhered.

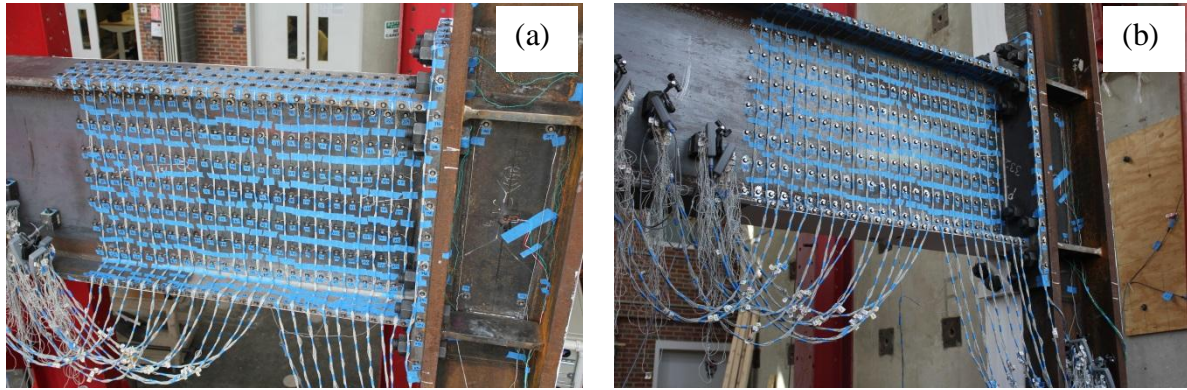


Figure 6 Instrumentation of HBS 4. (a) LED markers placed on beam top flange, beam web and web stiffeners, (b) LED markers placed on the sides of beam top and bottom flange, beam web and webstiffeners.

5. Test Results

5.1 Global Response of Modified BEEP Connection

Testing was carried out at the North Carolina State University Constructed Facilities Laboratory. Loads were applied at the beam tip in accordance with the 2010 ANSI/AISC 341 [17] seismic provision Appendix S loading protocol consisting of quasi-static increasing displacement cycles. Figure 7a shows the moment-rotation response of HBS 4. The global response is characterized by wide hysteretic loops indicating good energy dissipation. The specimen exceeded the 2010 AISC Seismic Provisions [17] special moment frame (SMF) qualifying 4% interstory drift angle without significant strength loss. Slight strength degradation began during the 1st loading cycle at 4% interstory drift and progressed during later loading cycles at 5% and 6% interstory drift. Loading was terminated during the second cycle at 6% story drift due to fracture in the location of significant beam flange buckling (see Figure 13b). The response of HBS 4 is further analyzed by plotting the total rotation contributions and the moment-plastic rotation curves for each component of the connection assembly which were calculated using data measured by instrumentation during the test and equations proposed by Popov *et al.* [18]. These graphs as shown in Figure 7b and Figure 8a-d

indicate that panel zone shear and column flexural deformations contributed only to the elastic behavior of the sub-assembly and as a result, inelastic action was entirely confined to the beam. It is of note that end plate separation was not recorded, however given the strong plate approach adopted in this modified BEEP connection, end plate inelastic flexural deformations and end plate separation are expected to be negligible.

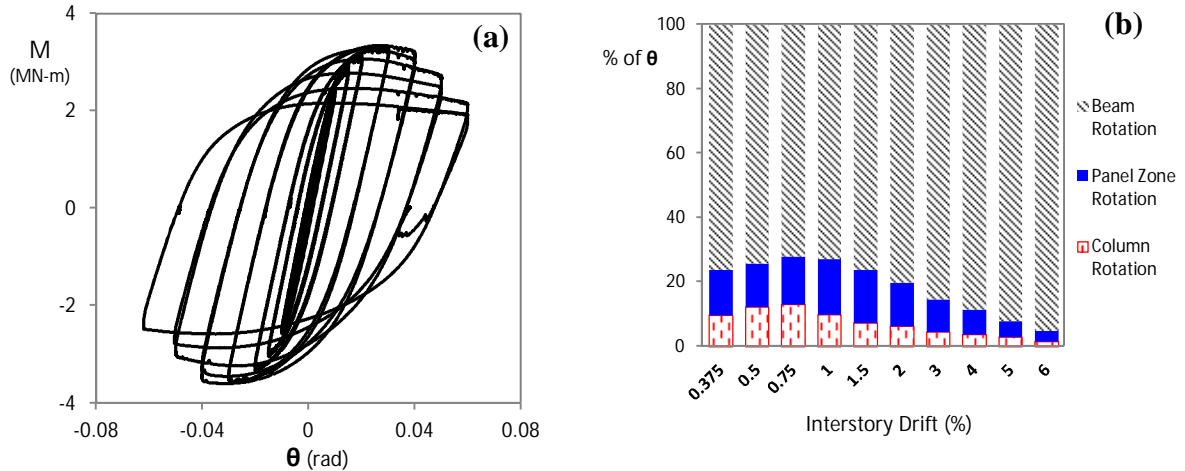


Figure 7 Experimental response of HBS 4. (a) Moment-rotation hysteresis response, (b) total rotation contributions.

5.2 Plastic Hinge Formation in the Modified BEEP Connection

Figure 9a-d illustrates the progression of inelastic action along the beam flange via bar graphs in which the distribution of longitudinal tensile strains (normalized by the yield strain) along the centerline of the beam flange at various stages of the loading history are plotted. Bars highlighted in red represent the strains in the heat-treated (weakened) regions. Strains were calculated by post processing data obtained from 3D noncontact spatial displacement measurement sensors placed along the beam flange as shown in Figure 6a. These plots illustrate the influence of the HBS in promoting majority of the inelastic action away from the beam flange to end plate connection. Similar observations have made in all welded connections modified with HBS [15]. The strain profiles indicate that flexural yielding initiates in the heat treated areas at 1% drift. As loading is continued longitudinal strains increase more in the heat treated areas than in the unheat-treated

regions adjacent to the beam flange to end plate welds. It is important to note that the beam length of 3.4 m (134 in) used in this test corresponds to a moment frame with a clear span of 6.8 m (22 feet). This relatively short span results in a large moment gradient which is reflected in the strain profiles. As drift angle increases from 3% to 4% longitudinal strain in the heat treated regions increase significantly while strains outside of the heat treated areas grow only slightly. This demonstrates that the large displacements imposed at the beam tip are mostly accommodated by flexural deformation in the HBS.

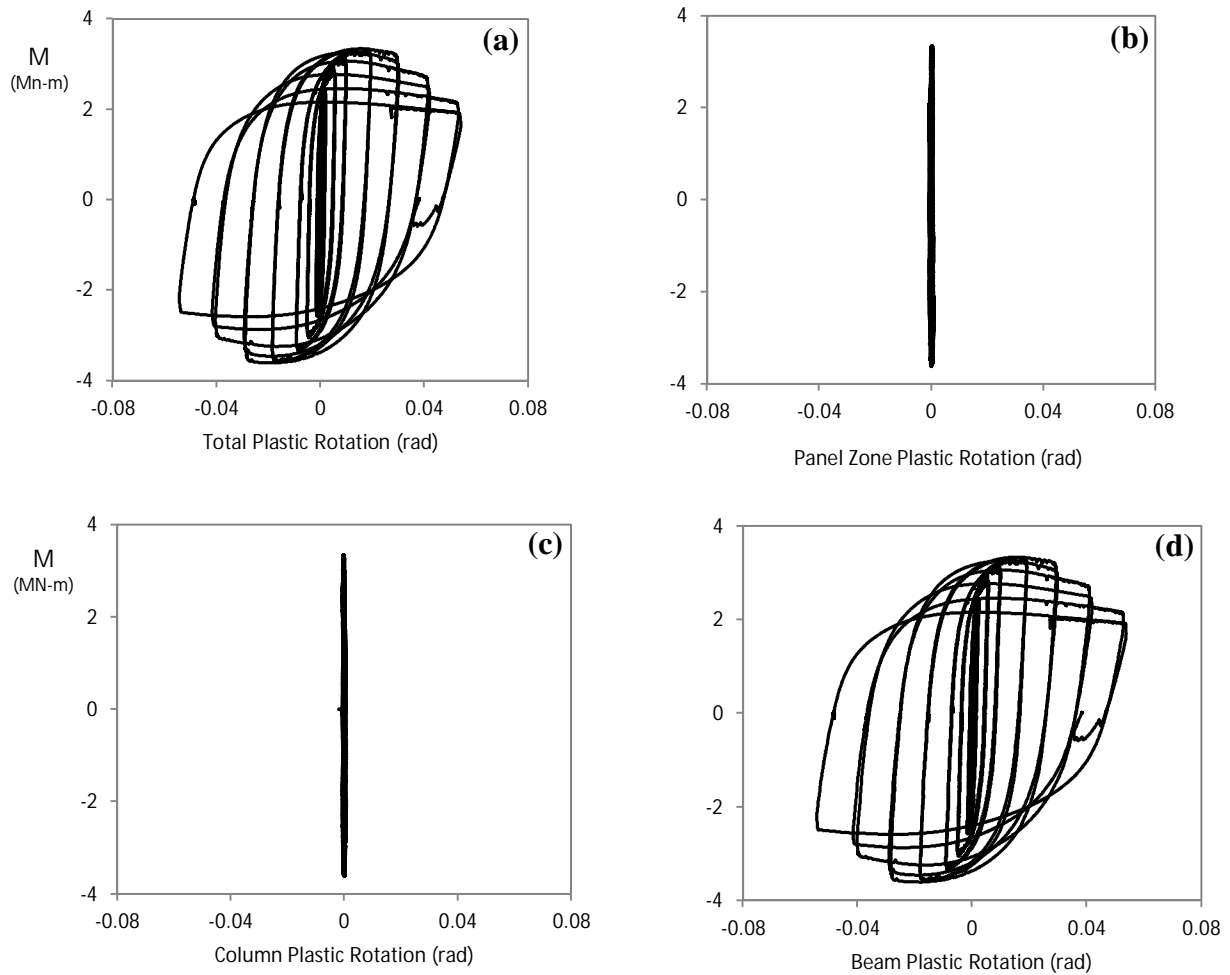


Figure 8 Plastic rotation contributions by components of HBS 4. (a) Total connection plastic rotation, (b) panel zone shear plastic rotation, (c) column flexural plastic rotation, and (d) beam plastic rotation.

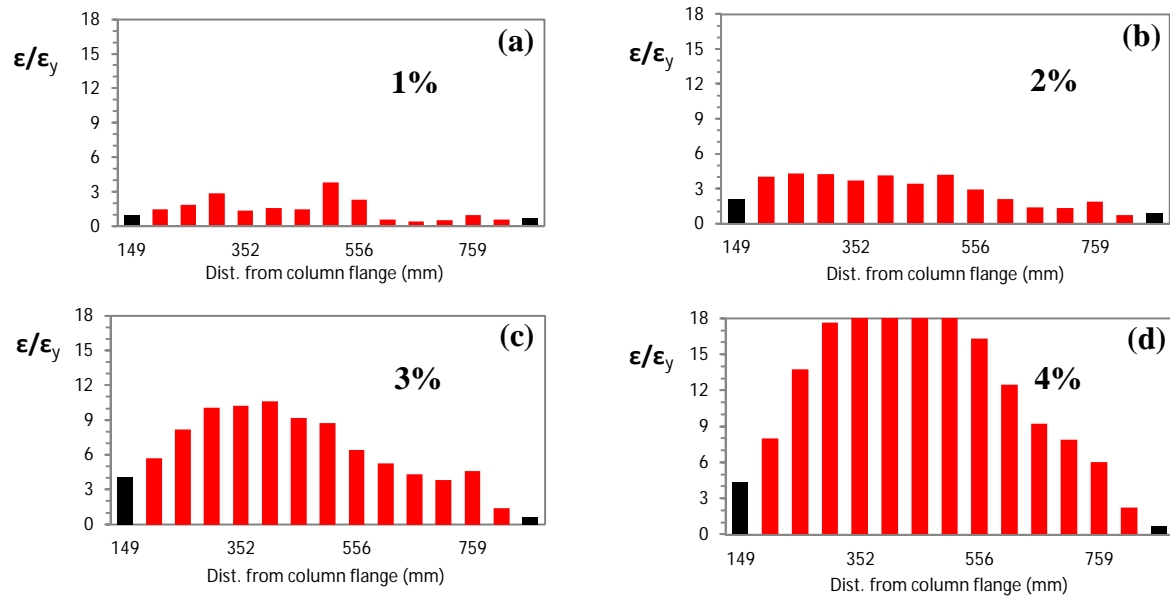


Figure 9 Recorded longitudinal strain along the center of top flange of the beam from HBS4.

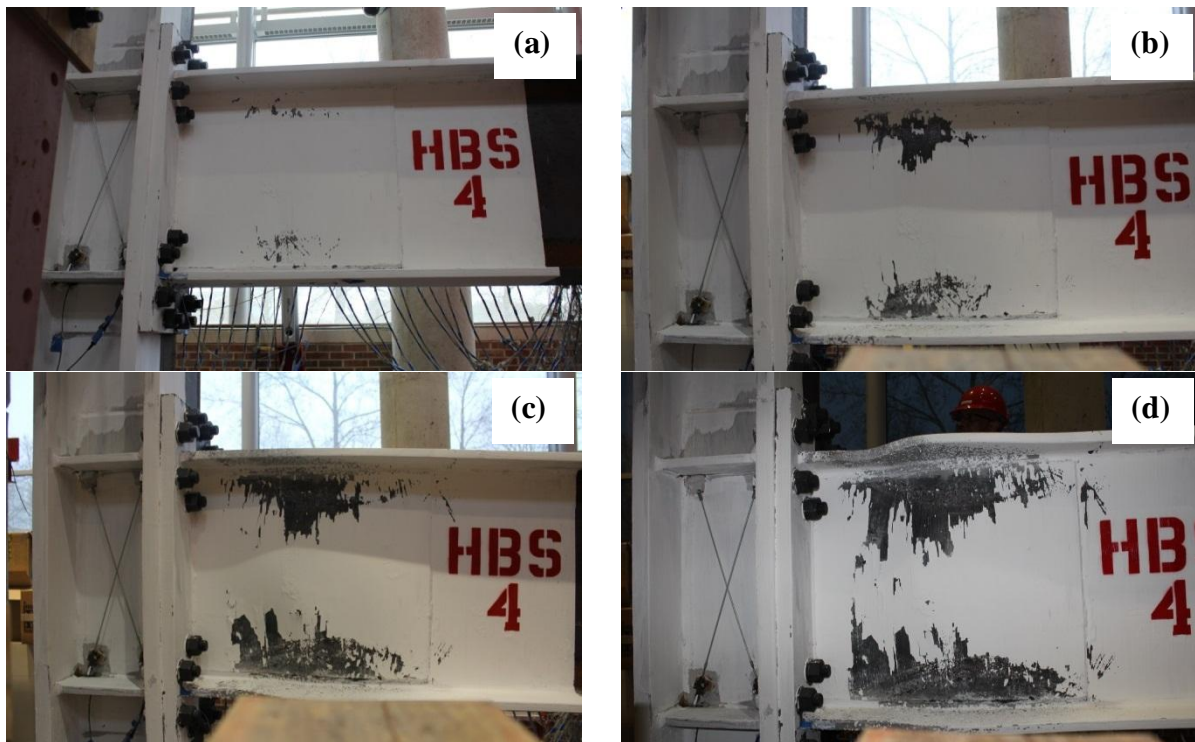


Figure 10 Progression of yielding and plastic hinge formation in HBS 4. (a) 1% drift, (b) 2% drift, (c) 3% drift, and (d) 4% drift.

The progression of the plastic hinge formation is also qualitatively reflected in the photographs shown in Figure 10a-d where it is observed that flaking of the white wash takes place away from the beam flange to end plate junction during loading cycles from 1% to 4% interstory drift. The beam tip load vs. longitudinal strains recorded from strain gages placed on the beam bottom flange at the weld toe and in the HBS region are shown in Figure 11. This figure further highlights the performance of the HBS in shifting inelastic action away from the beam welds. Here it can be inferred that the HBS acts like a damper for the connection providing energy dissipation in a location free of stress and strain concentrations (prior to the onset of local buckling) and resistant to fracture. As a result, locations which are relatively less ductile or fatigue resilient (e.g., the beam flange to end plate welds or beam flange to column flange welds in the case of all welded connections) are exposed to lower strain demands providing enhanced connection performance.

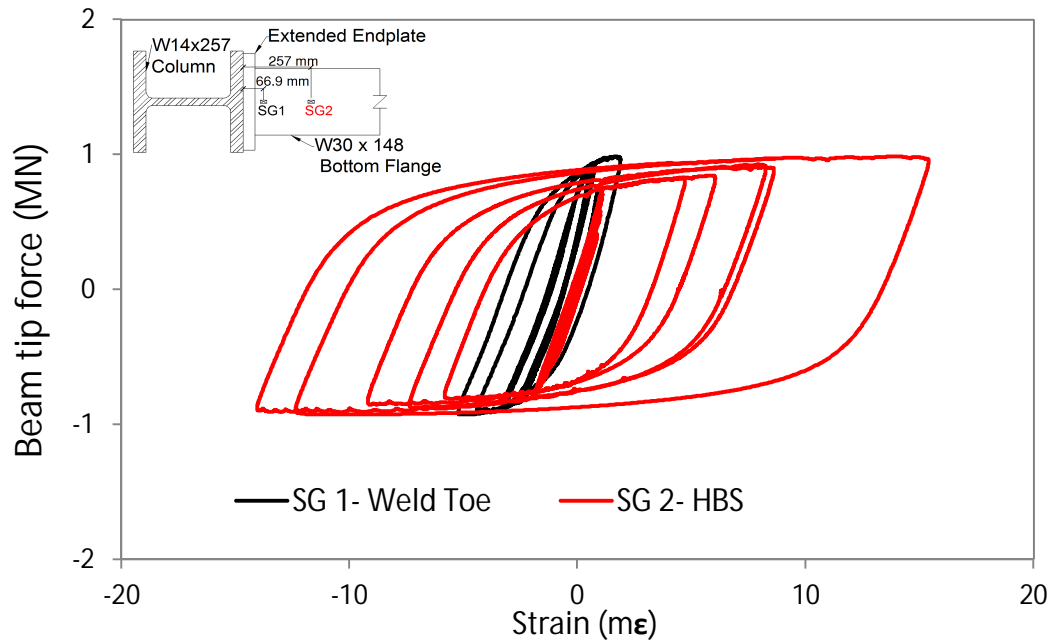


Figure 11 Measured flexural strains from strain gages placed on the bottom flange of HBS 4. Strains are shown from the beginning of test to the second cycle of 3% drift.

5.3 Bolt Response in the Modified BEEP Connection

The measured axial strains vs column centerline bending moment is shown in Figure 12 for the 4 bolts which were instrumented with strain gages. In general bolt axial strain behavior is characterized by increased strains during tensile excursions (i.e. negative bending of the beam) followed by a reduction in strain when the loading is reversed. In all cases a gradual relaxation of the bolt strains was observed with progressive loading. Note that the recorded tensile strains from the initial tightening of the bolts differ which reflects the variability in pretension forces that may be encountered when using the turn of nut method. Comparison of the inner and outer bolts (bolts 1 and 2) located above the top flange shows approximately a 10% difference in the peak tensile strain response of these bolts throughout the loading history (Figure 12a and 12b). Both bolts relaxed to approximately 75% of their pre-tension strain at the end of the test. The bolts located below the flange (Figure 12c and 12d) displayed larger strains (especially bolt 4) indicating that these bolts resisted a larger portion of the tensile forces. The difference in peak tensile strains between the inner and outer bolts (bolts 3 and 4) was approximately 10%. In particular bolt 4 showed a sharp increase in strain with applied moment. This was expected due to the relative proximity of this bolt to the stiff beam web to flange junction. The welding of the beam web, web stiffeners and beam flange in this region stiffens the end plate and attracts larger forces to the bolts nearest to this area. This behavior was captured by pretest finite element analyses [14] and though bolt 4 did experience slightly larger strains than the other instrumented bolts, no permanent set in bolt strains was observed nor was this behavior found to be detrimental to connection performance.

5.4 Failure Mechanism

Loading of the HBS 4 was terminated due to a fracture in the beam flange at the location of significant local buckling as shown in Figure 13a and 13b. This flange buckling mechanism appeared to have initiated during loading cycles at 3% drift and strength of the connection progressively deteriorated during loading cycles at 4%, 5% and 6% drift. The initiation of this strength degradation mechanism at 3% drift was unexpected based on pre-test FEA

(Figure15a). As mentioned before the edges of the web stiffener were continuously connected to the beam web and end plate with (4.76mm) fillet welds.

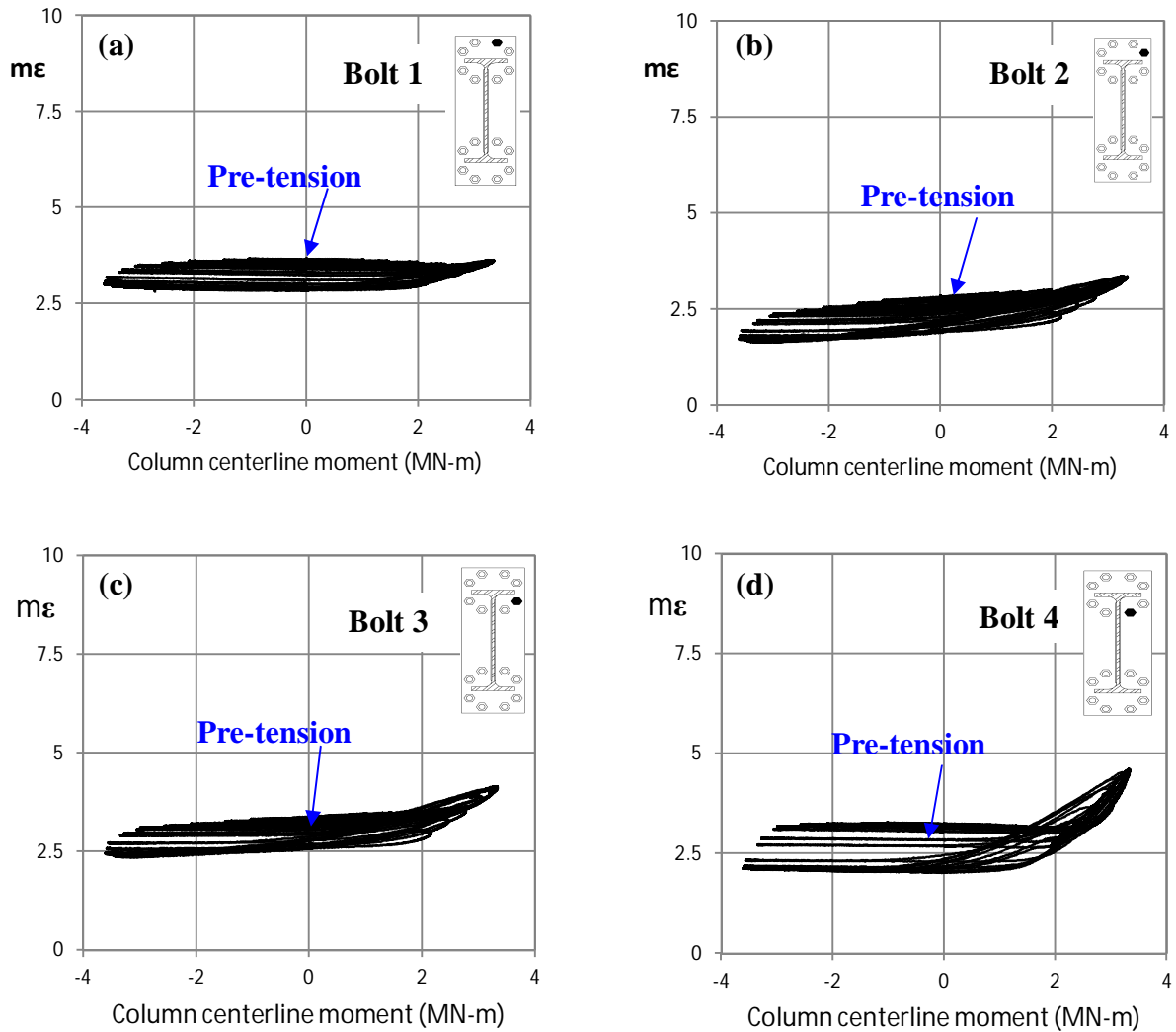


Figure 12 Recorded axial bolt strain vs column centerline moment.

These welds resulted in distortion (bowing outward) of the web stiffener plates. Based on pretest measurements obtained from the optotrak markers placed on the beam web and on the web stiffener plates it is estimated that at the center of the plates there was a maximum 19 mm gap between the beam web and the web stiffeners. During loading cycles at 1.5 % drift, loud noises similar to those created during a fast fracture were heard. It is believed that these

noises were created from impact occurring between the web stiffeners and the beam web. This impact was due to the buckling of the web stiffeners which was visually observed during loading cycles at 2% drift and continued for the remainder of the test. This early initiation of buckling limited the effectiveness of the web stiffeners in delaying the onset of beam local web buckling and strength degradation and will be discussed further in the following section.

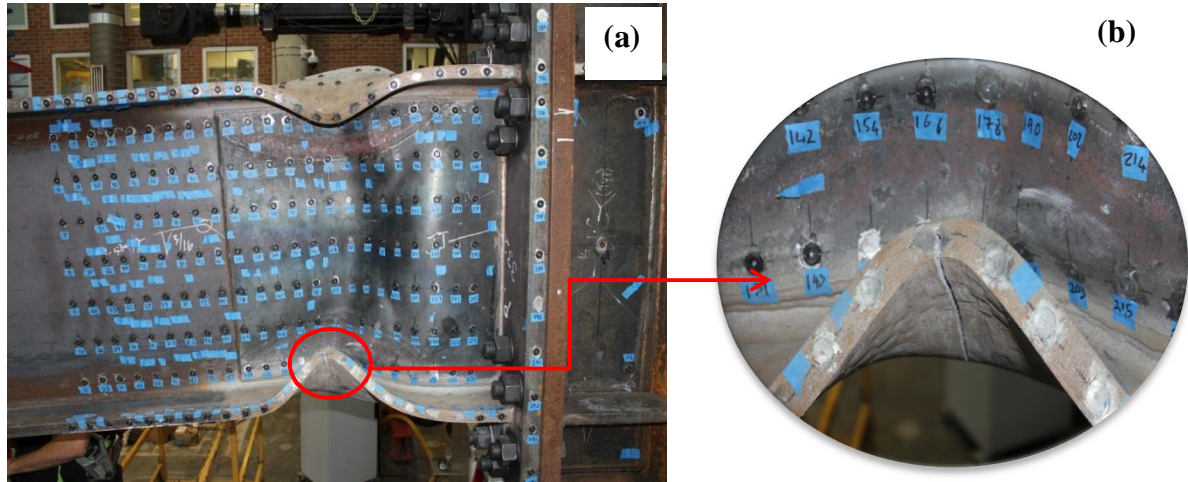


Figure 13 Local buckling failure of HBS 4. (a) Post test photograph showing flange and web local buckling, (b) photograph showing fracture of beam flange in the crest of flange buckle.

6. Post-Test FEA and Discussion

In order to more closely analyze the behavior of HBS 4, post-test FEA was conducted using general purpose finite element software ANSYS. The features of the finite element model including the element type, material model and material parameters were kept same as those presented in the pre-test numerical study [14]. However, an attempt was made in the post-test FEA to model the welding induced initial distortions in the web stiffener plates as shown in figure 14a. Estimates of geometry of the web stiffener plates were obtained from the pre-test displacement fields recorded by the Optotrak system. As noted previously Optotrak sensors were placed on the web stiffener plates and on the beam web. By assuming a nominal thickness of the web stiffener plate and no distortion in the beam web, estimates of the initial gap between the beam web and the web stiffener as well as the “distorted shape” of

the web stiffener could be made and included in the post-test FEA. Welding induced residual stresses and strains were not included in the model. Also, no geometric imperfections were included in the modeling of the beam and column. A comparison between the FEA prediction and the observed moment-rotation response is shown in Figure 14b. The FEA prediction is in good overall agreement with the experiment response both in terms of peak strength prediction and the rate of strength degradation. The predicted deflected shape is compared with a photograph of the test specimen during cycles at 6% drift in Figure 14c and 14d. Predictions of the top flange buckling amplitudes are also compared with the measured top flange deflections Figure 14e and 14f. These comparisons show that local deformations including buckling modes are reasonably predicted by the FEA model.

The finite element model was used to analyze the effect of the initial distortion of the web stiffener plates on the initiation and rate of strength degradation of HBS 4. Presented in Figure 15a is a comparison of the moment vs. interstory drift envelop in negative bending for a pre-test simulation including perfect geometry of the web stiffener plates (full initial contact between the web stiffener and the beam web), a post-test simulation including welding induced distortion of the web stiffener plates, and a post-test simulation with no web stiffener plates. As expected these results show that the welding induced distortions limited the effectiveness of the web stiffener plates.

From comparison of both post-test simulations (with and without the web stiffener) it is observed that web stiffener increases the moment capacity and slows the initial rate of strength degradation between 3% and 4% interstory drift. However, the rate of strength degradation between 4% and 6% is unaltered resulting in a strength loss of approximately 27% during cycles at 6% drift. This is approximately twice the amount of strength loss predicted by the pre-test simulations. This accelerated strength loss is accompanied by larger amplitudes of local flange buckling and larger plastic strains as shown in Figure 15b and 15c which compares the equivalent plastic strains for pre and post-test simulations of HBS 4.

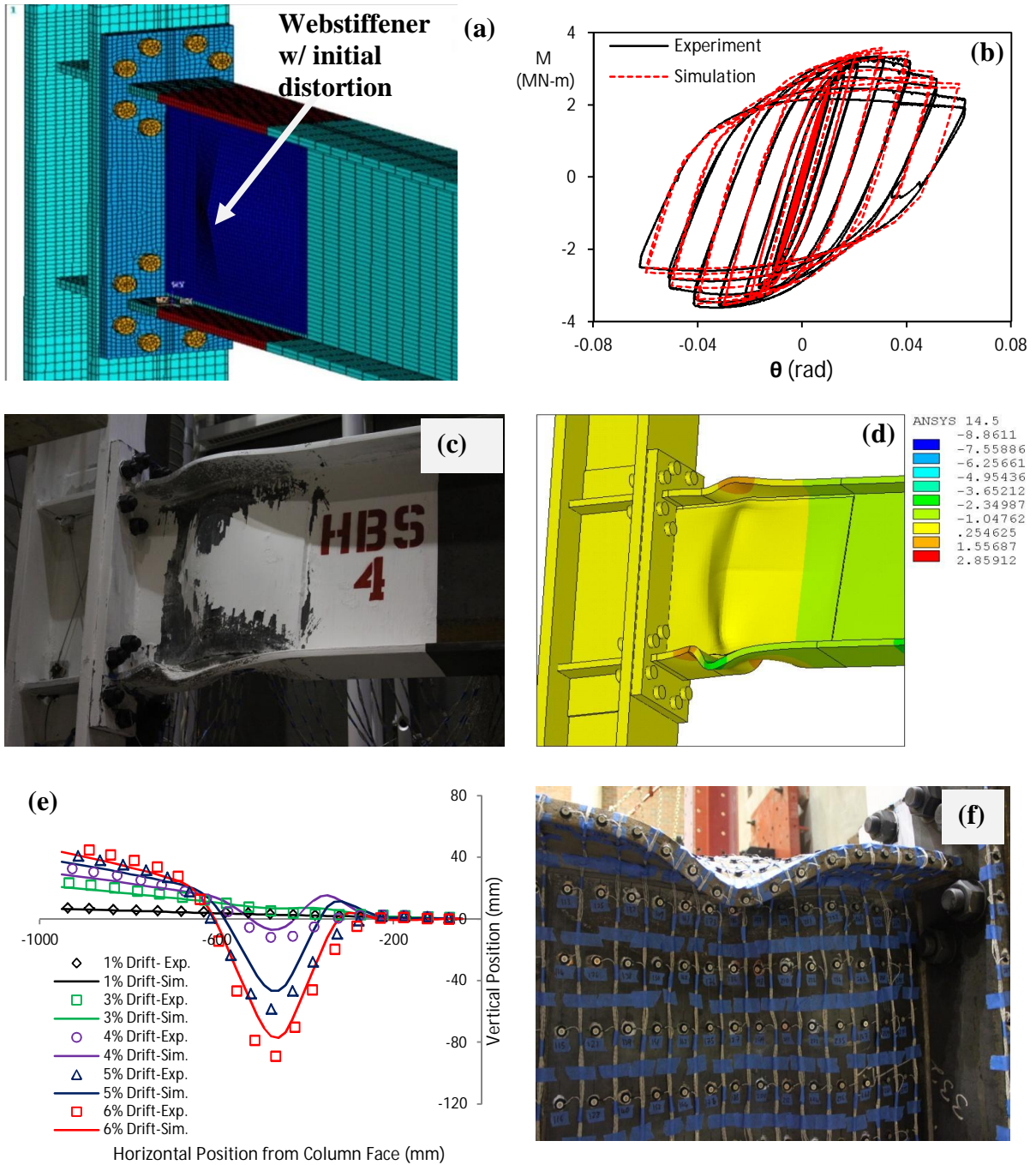


Figure 14 Validation of post-test FEA of HBS 4. (a) FEA discretization including initial distortion of web stiffener plates, (b) comparison between FEA prediction and the recorded moment-rotation response, (c) photograph of HBS 4 during loading cycles at 6% drift, (d) FEA prediction of deformation at 6% drift, (e) comparison between FEA predictions and recorded top flange vertical displacements during various stages of loading history, (f) photograph of HBS 4 top flange during loading at 4% drift.

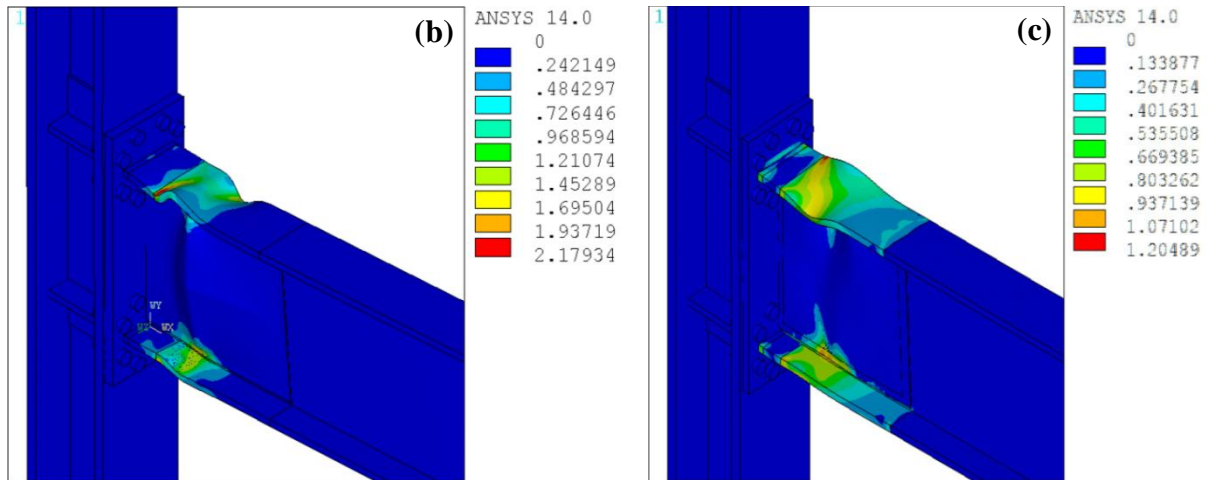
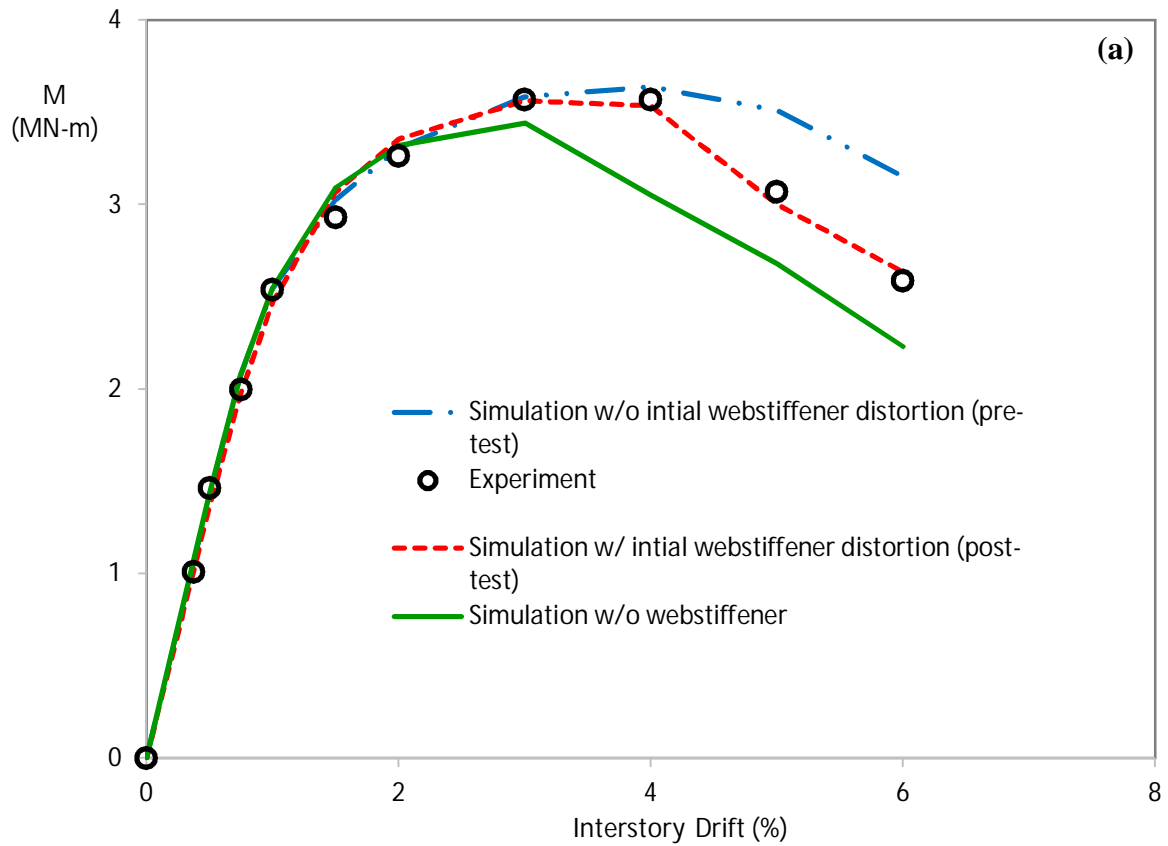


Figure 15 Post-test FEA simulation results showing the effect of initial web stiffener plate distortion. (a) Moment-rotation envelop, (b) plastic equivalent strain prediction at 5% drift for HBS 4 (post-test simulation with initial web stiffener distortion), (c) plastic equivalent strain prediction at 5% drift for HBS 4 (pre-test simulation without initial web stiffener distortion).

7. Future development of Modified BEEP Connections

Due to limited resources only 1 test specimen was evaluated in this study. This test specimen included 3 modifications all of which were judged to have had an influence on overall the performance of the connection. However, it is practically impossible to accurately access and quantify the effect of each modification on various performance parameters including ductility, strength, buckling resilience, reliability etc. from the result of one full scale test. As such future development of the modified BEEP connection should involve more experiments in which each performance enhancing modification can be studied individually to more narrowly quantify and analyze its effect. For example, in the FEA development of the modified BEEP connection it was found that the combination of a ‘strong’ end plate with the arrangement of bolts in the proposed hexagonal pattern significantly reduced strain demands in the bolts and end plate, however plastic hinging of this connection forms at the beam end and as a result high strain demands are placed on the beam flange to end plate welds. This motivated the use of the HBS as opposed to the currently used flange stiffener to shift plastic hinging away from the beam end without introducing stress or strain risers. Shifting the plastic hinge away from the beam end in such a manner reduces strain demands at the welded joint and so it is believed that this provides more reliable connection performance.

However, experimental evaluation of the modified unstiffened BEEP connection without the HBS may demonstrate that this connection can meet or exceed the performance requirements for use in SMF’s outlined in the AISC seismic provisions. This assertion is made based on the following factors which may contribute to enhanced ductility of EEP connections:

1. EEP connections are shop welded in more favorable conditions (year round) when compared to field welded connections, thus eliminating some problems related with field welding. In particular, shop welding ensures adequate access to perform welding and also to make sound visual inspections during and after welding. It is also possible to make all welds in the preferred ‘down hand’ position which is not possible in field welded connections such as the WUF-W or RBS.

2. Due to the fact that EEP connections are shop welded, no weld access holes are required to make flange to end plate welds. This reduces the inevitable stress and strain concentrations introduced by access hole cuts. It must be noted that as a consequence of the elimination of the access hole, the beam flange to end plate weld directly above the beam web is a partial-joint-penetration weld. However, this has not proved to be detrimental to connection performance in published experimental studies.

The combination of these factors with the use of ‘notch-tough’ low hydrogen welding electrodes with specified minimum Charpy V-notch toughness, strict quality control practices such as the careful cleaning and preparation of the weld root opening, careful visual inspection of root and subsequent weld passes, removal of weld run off tabs, compliance with AWS specified minimum preheat temperatures etc., may provide adequate ductility to modified 8 bolt EEP connections precluding the need for either reinforcing the connection or weakening the beam. Such a connection may prove to be more economical than the currently prequalified 8 bolt stiffened extended end plate connection and as such, future studies to evaluate its seismic performance are warranted.

7.1 Future work on web stiffener

In the current study the web stiffener plates seemed to provide some resistance to strength degradation but not to the extent that was predicted by pre-test analysis. It is noted here that the web stiffener concept may be extended to field welded connections in which a fuse is provided, for example the RBS and the recently validated HBS [15] connection. However, given the lessons learned in this current study, more consideration should be given to the attachment of the web stiffener. Further FEA studies evaluating various attachment details for e.g. use of plug welds and slot welds to provide more attachment points between the beam web and the web stiffener plates, thus improving the overall stiffness of the assembly may be useful towards more successful implementation of this technique. Thermo-mechanical simulations to include the effect of welding induced distortions and residual stresses may provide useful insight in this process. In addition, compact wide flange sections

readily achieve rotation capacities of 3 [19] or greater before the onset of significant local buckling and resulting strength loss. As such, carefully constructed moment connections utilizing these sections readily achieve the 2010 AISC Seismic Provisions [17] special moment frame (SMF) qualifying 4% interstory drift angle without more than 20% loss of nominal moment capacity. Therefore, the web stiffener technique may provide more added value to built-up beams with slender webs in which rotational capacities are reduced.

7.2 Design Development

Given that the proposed modified EEP connection deviates significantly from the configuration of existing prequalified EEP connections, design methodologies for the practical use of modified EEP connections in moment frames also need to be established, in particular the limits of beam and column size including flange thickness, depth etc. Also design equations or tables to proportion and configure the modified end plate are needed. In the current study, design of the end plate was partly guided by using equations based on yield line analysis to select trial end plate sizes. FEA was then used to optimize the design of the end plate and bolt arrangement. This type of exercise is not well suited for design practice and therefore future studies need to be conducted to develop prescriptive design procedures for the proposed modified 8 bolt unreinforced EEP connection.

8. Conclusions

The test results of a modified 8 bolted unstiffened extended end plate connection has been presented. Three (3) performance enhancement techniques were utilized in this connection. These include the removal of the flange stiffener and rearrangement of the bolts in a hexagonal pattern, heat treatment of the beam flanges in specified regions adjacent to the connection, and the welding of steel plates called ‘web stiffeners’ to the beam web. The modified BEEP connection displayed ductile seismic response which exceeded the 2010 AISC Seismic Provisions [17] SMF qualifying 4% interstory drift angle without much strength loss. Test data shows that the use of a strong end plate with a modified bolt arrangement performed well in distributing bolt forces uniformly amongst the bolt group

while the HBS was successful in shifting the majority of inelastic action away from the beam flange to end plate welds. The observations are consistent with pre-test FEA predictions [14]. The web stiffener, did not perform as predicted by pre-test FEA, however this discrepancy was shown by post-test FEA to be attributable to the presence of welding induced distortions of the web stiffener plates. Though the excellent seismic performance of HBS 4 shows the promise of the modified BEEP connection, future effort is needed to optimize this connection for both performance and economy. In addition, prescriptive design procedures for seamless inclusion of this connection in current seismic design practice and for prequalification in the ANSI/AISC 358 standard are required.

9. References

- [1] Murray TM, Sumner EA. AISC design guide series 4, extended end-plate moment connections. Chicago, 2003.
- [2] ANSI/AISC 358-10. Prequalified connections for special and intermediate steel moment frames for seismic applications. American Institute of Steel Construction 358, 2010.
- [3] Sumner EA. Unified design of extended end plate moment connections subject to cyclic loading. Ph.D. Dissertation, Virginia Polytechnic Institute and State University, Blacksburg, VA, 2000.
- [4] Mays TW. Application of the finite element method to the seismic design and analysis of large moment end-plate connections. Ph.D. Dissertation, Virginia Polytechnic Institute and State University, Blacksburg, VA, 2000.
- [5] Tsai K, Popov EP. Cyclic behavior of end-plate moment connections. *Journal of Structural Engineering* 1990;116(11):2917-2930.
- [6] Sumner EA, Murray TM. Behavior of extended end-plate moment connections subject to cyclic loading. *Journal of Structural Engineering* 2002;128(4):501-508.

- [7] SAC/BD-00/21. Cyclic testing of bolted moment end-plate connections. by Sumner, E.A., Mays, T., Murray, T.M.
- [8] Korol RM, Ghobarah A, Osman A. Extended end-plate connections under cyclic loading: behavior and design. *Journal of Constructional Steel Research* 1990;16(4):253-279.
- [9] Ghobarah A, Osman A, Korol RM. Behavior of extended end-plate connections under cyclic loading. *Engineering Structures* 1990;12(1):15-27.
- [10] Adey BT, Grondin GY, Cheng JJR. Cyclic loading of end plate moment connections. *Canadian Journal of Civil Engineering* 2000;27:683-701.
- [11] Shi G, Shi Y, Wang Y. Behavior of end-plate moment connections under earthquake loading. *Engineering structures* 2007;29(5):703-716.
- [12] Guo B, Gu Q, Liu F. Experimental behavior of stiffened and unstiffened end-plate connections under cyclic loading. *Journal of Structural Engineering* 2006;132(9):1352-1357.
- [13] FEMA-350, 2000, *State of the Art Report on Welding and Inspection*, prepared by the SAC Joint Venture for the Federal Emergency Management Agency, Washington, DC
- [14] Quayyum S, Hassan T. An improved unstiffened 8 bolt extended end-plate moment connection for special and intermediate moment frames, part I: numerical modelling and development. To be submitted to *Journal of Constructional Steel Research* 2014.
- [15] Morrison ML, Schweizer DQ, Hassan T. An innovative seismic performance enhancement technique for steel building moment resisting connections. Submitted to *Journal of Constructional Steel Research* 2014.

- [16] AISC. Manual of steel construction load and resistance factor design. 13th ed. Chicago, IL, 2006.
- [17] ANSI/AISC 341-10. Seismic provisions for structural steel buildings. American Institute of Steel Construction 341, 2010.
- [18] Popov EP, Amin N R, Louie JC, Stephen RM. Cyclic behavior of large beam-column assemblies. *Engineering Journal* 1986;23(1):9-23.
- [19] Bruneau M, Uang CM, Whittaker A. Ductile design of steel structures. New York: McGraw Hill Companies, 1998.

CHAPTER 4: INFLUENCE OF WELD SEQUENCE ON THE SEISMIC RESPONSE OF MOMENT RESISTING CONNECTIONS

Abstract

During the 1994 Northridge earthquake, moment resisting connections suffered from low-cycle fatigue failure near the beam-to-column welded joints and around weld access hole region. Two decades of research after the 1994 Northridge earthquake brought new and improved design of moment connections. However, still low-cycle fatigue failures have been observed in the post Northridge moment connections near the welded region and research studies indicate that welding induced residual stresses is one of the contributing factors to low-cycle fatigue damage in the connections. This study investigates the influence of welding sequence on the localized fatigue failure mechanisms of moment resisting connections. Two exterior sub-assemblages of welded unreinforced flange bolted web (WUF-B) connections were tested under displacement controlled constant amplitude cyclic loading, where the beam flanges were welded to the column flange with two different welding sequences. In both the connections tested, axial strain accumulation (known as ratcheting) was observed very close to the welded joints and around the weld access hole. Ratcheting is known to occur in metallic materials as they undergo inelastic cyclic loading, along the directions of force-controlled loading. Hence, it is anticipated that the occurrence of ratcheting at the welded joint under displacement-controlled loading could be influenced by residual stresses near the welded joints. Moreover, variability in the ratcheting rate was observed with two different weld sequences which led to different fatigue lives of the connections. The results of the experimental study demonstrated the effect of welding procedure as well as welding induced residual stresses on the low-cycle fatigue failure of the connections.

Keywords: Moment connections, weld sequence, residual stress, low-cycle fatigue, ratcheting.

1. Introduction

The design guidelines for moment resisting connections have been proposed in Steel Construction Manuals [1-3] considering the global performance of the structure with no emphasis on the basic correlation between localized member behavior and global structural performance. However, since the current engineering trend is moving towards performance-based design which emphasizes that the structural design of the structure should meet the inelastic seismic demands with a reliable global and local performance [4], it is essential that the cause and mechanism of local failure of welded steel moment frames (WSMFs) be understood along with the global failure mechanism to allow WSMFs effectively and reliably meet the seismic demands. Although the local condition at one location will not dictate the performance of a structure; the local condition of many structural members does dictate the performance of the entire structure [5]. While many design procedures can predict the performance of a global structural parameter under prescribed load conditions, those same procedures do not attempt to correlate these quantities with local structural performance. This is not a shortcoming of the current guidelines and design procedures; however it is a limitation on our knowledge of local failure conditions. Post-Northridge researchers have mainly addressed the global level mitigation of the failure risk; however the fundamental reasons for the brittle failures at the local level were not uncovered. More than ten years of research after the Northridge earthquake have developed modified designs of welded steel moment frames (WSMFs) [6-8]. While test results on the new connections demonstrated significant improvement with regard to ductility, many post-Northridge welded steel moment connections (WSMCs) exhibited failure initiated from low-cycle fatigue cracks near the beam flange weld toe [9-19]. The weld toe fatigue crack initiation motivated several investigations on weld material and the outcome was the recommendation of using high toughness weld material. However, the reason for the weld toe fatigue crack initiation in the post-Northridge design has yet to be investigated in a rational manner. The Structural Engineers Association of California (SEAOC) Seismology Committee emphasizes the importance of localized failures, as indicated in their commentary and recommendation on FEMA 350 [20]. The SEAOC committee identified research needs on weld interface field

conditions and low-cycle fatigue failure mechanisms towards developing fully rational design guidelines. Another important aspect of characterizing the local failure mechanism is that a steel structure that did not crack during an earthquake even may not always be safe for continued operation. It may however accumulate enough fatigue damage due to repeated yielding and may fail subsequently under service loading or another event.

Research programs at NC State University demonstrated that the welding sequence, thereby the welding residual stress, has significant influence on fatigue crack initiation at the weld toe of piping joints [21-23]. These studies demonstrated the effect of welding residual stress on strain ratcheting leading to crack initiation in the piping joint. Welding sequence thus can have a significant effect on the fatigue life of welded joints as demonstrated by these studies. Ratcheting is known to be demonstrated by metallic materials under inelastic cyclic loading along the directions of force-controlled loading—steady or fluctuating [24]. Hence, it was anticipated that the occurrence of ratcheting at the welded piping joints under displacement-controlled loading could be influenced by its residual stresses. The influence of residual stress on fatigue crack initiation at the weld toe in WSMCs was speculated [25], but the failure mechanism is yet to be investigated. Due to the complexity involved in residual stress calculation, most analyses either do not consider residual stresses or use simplified methods of analysis [26-27]. Dong and his coworkers [28-29] performed residual stress analysis in their investigation of WSMC failures. Their calculations demonstrated that the magnitude of residual stresses in some locations can be greater than the yield stress of the material. They studied crack propagation of preexisting cracks at the backing bars and demonstrated that the triaxial residual stress greatly reduced the plastic deformation and thus induced brittle fracture. Suita *et al.* [9] demonstrated a significant increase in the accumulated axial strain in the vicinity of beam-column welded connection during cyclic loading. The amount of strain accumulated decreased with distance from the weld interface. They reported both brittle mode fracture and progressive local plastic strain accumulation. More recent studies at NC State University by Royster [30] on bottom beam flange tee joint showed the influence of welding sequence on the fatigue failure of the connections. It was observed that different welding sequences induced different low-cycle fatigue responses of

the connections. Significant amount of ratcheting was observed in these experiments near the welded joints, which was thought to be the contributing factors in the premature fatigue failure of the connections. Moreover, variability of ratcheting response was observed for different welding sequences. Based on the observations from the study it was concluded that the ratcheting phenomena under displacement controlled loading could be attributed to the different residual stresses induced by the different welding sequences. From the literature it is apparent that low-cycle fatigue response of WSMCs can be influenced by the presence of residual stresses and the sequence at which the welding was performed. A detailed investigation on the WSMC residual stress and welding sequence is essential to explore its low-cycle fatigue failure response. If the influence of residual stress on fatigue damage accumulation in WSMC is revealed, fatigue life can be enhanced through optimizing the weld sequence. The SAC Joint Venture did not investigate any aspect of the welding procedure (number and size of weld beads and their sequence and the weld speed) and its influence on strain accumulation near the weld toe and base metals due to high temperature cycles during welding. Thus, a study is needed to capture the influence of welding procedure on failures of welded steel moment connections. The objective of this research is to investigate the influence of weld sequence on localized low-cycle fatigue failure mechanisms observed in welded steel moment connections. Two exterior beam-column sub-assemblages of welded unreinforced flange bolted web (WUF-B) moment connections were tested under displacement controlled constant amplitude cyclic loading. The beam-to-column flange groove welds were filled with different weld sequences in an attempt to investigate the effect of weld sequence on the low-cycle fatigue response of the connections.

2. Cyclic Testing of WSMCs

The cyclic testing of welded steel moment connections (WSMCs) consisted of two full scale exterior welded unreinforced flange bolted web (WUF-B) moment connections (referred to as specimens MC1 and MC2) where a single W18×55 ASTM A992 beam was attached to a W14×74 ASTM A992 column. The beam-to-column connection was designed and detailed in accordance with the AISC Seismic Design Provisions [1, 3, 6], and AWS

D1.1 [32]. The flanges of the beam were welded to that of the column flange along the strong axis of the column using a complete joint penetration (CJP) groove weld in accordance with the post-Northridge design recommendations [6]. The web of the beam was connected to column flange with four ASTM A325 high strength bolts connected through a 7.9375 mm (5/16 in) shear tab ASTM A36 steel which was shop welded on the column. Also, the column was reinforced with 15.875 mm (5/8 in) continuity plates that coincide with the top and bottom beam flanges and a 12.7 mm (1/2 in) doubler plate in the column panel zone between the continuity plates. The connection configuration is as shown in Figure 1.

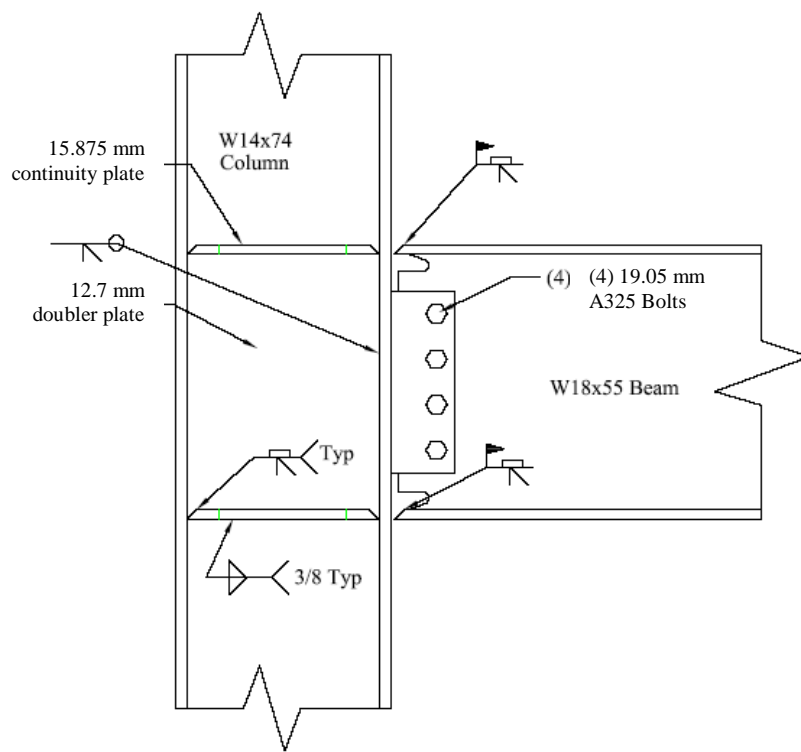


Figure 1 Sketch of the full-scale exterior WUF-B connection tested in this study.

2.1. Welding Procedure & Welding Details

The top and bottom flange of the beam were beveled as per AWS D1.1 [32] and the weld access hole geometry is designed as per the recommendations in AISC Specification Section J1.6 [1]. The welds were made using the Shielded Metal Arc Welding (SMAW) process and

E70T welding electrodes. While welding the bottom beam flange to the column flange the web of the beam hinders the completion of a single pass across the width of the beam. Whereas the top beam flange does not have any obstacle like the bottom beam flange. Therefore, weld is not uniform in the bottom beam flange when compared to the top flange. Further, the start and stop points in the bottom flange weld may cause discontinuities or higher residual stresses in the joint that lead to low cycle fatigue failure. To gain an understanding of the effect of the weld procedure on connection performance, welding was closely monitored. Weld sequence, start and stop locations, bead size and length of the weld, weld speed, weld direction, temperature cycles, voltage, and current were recorded. The diameter of the electrode used in welding was 3.175 mm (1/8 inch). The voltage and current measured at the arc were 28 volts and 160 amperes respectively. The polarity of welding machine was set such that the electrode was negatively charged. The average velocity with which the weld was laid was 2 mm/s.

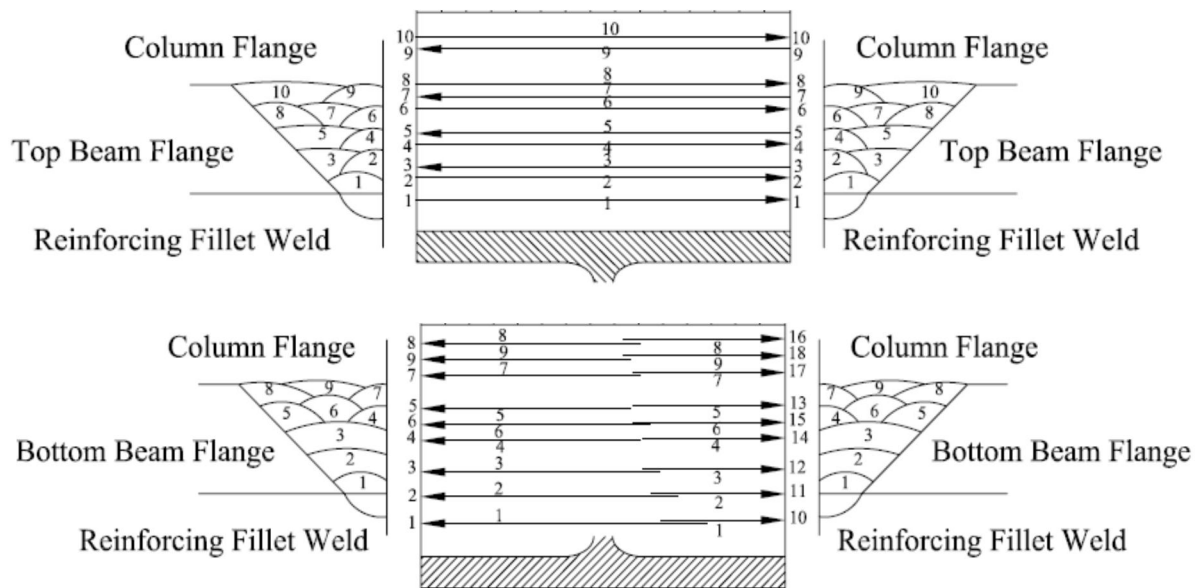


Figure 2 Sketch of weld sequences at the beam top and bottom flange for specimen MC1 showing number of welding passes in order of completion.

There are numerous ways of filling the CJP groove welds of the bottom beam flange to column flange when using a weld access hole. In the current research two such weld sequence options were studied in order to investigate the effect of welding sequence on the residual stress distribution as well as on the low-cycle fatigue response of WSMCs. These two welding sequences were denoted as weld sequence A (for specimen MC1) and B (for specimen MC2). The details of the bead size of the weld and the sequence in which the passes and beads were placed on the beam bottom flange and beam top flange for specimens MC1 and MC2 are presented in Table 1 and Table 2, and Figure 2 and Figure 3. As can be observed, the top flange welds were deposited in a similar fashion (from one end of the flange to the other end) for both the specimens, only the number of beads and the size of the beads were different. On the other hand, the bottom beam flange welds were laid in a completely different manner for the two specimens.

Table 1 Details of weld sequence for specimen MC1

Bead#	Beam Bottom Flange									
	Direction of weld: Right to Left					Direction of weld: Left to Right				
	Pass #	Length (mm)	Depth (mm)	Width (mm)	Time (s)	Pass#	Length (mm)	Depth (mm)	Width (mm)	Time (s)
1	1	150	5	8	90	10	65	5	8	30
2	2	135	5	12	70	11	70	5	12	40
3	3	125	5	15	60	12	75	5	15	40
4	4	115	5	11	60	14	75	5	10	40
5	5	110	5	14	60	13	80	5	6	40
6	6	120	5	10	60	15	80	5	10	40
7	7	115	5	15	60	17	80	5	12	40
8	8	115	5	10	60	16	85	5	10	40
9	9	110	4	8	60	18	85	5	12	40
Bead#	Beam Top Flange									
	Direction of Welding: Right to Left					Direction of Welding: Left to Right				
	Pass#	Length (mm)	Depth (mm)	Width (mm)	Time (s)	Pass#	Length (mm)	Depth (mm)	Width (mm)	Time (s)
1						1	195	5	10	130
2						2	195	5	6	130
3	3	193	5	10	130					
4						4	195	5	6	130
5	5	193	5	15	130					
6						6	195	5	6	130
7	7	190	5	8	130					
8						8	195	5	10	130
9	9	195	5	8	130	10	195	5	12	130

In specimen MC1 with weld Sequence A, the welder makes all the passes in different layers with the welding material, required to fill the groove starting from one side of the beam web (as shown in Figure 2). After the root pass is made, the passes in the next layer are stepped back slightly than the previous layer in order to avoid the start and stop points falling on top of each other. Also, care is taken to prevent placing of the start and stop points directly under the beam web. Once one side of the web is completed, the welder finishes the vacant groove on the opposite side of the beam web (as shown in Figure 2). As a result of this weld sequence, the average temperature on side of the beam, where the groove is filled first, is higher than the average temperature on opposite side of the beam, where welding is done later. This creates a non-uniform temperature gradient along the width of the beam flange. When the weld is allowed to cool, the nonuniform cooling distorts the specimen.

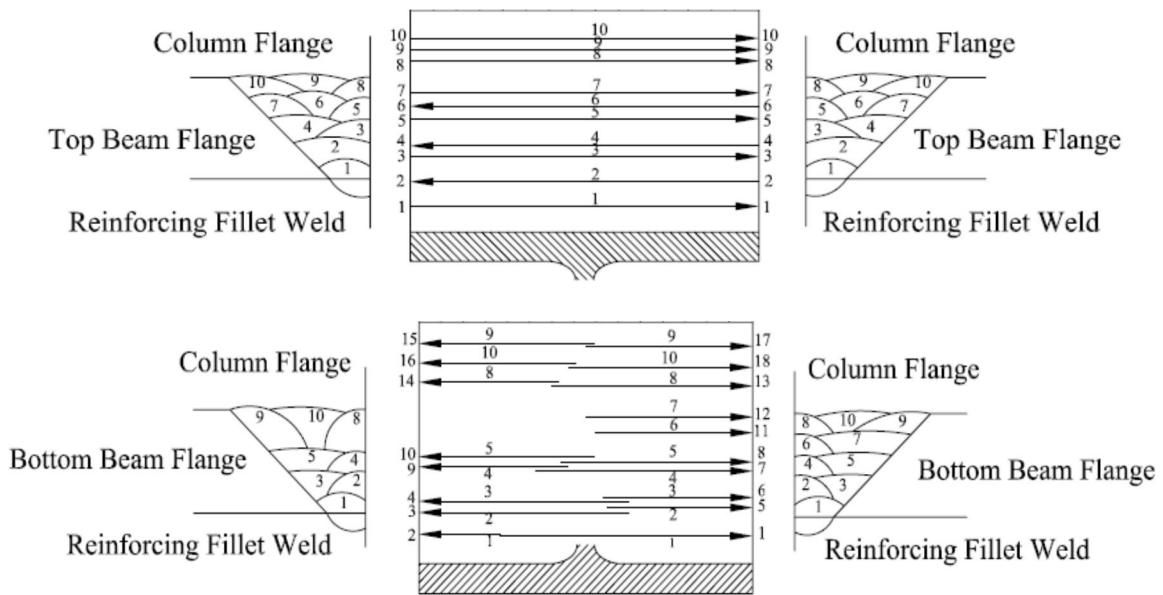


Figure 3 Sketch of weld sequences at the beam top and bottom flanges for specimen MC2 showing number of welding passes in order of completion.

On the contrary, for specimen MC2 with weld Sequence B, the welder alternates sides of the web after placing each weld bead. This sequence fills the groove evenly from the bottom to the top as opposed to filling one side of the groove at a time. In this sequence, the welder

lays the first bead from one side of the beam web, and then completes the bead by moving to the other side of the beam (Figure 3). All the beads in a particular layer of weld placed on one side and are completed from the other side of the beam in the same order in which they were laid first. Each layer is completed across the full width of the beam flange before beginning of the next layer.

Table 2 Details of weld sequence for specimen MC2

Bead #	Beam Bottom Flange									
	Direction of weld: Right to Left					Direction of weld: Left to Right				
	Pass #	Length (mm)	Depth (mm)	Width (mm)	Time (s)	Pass#	Length (mm)	Depth (mm)	Width (mm)	Time (s)
1	2	155	4	9	90	1	145	4		90
2	3	120	5	4	60	5	83	5	6	40
3	4	110	5	7	60	6	86	5	10	45
4	9	85	5	4	40	7	124	5	6	60
5	10	100	5	12	60	8	110	5	10	65
6						11	90	5	6	50
7						12	95	5	7	55
8	14	80	4	5	40	13	115	5	5	65
9	15	100	4	5	60	17	95	4	5	50
10	16	90	5	5	50	18	105	5	7	60
Bead #	Beam Top Flange									
	Direction of Welding: Right to Left					Direction of Welding: Left to Right				
	Pass#	Length (mm)	Depth (mm)	Width (mm)	Time (s)	Pass#	Length (mm)	Depth (mm)	Width (mm)	Time (s)
1	2	195	8	7	125	1	195	6	7	13
2										
3	4	190	8	8	125	3	195	6	6	13
4										
5	6	195	8	8	125	5	195	8	6	13
6										
7						7	195	8	8	13
8						8	195	5	5	13
9						9	195	5	5	13
10						10	195	5	8	13

The next layer is then started from the same side as that the last bead was finished from and pulled from the opposite side of the web to the outer edge of the flange. This bead is then completed by switching sides of the beam and completing the pass (Figure 3). For each layer the weld start and stop points are on the opposite side of the beam web when compared to the previous layer. These two weld procedures may cause different residual stress distributions in

the bottom beam flange and the column flange. One of these weld sequence options can adversely affect the fatigue life of the connection. Due to similar reasons, weld bead size can also cause differences in fatigue life of the welded steel moment connection. None of these factors are taken into consideration in the design of the connection, yet they can greatly influence the service life of the joint.

2.2. Test Setup

As already mentioned, the beam-to-column sub-assembly was modeled as an exterior beam-to column WUF-B connection. The dimensions and the support conditions of the specimens were chosen to represent the theoretical inflection points of the beam and the column in a typical frame building. The specimen supports were designed to mimic the support conditions of hinge support. Figure 4 shows a schematic view of the test setup. Test specimen was treated as a cantilever beam connected to a column flange. The specimen was held vertically during testing to represent their position in a building. Thus, the column was vertical and parallel to the strong wall. This position of the specimen is optimal because it enables unobstructed access to both sides of the connection, provides for lateral bracing, and keeps the expected failure zone convenient for necessary measurement. The far end of the beam was connected to the actuator which was suspended from a large loading frame. Lateral supports for the specimen were provided on either side of the beam using I-beams bolted firmly to the loading frame. Lateral supports were provided for the beam at a distance of 2 m 57.4 mm (6 ft. 9 in.) from the centerline of the column. No lateral supports were provided for the column. The loading is applied to the beam at a distance of 2 m 641.6 mm (8 ft. 8 in.) from the face of the column. Great care was taken to minimize slipping between the test setup elements and the laboratory floor and between the specimen and its supports.

The specimens were extensively instrumented in order to acquire the global and local responses under the prescribed loading. The instrumentation pattern for the test includes a combination of linear potentiometers (POTs), string POTs and LVDTs to monitor the global response of the specimen: beam end displacement, joint rotation, panel zone shear deformation and possible movement of the support. A variety of strain gages were used to

investigate the local response of the beam flanges, column panel zone and the continuity plates. The strain gages on the flanges of the beam were moved closer to the weld toe to get a better insight of the local strain response in the heat affected zone as this was the main area of interest and the research is focused on the local failure mechanism near the weld. To monitor the displacements along the length of the beam while testing, Optotrack was used. The loading unit comprised of an actuator and a controller. The actuator used has a push-pull hydraulic actuator manufactured by MTS Systems Corporation with 508 mm (20 inch) stroke maximum capacity of 489 kN (110 kips) both in tension and compression. The actuator was mounted vertically between the free end of the beam and the loading frame.

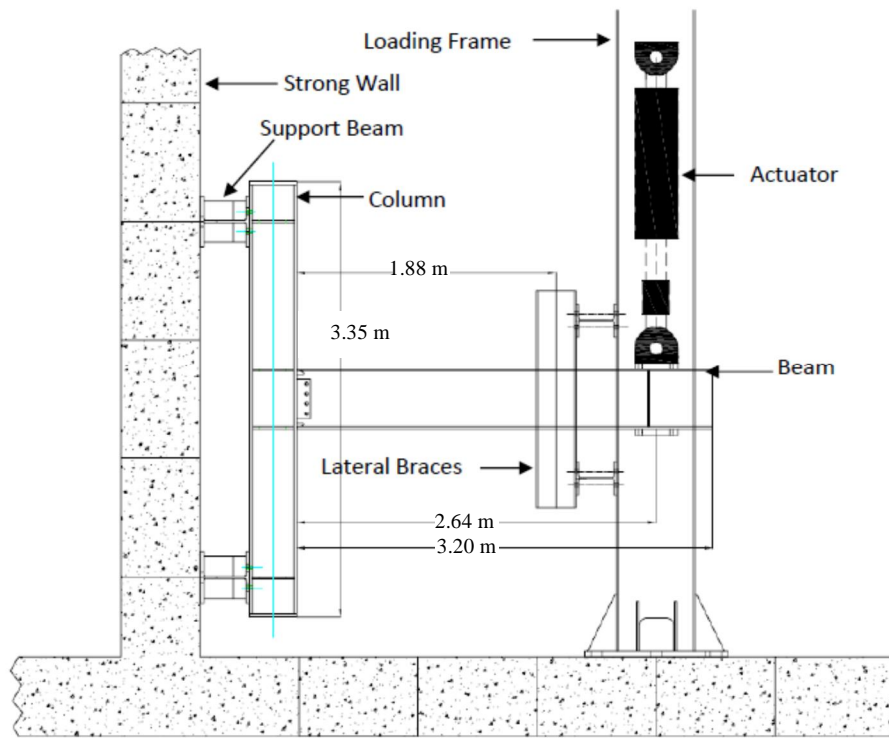


Figure 4 Schematic of the test setup used for cyclic testing of WUF-B Connections.

2.3. Loading History

In order to investigate the influence of welding sequence on the localized failure mechanisms of WUF-B connections, the specimens were subjected to low-cycle fatigue

loading. Traditionally, cyclic tests are carried out with reference to standard procedures such as [33-35] which use loading histories consisting of groups of cycles at increasing amplitudes as shown in Figure 5a. Such loading histories present the advantage of allowing on a single specimen a satisfactory appraisal of the cyclic performance of the component. However, they appear inadequate for the development of cumulative damage models useful not only for the seismic design of new structures but also for the assessment of safety and reliability of damaged structures and for the development of adequate repair procedures. Hence it has been proposed by various authors both in Europe and U.S. [34, 36-40] to perform tests with cycles at a constant amplitude. Such a procedure presents the advantage of allowing a clear understanding of the damage accumulation process as well as of the key parameters governing it [38].

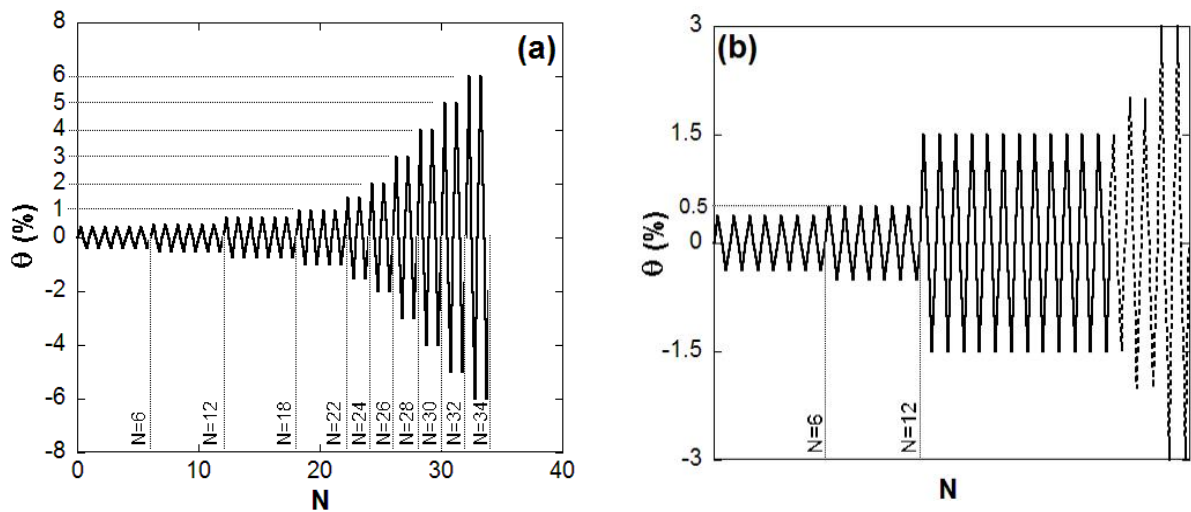


Figure 5 (a) SAC loading protocol [35], (b) non-standard loading history prescribed in the experiments.

In this study a non-standard loading history was prescribed which was primarily comprised of constant amplitude loading cycles in the inelastic range (Figure 5b). Initially 12 cycles were prescribed in the elastic range, six cycles each corresponding to a rotation of 0.375% and 0.5% in the elastic phase (denoted as phase 1 and 2) analogous to the elastic

phase of SAC loading protocol. Later in the next phase (phase 3), constant cycles equivalent to a rotation of 1.5% was chosen till the crack initiation. For further crack propagation and strength deterioration of the specimen, two cycles each of rotations corresponding to 2%, 3% so and so forth until failure, were applied. It is interesting to note here that the amplitude of constant loading cycles were kept slightly in the inelastic range, as higher amplitude of loading in the inelastic range may produce local buckling of the beam flange and web which hinders accumulation of damage due to low-cycle fatigue.

3. Cyclic Response of WUF-B Connections

The WUF-B specimens with two weld sequences showed ominously different low-cycle fatigue responses during experimental investigation although they had similar test setup and beam-column configurations. It is anticipated that the fatigue lives of the specimens were different because of the different weld sequences in the CJP groove welds between beam and column flanges. The results of the experimental investigation are presented in the following articles in terms of global and local responses.

3.1. Global Response

Specimen MC1

The response of the specimen MC1 is plotted in terms of moment-total rotation plot as shown in Figure 6a. The joint remained elastic during phase 1 and 2 of the loading which corresponded to rotation of 0.375% and 0.5% respectively. With the onset of phase 3 loading which corresponded to 1.5% rotation with constant amplitude loading cycles, yielding occurred in beam web and beam flange. In addition small yielding occurred in the column panel zone at the beginning. The response of the specimen was stable hysteretic closed loops with no indication of drop in load. The failure was a sudden and abrupt fracture of the top beam flange with a bang sound at 29th cycle during phase 3 loading. The failure could not be assessed from the global response of the specimen. No sign or indication of distress was seen in the specimen. Neither there was any crack initiation observed in the complete joint penetration weld nor in the reinforcing fillet weld. The rupture in the top flange propagated

suddenly almost across the top flange as shown in Figure 6b. Another interesting observation made during the test was that considerable amount of necking in the beam flanges were observed very close to the weld toe which is a sign of significant plastic damage accumulation. The panel zone and the column responded elastically and their contributions towards the total rotation or the plastic rotation of the joint were low. Most of the plastic rotation contribution to the joint was observed from beam. A review of the local response of the beam flanges is necessary to assess and understand the sudden failure observed in this test.

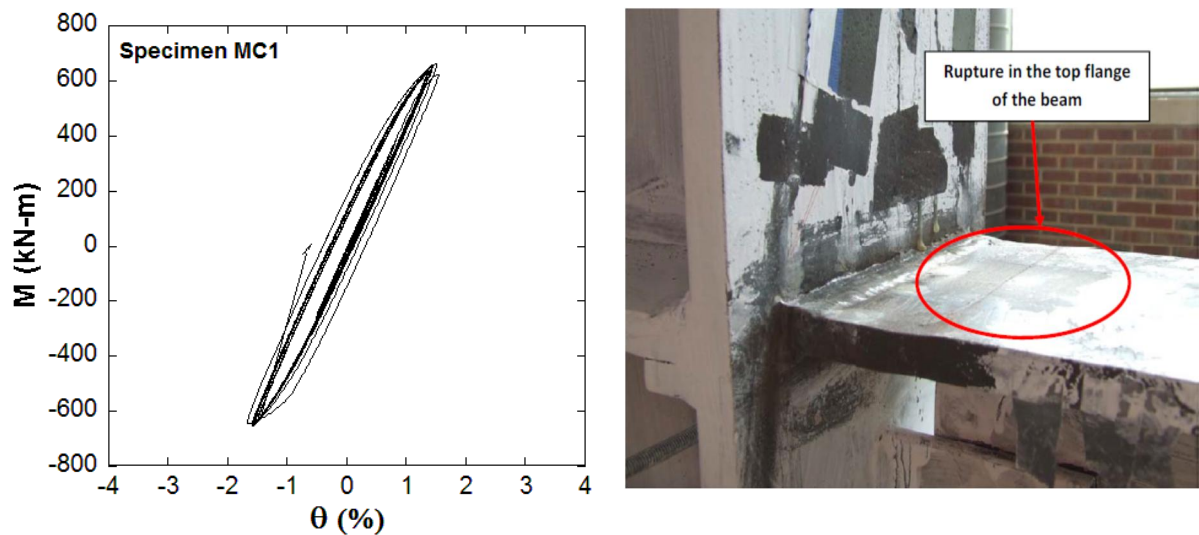


Figure 6 Response of specimen MC1. (a) moment-rotation hysteresis response, (b) rupture in the beam top flange.

Specimen MC2

For the specimen MC2, elastic response was observed during the first two phases of loading. When the phase 3 loading started stable hysteresis response was observed as shown in Figure 7a. With the first cycle of 1.5% rotation, beam flange yielded with very little yielding in column panel zone. No further yielding was observed in the column panel zone indicating that the panel zone remained elastic. Similarly, the column contribution towards the total rotation or the plastic rotation of the joint was very small and the column also

remained elastic. Hence most of the total rotation as well as the plastic rotation of the joint were seen from the beam rotation, indicating higher distress in the welded joint. Visible cracks were observed at the weld toe of reinforcing fillet weld in the bottom beam flange (Figure 7b) and near the complete joint penetration groove weld along with the base metal-weld metal interface of the top beam flange (Figure 8b) at 59th cycle during phase-3 of loading cycle, which corresponds to a total rotation of 1.5%. The cracks propagated during the phase-4 (2% rotation) of loading at both bottom and top beam flanges weld toe. The cracks were visible at the edges of the flanges and the outside of the beam flange near the weld.

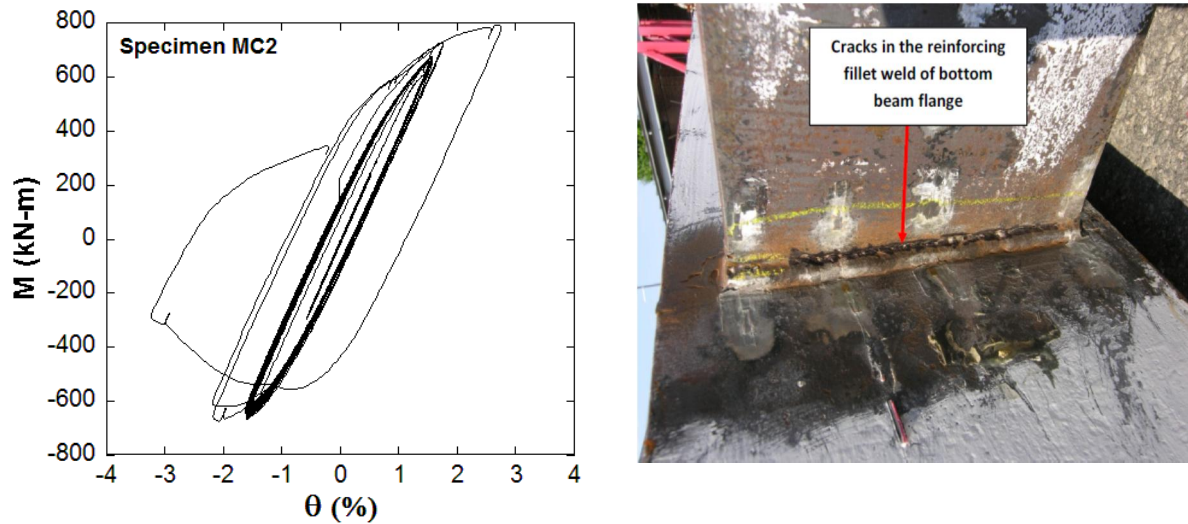


Figure 7 Response of specimen MC2. (a) moment-rotation hysteresis response, (b) cracks in the reinforcing fillet weld of bottom beam flange.

The specimen failed in a ductile manner due to gradual tear in the beam top flange, midway of the weld access hole during phase-5 (rotation 3%) of the loading (Figure 8b). The rupture in the top flange was initiated at the flattened part of the weld access hole in the top flange as shown in Figure 8a. The specimen sustained a total rotation of 3% at a ductility level equal to 4 prior to the top flange failure. The ductile type failure can also be assessed from the drop in the load seen during testing (Figure 7a). Neither local buckling of the beam

flanges nor the plastic hinge formation took place in the specimen during testing. As the beam was securely braced, lateral torsional buckling was insignificant during testing of the specimen. Prior to failure, the beam flanges yielded during first few cycles of phase 3 of the loading up to a distance of half the beam depth from the column face.



Figure 8 Response of specimen MC2. (a) rupture of the top flange initiated at the flattened portion of the weld access hole, (b) cracks in the weld-base metal interface of top beam flange.

From the experimental responses, it is apparent that both the specimens showed localized low-cycle fatigue failure occurring close to the weld toe of the beam top flange. Similar type of failure was also observed during the failure analysis of the post-Northridge connection tests conducted at the University of Michigan and Lehigh University. These studies demonstrated that fatigue cracks were initiated either near the bottom weld access hole or the beam flange weld toe (SAC/BD-99/23, SAC/BD-00/24). In the University of Michigan tests 89% of the connections showed crack initiation near the weld access hole and 50% showed crack initiation at the weld toe. In the Lehigh tests, 80% of the fatigue cracks were initiated at the weld toe. Based on the responses of the tests conducted and from the literature it is evident that the connection regions around the beam flange weld toe and the weld access hole are prone to fatigue crack initiation during low-cycle fatigue loading, and hence, it is

essential to investigate the cause and mechanism of such mode of failure. Although both the specimens tested showed low-cycle fatigue failure close to the weld toe, the fatigue lives of the specimens were different, where specimen with weld sequence A withstood only 29 loading cycles prior to failure, whereas, specimen with weld sequence B survived 61 loading cycles. However, it is interesting to note that the specimens resembled each other in every aspect, except the welding procedure, during the design and test setup for the connections. From the global response of the connections tested, it is apparent that the global behavior was not influenced by the welding procedure, hence the difference in the fatigue lives as well as the mode of failure for two different welding sequences might be attributed to the different localized failure mechanisms induced by different welding procedures. Hence, it is essential that the local response of the connections be investigated to understand the localized failure mechanisms involved.

3.2. Local Response

In order to investigate the local response of the connections, strain gage measurements were taken at different locations of the connections. The strain gage measurements were presented as mean strain and strain amplitude to elaborate the local response of the connections. Mean strain gives an indication of plastic damage accumulation with the progression of loading cycles, whereas strain amplitude gives an indication of the magnitude of imposed loading. Although several strain gages were used in the experiments, results of only few of the strain gages are presented in this paper. The axial mean strain and strain amplitude responses for beam top flange, beam bottom flange and column flange for both weld sequences are presented in Figure 9 through Figure 12, where the locations of the strain gages are clearly indicated in the insets. In each of the plots, the dark strain gage indicates the corresponding strain measurement location. For both the specimens, larger strain has developed in the beam flanges and column flange close to the weld toe compared to the other locations of the connection. Large amount of axial strain was also observed around the weld access hole region. Despite the symmetrical total response due to the symmetrical imposed

displacement a lack of symmetry was observed in strain gage responses close to the weld toe and weld access hole.

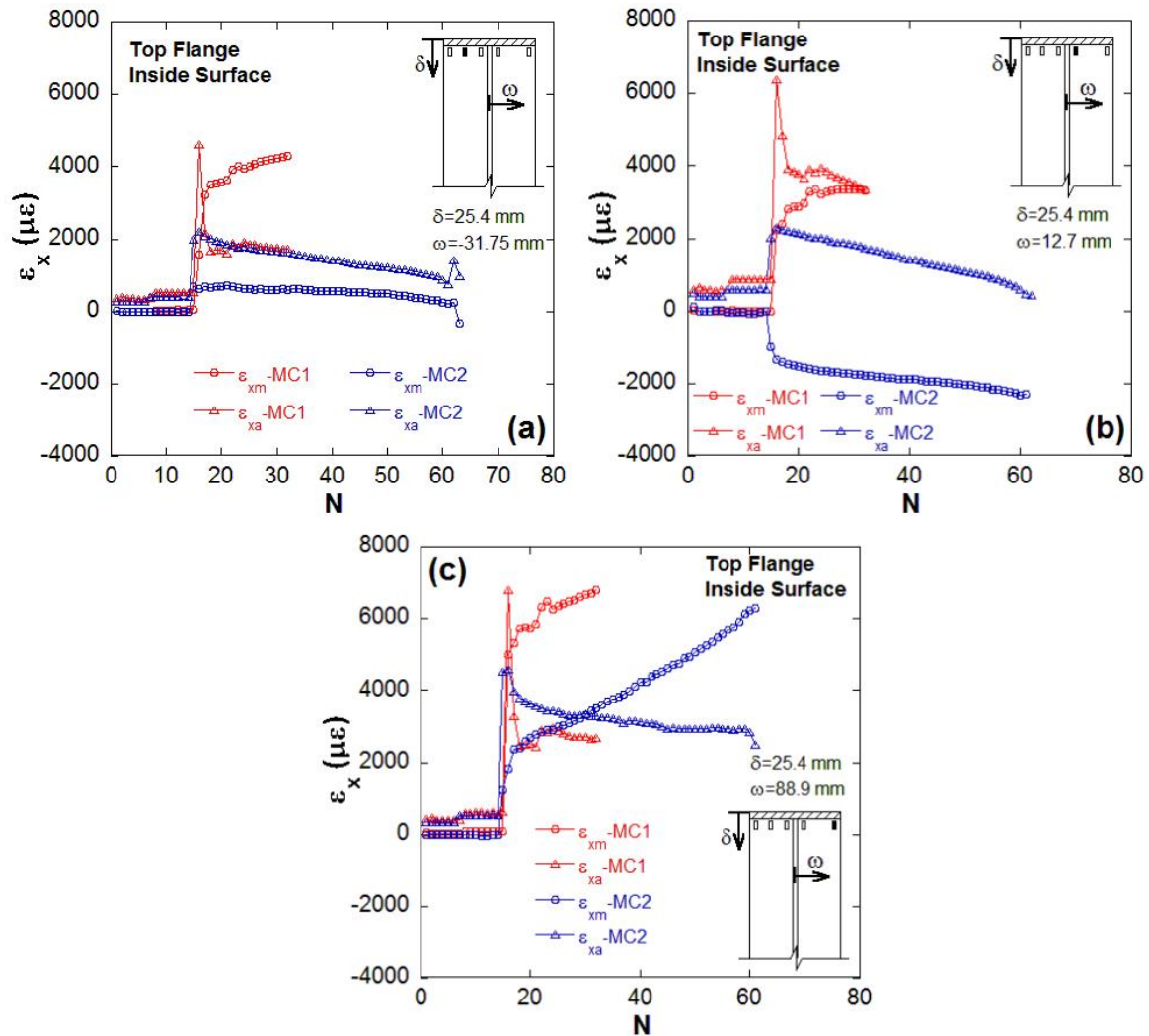


Figure 9 Mean axial strain and amplitude plotted against number of loading cycles recorded at the top flange (inside surface) of the connections.

It was observed that for both the specimens, the axial mean strain and amplitude were increasing slowly with number of loading cycles at every strain gage location during loading phases 1 and 2 i.e. during elastic loading cycles. As the loading amplitude was increased

from elastic to inelastic cycles during loading phase 3, there was a sharp jump in the axial mean strain and amplitude, and after that jump, the axial mean strain continued to increase gradually with number of loading cycles, whereas the axial strain amplitude either decreased or remained constant. As a result, axial mean strain accumulated close to the weld toe and around the weld access hole both at the top (Figure 9) and the bottom beam flanges (Figure 10 and Figure 11).

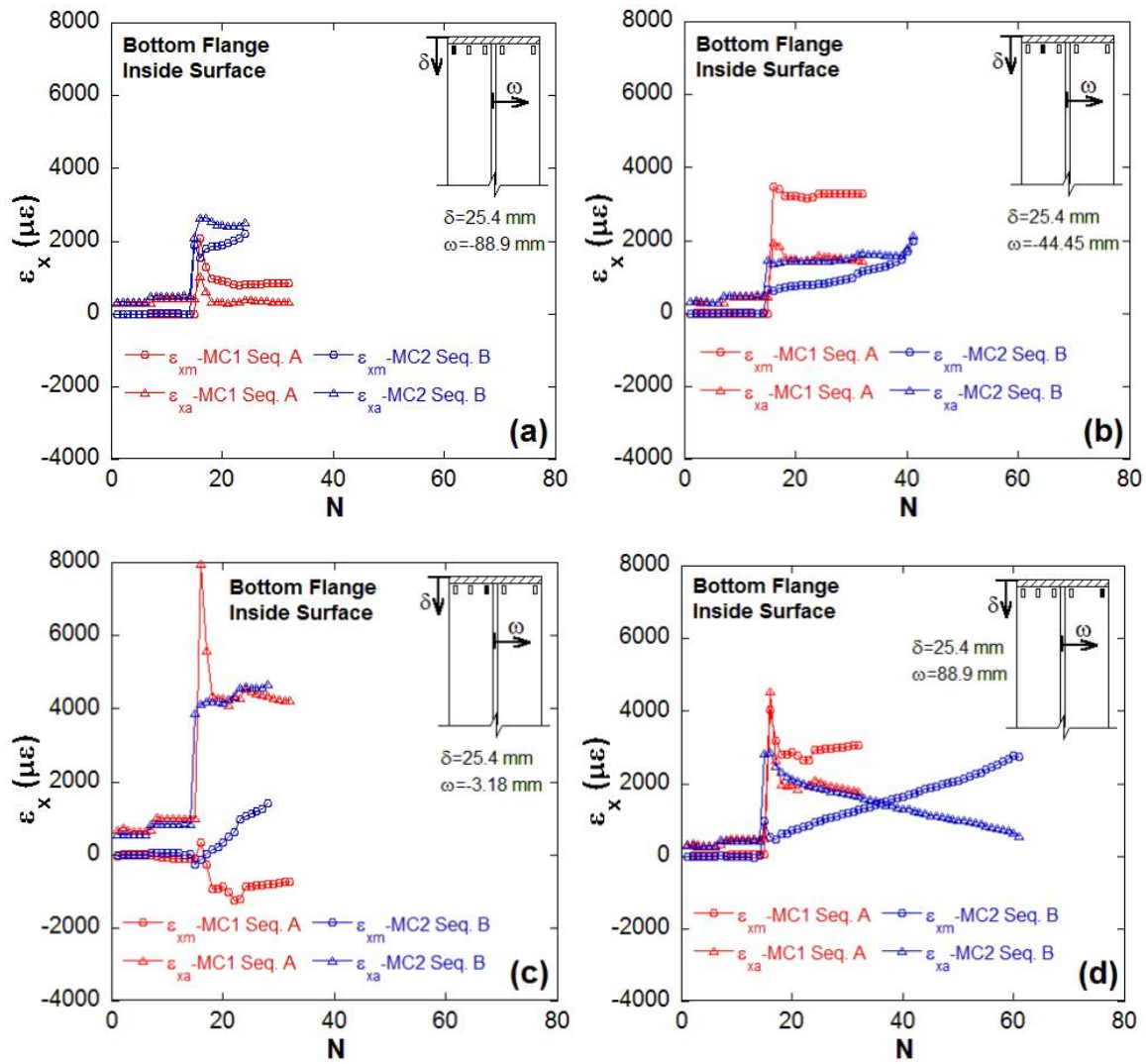


Figure 10 Mean axial strain and amplitude plotted against number of loading cycles recorded at the beam bottom flange (inside surface) of the connections.

Considerable amount of axial mean strain accumulation was also observed in the column flange close to the weld toe (Figure 12). Since the cracks were initiated near the weld toe region, it is anticipated that the axial strain accumulation with number of loading cycles might have led to fatigue crack initiation near weld toe of the beam flanges of the connections. Because of the axial strain accumulation near the weld toe region, necking of the beam flanges near the weld toe was observed for the both the specimens tested which is a sign of large plastic damage accumulation (Figure 7b, Figure 8b). This phenomenon of axial strain accumulation with number of loading cycles is well known as ratcheting or sometimes referred to as cyclic creep. Ratcheting is known to occur in metallic materials as they undergo inelastic cyclic loading, along the directions of force-controlled loading [24, 41-42]. It is quite interesting to find that the ratcheting in the tests reported herein has occurred under displacement-controlled loading which is kinematically inadmissible. Ratcheting phenomenon under displacement controlled loading is only possible if there are prior mean stresses that work as a driving force for ratcheting. Similar type of ratcheting response near the weld toe of the SS304 piping joints has been demonstrated by Lu [21] and Cheng [23] and it was concluded that residual stresses at the toe of the weld might be a key factor for the occurrence of ratcheting under displacement controlled loading. Castiglioni [38] also demonstrated presence of ratcheting near welded joint in the steel beam-column connection under constant amplitude loading cycles and a decreasing trend in the amount of ratcheting was observed as the distance from the weld toe was increased. Similar response was also observed in the tests of this study, where the amount ratcheting was decreasing as the distance from the weld toe increased. From the observations of the study it is evident that the stresses that is working as driving force for ratcheting is not prevailing away from the weld toe. Hence it is anticipated that the axial residual stress at the weld toe acts as a mean stress to the stress cycle in the axial direction and causes ratcheting in this direction. When the strain responses at different strain gage locations were compared between the two specimens with different weld sequences, the lower fatigue life of the specimen MC1 is justified. The specimen MC1 showed higher mean axial strain compared to the specimen MC2 close to the weld toe of the top flange of the beam as shown in Figure 9, indicating higher axial strain

accumulation at the weld region of specimen MC1 compared to MC2 (Figure 9). This demonstrates that specimen MC1 might have induced more residual stresses than specimen MC2 at the beam top flange.

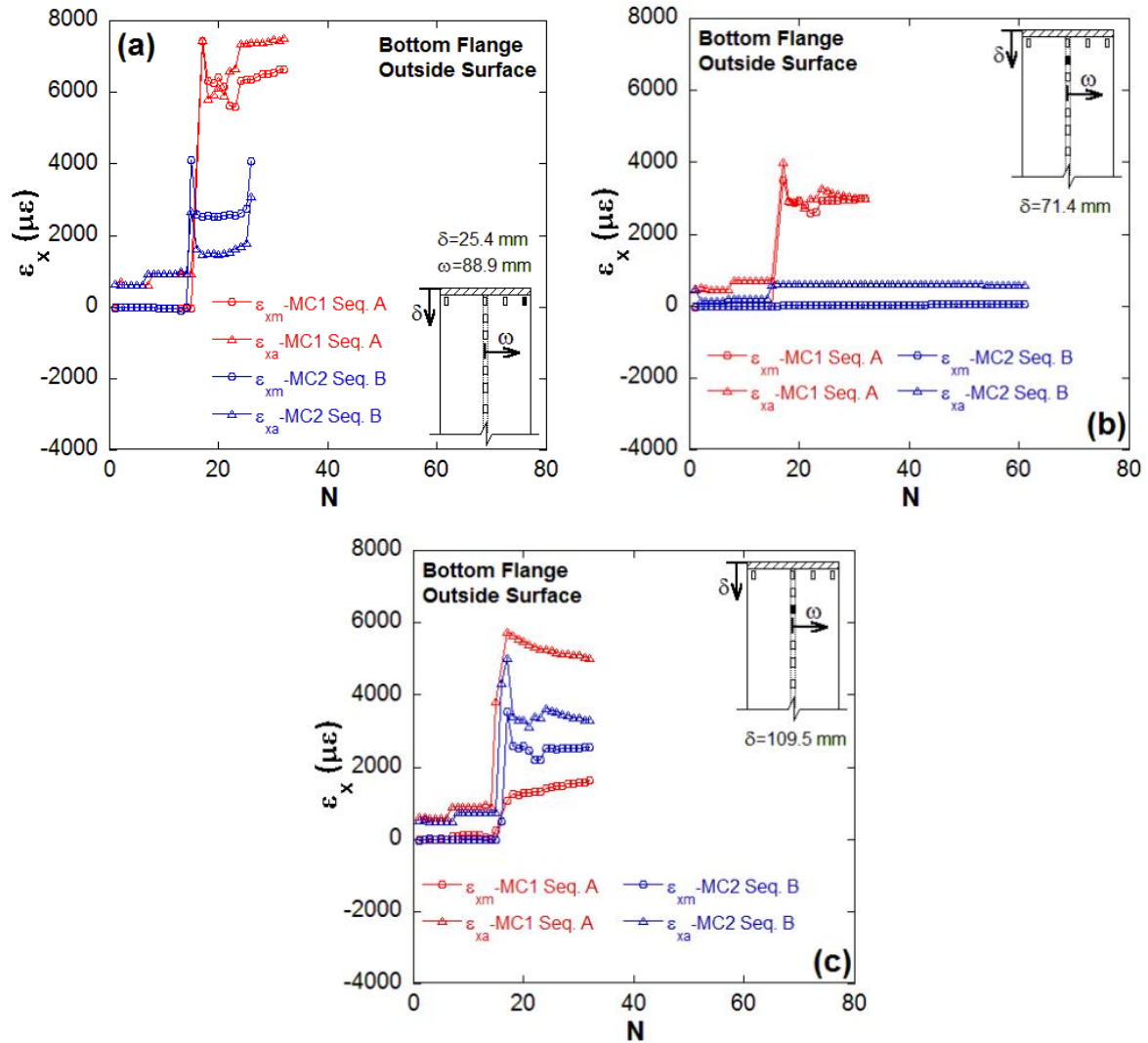


Figure 11 Mean axial strain and amplitude plotted against number of loading cycles recorded at the beam bottom flange (outside surface) of the connections.

Similarly, the strain responses at most of the locations close to the weld toe of the beam bottom flange showed higher mean axial strain for specimen MC1 with weld sequence A

compared to specimen MC2 with weld sequence B (Figure 10 b, c, d and Figure 11 a, b), whereas there were few locations where mean axial strain response of specimen MC1 was lower than that of specimen MC2. Hence, it is evident that the mean axial strain or axial strain accumulation is significantly influenced by the welding procedure. On the other hand, the influence of welding procedure on the axial strain amplitude response was inconclusive. There was no specific trend observed in the axial strain amplitudes for both the specimens based on the weld sequence. There were several locations at beam top and bottom flanges where specimen MC1 showed higher axial strain amplitude compared to that of specimen MC2 (Figure 10b, Figure 11), whereas there were several other locations where specimen MC2 exhibited larger axial strain amplitude compared to that of specimen MC2 (Figure 9c, Figure 10a). The local strain responses in the column flange near the weld toe showed that the mean axial strain and amplitudes were comparable for the two specimens near the beam top flange, whereas specimen MC1 showed higher mean and lower amplitude near beam bottom flange (Figure 12).

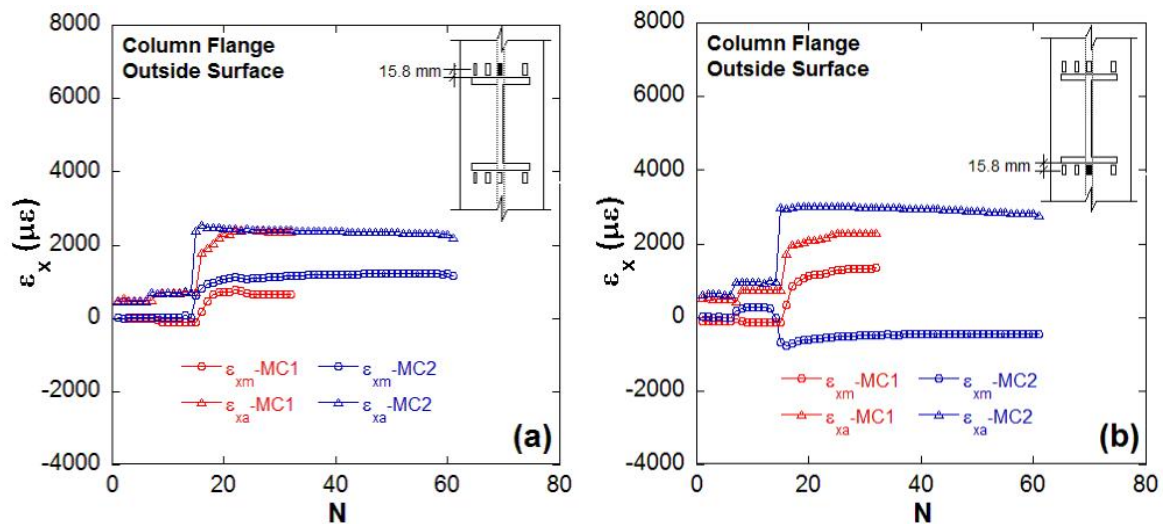


Figure 12 Mean axial strain and amplitude plotted against number of loading cycles recorded at the column flange of the connections.

Therefore, based on the local strain responses obtained from this study it is apparent that mean axial strain plays more important role on the localized fatigue failure mechanism of the connection compared to axial strain amplitude. For specimen MC1, axial strain accumulation was higher in the welded region of the connection compared to specimen MC2, and hence, specimen MC1 exhibited lower fatigue life than that of specimen MC2. From the experimental observations, it is believed that the mechanism that could have influenced the axial strain accumulation/ratcheting as well as the fatigue lives of the specimens is the residual stresses induced from the welding procedure. Therefore, it is anticipated that the welding procedure might have significant influence on the magnitude and distribution of residual stresses in the beam-column connections, which eventually influences the low-cycle fatigue response of the connections.

4. Conclusions

Two full-scale WUF-B connections were tested under displacement controlled constant amplitude cyclic loading to investigate the effect of weld sequence on the low-cycle fatigue failure mechanism of the connections. The results of the study led to the following conclusions:

- Welding procedure does not influence the global response of the connections and hence, it is essential that the local response of the connections be investigated along with the global response to understand the failure mechanism of the connections.
- Axial strain accumulation/ratcheting was observed close to the weld toe for both the specimens under investigation. Axial strain ratcheting under displacement controlled loading is kinematically inadmissible, and hence it is anticipated that welding induced residual stresses might be working as mean stress to the stress cycle in the axial direction and causing ratcheting in this direction.
- Different welding sequences might have induced different amount and distribution of residual stresses in the connection regions. Hence the ratcheting phenomena were different based on the welding procedures which eventually led to variability in the fatigue lives of the connections.

- The weld sequence where the welder switches sides of the beam web before welding each bead showed better performance compared to the one where the welder finishes all welding beads on one side of the beam web before switching to the other side.
- Welding induced residual stresses and the procedure of welding has significant effect on the low-cycle fatigue response of the welded steel moment connections. It is believed that based on the analysis of a large number of welding sequences, an optimized weld sequence can be achieved which will reduce the residual stresses significantly and thereby, increase the fatigue life of the connection.

5. References

- [1] AISC. Manual of steel construction load and resistance factor design. 13th ed. Chicago, IL, 2006.
- [2] AISC. Prequalified connections for special and intermediate steel moment frames for seismic applications. American Institute of Steel Construction 358, AISC 358-10, 2010a
- [3] AISC. Seismic provisions for structural steel buildings. American Institute of Steel Construction 341, AISC 341-10, 2010b.
- [4] SEAOC. Recommended lateral force requirements and commentary 7th edition. Structural Engineers Association of California Seismology Committee, 1999.
- [5] Rodgers JE, Stephen AM. Effects of connection fractures on global behavior of steel moment frames subjected to earthquakes. Journal of Structural Engineering 2006;132(1):78-88.
- [6] FEMA-350. Recommendation and seismic design criteria for new steel moment-frame buildings. prepared by the SAC Joint Venture for the Federal Emergency Management Agency, Washington, DC, 2000.

- [7] FEMA-353. Recommended specifications and quality assurance guidelines for steel moment- frame construction for seismic applications. prepared by the SAC Joint Venture for the Federal Emergency Management Agency, Washington, DC, 2000.
- [8] FEMA-355D. State of the art report on connection performance. prepared by the SAC Joint Venture for the Federal Emergency Management Agency, Washington, DC, 2000.
- [9] Suita K, Nakashima M, Morisako K. Tests of welded beam-column subassemblies II: Detailed behavior. *Journal of Structural Engineering* 1998;124(11):1245-1252.
- [10] Nakashima M, Suita K, Marisako K, Maruoka Y. Tests of welded beam-column subassemblies. I. Global behavior. *Journal of Structural Engineering* 1998;124:1236-1244.
- [11] SAC/BD-99/23. Failure analysis of welded beam to column connections. by Barsom, JM, Pellegrino JV.
- [12] Mazzolani FM. (Editor). *Moment resistant connections of steel frames in seismic areas: design and reliability.* E&FN Spon, 2000.
- [13] Stojadinovic B, Goel SC, Lee KH, Margarian AG, Choi JH. Parametric tests on unreinforced steel moment connections. *Journal of Structural Engineering* 2000;126:40-49.
- [14] SAC/BD-00/24. Development and evaluation of improved details for ductile welded unreinforced flange connections. by Ricles JM, Mao C, Lu LW, Fisher JW.
- [15] SAC/BD-00/22. Cyclic response of RBS moment connections: loading sequence and lateral bracing effects.” by Yu S, Gilton C, Uang CM.

- [16] Uang CM, Yu QS, Noel S, Gross J. Cyclic testing of steel moment connections rehabilitated with rbs or welded haunch. *Journal of Structural Engineering* 2000;126:57-68.
- [17] Ricles JM, Fisher JW, Lu LW, Kaufmann EJ. Development of improved welded moment connections for earthquake-resistant design. *Journal of Constructional Steel Research* 2002;58:565-604.
- [18] Stojadinovic B. Stability and low-cycle fatigue limits of moment connection rotation capacity. *Engineering Structures* 2003;25:691-700.
- [19] Lee D, Cotton SC, Hajjar JF, Dexter RJ. Cyclic behavior of steel moment-resisting connections reinforced by alternative column stiffener details, I. Connection performance and continuity plate detailing. *Engineering Journal* 2005;4th Quarter:189-213.
- [20] SEAOC. Commentary and recommendations on FEMA 350. Structural Engineers Association of California Seismology Committee, FEMA 350 Task Group, 2002.
- [21] Lu X. Influence of residual stress on fatigue failure of welded joints. Ph.D. Dissertation, North Carolina State University, Raleigh, NC, 2002.
- [22] Humphreys AE. Influence of residual stress on the initiation of fatigue cracks at welded piping joints. MS Thesis, North Carolina State University, Raleigh, NC, 2004.
- [23] Cheng PY. Influence of residual stress and heat affected zone on fatigue failure of welded piping joints. Ph.D. Dissertation, North Carolina State University, Raleigh, NC, 2009.
- [24] Hassan T, Kyriakides S. Ratcheting of cyclically hardening and softening materials: I. Uniaxial behavior. *International Journal of Plasticity* 1994;10:149-184.
- [25] SAC/BD-99/24. Weld acceptance criteria for seismically-loaded welded connections. by Mohr W.

- [26] SAC/BD-97/05. Finite element fracture mechanics investigation of welded beam-to-column connections. by Chi WM, Deierlein GG, Ingraffea A.
- [27] Matos CG, Dodds Jr RH. Probabilistic modeling of weld fracture in steel frame connections part ii: seismic loading. *Engineering structures* 2002;24(6):687-705.
- [28] SAC/BD-99/04. Effects of strength/toughness mismatch on structural and fracture behaviors in weldments. by Dong P, Kilinski T, Zhang J, Brust FW.
- [29] Zhang J, Dong P. Residual stresses in welded moment frames and implications for structural performance. *Journal of Structural Engineering* 2000;126(3):306-315.
- [30] Royster PB. Localized low cycle fatigue failure of welded steel moment connections. MS Thesis, North Carolina State University, Raleigh, NC, 2007.
- [31] Syed S. Influence of weld sequence on the seismic failure of welded steel moment connections in building structures. MS Thesis, North Carolina State University, Raleigh, NC, 2009.
- [32] ANSI/AWS D1.1. Structural welding code-steel. The American Welding Society, 2008.
- [33] European Convention for Constructional Steelworks, ECCS. Recommended testing procedure for assessing the behavior of structural elements under cyclic loads. TWG 1.3—Seismic Design, ECCS Publication No. 45, Technical Committee 1, 1986.
- [34] ATC. Guidelines for cyclic seismic testing of components of steel structures. ATC-24, Redwood City, Calif., 1992.
- [35] SAC/BD-97/02. Protocol for fabrication, inspection, testing and documentation of beam-column connection tests and other experimental specimens. by Clark P, Frank K, Krawinkler H, Shaw R.

- [36] Krawinkler H, Zohrei M. Cumulative damage in steel structures subjected to earthquake ground motions. *Computers and Structures* 1983;16:531–541.
- [37] Ballio G, Castiglioni CA. Seismic behavior of steel sections. *Journal of Constructional Steel Research* 1994, 29:21-54.
- [38] Castiglioni CA. Effects of the loading history on the local buckling behavior and failure mode of welded beam-to-column joints in moment-resisting steel frames. *Journal of Engineering Mechanics* 2005;131:568-585.
- [39] Mander JB, Chen SS, Pekan G. Low-cycle variable amplitude fatigue modelling of top-and-seat angle connections. *Engineering Journal* 1994a;2:54–62.
- [40] Mander JB, Chen SS, Pekan G. Low-cycle fatigue behavior of semi-rigid top-and-seat angle connections. *Engineering Journal* 1994b;3:111–122.
- [41] Corona E, Hassan T, Kyriakides S. On the performance of kinematic hardening rules in predicting a class of biaxial ratcheting histories. *International Journal of Plasticity* 1996;12(1):117-145.
- [42] Hassan T, Kyriakides S. Ratcheting of cyclically hardening and softening materials: II. multiaxial behavior. *International Journal of Plasticity* 1994;10:185-212.

CHAPTER 5: SIMULATION OF INITIAL RESIDUAL STRESSES IN HOT-ROLLED WIDE FLANGE SHAPES

Abstract

After the wide flange members are hot-rolled to their final shape they are air cooled during which residual stresses are developed due to nonuniform cooling. No numerical methods are available in the literature to simulate the residual stresses developed in the W shapes. Because of the complexity involved in the residual stress calculation, most of the works in the literature either ignore the presence of residual stresses or assume simplified distribution of residual stresses. However, the residual stresses developed due to uneven cooling (denoted as initial residual stresses) can be as high as one-half of the yield stress and can affect significantly the load carrying capacity and deformation of structural members especially under fatigue loading. Hence, it is essential to accurately predict the magnitude and distribution of initial residual stresses to investigate its influence on the structural performance. This study developed a numerical scheme to simulate the real time residual stress distribution in hot-rolled W shapes. The numerical technique developed for simulating residual stress distribution for different size W shapes was validated against the initial residual stress data in the literature. Good conformity was observed between the simulated and experimental responses. The simple numerical scheme developed in this study provides experimentally validated technique for simulating the initial residual stresses in hot-rolled W shapes for structural analysis and design of moment resisting connections.

Keywords: Finite element, W shape, uneven cooling, hot-rolled, residual stress

1. Introduction

Internal residual stresses develop in hot-rolled W shape sections during manufacturing processes of hot-rolling and subsequent cooling. Such self-equilibrated residual stresses are developed because of nonuniform cooling and nonuniform geometry. When W shape section

with initial residual stresses is loaded, the total stresses due to the external forces are superimposed on initial residual stresses and consequently certain portions of the cross-section may be stressed beyond the yield point [1-4]. Furthermore, the fatigue life will be shortened due to the existence of residual stresses when the member is subjected to dynamic loads such as seismic or wind loads. The effect of initial residual stresses on the performance of steel structures has been addressed in quite a few literature. It has been shown that the ultimate strength of beams is not affected by the presence of residual stress, although deflections are increased near the ultimate [5-6]. For beam with intermediate slenderness ratio, the influence of residual stresses was found significant in the lateral-torsional buckling of the beams [6]. In columns, residual stresses lower the ultimate strength and for this reason their evaluation is of great importance [6, 8-10]. Beedle and Tall [10] observed 30% reductions of the compressive strength of structural steel columns made of W shapes or built-up steel members. The numerical study of Lamarche and Tremblay [11] showed that residual stresses reduce the compressive resistance of columns, especially at the first buckling. Residual stress effects tend to gradually diminish in the post-buckling range, which suggests that they may not be critical for prediction of the collapse of structures once the column capacity is exceeded. Similar observations were also made in the studies by Okazaki *et al.* [12], Lu and MacRae [13] and Mathur *et al.* [14] where the effects of initial residual stresses were evaluated under cyclic loading response of steel framed structures. These studies showed a decrease in the lateral strength of the structure when high axial compressive loads were considered. However, the effects of residual stresses on cyclic stability behavior were noticeable only after the peak lateral strength has been reached and afterwards, the effect of initial residual stresses seemed to diminish with the progression of large inelastic cycles. From the literature, it is apparent that initial residual stresses can be an important factor in buckling [15], fatigue [16], stress corrosion [17] and brittle fracture [18] of structural members. Therefore, the actual magnitude and distribution of residual stresses as well as the factors which influence the formation of residual stresses are of considerable significance.

An investigation of residual stresses can be experimental, analytical or numerical. However, the actual distribution of residual stresses in a single specimen can be verified only

by experimental measurements. The accurate measurements of residual stresses through experiments are very tedious and expensive, and it is practically impossible to carry out measurements on more than a few specimens out of all existing types of different shapes. Moreover, the residual stress distribution may vary from specimen to specimen, implying several measurements to be made on each shape to obtain a statistically significant result [19]. On the other hand, analytical attempts have been made in some studies to calculate the residual stresses which resulted in too simplified distribution of residual stresses and are not widely applicable [2-3, 20]. Considering these facts, numerical methods appear to be useful for the investigation of residual stresses and the variables which influence their formation provided that the initial material characteristics and boundary conditions are properly assumed. Several researchers showed that the finite element method could be used to simulate the real processes by comparing the results with some experimental data. Kamamoto *et al.* [20] have analyzed residual stresses and distortion of large steel shafts due to quenching. The results showed that residual stresses are strongly related to the transformational behavior. Toparli and Aksoy [21] analyzed residual stresses during water quenching of cylindrical solid steel bars of various diameters by using finite element technique. Jahanian [22] modeled heat treatment (quenching) and calculated the residual stress in a long solid cylinder by using theoretical and numerical methods with different cooling speeds. Fa-rong and Shang-li [23] used finite element program to analyze the transient temperature and residual stress fields for a metal specimen during quenching. Yamada [24] presented a method of solving uncoupled quasi-static thermoelastic problems in perforated plates. In their analysis, a transient thermal stress problem was solved for an infinite plate containing two elliptic holes with prescribed temperature. In all these models, many assumptions were made to simplify the actual process. That is obviously too complex to simulate all the parameters in details. However, reasonably good models [21, 24-25] were developed in these past investigations by considering the key factors that affect the formation of residual stresses. Many of these models produced results that had excellent agreement with the results obtained from the experiments. However, no numerical studies were found in the literature that dealt with the distribution of residual stresses developed during cooling of hot-

rolled steel sections. This necessitates the development of a numerical scheme to accurately predict the formation and distribution of residual stresses due to uneven cooling of hot-rolled steel sections which is the subject of this study. This study developed a scheme to numerically simulate the initial residual stresses (IRS) of structural W shapes during the cooling process after hot-rolling through advanced finite element modeling techniques. The method is based on a calculation of the temperature and the resulting thermal stress distribution throughout the cooling process, and simulating the actual cooling conditions, including variable material coefficients. A sequentially coupled nonlinear transient thermo-mechanical analysis was performed to calculate temperature history and residual stresses. First a transient thermal analysis was performed during which the time-dependent temperature distribution was determined during the cooling phase of the hot-rolled W shapes. The temperature field at each time step was then used as an input for evaluating the stress and strain field in the W shapes. The residual stresses obtained from the finite element simulation was validated against the experimental data available in the literature.

2. Manufacturing Process of Structural Shapes and Formation of Initial Residual Stress

The schematic diagram of Figure shows the production process of structural steel shapes, which consists of three main operations: melting, casting and rolling. To begin production, the scrap material is melted in highly efficient and environmentally friendly electric arc furnaces. The steel is then refined in a ladle furnace, and its temperature and chemistry is regulated before the casting process. In a continuous caster, the steel is solidified to a semi-finished product called a beam blank which is similar in shape to a steel beam. This is done through a hollow interior of an oscillating mold (shown in Figure 2a) that have inside dimensions corresponding to the width and thickness of the billets, beam blanks, and near-net shape profile that is being cast. After casting, the beam blanks are directly reheated to rolling temperature or stocked for later rolling. Depending upon the temperature of the entering beam blank it may be necessary to reheat it in a furnace to a temperature of 1200-1300°C. The beam blank is then rolled in a number of passes in two or more rolling stands. In each pass the cross section is reduced in a certain manner until the shape has reached its final cross

section in the finishing stand. After finish-rolling, the material is conveyed to a hot saw where it is cut into lengths which can be conveniently transported. The member is then allowed to cool down to ambient temperature on a cooling bed, that is, a metal structure which permits the air to circulate around the rolled members. The detailed arrangement of the shapes on the cooling bed varies with different mill practice and different shape of the material. Residual stresses will result after the cooling because of the non-uniform temperature distribution through the cross section during the cooling process. Figure 2b and Figure 2c show sketches of the cross-sectional view of the semi-finished product after continuous casting (beam blank) and finished product after all the manufacturing operations, respectively.

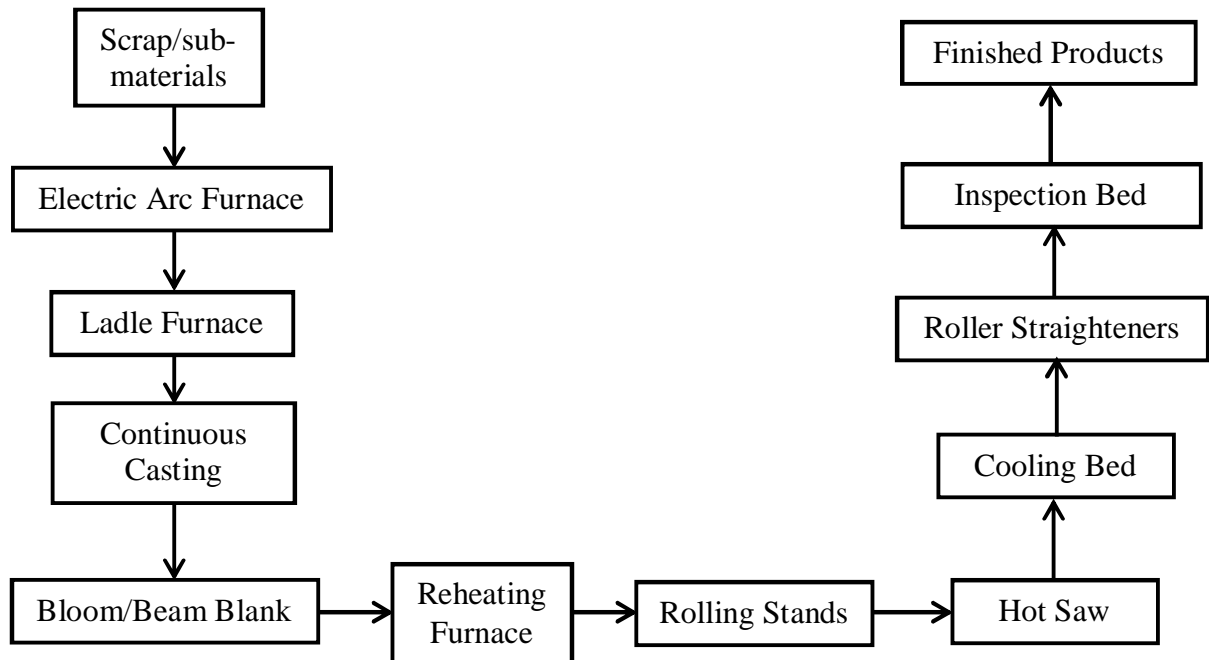


Figure 1 Schematic diagram showing the manufacturing process of structural steel shapes [20, 26].

Due to uneven cooling conditions on the cooling bed, many members are crooked after cooling. Therefore, most shapes have to be straightened in some manner. This is accomplished in a roller-straightener where the member is passed through a number of rolls

which bend the shape in alternating directions about its weak axis. The straightening operations are expected to influence the initial residual stress pattern; however, practical measurements have indicated that residual stresses in delivered shapes often show the basic pattern to be expected from the cooling process [19].

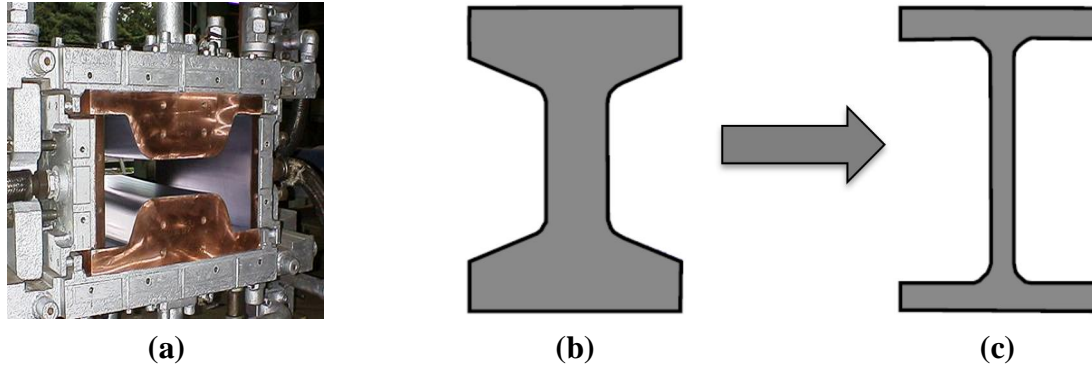


Figure 2 (a) Beam blank continuous caster mold, (b) cross-sectional view of beam blank, (c) cross-sectional view of finished product after hot-rolling.

3. Finite Element Modeling of the Cooling Process

In order to simulate the residual stresses developed due to uneven cooling of hot rolled W shapes, finite element method has been implemented in this study. Only the residual stresses developed during the cooling phase of the W shapes was simulated, and the process of hot-rolling was not accounted for. However, rolling would be important if initial material state need to be calculated. In cooling process simulation, sequentially coupled, nonlinear, transient, thermo-mechanical analyses were employed to calculate temperature history and initial residual stresses. Initially a transient thermal analysis was performed on structural W shapes to get a real time temperature distribution during the cooling process of reheated rolled specimens. The temperature field at each time step is then used as an input for evaluating the stress and strain field in the W shapes. In this approach the heat transfer analysis is solved independently of the stress analysis. The link between the heat transfer analysis and stress analysis is obtained through the temperature history, which is input as the

thermal load in the residual stress calculation. The details of the thermal and residual stress analyses are presented next.

3.1. Thermal Analysis

In the thermal finite element analysis, 3D finite element models of structural W shapes were generated by using nonlinear finite element software ANSYS. The W shape model was discretized by twenty noded thermal solid elements with one degree of freedom, temperature, at each node. Four different size W shapes were chosen for the finite element simulation, viz. W14×43, W16×50, W27×102, W36×150. These sections were chosen since residual stress measurements were available in the literature to validate the finite element simulation results [1, 3, 20]. Figure 3 shows a typical finite element mesh developed for the thermal finite element analysis of a 2.7m long W36×150 beam. For the thermal finite element analysis, temperature was given as input which was assumed to be constant and uniform all over the body before the start of the cooling process. The initial uniform temperature that was assigned to the W shape specimen was 1300°C which falls within the range of the reheating temperature (1200°C-1300°C) during rolling of the specimens. The temperature was kept constant for 10 minutes before air cooling of the specimen. It is to be mentioned here that air cooling was simulated in thermal finite element analysis by allowing free heat transfer (convection, conduction, radiation into air) in all directions.

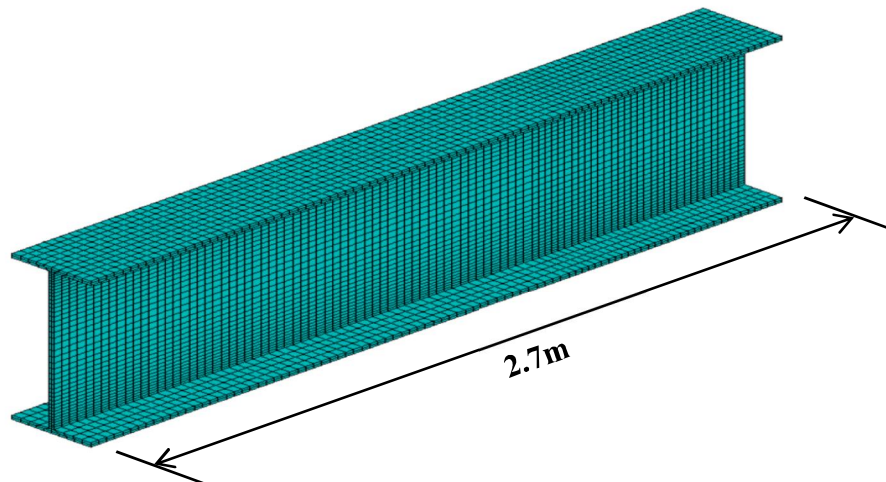


Figure 3 Finite element mesh for thermal finite element analysis of W36×150 shape.

During heating and slow air cooling, the governing equations follow the differential equations of three dimensional heat flow in a solid body under non-stationary conditions which is given in Eq. 1. This is a generalized Fourier heat-conduction equation [26] and is valid for the interior of the body.

$$\frac{\partial}{\partial x}\left(k \frac{\partial T}{\partial x}\right) + \frac{\partial}{\partial y}\left(k \frac{\partial T}{\partial y}\right) + \frac{\partial}{\partial z}\left(k \frac{\partial T}{\partial z}\right) + Q = \rho c_p \frac{\partial T}{\partial t} + \frac{E\alpha}{1-2\nu} \left(\frac{\partial \varepsilon_x}{\partial t} + \frac{\partial \varepsilon_y}{\partial t} + \frac{\partial \varepsilon_z}{\partial t} \right) \quad (1)$$

where k = thermal conductivity, Q = generated heat energy, ρ = density, c_p = specific heat, T = temperature, E = modulus of elasticity, α = coefficient of linear expansion, ν = poisson's ratio, ε = mechanical strain, t = time, x, y, z = Cartesian coordinates.

The boundary condition for solving Eq. 1 is given in Eq. 2 and is valid at the surface.

$$-k \frac{\partial T}{\partial n} = h(T - T_{atm}) \quad (2)$$

where h = surface coefficient of heat transfer, n = coordinate normal to surface. However, for solving the heat flow equation numerically, in the thermal finite element analysis it was assumed that the material is homogeneous and isotropic throughout the cross section and the material coefficients are known as functions of temperature.

For a body subjected to cooling in the atmosphere with no sharp variation in the time-temperature history, the coupling effect of temperature and strain can be neglected [27]. Hence, the 2nd term in the right hand side of Eq. 1 can be neglected. Furthermore, $Q=0$ since there is no heat generated in the body. These assumptions simplified Eq.1 as follows:

$$\frac{\partial}{\partial x}\left(k \frac{\partial T}{\partial x}\right) + \frac{\partial}{\partial y}\left(k \frac{\partial T}{\partial y}\right) + \frac{\partial}{\partial z}\left(k \frac{\partial T}{\partial z}\right) = \rho c_p \frac{\partial T}{\partial t} \quad (3)$$

After discretization over the region, the heat-conductivity equation can be reduced to the following matrix equation [28]:

$$[C]\{\dot{T}\} + [K]\{T\} = \{Q\} \quad (4)$$

Where $\{T\}$ is the vector of nodal temperatures, $[C]$ is the heat-capacity matrix, $[K]$ is the heat conductivity matrix, $\{Q\}$ is the vector of heat energy which is zero for this case. Eq. 4 is integrated numerically to get the temperature distribution during the entire cooling process of

the W shape specimen. The material coefficients that are required to solve Eq. (4) are density, thermal conductivity, specific heat and surface coefficient of heat transfer.

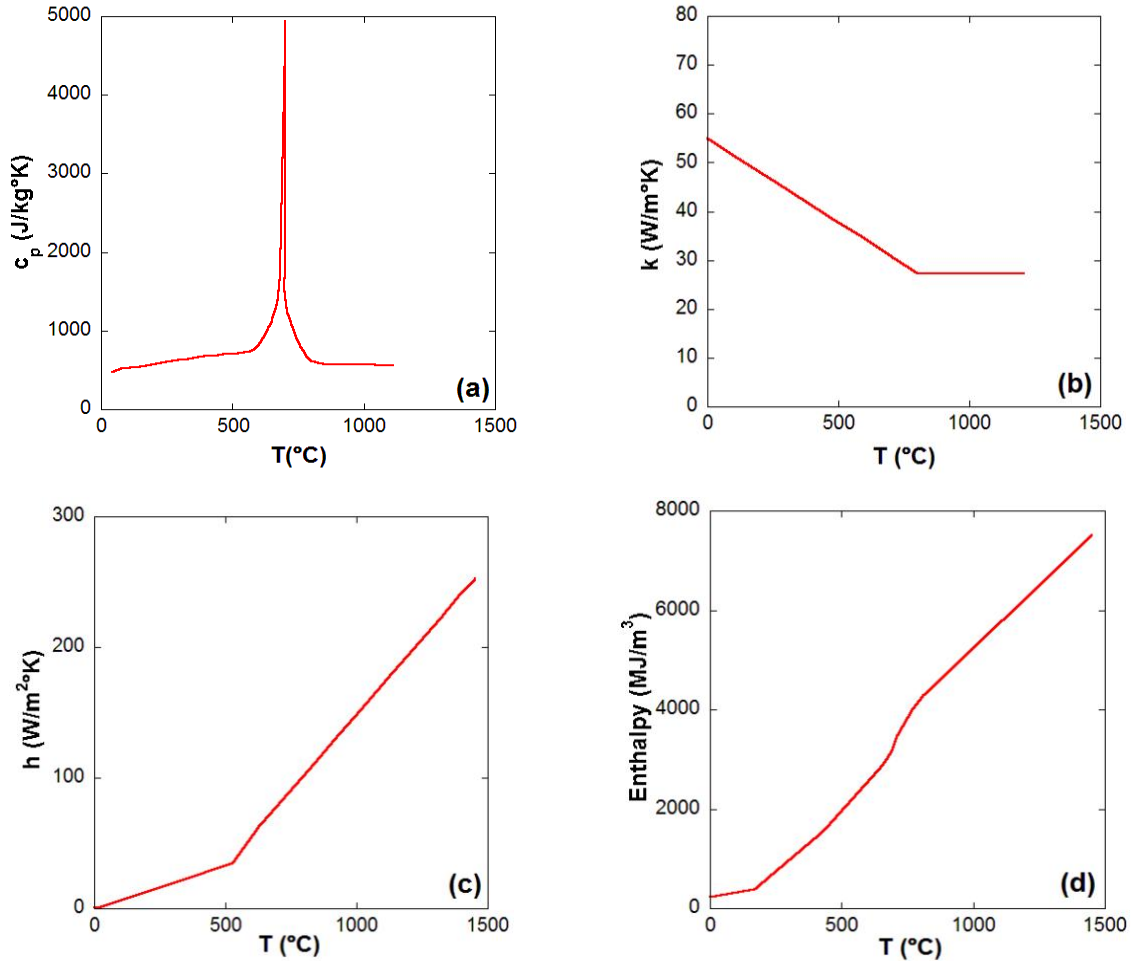


Figure 4 Material coefficients of structural steel as a function of temperature used in thermal finite element analysis. (a) Specific heat [31], (b) thermal conductivity [31], (c) heat transfer coefficient [32], (d) enthalpy [33].

Of the material coefficients, density was assumed constant, whereas other material coefficients were made as functions of temperature in the thermal finite element analysis. Latent heat/phase transformation was accounted for by defining enthalpy of the material as a

function of temperature [30-31]. Figure 4 shows the material coefficients used in the thermal finite element analysis. The discontinuity of specific heat at 650-760°C is a result of the phase transformation from ferrite (α -Fe) to austenite (γ -Fe). The surface coefficient of heat transfer includes the effect of convection, conduction and radiation. Using these material coefficients along with the method outlined above, thermal finite element analyses were performed on the aforementioned four different sizes of W shape specimens to get the real time temperature distribution during the cooling process after hot-rolling.

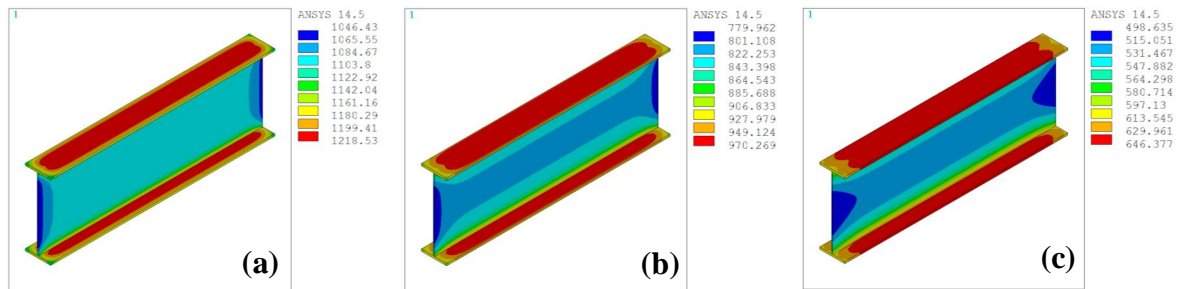


Figure 5 Contour showing temperature distribution (in °K) during the cooling process of hot rolled W36×150 section from initial 1300°C reheat temperature. (a) after 15 minutes, (b) 30 minutes, (c) 45 minutes.

It was interesting to note that the general trend of temperature distribution for all the W sections was similar during the cooling process, although variations were observed in the magnitudes and gradients of temperature at different locations for different size W shapes. However, all the sections cooled down to room temperature from initial 1300°C reheat temperature within two hours regardless of the section size. Figure 5 shows the temperature distribution for a W36×150 section at different stages of cooling upto 45 minutes. In the beginning of the cooling process, the flange tips and web cooled much faster than the web-flange junction and neighboring region. Also the cooling process was much faster in the edge of the beam flanges and mid-depth of the beam web compared to the mid-section flanges of the beam. When the coolest part reached the phase transformation temperature (650-760°C), the cooling curves tend to level out due to the transformation heat (Figure 6a). After the

transformation was finished, the cooling curves then proceeded with a slope almost as if they were a continuation of the curves before the transformation, the cooling only being delayed for a certain time. The curves continue smoothly until the temperature of the whole cross section eventually approached the ambient temperature. In Figure 6b, it can be seen that there is a fairly large temperature gradient through the cross section. These temperature differences were the cause of residual stresses to be formed during cooling. The temperature differences increased at first very rapidly, reach a maximum and then start to decrease indicating that the material transformation has started in the coolest point. After a time the curves increased again (for the flange points a very small increase) corresponding to the situation when transformation has started in the hotter point while the transformation is finished in the other point.

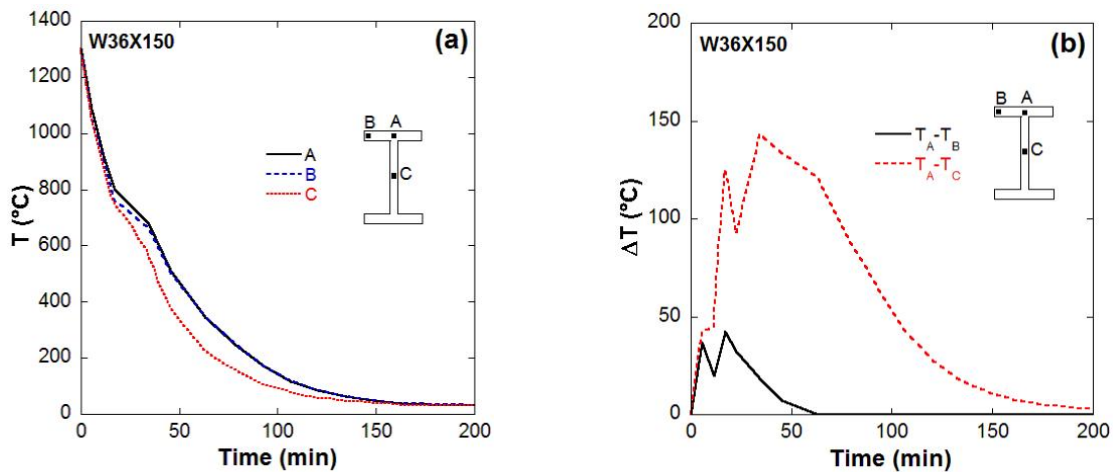


Figure 6 (a) Cooling curves at three different locations over the cross section of a W36×150 section, (b) temperature difference as a function of cooling time over the cross section of a W36×150 section.

A new maximum is then reached, marking the situation where the transformation is finished in both points, and after that the temperature differences decrease gradually to zero as ambient temperature is reached. These observations from the finite element analysis are in

well agreement with the experimental results reported by Alpsten [19] for European shape HE 200 B. This validates the fidelity of the developed thermal finite element analysis. This demonstrates that the implemented analysis technique provides the time-temperature history during cooling process with a reasonable accuracy. This, however, requires the thermal parameters in Figure 4 to be determined accurately and the actual 3D geometry of the model needs to be accurate.

3.2. Residual Stress Analysis

The residual stress analysis was conducted after the thermal analysis was finished and the time-temperature history during the cooling process of the structural W shape was determined. The temperature solution obtained from the thermal analysis, which normally depends on position and time, was input into the stress analysis as a predefined field i.e. the nodal temperature field at each time step from the thermal analysis was applied as thermal load to the corresponding node in the structural model. As a result, the node labels for the structural mesh must match those from the heat transfer mesh. This was accomplished by changing the element types in the thermal model from thermal solids to structural solids by using ETCHG command available in ANSYS. Once the real time temperature fields were fed into the structural model for each of the nodes at each time step, then residual stresses were calculated based on the temperature dependent material properties of structural steel and relevant constitutive equations. Since the experimental residual stress data available in the literature was based on ASTM A36 steel, this steel grade was chosen for validation of the residual stress simulation technique. It is to be mentioned here that in the finite element analysis for residual stress calculation both material and geometric nonlinearity was incorporated in the finite element models.

The material properties used for the residual stress analysis in finite element simulation were density, initial yield stress, elastic modulus, Poisson's ratio and thermal expansion coefficient for structural steel. The density was assumed constant, whereas all other material parameters were used as a function of temperature. Figure 7 shows the variation of Poisson's ratio and thermal expansion coefficient for structural steel as a function of temperature. The

initial yield stress and the elastic modulus were obtained from the elevated temperature stress-strain response of ASTM A36 steel under monotonic tension loading. The monotonic stress-strain response of ASTM A36 steel was obtained from Harmathy and Stanzak [34] upto 650°C Figure 8a. For temperatures over 650°C, no stress-strain data was available in the literature for ASTM A36 steel.

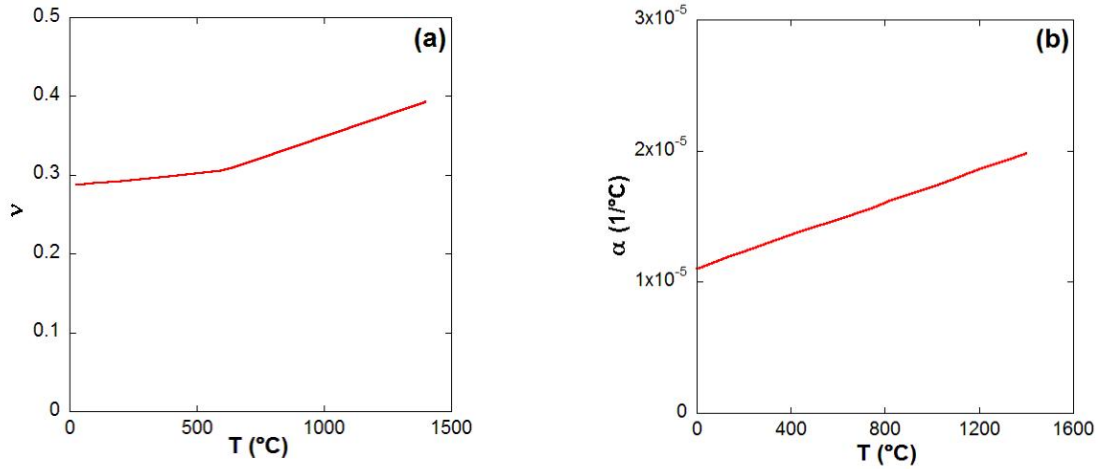


Figure 7 (a) Poisson's ratio [36] and (b) thermal expansion coefficient [37] of structural steel plotted as a function of temperature.

However, monotonic stress-strain data was available for ASTM A992 steel at temperatures over 650°C [35] as shown in Figure 8b, and this data was scaled to obtain the stress-strain response of ASTM A36 steel at temperatures over 650°C as shown in Figure 8a. The elevated temperature stress-strain response of ASTM A36 steel was implemented in the finite element simulation by using multilinear kinematic hardening model available in ANSYS which incorporates von-Mises yield criterion and associative flow rule as given by Eq. 5 and Eq. 6 respectively.

$$f(\underline{\sigma}) = \left[\frac{3}{2} (\underline{s} - \underline{a}) \cdot (\underline{s} - \underline{a}) \right]^{1/2} - \sigma_0 = 0 \quad (5)$$

$$d\underline{\varepsilon}^p = d\lambda \frac{\partial f}{\partial \underline{\sigma}} \quad (6)$$

where $\underline{\sigma}$ is the stress tensor, \underline{s} is the deviatoric stress tensor, \underline{a} is the current center of the yield surface in the deviatoric stress space, σ_0 is the initial size of the yield surface, $d\lambda$ is plastic multiplier which corresponds to the equivalent plastic strain increment as

$$dp = \left[\frac{2}{3} d\underline{\varepsilon}^p \cdot d\underline{\varepsilon}^p \right] \quad (7)$$

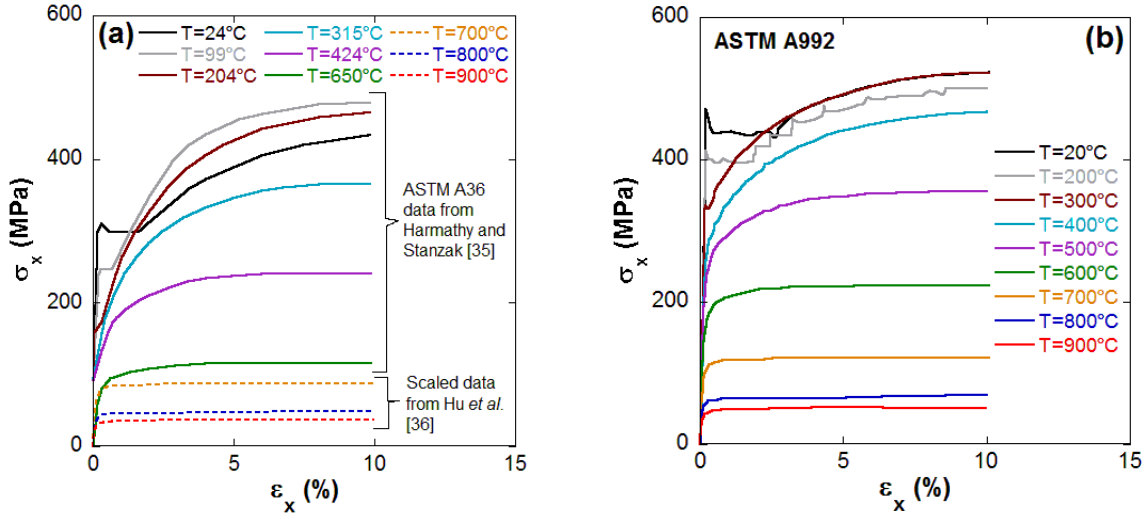


Figure 8 (a) Monotonic stress-strain response of ASTM A36 steel at different temperatures, (b) monotonic stress-strain response of ASTM A992 steel at different temperatures [35].

In the solution of residual stress fields, it is usually assumed that the total strain increment can be decomposed as

$$d\underline{\varepsilon} = d\underline{\varepsilon}^e + d\underline{\varepsilon}^p + d\underline{\varepsilon}^T \quad (8)$$

where $d\underline{\varepsilon}^e$, $d\underline{\varepsilon}^p$ and $d\underline{\varepsilon}^T$ are the elastic, plastic and thermal strain increment respectively.

Based on the von mises yield criterion, the constitutive relation can be written as

$$\{d\sigma\} = [D]\{d\varepsilon\} - [C^{th}]\{dT\} \quad (9)$$

where $\{d\sigma\}$ is the stress increment, $[D]$ is consistent tangent modulus matrix, $\{d\varepsilon\}$ is strain increment, $[C^{th}]$ is thermal stiffness matrix, and $\{dT\}$ is temperature increment.

4. Results and Discussion

The initial residual stress simulations were performed for four different W sections (W14×43, W16×50, W27×102, W36×150) to validate the fidelity of the finite element models developed. Figure 9 shows longitudinal residual stress contours for a W36×150 section at different stages of the cooling process. It was evident from the thermal analysis that the beam flange tips and web cooled faster than the beam flange-web junction. Thermal contraction of the junction between the beam flange and web would be greater than that of the cooler flange tips and web. However, due to the symmetry, the compatibility conditions require that the contraction is equal throughout the cross section [19]. This will introduce tensile stresses in the central flange-web junction, balanced by compressive stresses in the regions which were cooling faster i.e. flange tips and web. The resulting residual stress distribution after cooling to ambient temperature is shown in Figure 10a,b for a W36×150 section. The results exemplify the rule of thumb that the portions of the cross section to cool faster (flange tips and web) will be left in a state of compressive residual stress.

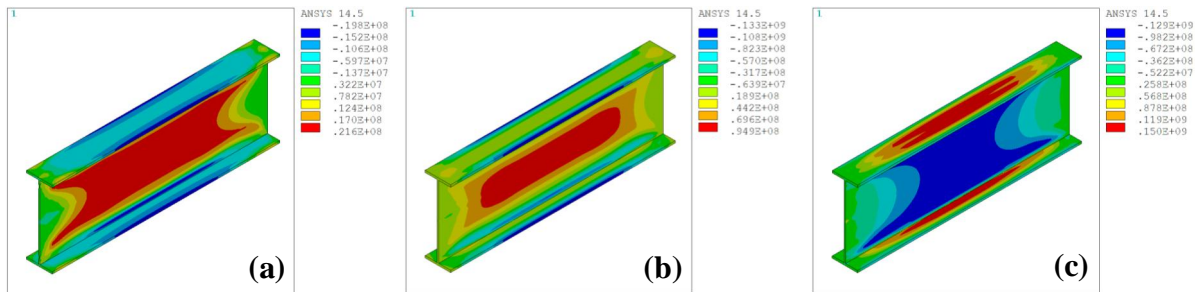


Figure 9 Contour showing longitudinal stress distribution during the cooling process of hot rolled W36×150 section. (a) after 15 minutes, (b) 1 hour, (c) 2 hours.

The simulated residual stresses were compared to the measured residual stresses (reported in [3]) for the flange and web of the section at the centerline of the beam length at the end of the cooling process and the simulated responses resembled the experimental responses very well as shown in Figure 10a,b. The longitudinal residual stress distribution and the peak stresses were predicted accurately by the finite element analysis which validates

the fidelity of the finite element technique implemented. The distribution of the residual stress across the flanges was of a general parabolic form and had a tensile residual stress value at the flange center (Figure 10a). The residual peak stress in the beam flange was seen to be as high as one-third of the yield stress of the material. On the contrary, the residual peak stress in the web of the beam was in between one-third to one-half of the yield stress (Figure 10b) and the distribution of the residual stress was also of a general parabolic form. In addition, it was observed that initial residual stresses showed an increasing trend along the length of the beam with peak stresses obtained at the center of the beam (Figure 10c). The variation of longitudinal stresses along the length of the beam was observed for all the locations across the cross section i.e. flange tip, web and flange-web junction. However, at the ends of the beam section, the longitudinal residual stresses had very small value for a distance of about equal to the depth of the beam (Figure 10c). Similar observations were also seen in the measured trend of longitudinal residual stress by Alpsten [19]. Hence, it is apparent that the influence of initial residual stresses would be dominant from a distance of equal to the beam depth of the beam. When the residual stresses at different locations of the beam cross section were plotted against the time of cooling, it was noticeable that the fastest cooling part (flange tips and web) developed tensile stresses initially, whereas slowest cooling part (flange-web junction) developed compressive stresses.

As the cooling progressed, the tensile stresses in the fastest cooling part turned finally to compressive stresses and the compressive stresses in the slowest cooling part turned to tensile stresses. Another interesting thing to note here that after about two hours of cooling, the initial residual stresses stabilized to a steady state value, and no change was observed in the initial residual stress distribution. To further validate the finite element modeling features adopted in this study, residual stress simulations were also compared to the experimental measured values for W14×43, W16×50, W27×102 sections as shown in Figure 11 through Figure 13, where flange and web longitudinal residual stresses are plotted at the center of the beam length. Very good conformity between the measured and simulated responses was observed for all the W sections investigated. The validation of the simulated responses

against experimental measurements for a wide range of W sections shows the robustness of the finite element technique implemented in this study.

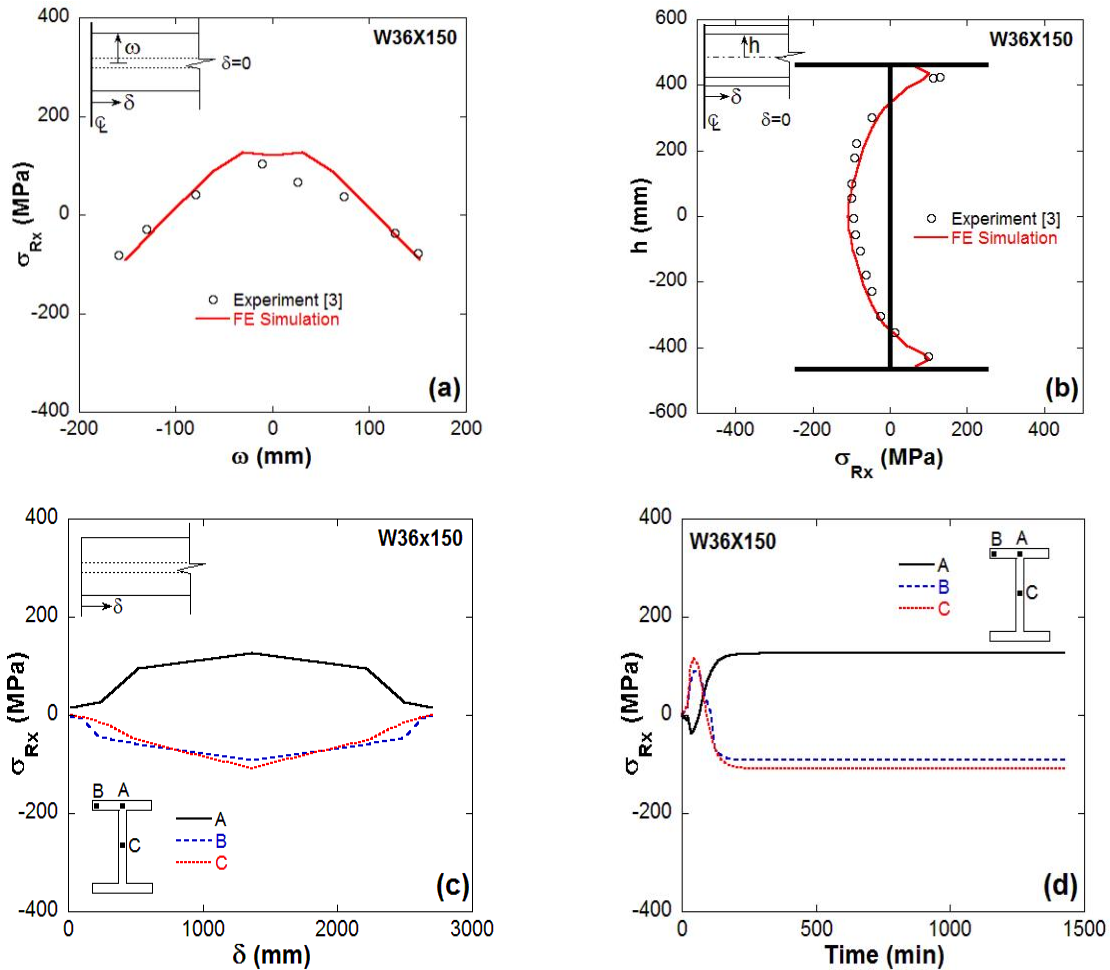


Figure 10 Residual stress analysis results for a W36×150 section. (a), (b) Measured [3] and simulated longitudinal residual stresses at the centerline along the beam length, (c) simulated longitudinal residual stress distribution along the length of beam, (d) simulated longitudinal residual stresses plotted against cooling time at different locations of the beam section.

While it cannot be expected that all experimental results will correlate well with finite element simulation based on nominal shape dimensions, average material properties and

certain assumptions on the heat transfer in cooling, the comparisons between computed and measured initial residual stresses (IRS) made in this study gives an idea of the applicability of the method which can serve as a guide for analysis of other shapes. Moreover, since cooling conditions can be variable in the cooling bed because of stacking side by side, residual stresses may have different distributions and magnitudes even in the same shape depending on the imposed condition of cooling. The simulations made in this study pertains to the assumption of free heat transfer, and any change in the cooling condition other than free cooling condition must be accounted for in order to predict the actual scenario.

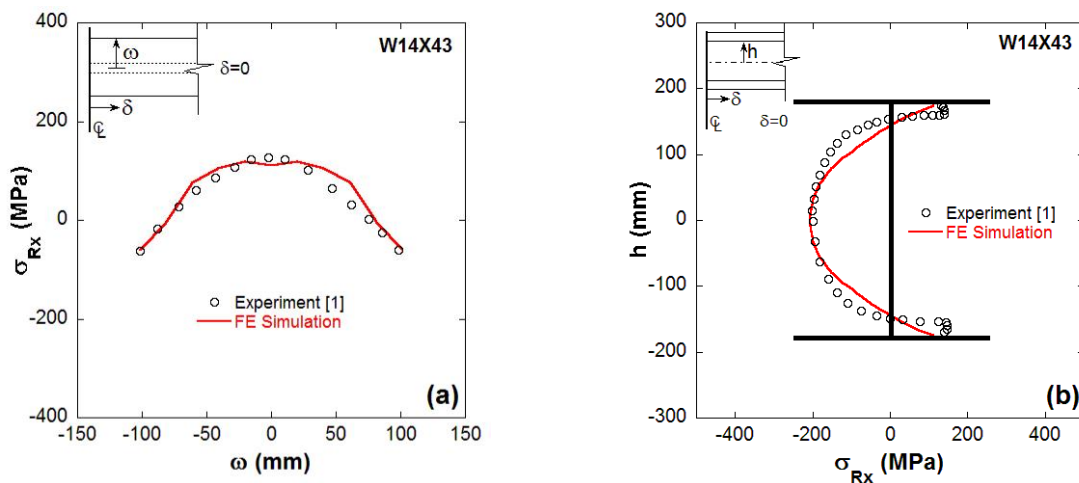


Figure 11 Measured [1] and simulated longitudinal residual stresses at the centerline along the beam length for a W14×43 section.

5. Influence of IRS on Buckling Response of Wide Flange Steel Columns

With the developed simulation technique, the actual distribution of the initial residual stresses can be simulated for all the structural shapes commonly used as beams and columns in moment resisting building frames, and it can be included in the analysis of moment resisting frames under different types of loading conditions such as seismic analysis, fire performance evaluation, buckling resistance evaluation for columns, and wind damage analysis. The presence of initial residual stresses (IRS) is more crucial for compression

members such as column, where it is expected that IRS will reduce the ultimate strength of the column and thereby reduce the buckling strength. In literature most of the works related to the analysis of steel building frames either did not consider initial residual stresses or assumed a simplified linear distribution due to the complexity involved in IRS calculation.

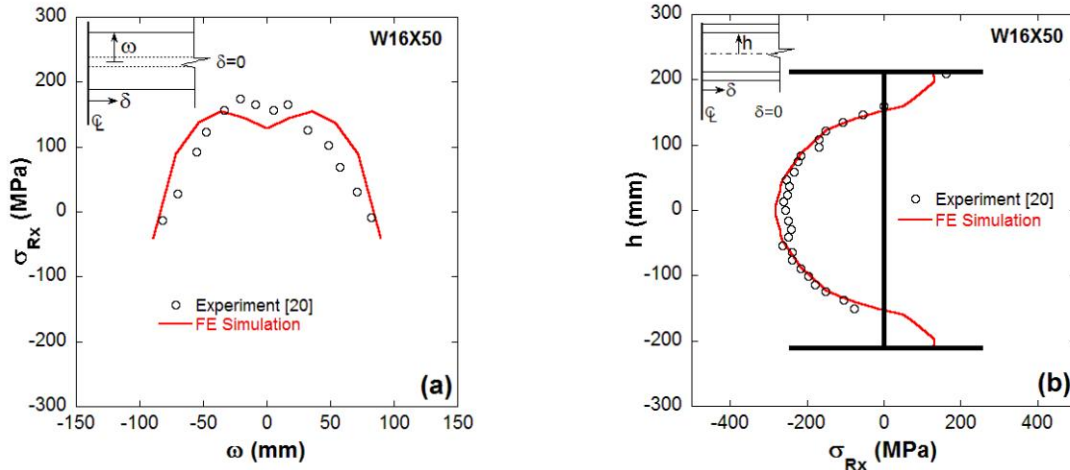


Figure 12 Measured [19] and simulated longitudinal residual stresses at the centerline along the beam length for a W16×50 section.

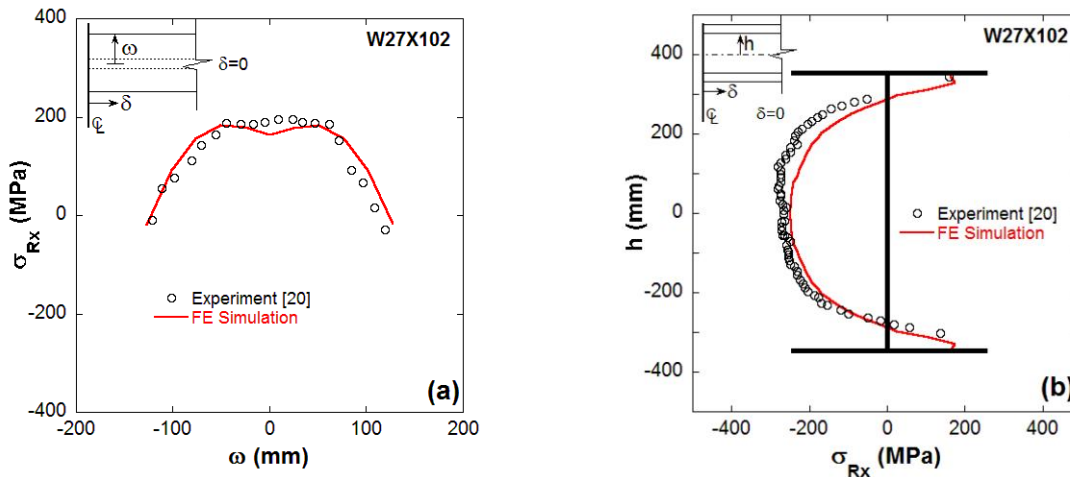


Figure 13 Measured [19] and simulated longitudinal residual stresses at the centerline along the beam length for a W27×102 section.

Hence there is a lack of understanding of the influence of initial residual stresses on the cyclic response of wide flange steel columns. With the implemented IRS simulation technique, the actual distribution of IRS can be obtained and accounted for in the analysis and design of steel structures. A study on the influence of initial residual stresses on the cyclic response of wide flange steel columns has been conducted in this study to demonstrate the applicability of the simulation technique. Wide flange steel columns have widespread applications in moment resisting frames and bridge piers. However, due to the relative large slenderness ratios of the columns, structures of this type may be susceptible to damage caused by local buckling under constant axial load and cyclic lateral forces. To provide a basis for performance evaluation of columns under cyclic lateral loads with residual stresses, wide flange steel columns have been subjected to numerical investigation in this study. Firstly, the finite element model and the technique of residual stress calculation has been validated against the experimental data from Lamarche and Tremblay [11] where they studied the response of wide flange steel columns under axial compression.

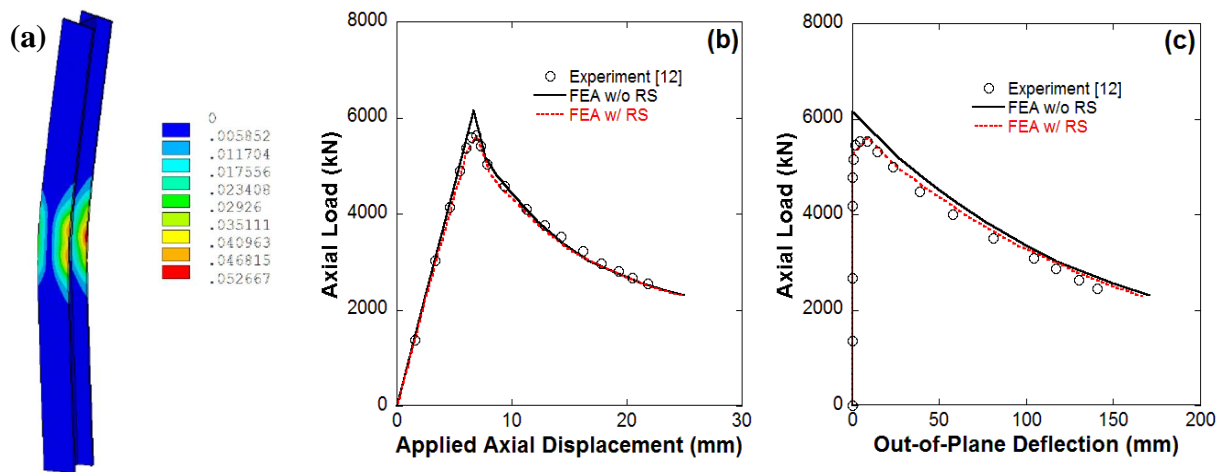


Figure 14 (a) Equivalent plastic strain contour of W12×87 column under axial compression, (b) simulated and experimental [11] axial load-displacement response, (c) simulated and experimental [11] out-of-plane deflection response.

A finite element model was developed for an ASTM A992 W12×87 (W310×129 in mm) wide flange steel column having 3725 mm length and its performance was evaluated under axial compression. The loading was displacement controlled and the analysis was performed with and without the presence of IRS. As can be observed in Figure 14 that the simulated response from the finite element analysis with IRS predicted the experimental responses better than without IRS. The axial load-displacement response (Figure 14b) as well as the out-of-plane deflection (Figure 14c) was predicted very well by the simulation with IRS. Although the simulated response without IRS was able to predict the experimental trend reasonably well, but the peak strength was over predicted. This validates the finite element modeling and the implemented technique of residual stress calculation in predicting the response of wide flange steel columns.

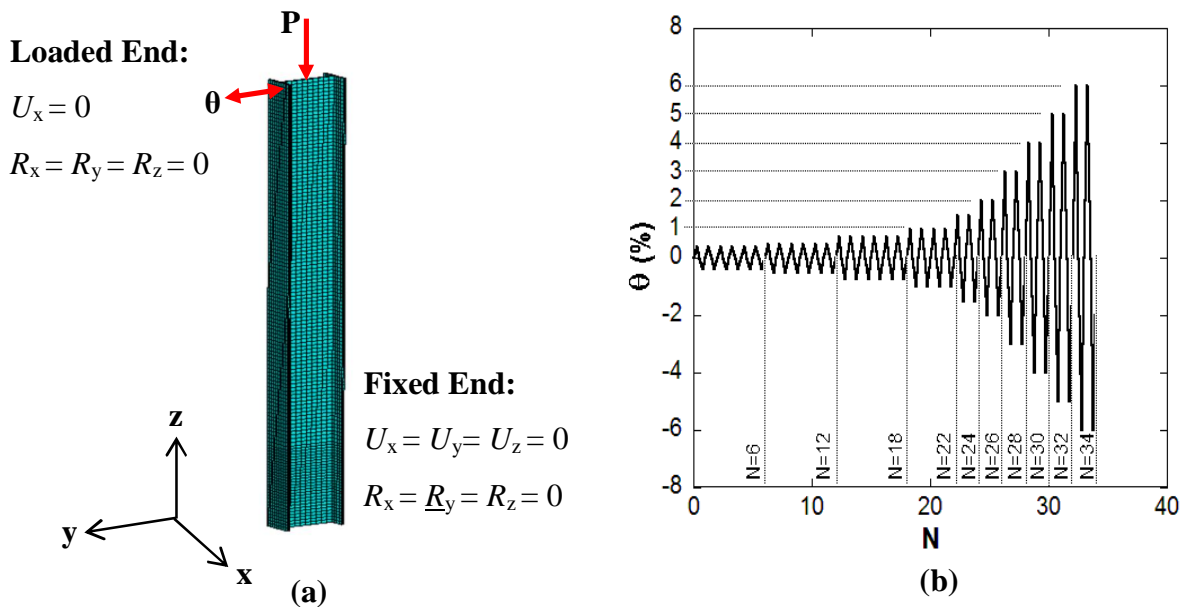


Figure 15 (a) Finite element mesh used in the cyclic response evaluation of wide flange column sections, (b) displacement-based simulated earthquake loading history [41].

After validation of finite element technique, a detailed finite element analysis was performed on wide flange steel columns to investigate the influence of initial residual stresses on the cyclic response. Since the influence of IRS on the cyclic response of wide

flange steel columns can be a function of depth of the beam or the width-thickness ratio [39-40], four different sizes of wide flange steel columns having different width-thickness ratio were investigated in the finite element study. The column sections chosen for the analysis consisted of W14×132, W24×131, W24×250, W36×230 and their performance was evaluated under combined axial compression and cyclic loading for both the cases with and without IRS. Table 1 shows the width-thickness ratios for different column sections used in this study. In the finite element modeling, the experimental setup of Newell and Uang [38] was simulated where 4572 mm long wide flange steel columns were tested under combined axial and lateral loads. The wide flange steel columns were discretized by twenty noded solid brick elements and the boundary conditions simulated those used for experimental testing of the steel column specimens [38]. Figure 15a shows the column model boundary conditions and finite element mesh.

Table 1 Width-thickness ratio for different column sections

Column Section	h/t_w
W14×132	17.7
W24×131	35.6
W24×250	20.7
W36×230	42.2

At the fixed end of the model all six translational and rotational degrees of freedom were constrained to be zero. At the loaded end of the model the out-of-plane translational (U_x as shown in Figure 15a) and all three rotational degrees of freedom were constrained to be zero. Lateral drift displacement was applied in the U_y direction and constant axial load was applied in the U_z direction. A rigid constraint was imposed on edges at the column ends to prevent stress concentrations at the loading and reaction points. A compressive load equal to the 30% of the nominal axial load capacity [40] of the column was applied at the loaded end of the column and a displacement-based artificial loading protocol offered by SAC/BD-97/02 [41] was applied at the tip of the column in the lateral direction as the cyclic load. The displacement based time history was based on the SAC Test Protocol and consisted of

imposing a series of prescribed quasi-static cyclic displacements to the end of the column [41]. The prescribed displacements included six cycles of 0.375, 0.5 and 0.75% interstory drift, followed by four cycles of 1.0% interstory drift and two cycles each of 1.5, 2, 3, 4, 5, 6% and so forth interstory drift. A schematic of the loading protocol is shown in Figure 15b.

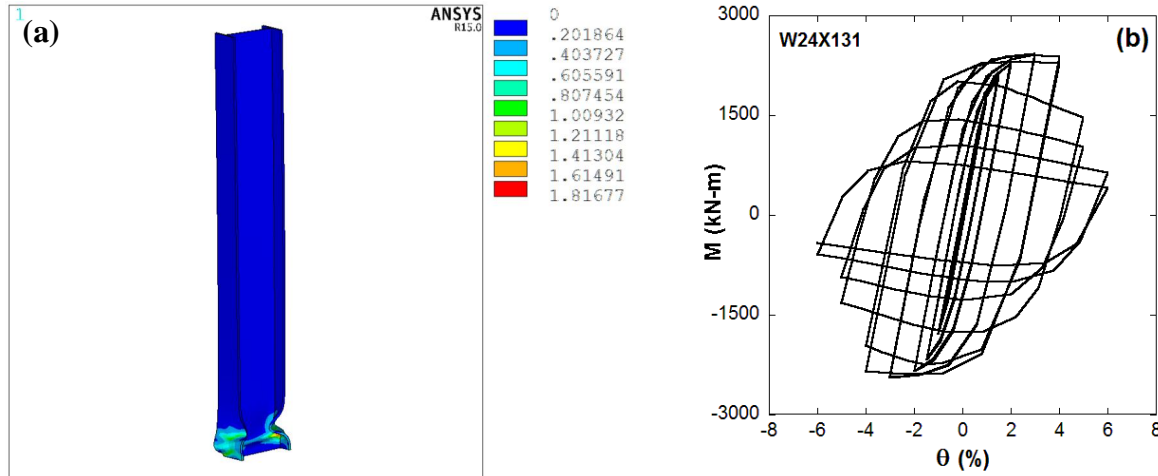


Figure 16 Cyclic response of W24×131 column without considering IRS. (a) Equivalent plastic strain contour, and (b) moment-rotation hysteresis response at the end of 6% interstory drift angle.

The finite element results revealed that under cyclic loading, all the columns developed plastic hinge near the fixed end of the column by inelastic local buckling of the flanges and web regardless of the presence of IRS. Figure 16 and Figure 17 show the equivalent plastic strain contours and moment-rotation hysteresis plots of a W24×131 column without and with initial residual stresses respectively under combined axial compression and cyclic lateral loading. The moment-rotation envelopes of peak moments at each loading cycle for all the column sections are shown in Figure 18. It can be observed that for all the column sections, when IRS was included in the analysis, the strength of the connection started to degrade earlier compared to when IRS was not considered in the analysis. For column section W14×132, there was almost no strength degradation for cyclic loading upto 6% interstory drift angle when IRS was not included in the analysis, whereas the strength of the column

started to degrade at 5% interstory drift angle when IRS was included in the analysis, and the strength degraded by around 37% at the end of 6% interstory drift angle (Figure 18a). Similarly for W24×131 and W36×230 column sections, the strength degradation started at 4% interstory drift angle when IRS was not considered in the analysis, whereas the strength degraded at 3% and 2% interstory drift angle for W24×131 and W36×230 column sections respectively, when IRS was considered (Figure 18b, d). This demonstrates that presence of initial residual stresses initiates inelastic buckling of the columns earlier and hence, the strength of the column will be overpredicted without considering the effect of IRS.

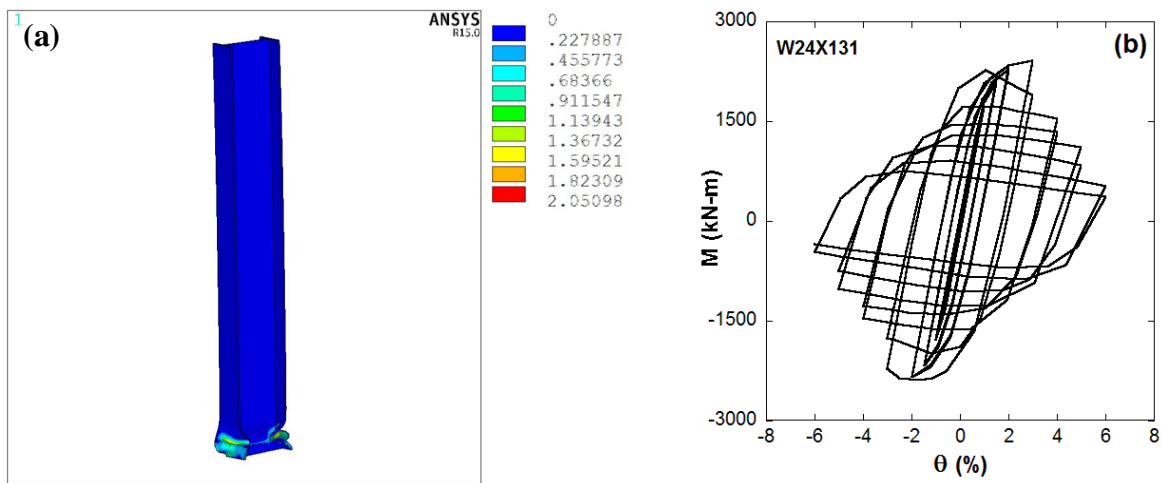


Figure 17 Cyclic response of W24×131 column considering IRS. (a) Equivalent plastic strain contour, and (b) moment-rotation hysteresis response at the end of 6% interstory drift angle.

It was also noticed that as the slenderness of the column section increases (Table 1), there is more degradation in the strength of the column (Figure 18). This indicates that the influence of IRS is more protuberant for columns with high slenderness ratio compared to more compact column section such as W14×132. This is more evident when the cyclic response of W24×250 column was compared with W24×131 column (Figure 18c). Although both the section’s depth was similar, their width-thickness ratio was significantly different.

W24×250 had a width-thickness ratio almost twice that of W24×131. As a result, the influence of IRS was insignificant on the cyclic response of W24×250 column upto 6% interstory drift angle.

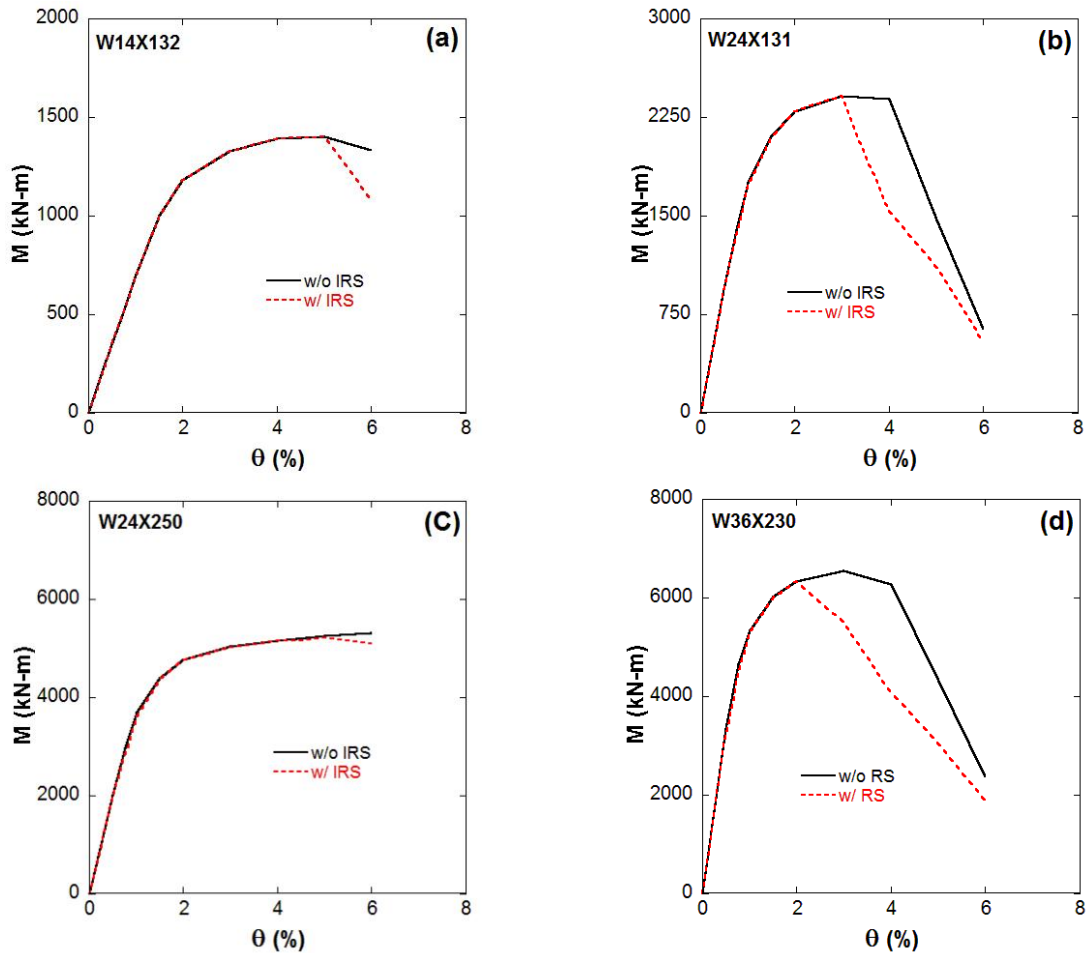


Figure 18 Moment-rotation envelope showing peak moment at each loading cycle for different column sections with and without IRS. (a) W14×132, (b) W24×131, (c) W24×250, (d) W36×230.

The moment-rotation envelope of peak moments at each loading cycle (Figure 18c) shows that the column showed similar response for both with and without IRS upto 6% interstory drift angle. Hence it can be concluded that the cyclic response of wide flange column is directly influenced by the presence of the IRS and the influence of IRS increases

with the width-thickness ratio of the member. Another interesting phenomenon that was observed for all column sections is that for both the cases with and without IRS, plastic hinge formed at the fixed end of the column and when IRS was included in the analysis the plastic hinge moved more towards the fixed end of the column indicating a reduction in the strength of the column. Based on the observations from the finite element analysis, it is evident that the presence of initial residual stresses significantly influences the cyclic response of wide flange steel columns, especially columns with high width-thickness ratio and henceforth, need to be addressed during the design calculation for steel building moment resisting frames. The IRS simulation technique presented in this study can be beneficial in order to account for the actual distribution of initial residual stresses in wide flange steel members and thereby, provide a conservative estimate of the strength.

6. Conclusions

An advanced numerical technique has been developed to simulate initial residual stresses developed during the cooling process of hot-rolled wide flange steel members based on a sequentially coupled transient thermo-mechanical analysis. The simulated residual stresses for different size of W shapes were evaluated against the experimental data available in the literature which validates the robustness of numerical modeling scheme developed. An example of the applicability of the method is presented in this study on the cyclic response simulation of wide flange steel columns which demonstrated the importance of considering initial residual stresses in the design of steel building moment resisting frames. The measurements of residual stresses based on developed simulation technique should be beneficial for an estimate of the magnitude and distribution of residual stresses likely to be encountered, which can be used in the analysis of moment resisting building frames under different types of loading conditions and can provide a conservative estimate of the strength of members or connections.

7. References

- [1] Fujita Y. The magnitude and distribution of residual stress. Fritz Engineering Laboratory Report No. 220A.20, Lehigh University, Bethlehem, PA, 1955.
- [2] Ketter RL, Kaminsky FL, Beedle LS. Plastic deformation of wide-flange beam columns. ASCE Trans. 1955;120, 1019, Reprint No. 91 and 101.
- [3] Huber AW. The influence of residual stress on the instability of columns. Ph.D. Dissertation, University Microfilms, Inc., Ann Arbor, Michigan, 1956.
- [4] Ketter RL. The influence of residual stresses on the strength of structural members. Welding Research Council Bulletin 44 1958; Reprint No. 132 (58-6).
- [5] Luxion WW, Johnstone BG. Plastic behavior of wide flange beams. The Welding Journal 1948;27(11), Research Supplement, 538-s to 554-s.
- [6] Yang CH, Beedle LS, Johnstone BG. Residual stress and the yield strength of steel beams. The Welding Journal 1952;31(4), Research Supplement, 205-s to 229-s.
- [7] Real PMMV, Cazeli R, Silva LSD, Santiago A, Piloto P. The effect of residual stresses in the lateral-torsional buckling of steel I-beams at elevated temperature. Journal of Constructional Steel Research 2004;60:783-793.
- [8] Russel TF. Some mathematical considerations on the heating and cooling of steel. 1st Report of the Alloy Steels Research Committee, Iron and Steel Institute, London, 1936.
- [9] Huber A, Beedle LS. Residual stress and the compressive strength of steel. The Welding Journal 1954;33(12).
- [10] Ding Y. Residual stresses in hot-rolled solid round steel bars and their effect on the compressive resistance of members. MS Thesis, The University of Windsor, Windsor, Ontario, Canada, 2000.

- [11] Beedle LS, Tall L. Basic column strength. *Journal of the Structural Division* 1960;86 (ST7):139–73.
- [12] Lamarche CP, Tremblay R. Seismically induced cyclic buckling of steel columns including residual-stress and strain-rate effects. *Journal of Constructional Steel Research* 2011;67:1401-1410.
- [13] Okazaki TO, Parkolap M, Fahnestock LA. Interface of the direct analysis method and seismic design. *Proceedings, ASCE Structures Congress 2009, Austin, TX, May 2009.*
- [14] Lu AYC, MacRae GA. Residual stress effects on the seismic performance of low-rise steel frames. *Proceedings of the 9th Pacific Conference on Earthquake Engineering Building an Earthquake-Resistant Society, Auckland, New Zealand, 2011.*
- [15] Mathur K, Fahnestock LA, Okazaki T, Parkolap MJ. Impact of residual stresses and initial imperfections on the seismic response of steel moment frames. *Journal of Structural Engineering* 2012;138 (7):942-951.
- [16] Nishino F, Tall L. Residual stress and the local buckling strength of steel columns. *Fritz Engineering Laboratory Report No. 290.11, Lehigh University, Bethlehem, PA, 1967.*
- [17] Lammi CJ. The effects of processing residual stresses on the fatigue crack growth behavior of structural materials. *Doctoral dissertation, Worcester Polytechnic Institute, 2009.*
- [18] Toribio J. Residual stress effects in stress-corrosion cracking. *Journal of materials engineering and performance* 1998;7(2):173-182.
- [19] Yamashita Y, Minami F. Evaluation of residual stress effects on brittle fracture strength based on weibull stress criterion. *Journal of ASTM International* 2008;5.

- [20] Alpsten GA. Thermal residual stresses in hot-rolled steel members. Fritz Engineering Laboratory Report No. 337.3, Lehigh University, Bethlehem, PA, 1968.
- [21] Kamamoto S, Nihimori T, Kinoshita S. Analysis of residual stress and distortion resulting from quenching in large low-alloy steel shafts. *Journal of Material Science and Technology* 1985;1:798-804.
- [22] Toparli M, Aksoy T. calculation of residual stresses in cylindrical steel bars quenched in water from 600°C. *Proceedings of AMSE Conference 1991, 4, New Delhi, India, 93-104.*
- [23] Jahanian S. Residual and thermoelastoplastic stress distributions in a heat treated solid cylinder. *Materials at High Temperatures* 1995;13(2):103-110.
- [24] Fa-rong Y, Shang-li W. Transient-temperature and residual-stress fields in axisymmetric metal components after hardening. *Journal of Material Science and Technology* 1985;1(10):851-856.
- [25] Yamada K. Transient thermal stresses in an infinite plate with two elliptic holes. *Journal of Thermal Stresses* 1988;11:367-379.
- [26] Kozak B, Dzierzawski J. *Continuous casting of steel: basic principles.* Washington: AISI Learning Center 2002;9.
- [27] Fourier J. *Analytical theory of heat.* Dover Publications, New York, 1955.
- [28] Boley BA, Weiner JH. *Theory of thermal stress.* John Wiley & Sons, Inc, 1960.
- [29] Nyashin YI. Examination of residual stresses in hot-rolled flange beams and their effect on beam stability. *Strength of Materials* 1982;14(2):258-261.
- [30] Shamsundar N, Sparrow EM. Analysis of multidimensional conduction phase change via the enthalpy model. *Journal of heat transfer* 1975;97(3):333-340.

- [31] Comini G, Guidice D. Finite element solutions of non-linear heat conduction problems with special reference to phase change. *International Journal of Numerical Methods in Engineering* 1979;8:613-624.
- [32] Eurocode 3. Design of steel structures, part 1.2, general rules, structural fire design. EN1993-1-2 European Committee for Standardization, 2005.
- [33] Brickstad B, Josefson BL. A parametric study of residual stresses in multi-pass butt-welded stainless steel pipes. *International Journal of Pressure Vessels and Piping* 1998;75(1):11-25.
- [34] Wickström U. TASEF-2: A computer program for temperature analysis of structures exposed to fire. Report No. 79-2, Lund Institute of Technology, Lund, Sweden, Department of Structural Mechanics, 1979.
- [35] Harmathy TZ, Stanzak WW. Elevated-temperature tensile and creep properties of some structural and prestressing steels. *Fire Test Performance, ASTM STP 464*, American Society for Testing and Materials, 1970, 186-208.
- [36] Hu G, Morovat MA, Lee J, Eschell E, Engelhardt M. elevated temperature properties of ASTM A992 steel.” In: *Proceedings of ASCE structure congress 09*, Austin, TX, USA, 2009.
- [37] Wikander L, Karlsson L, Nasstrom M, Webster P. Finite element simulation and measurement of welding residual stresses.” *Modelling and Simulation in Materials Science and Engineering* 1994;2(4):845.
- [38] AISC. *Manual of steel construction: load and resistance factor design—Volume I: Structural members, specifications and codes*. 2nd Ed., American Institute of Steel Construction, 1994.

- [39] Newell JD, Uang CM. Cyclic behavior of steel wide-flange columns subjected to larger drifts. *Journal of Structural Engineering* 2008;134(8):1334-1342.
- [40] Newell JD. Cyclic behavior and design of steel columns subjected to large drift. Doctoral Dissertation, University of California, San Diego, CA, 2008.
- [41] Xiao Y, Li H, Zhou T. Seismic behavior of wide-flange steel column with confined potential plastic hinge. *Journal of Constructional Steel Research* 2009;65:808-817.
- [42] SAC/BD-97/02. Protocol for fabrication, inspection, testing and documentation of beam-column connection tests and other experimental specimens.” by Clark, P., Frank, K., Krawinkler, H., and Shaw, R.

CHAPTER 6: INFLUENCE OF WELDING ON THE SEISMIC PERFORMANCE OF MOMENT RESISTING CONNECTION

Abstract

In an experimental study of the influence of welding on the seismic performance of moment resisting connections, it was observed that that welding influences the localized low-cycle fatigue failure response. Analysis of strain responses near the beam weld toe and weld access hole region led to the conclusion that weld induced residual stresses influence the localized fatigue responses. In order to get an understanding of the residual stresses and their influence on the localized failure mechanism of welded steel moment resisting connections, this study developed a numerical technique based on sequentially coupled transient nonlinear thermo-mechanical analysis to simulate the welding residual stresses and their influence on localized fatigue responses. The finite element simulation technique was validated against the experimental temperature and strain measurements. The simulated response of residual stresses showed development of very high residual stresses close to the weld region. The welding induced residual stresses together with the initial residual stresses in wide flange shapes were included for the seismic analysis of moment resisting connections, which demonstrated the influence of the residual stresses on the low-cycle fatigue failure mechanism of the connections. The results of the finite element investigation also explain the variability of the low-cycle fatigue failure response for different weld sequences. Finally, a method to reduce the magnitude of the residual stresses has been proposed based on the concept of post weld heat treatment which showed improved performance under seismic type of loading.

Keywords: Moment connection, Weld, Residual stress, Weld sequence, Low-cycle fatigue, Seismic analysis

1. Introduction

The 1994 Northridge Earthquake demonstrated the inability of many moment connections to meet the seismic demands, where a large number of steel buildings were damaged by cracking near the weld region [1-3]. Many connections failed by brittle cracking of the weld between the bottom beam flange and the column flange. Over the past two decades, the root causes of the connection failures were learned, and many were addressed through research. The lack of ductility displayed in the pre-Northridge welded steel moment connections (WSMCs) prompted research by the Federal Emergency Management Agency (FEMA) as well as the SAC Joint Venture. Weld metal matching, base metal and weld metal toughness, backing bar effects, fillet weld reinforcement, residual stress effects, continuity plates, panel zone deformations, reduced beam section details, weld access hole details, and column flange through-thickness fractures have all been investigated and several modifications were made in the existing design of moment connections [1-8]. While test results on the post-Northridge modified connections demonstrated significant improvement with regard to ductility and energy dissipation capacity; however, many localized failures have also been demonstrated. Testing of post-Northridge welded steel moment connections have shown that many failures are initiated from localized, low-cycle fatigue cracks near the weld toe [4-5, 7-13]. The weld toe fatigue crack initiation motivated several investigations on weld material and the outcome was the recommendation of using high toughness weld material [28]. However, the reason for the weld toe fatigue crack initiation in the post-Northridge design has yet to be investigated in a rational manner.

The low-cycle fatigue cracks near the weld toe has also been observed for piping joints and research studies revealed that welding induced residual stress has significant influence on fatigue crack initiation at the weld toe of piping joints [15-26]. Moreover, several studies on piping joints addressed the influence of weld sequence on the amount and distribution of residual stresses which led to the conclusion that the welding procedure can have a significant effect on the residual stress and thus the fatigue life of a joint [27-32]. The influence of weld sequence on the residual stress distribution was also addressed for welded plate and T-joint specimens [33-39]. Thus literature suggests that welding induced residual

stresses can be one of the contributors to the low-cycle fatigue failure of the moment resisting connections. The influence of residual stress on fatigue crack initiation at the weld toe in WSMCs was speculated [40-46], but the failure mechanism is yet to be investigated. However not much attention was paid to the influence of residual stress on the moment resisting connections because of the common notion that the residual stress relaxes after a couple of inelastic loading cycles. Due to the complexity involved in residual stress calculation, most analyses either do not consider residual stresses or use simplified methods of analysis [40, 45]. However, Dong and his coworkers [14, 47] did include detailed residual stress analysis in their investigations. Their calculations demonstrated that the magnitude of residual stresses in some locations can be greater than the yield stress of the material. They performed fracture analysis for crack propagation of preexisting cracks at the backing bars and demonstrated that the triaxial residual stress greatly reduced the plastic deformation capacity of the welded joint and thus induced brittle fracture. In addition, an increase in fracture driving force was observed in presence of high tensile residual stresses. However, the analysis was two dimensional and hence, the influence of weld sequence was not accounted for across the width of the beam flanges. Moreover, the influence of residual stresses on the fracture behavior was investigated based on fracture mechanics analysis. No light was shed on the low-cycle fatigue failure response of the moment connections in presence of residual stresses. Nevertheless this study showed that even though the residual stress relaxes after few inelastic loading cycles, it can influence the fracture behavior at the welded joint of the moment connection. After that study, the influence of welding induced residual stresses on the failure response of moment resisting connection was not studied in detail and most of the literature either ignored or assumed simplified distribution of residual stresses.

An experimental study on welded unreinforced flange bolted web (WUF-B) connections demonstrated the influence of welding sequence on the fatigue failure of the connections which was presented in Chapter 4. It was observed that different welding sequences induced different strain responses of the connections. In addition, a phenomenon called strain ratcheting was observed in these experiments near the weld toe, which can lead to crack

initiation. However, residual stress measurements could not be made in experiments, and hence, the residual stress influence on the fatigue crack initiation could not be studied. Hence, knowledge on WSMCs is required to understand the influence of residual stresses and welding sequence on the fatigue response of the connections. In this study, a detailed 3D finite element investigation was performed on welded steel moment connection considering the effect of both initial (residual stresses due to uneven cooling of hot-rolled W shapes) and welding induced residual stresses. The external sub-assembly of beam-column connection discussed in Chapter 4 was simulated in ANSYS to understand the local and global response of the connection under constant amplitude loading with the presence of initial and welding induced residual stresses. Advanced numerical schemes were developed to simulate welding process, and hence the residual stress and subsequent fatigue responses of welded joints. In welding process simulation, sequentially coupled, nonlinear, transient, thermo-mechanical analyses were employed to calculate temperature history and residual stresses. Finally, the fatigue responses of welded joints with the initial and welding residual stress fields were simulated by prescribing displacement controlled cyclic loading. At the end, post weld heat treatment technique was implemented to improve the fatigue resistance of the connections by reducing the residual stresses.

2. Numerical Scheme for Weld Residual Stress Simulation

The thermo-physical and thermo-mechanical processes associated with weld residual stress evolution during welding are extremely complex. Currently, no model is available to realistically account for the arc physics, the weld pool phenomena, and finally, the deformation and heat conduction in the solid metal [47]. In this study, the welding process was simulated by employing sequentially coupled, nonlinear, transient, thermo-mechanical analyses to calculate temperature history and subsequently the welding induced residual stresses. First a transient thermal analysis was performed during which temperature history in the connection from the heat input of the successive build-up of the welding passes was determined. The temperature field at each time step was then used as an input into a transient thermo-mechanical analysis for evaluating the residual stress and strain field in welded

joints. This analysis scheme was sequentially integrated to analysis of initial residual stress in the wide flange beam of the WUF-W connection [48]. Finally, the cyclic loading responses of welded joints with the residual stress fields were simulated by prescribing displacement controlled cyclic loading. Figure shows a schematic of the sequentially coupled thermo-mechanical analysis steps performed in this study.

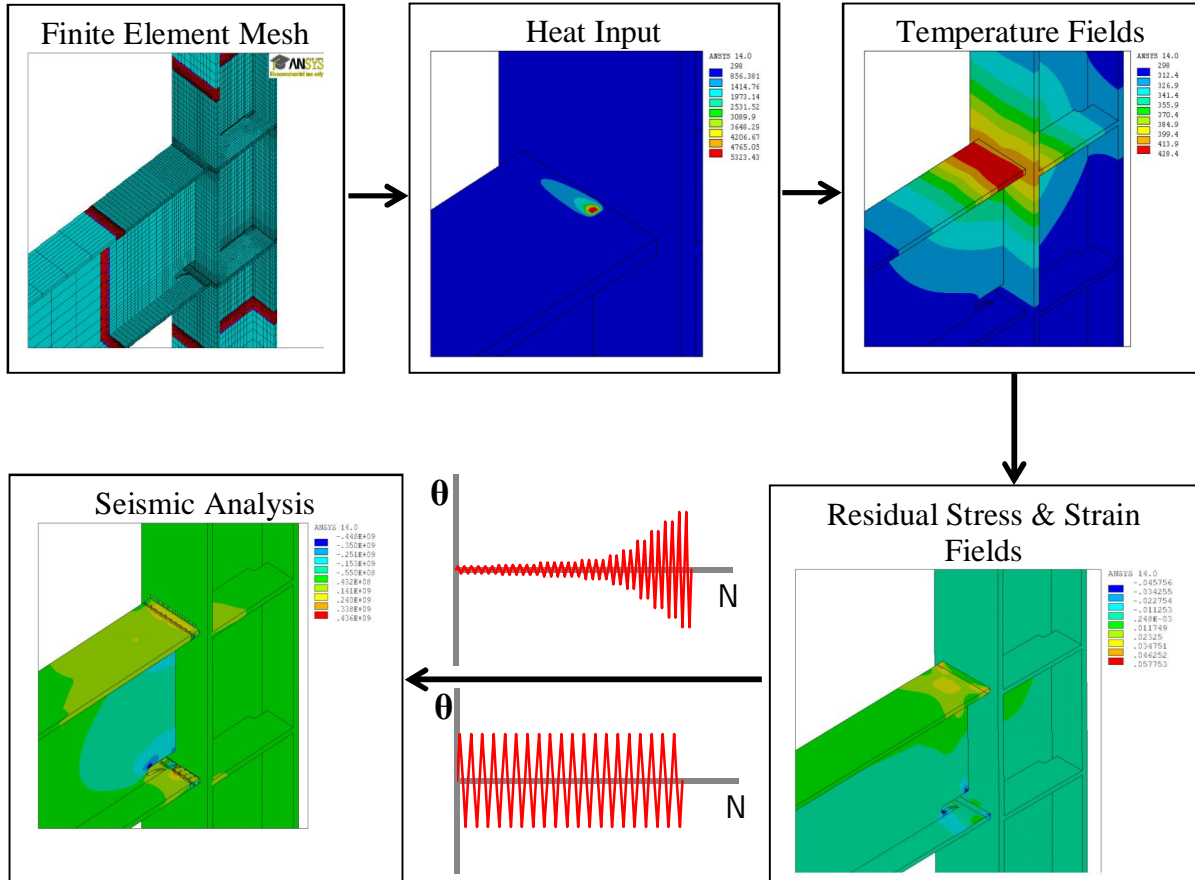


Figure 1 Steps performed in the thermo-mechanical analysis of WUF-W connection.

In order to study the development of weld residual stresses and its influence on the seismic response of moment resisting connections, advanced 3D numerical schemes were developed with finite element (FE) program ANSYS to simulate welding process, and hence the residual stress and subsequent fatigue response of WSMCs. 3D FE models of the exterior

sub-assembly of the WUF-B connections presented in Chapter 4 were simulated, where a single W18×55 ASTM A992 beam was attached to a W14×74 ASTM A992 column. However, in the experiments, the beam web was connected to column flange through bolted shear tab, whereas in the simulation, the web was assumed welded to the column flange which is the conventional WUF-W (welded unreinforced flange welded web) connection. Since the main focus of this study was to study the development and influence of weld residual stresses in the weld toe region of the connection, it was thought to be sufficient to investigate WUF-W connection instead of WUF-B connection to avoid the complicated contact geometries of the bolted web connection.

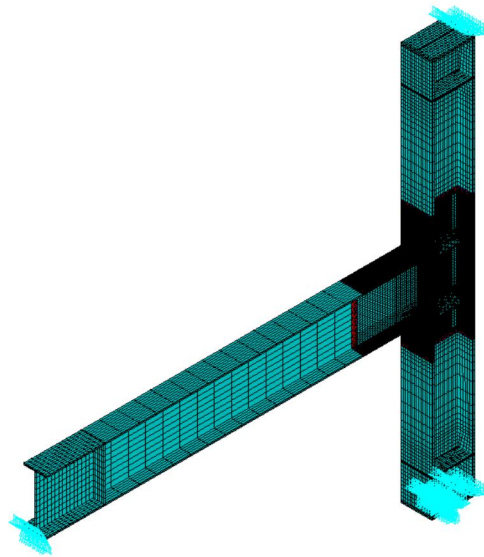


Figure 2 Finite element mesh of WUF-W connection used in the study.

Nevertheless, the weld access hole geometry and boundary conditions of the connections were simulated exactly to mimic the experimental setup. The connection region was discretized by using twenty noded solid elements with very fine mesh in order to capture the behavior of the connection region precisely since most of the inelastic actions occur in the connection region. Whereas the other parts of the connection which are expected to remain

elastic was discretized with eight noded solid elements with coarse mesh in order to reduce the computational time and complexity. Figure 2 shows the FE mesh generated for the analysis of the connection with the imposed boundary conditions. The bottom part of the column was supported by a hinge whereas the top part of the column was supported by a roller to represent the theoretical inflection points of a column in a typical floor system and the free end of the beam was supported on a roller. No constraint was applied near the connection region.

3. Thermal Analysis

Thermal analysis was performed in order to calculate transient temperature distribution from the welding sequence and subsequent cooling. In thermal finite element analysis, heat loss occurred from the material surface through both convection and radiation, which were determined using the heat transfer coefficient in Fourier heat transfer equation [49]. The temperature-dependent material properties (specific heat c_p , thermal conductivity k , enthalpy, heat transfer coefficient h) of structural steel used in the heat transfer analysis are shown in Figure 3, where the material parameters were defined as a function of temperature. Latent heat/phase transformation was accounted for by defining enthalpy of the material as a function of temperature [52-53].

The principal parameter of the welding heat source for the temperature field is heat flow Q (Joule/sec), which can be expressed as [52]:

$$Q = \eta UI \quad (1)$$

where,

η – arc efficiency, which account for radiative and other losses from the arc to the ambient environment and its value ranges between 0 and 1

U – arc voltage (in Volt)

I – arc current (in Amp)

The equivalent heat input can be assumed as the combination of both surface and body heat flux components [53]. Hence the total heat input

$$Q = Q_s + Q_b \quad (2)$$

where Q_s and Q_b indicate heat contents resulting from a specific surface heat flux and body heat flux, respectively.

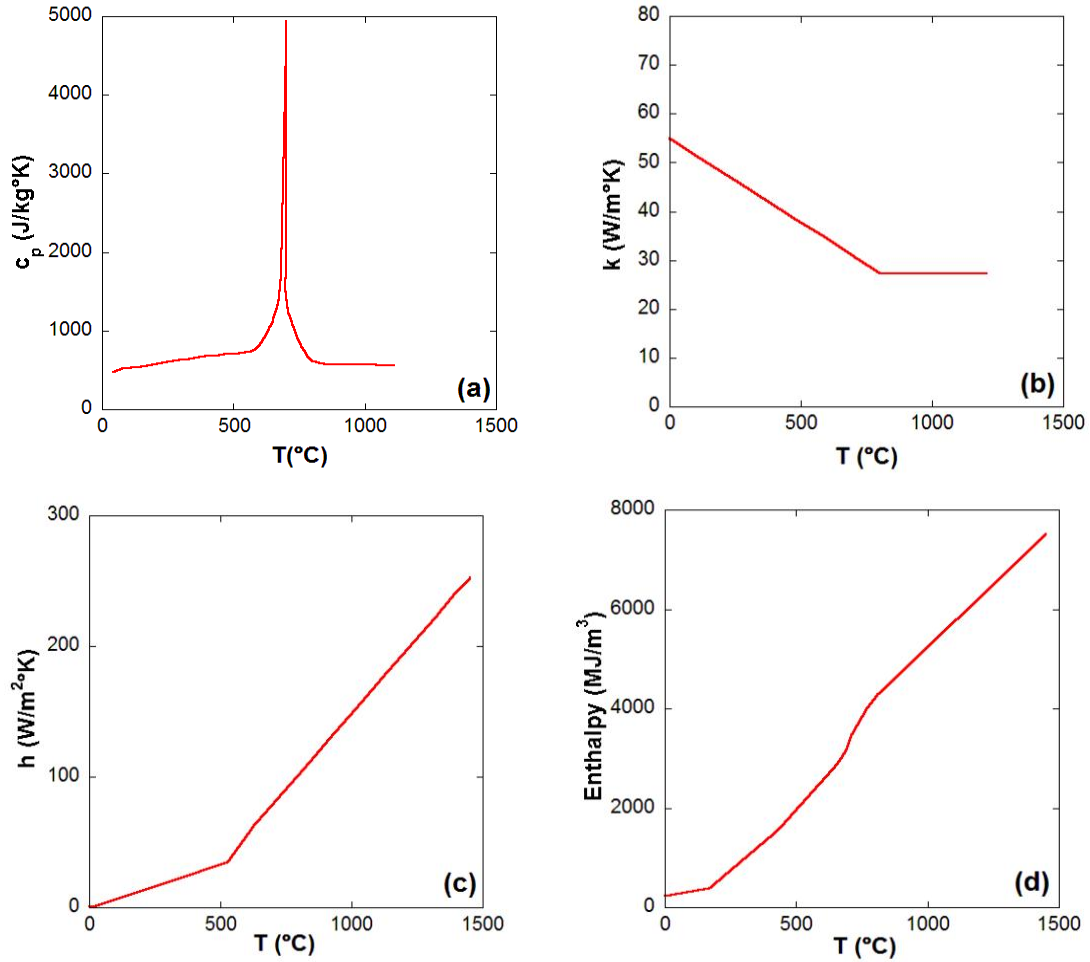


Figure 3 Material coefficients of structural steel as a function of temperature used in thermal analysis. (a) Specific heat [54], (b) thermal conductivity [54], (c) heat transfer coefficient [19], (d) enthalpy [33].

The specific surface heat flux (area-specific heat flow density) q_s and specific body heat flux (volume-specific heat flow density) q_b can be expressed by,

$$q_s = \frac{Q_s}{S} \tag{3}$$

$$q_b = \frac{Q_b}{V} \quad (4)$$

where, S is the surface area, and V is the volume of each element.

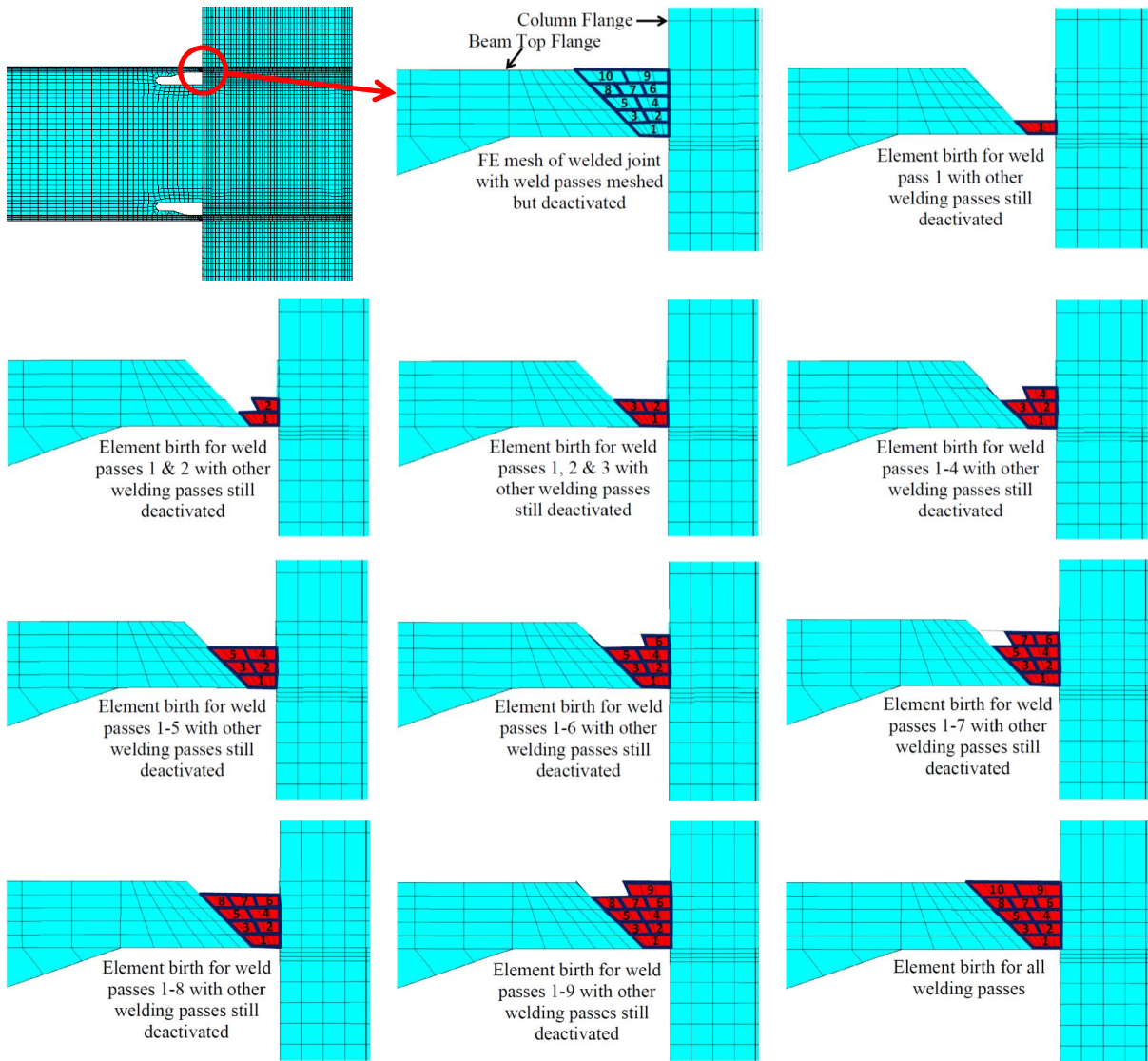


Figure 4 Element birth and death technique in the FE simulation of welding process.

In order to simulate the multi-pass welding process, one needs to model the addition of filler material as new weld passes are deposited and the geometry of the welded joint is built-up. This was done through the element birth/death technique in ANSYS. The steps of using

this technique are depicted in Figure 4 for the beam-column welded joint of a WUF-W connection. With this technique, a finite element mesh of the welded joint including the weld beads is generated first. Subsequently, the element groups representing each weld pass are deactivated (element death) before welding is included in the analysis. These elements are reactivated (element birth) sequentially as the welding arc (heat source) advances along the beam flange width direction. An example of the moving temperature field during the last welding pass of the beam top flange groove weld for a welded steel moment connection is demonstrated in Figure 5, where it can be seen that the high temperature field moves with the welding arc (Figure 5a-e). The distribution of the temperature after cooling of the weld pass is shown in Figure 5f. In the finite element simulation, it was assumed that the top and bottom beam flange welds were made using the Shielded Metal Arc Welding (SMAW) process and E70T welding electrodes as used in the experiments.

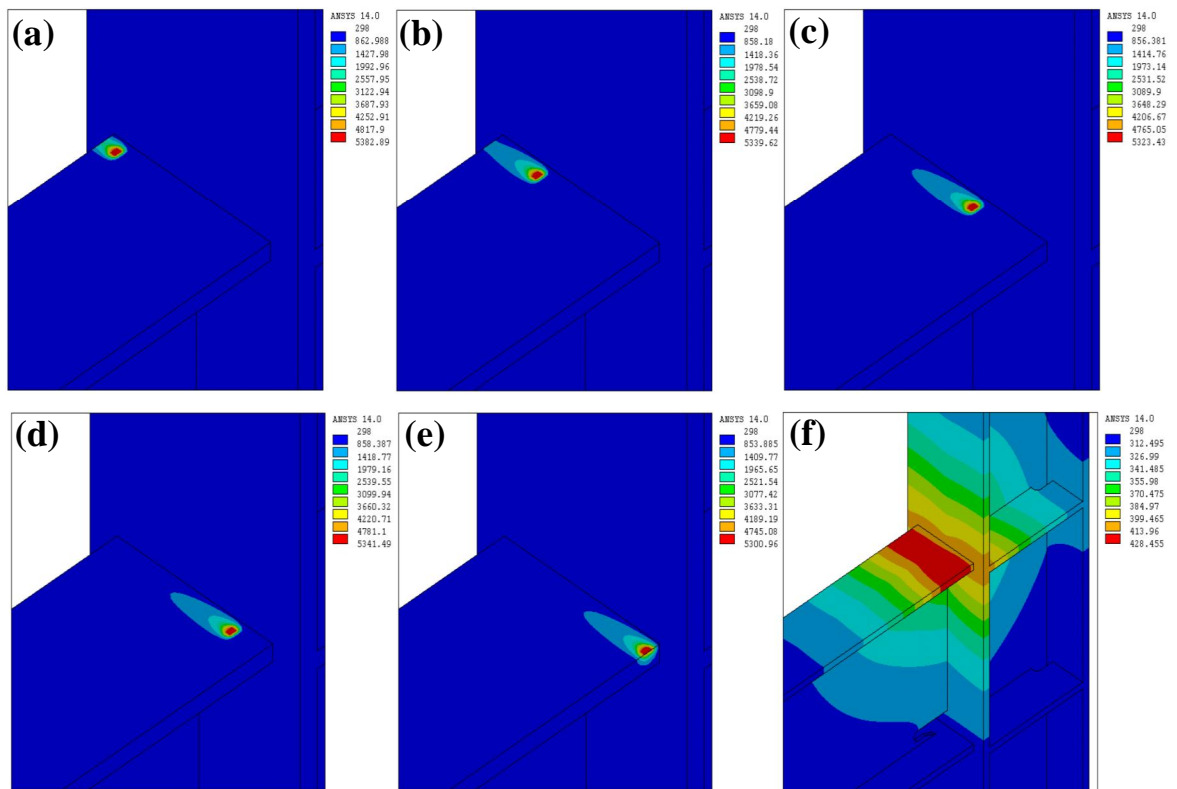


Figure 5 Illustration of moving temperature (in Kelvin) field during the final welding pass in the top flange of a welded steel moment connection (a-e) and cooling (f).

While welding the beam bottom flange to the column flange the web of the beam hinders the completion of a single pass across the width of the beam. Whereas the beam top flange does not have any obstacle like the bottom beam flange. Therefore, weld is not uniform in the bottom beam flange when compared to the top flange. Further, the start and stop points in the bottom flange weld may cause discontinuities or higher residual stresses that may lead to low-cycle fatigue failure of the connection. In order to investigate the development of residual stresses due to welding, and the effect of welding sequence on the residual stress distribution as well as on the low-cycle fatigue response of WSMCs, two specimens of WUF-W connection (namely MC1 and MC2) were considered in the finite element analysis, where each specimen had different weld sequence at the beam bottom flange, whereas beam top flange was welded in a similar fashion for both the specimens. The welding details of the two specimens are shown in Figure 6 and Figure 7.

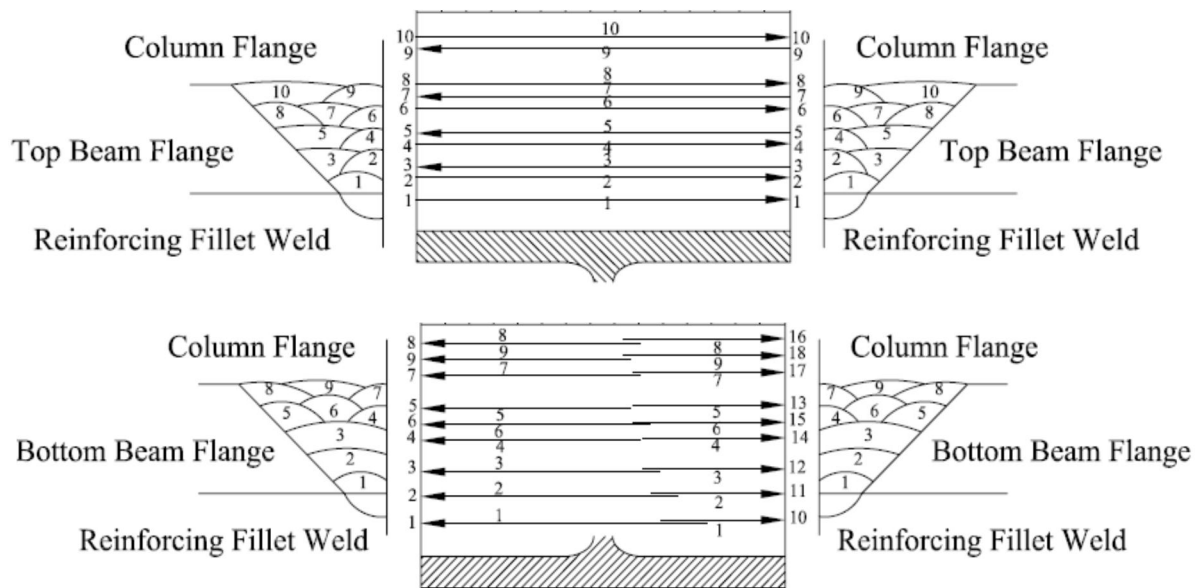


Figure 6 Sketch of weld sequences in beam top and bottom flanges for specimen MC1 showing number of welding passes in order of completion.

These two specimens were used in the experimental investigation presented in Chapter 4 and were denoted by MC1 and MC2. The welding sequences used at the beam bottom flange

of specimens MC1 and MC2 were denoted by weld sequence A and weld sequence B respectively. As can be observed from Figure 6 and Figure 7, the top flange welds were deposited in a similar fashion for both the specimens, only the number of beads and the size of the beads were different. On the other hand, the bottom beam flange welds were laid in a completely different manner for the two specimens. In welding sequence A (specimen MC1), the welder fills the groove with all the welding beads on one side of the beam web before he switches to the other side of the beam web to complete the weld (Figure 6). This type of welding sequence gives rise to nonuniform temperature gradient across the width of the beam flange. On the contrary, in welding sequence B (specimen MC2), the welder alternates sides of the beam web after placing each weld bead (Figure 7). This sequence fills the groove more uniformly compared to sequence A.

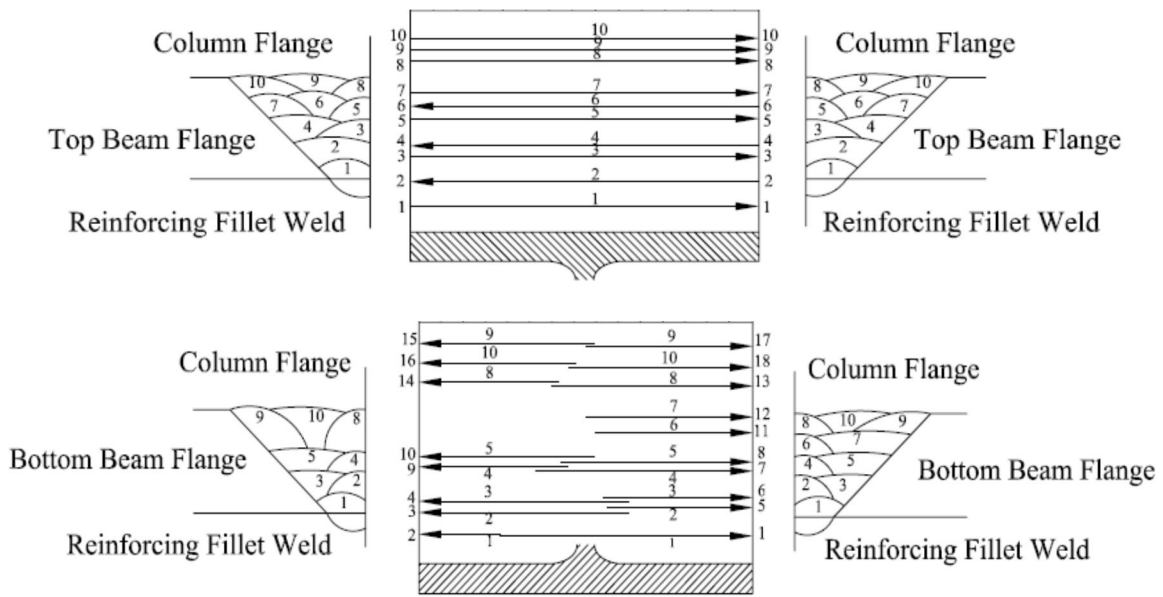


Figure 7 Sketch of weld sequences in beam top and bottom flanges for specimen MC2 showing number of welding passes in order of completion.

All the welding sequences in beam top and bottom flange for specimens MC1 and MC2 were simulated accordingly in the finite element analysis by using the element birth and

death technique. Figure 8 shows comparison between the measured and simulated temperature profiles during the welding process for both the specimens at the top flange of the beam measured at a distance of 75 mm away from the weld toe and 50 mm away from the edge of the beam flange. It was observed that the simulated responses resembled the experimental temperature profiles closely for both the specimens. This validates the thermal finite element model and it indicates that the element birth-death technique can simulate the welding process well.

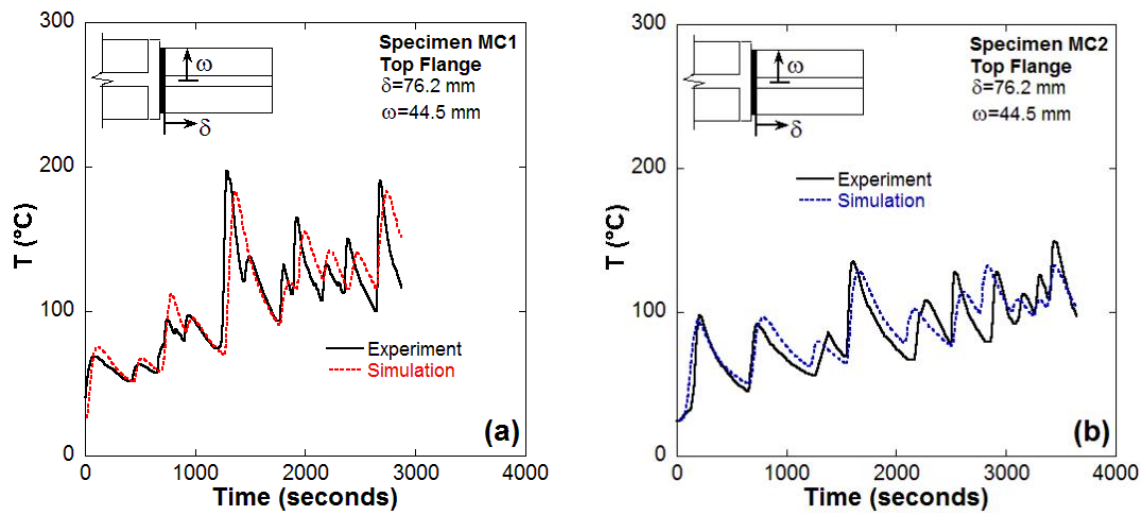


Figure 8 Measured and simulated temperature profiles at the beam top flange for the two specimens. (a) Specimen MC1, (b) specimen MC2.

When temperature profiles of the two specimens were compared it was interesting to note that the temperature profiles were different for different welding sequences for both the top and bottom flanges measured at the same location. Although the top flange welds were laid in a similar fashion for both the specimens, the temperature profiles varied (Figure 9a) as a consequence of difference in the number of beads and bead sizes. However, in both the cases, the mean temperature showed an increasing trend with time, and specimen MC1 produced higher mean temperature than specimen MC2. On the other hand, the temperature profiles for the bottom beam flange showed significant difference for the two welding sequences. As

anticipated, for welding sequence A in specimen MC1, the average temperature on one side of the beam, where the groove was filled first, was higher than the average temperature on opposite side of the beam, where welding was done later, whereas for welding sequence B in specimen MC2 the average temperatures were similar on both sides of the beam web (Figure 9b). The contour plots in Figure 10 and Figure 11 show the temperature distribution in the bottom flange of the beam during the first two welding passes for weld sequences A and B respectively.

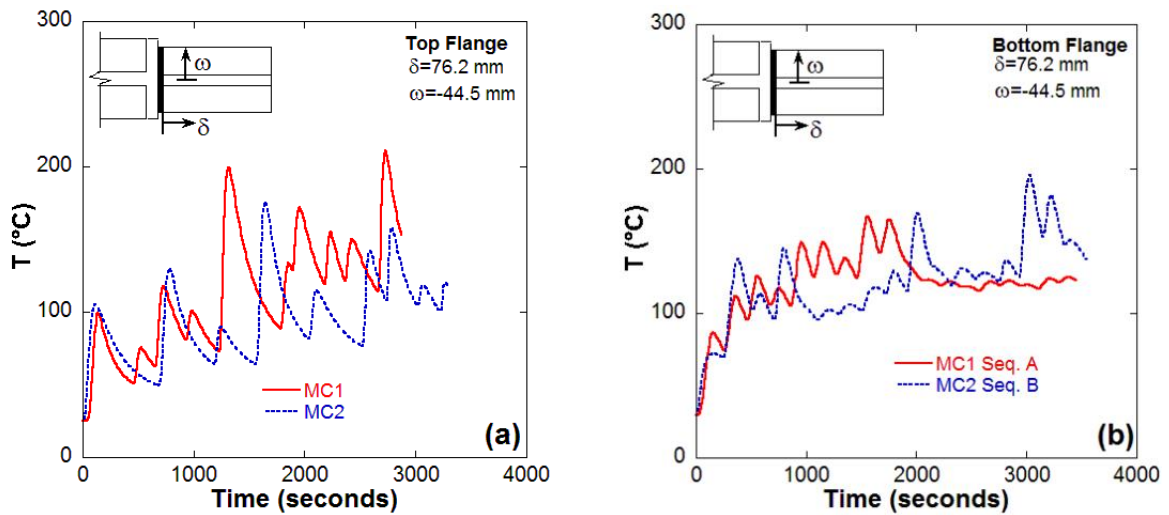


Figure 9 Simulated temperature profiles at the top and bottom flange of the beam showing variation for two different welding sequences. (a) Top flange, (b) bottom flange.

It is clearly seen that the two welding passes for weld sequence A developed higher temperatures only on one side of the beam bottom flange since both the passes were completed only on one side of the beam (Figure 10) and hence, the temperatures were distributed nonuniformly across the beam flange. On the contrary, the two passes for weld sequence B were completed on the two sides of the beam bottom flange by switching sides once one pass is completed (Figure 11), and hence, weld sequence B generated an even distribution of temperature across the beam flange.

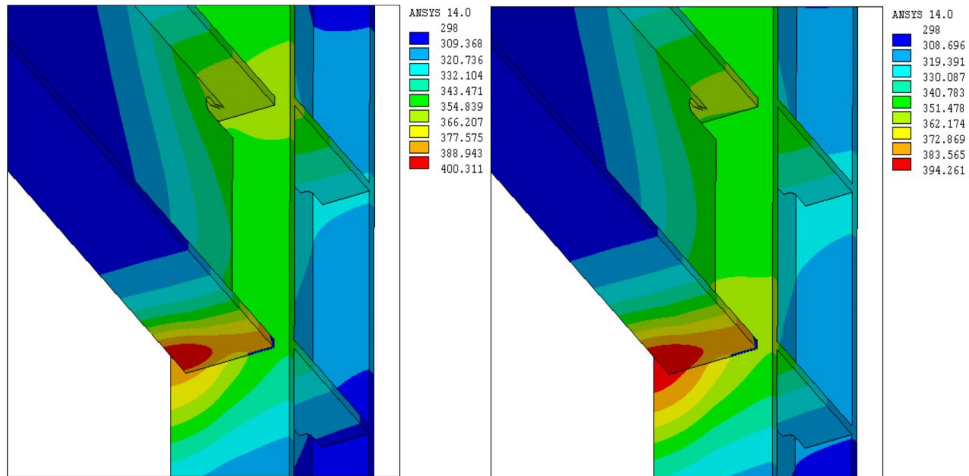


Figure 10 Temperature distribution (in Kelvin) at the end of weld passes 1 and 2 of welding sequence A at the beam bottom flange of specimen MC1 showing nonuniform temperature on both sides of the beam web.

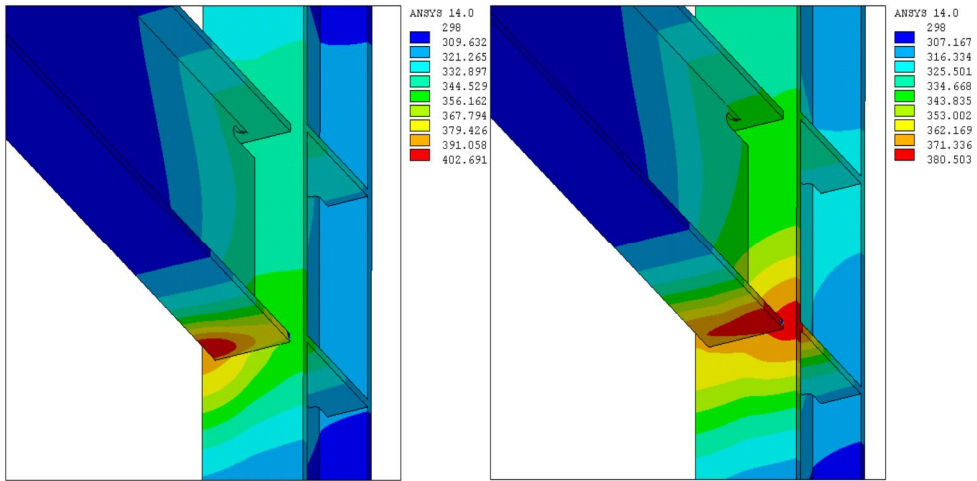


Figure 11 Temperature distribution (in Kelvin) at the end of weld passes 1 and 2 of welding sequence B at the beam bottom flange of specimen MC2 showing uniform temperature on both sides of the beam web.

4. Residual Stress Analysis

The residual stress analysis was conducted after the thermal analysis was finished and the time dependent temperature field during the welding process was determined. The temperature solution obtained from the thermal analysis, which normally depends on position and time, was read into the stress analysis as a predefined field i.e. the nodal temperature field at each time step from the thermal analysis was applied as thermal load to the corresponding node in the structural model. As a result, the node labels for the structural mesh must match those from the heat transfer mesh. Similar to the thermal analysis, element birth/death was used in the residual stress analysis. Once the real time temperature fields were fed into the structural model for each of the nodes at each time step, then residual stresses were calculated based on the temperature dependent material properties of structural steel and relevant constitutive equations. The material properties used for the residual stress analysis in finite element simulation were density ρ , initial yield stress σ_0 , elastic modulus E , Poisson's ratio ν and thermal expansion coefficient α for structural steel as shown in Figure 12b,c and Figure 13. The elevated temperature stress-strain response of ASTM A992 steel under monotonic tension loading was obtained from Hu *et al.* [56] as shown in Figure 12a. The initial yield stress and elastic modulus of ASTM A992 steel obtained from these experiments are plotted separately in Figure 12b and Figure 12c along with comparison with AISC [57] and Eurocode 3 [54] prescribed values. The elevated temperature stress-strain response of ASTM A992 steel was implemented in the finite element simulation by using bilinear kinematic hardening model available in ANSYS which incorporates von-Mises yield criterion and associative flow rule. The bilinear kinematic hardening model was chosen to reduce the complexity of the model and computational time and cost. The bilinear kinematic hardening model parameters were obtained through fitting the stress-strain response of A992 steel as shown in Figure 12a. Note that there was no material data available for the temperature range 900-1400°C, for which linear interpolation method was used to obtain the model parameters.

During welding, the base material is exposed to high temperatures which will induce microstructural changes in the material leading to change in the material properties. The

region which exhibits microstructural change due to high temperature exposure is referred to as the heat affected zone (HAZ). Studies on stainless steel SS304 by Johnson and Ramirez [60] showed five different microstructures depending on the temperature levels experienced by the base metal during welding.

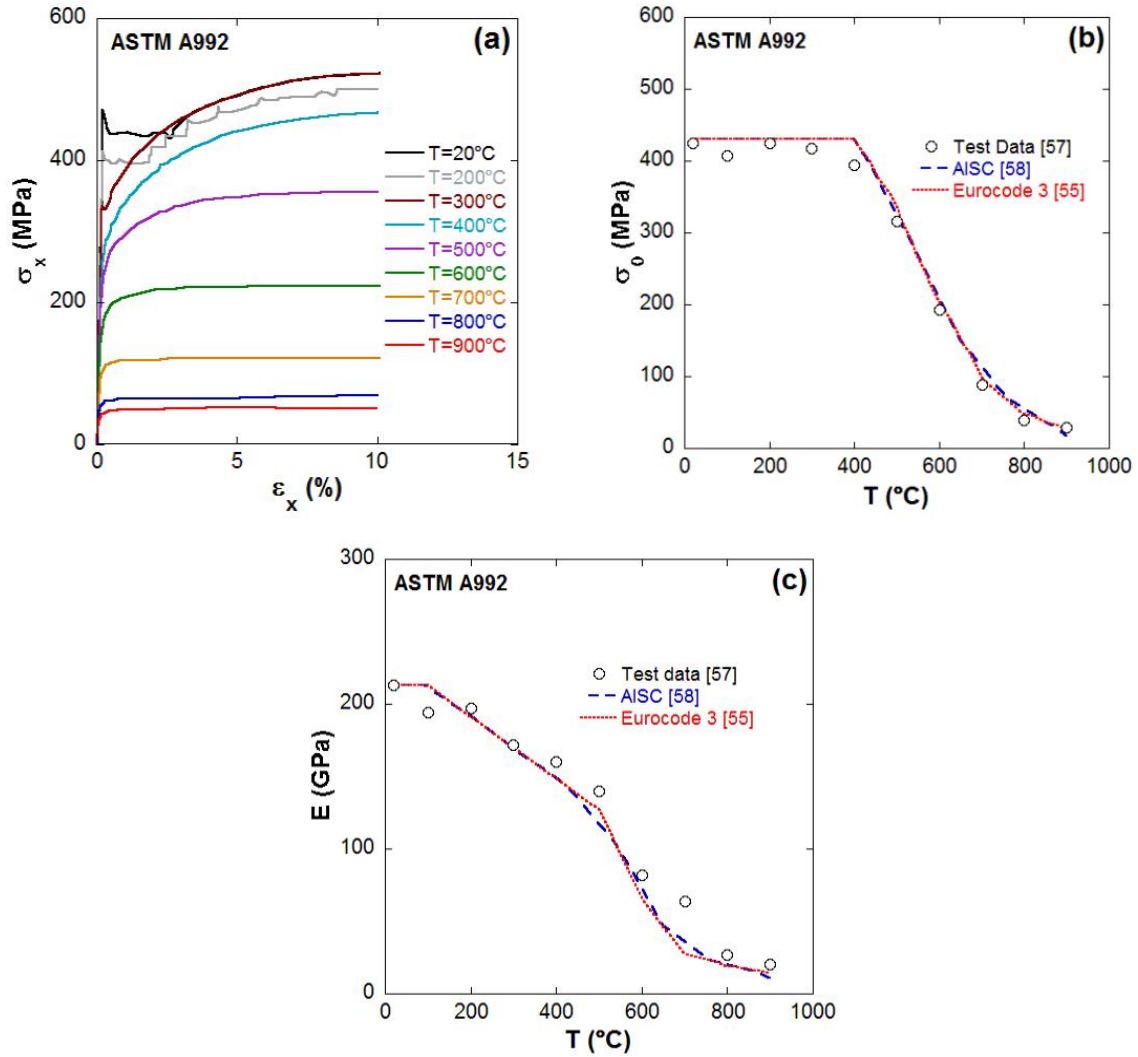


Figure 12 Monotonic tension test response of ASTM A992 steel at different temperatures [56]. (a) Monotonic stress-strain response, (b) initial yield stress plotted as a function of temperature, (c) elastic modulus plotted against temperature.

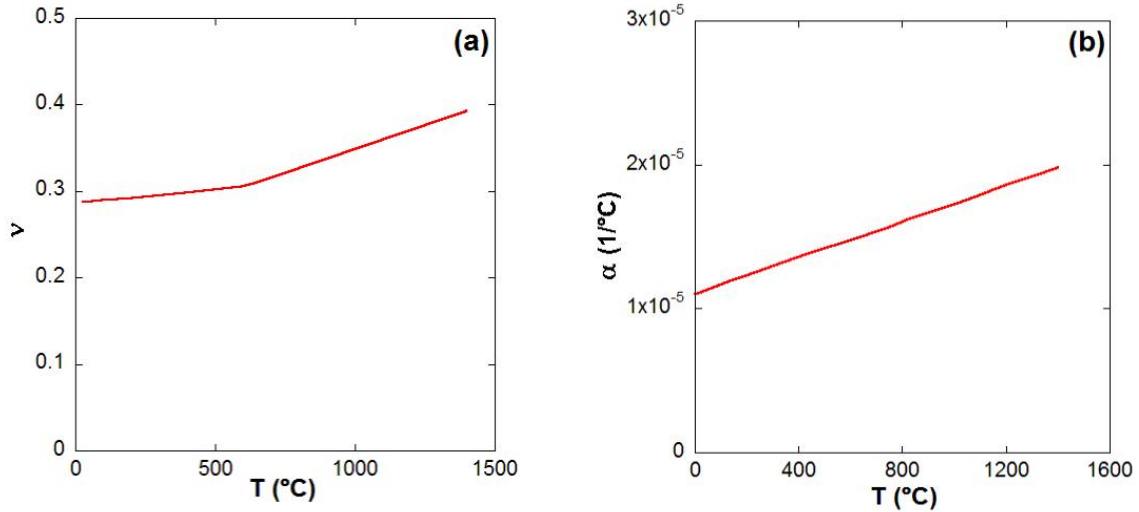


Figure 13 (a) Poisson's ratio [58] and (b) thermal expansion coefficient of structural steel plotted as a function of temperature [59].

These are referred to as course grained HAZ (1100°C and above), fine grained HAZ (875°C-1100°C), intercritical HAZ (700°C-875°C), subcritical HAZ (575°C-700°C) and the base metal is unaffected below 575°C. To properly simulate the welding induced residual stresses, it is required to account for the heterogeneity in the material properties in the HAZ [29]. To determine the material properties of ASTM A992 steel for the five HAZ discussed above, monotonic tension tests were performed on steel coupons [61]. The coupons were conditioned at different peak temperatures; hold the peak temperature for 15 minutes followed by slow air cooling until it reaches room temperature. The stress-strain response of one set of monotonic tension tests is shown in Figure 14a. It was observed that as the maximum temperature increased both the yield and ultimate stresses of the steel gradually decreased by downward shift of the stress-strain curves. The reduction in yield stress with maximum temperature of 1200°C is about 40%. The response from the monotonic tension tests demonstrated that the yield stress of ASTM A992 decreased with increasing temperature, and upon removal of the temperature the yield stress never went back to the room temperature value, rather it reduced from that of the room temperature value. The yield stress values of unconditioned ASTM A992 coupons tested at different temperatures up to

900°C was obtained from Hu *et al.* [56] as shown in Figure 12a. However, for steel coupons conditioned at different high temperatures, no stress-strain data was available for higher temperatures. Hence, least square method was adopted to establish a relationship between temperature and yield stress (solid line in Figure 14b) using the data from Hu *et al.* [56] for unconditioned A992 steel (solid circles in Figure 14b).

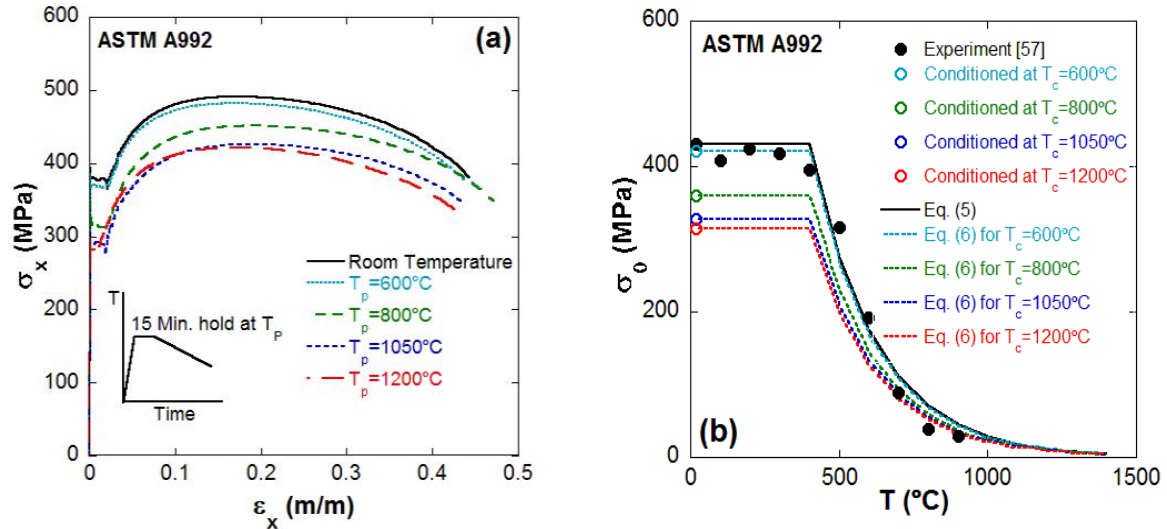


Figure 14 (a) Stress-strain response of ASTM A992 coupons conditioned at different peak temperatures [61], (b) temperature dependent yield stress of ASTM A992 for five temperature levels to account for the material heterogeneity.

The relation can be expressed as follows:

$$\left. \begin{aligned} \sigma_0(T) &= \sigma_{0_{RT}} && \text{for } T \geq 400^\circ\text{C} \\ \sigma_0(T) &= \sigma_{0_{RT}} e^{-c_0(T-400)} && \text{for } T > 400^\circ\text{C} \end{aligned} \right\} \quad (5)$$

where, $\sigma_{0_{RT}}$ is the yield stress for unconditioned A992 steel at room temperature (MPa), $c_0 = 0.0045$ is determined by the least-square fit, and T is the current temperature ($^\circ\text{C}$). Eq. (5) was modified for conditioned A992 steel using the yield stress reduction factor from Figure 14a and assuming that the evolution of the yield stress during cooling for different conditioning temperature follow the same trend as the unconditioned case. The modification

of Eq. (5) led to the following generalized expression of yield stress as a function of current and conditioning temperatures:

$$\left. \begin{aligned} \sigma_0(T) &= \sigma_{0_{RT}} && \text{for } T \geq 400^\circ\text{C} \\ \sigma_i(T, T_c) &= \sigma_{0_{RT}} \left[1 - \left(\frac{T_c - 25}{1650} \right)^2 \right]^{\frac{1}{2}} e^{-c_i(T-400)} && \text{for } T > 400^\circ\text{C} \end{aligned} \right\} \quad (6)$$

where $c_i = \frac{\ln \left[\frac{e^{-0.0045(T_c-25)}}{\left(1 - \left(\frac{T_c - 25}{1650} \right)^2 \right)^{\frac{1}{2}}} \right]}{25 - T_c}$, T_c is conditioning temperature ($^\circ\text{C}$).

Five sets of temperature-dependent material properties were defined depending on the temperature level to incorporate the material heterogeneity in the finite element modeling of residual stresses as shown in Figure 14b, where solid circles represent test data for unconditioned A992 steel [56], the open circles represent yield stresses for conditioned A992 steel at different temperatures from the experiments [61], the solid line represents the model fit by using least squares for unconditioned case, whereas dashed lines represent the model fit assumed for conditioned cases.

Initially, finite element analysis was performed considering only the welding induced residual stresses. The residual stress distributions in longitudinal and transverse directions for specimens MC1 and MC2 are shown in Figure 15 and Figure 16, respectively. It is evident that significant amount of residual stresses developed close to the welded region of the connection both in longitudinal and transverse direction. The magnitude of the residual stresses at several locations near the weld toe were very close to the yield stress of the base metal, and around the weld access hole the residual stresses were higher than the yield stress. The residual stresses in the longitudinal direction were higher at the weld toe and weld access hole, and it gradually decreased as the distance from the weld toe increased. However, the magnitude of residual stresses in the transverse direction was only high near the welded region, and there were barely any residual stresses away from the weld toe. This is attributed to the severe structural restraint in the welded region which induced higher magnitudes of

transverse residual stresses, and away from the welded region, there was not much restraint to induce transverse residual stresses.

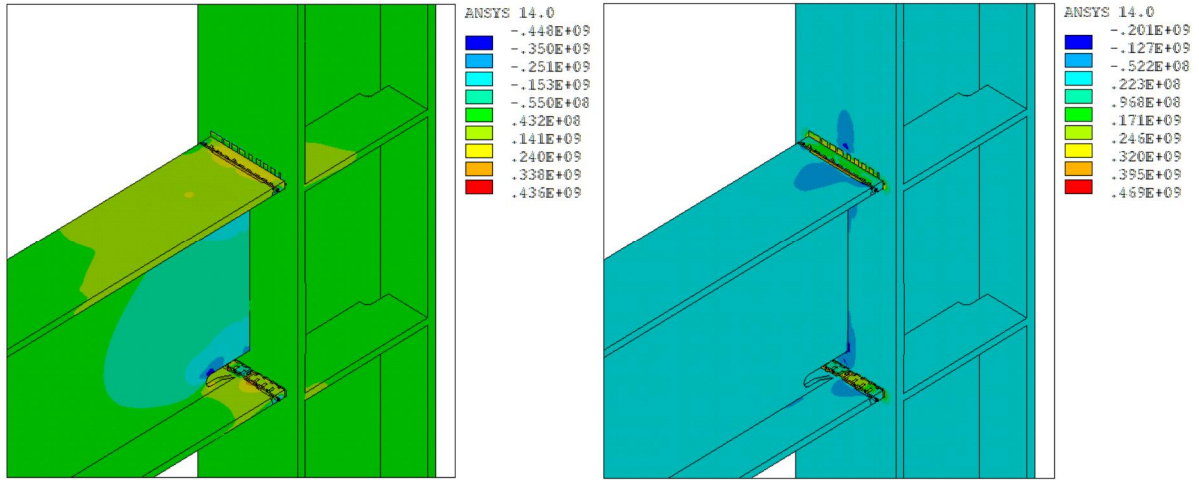


Figure 15 Residual stress distribution (in Pa) for specimen MC1. (a) Longitudinal direction, (b) transverse direction.

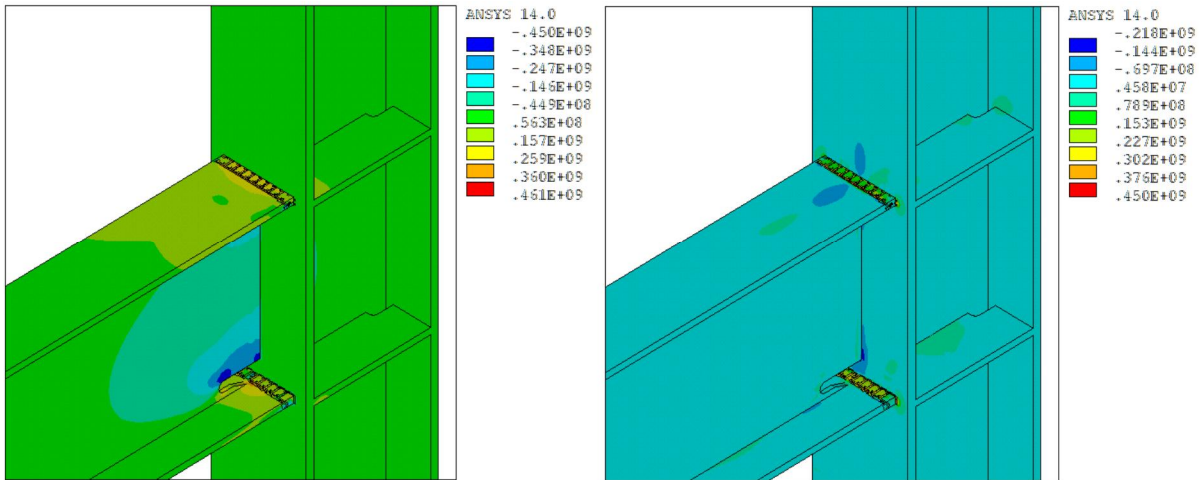


Figure 16 Residual stress distribution (in Pa) for specimen MC2. (a) Longitudinal direction, (b) transverse direction.

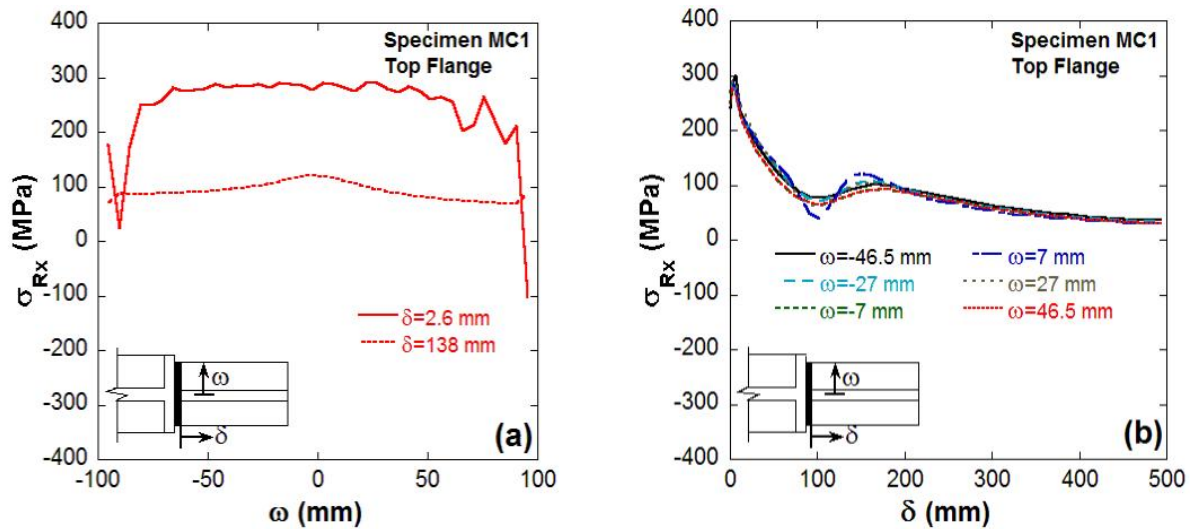


Figure 17 Welding induced residual stress distribution in the beam top flange of specimen MC1. (a) Across width, (b) across length.

Nevertheless, for seismic response of moment resisting connections, the longitudinal direction is of particular interest, and hence, the further discussion on the residual stresses will be addressed only for the longitudinal direction. The longitudinal residual stress distribution across the width and length of beam top and bottom flanges are presented in Figure 17 through Figure 20. It was observed that significant amount of residual stresses developed very close to the weld toe of the beam-column joints for both top and bottom beam flanges. The peak stresses were around 300 MPa on both the top and bottom flanges, which were about two-thirds of the yield stress of A992 steel. For top flange, the residual stresses were tensile and almost constant throughout the width of the flange, only at the edges of the flange compressive residual stresses developed. The peak residual stress was tensile with 300 MPa value, whereas the compressive stresses varied between 100 to 200 MPa. On the other hand, for bottom flange, significant amount of compressive stresses developed across the width of the beam flange, however at stop and start locations of welding passes tensile residual stresses also developed. The peak compressive stresses were 300 MPa, whereas the tensile stresses varied between 0 to 100 MPa. It is interesting to note that for

both top and bottom flanges, the residual stress values showed a decreasing trend as the distance from the weld toe increased with almost zero values after 200 mm away from the weld toe. Based on the observations from the finite element study, it is evident that very high values of residual stresses develop close to the weld toe and around the weld access hole for both the specimens which may play a significant role under service conditions. Similar type of residual stresses was also observed in the studies on piping joints by Lu [21] and Cheng [29] and it was shown that these residual stresses worked as a driving force for axial strain accumulation near weld toe.

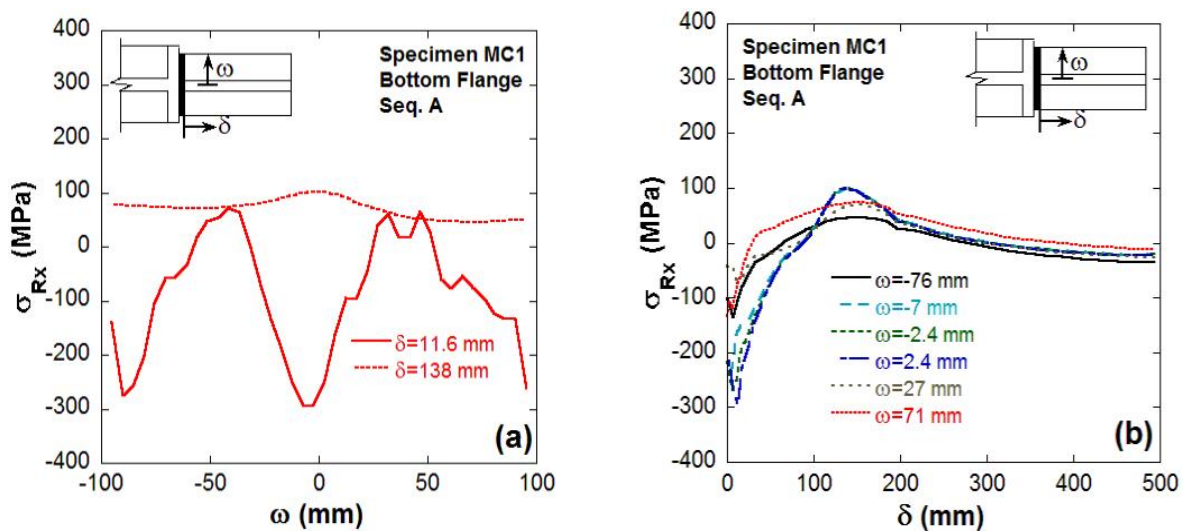


Figure 18 Welding induced residual stress distribution in the beam bottom flange of specimen MC1 for weld sequence A. (a) Across width, (b) across length.

To investigate the influence of the welding sequences on the residual stress distribution, the residual stresses were plotted across the width of the beam flange at the location of peak residual stresses as shown in Figure 21. It was observed that for the top flange, specimen MC1 developed more residual stresses compared to specimen MC2. It is interesting to note that the residual stresses at the beam top flange were almost constant along the width of the flange except at the edges of the flange. This is expected as each of the welding beads in the top flange weld was laid in one pass with no discontinuity during welding. For beam bottom

flange, there were several locations across the width of the beam flange where welding was stopped and restarted, and hence depending on the temperature distribution, the two specimens experienced different amount of residual stresses and distribution across the width of the flange for the two weld sequences A and B. It was observed that welding sequence A developed more residual stresses in the beam bottom flange of specimen MC1 than welding sequence B in specimen MC2 as anticipated. The nonuniform temperature gradient produced in the beam bottom flange during welding sequence A led to the development of higher residual stresses compared to weld sequence B. It was observed that the residual stresses had larger values at the start and stop location of the weld as can be seen from Figure 21b.

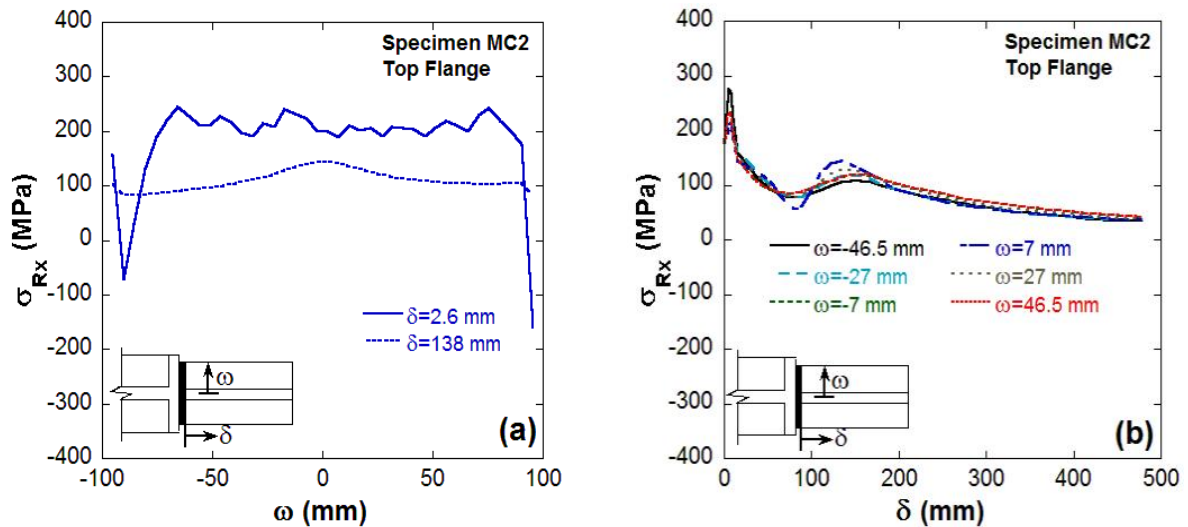


Figure 19 Welding induced residual stress distribution in the beam top flange of specimen MC2. (a) Across width, (b) across length.

The results from the residual stress analysis clearly shows that significant amount of residual stress can be developed from the welding procedure, and the distribution and the peak values of the residual stresses is influenced by the welding sequences employed during welding. No experimental measurements of the residual stresses were available from the experiments and hence, the residual stress values and distribution obtained from the finite element analysis (FEA) could not be validated. However, the results of the analysis

qualitatively demonstrates that residual stresses induced by welding can be as high as two-thirds of the yield stress of the base metal at the weld toe and higher than the yield stress at the weld access hole, and the welding sequence can significantly change the distribution and peak values of the residual stresses.

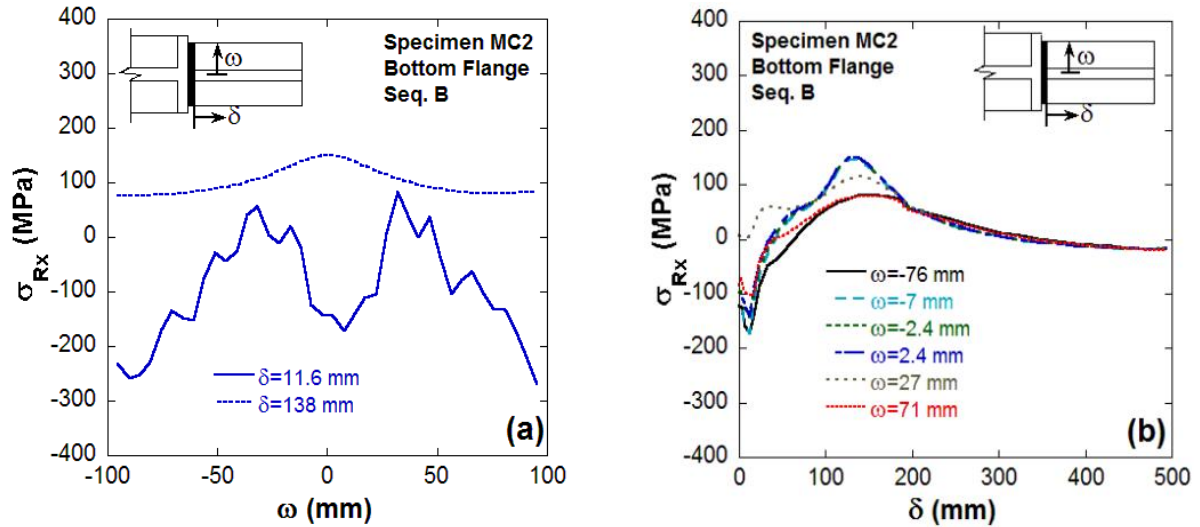


Figure 20 Welding induced residual stress distribution in the beam bottom flange of specimen MC2 for weld sequence B. (a) Across width, (b) across length.

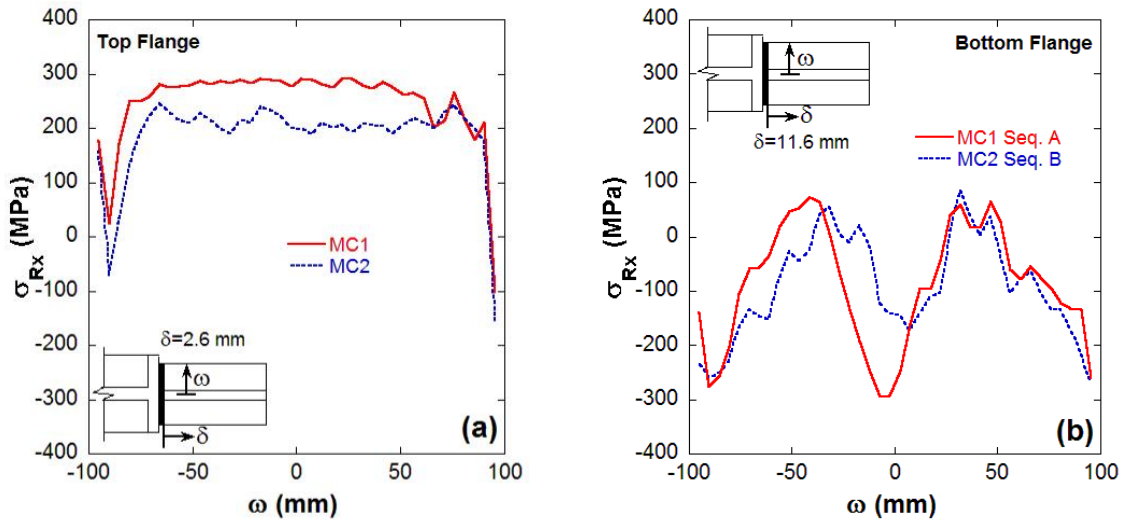


Figure 21 Welding induced residual stress distribution across the width of beam flange near weld toe for the two specimens. (a) Top flange, (b) bottom flange.

5. Influence of Initial Residual Stresses

When a wide flange section is hot-rolled followed by cooling, the final section will have residual stresses. Welding during fabrication further induces residual stresses to the beam-column connection as shown in this study. Studies by Ketter *et al.* [61], Huber [63], Ketter [64], Alpsten [65] showed that the residual stresses during cooling of hot-rolled sections can be as high as one-half of the yield stress. In their study they demonstrated the distribution of residual stresses due to cooling and the mechanism involved in the development of residual stresses have been discussed. In order to determine the residual stresses developed during cooling of hot-rolled wide flange sections (denoted as initial residual stress in this study), an advanced numerical scheme based on a sequentially coupled transient thermo-mechanical analysis was developed in a study by Quayyum and Hassan [48]. In this analysis, a wide flange section was heated up to 1300°C and then air cooled until the section reached the room temperature. The temperature transients obtained from the thermal analysis were then used as input for the residual stress analysis similar to the analysis scheme used in this study. The scheme was used to evaluate the initial residual stresses for a W18×55 beam section, which is the beam section used in the WUF-W connection in this study. It is to be mentioned here that the initial residual stresses were not considered for the column sections since it was observed that the magnitude and distribution of weld induced residual stresses at the weld toe and near the welded region and weld access hole was not altered noticeably by the addition of column initial residual stresses. Hence, in this study column initial residual stresses were not considered to reduce the complexity in the FE model and computational time and cost.

In order to study the influence of initial residual stresses due to uneven cooling of wide flange beam section on the overall distribution of residual stresses after the welding process, the simulated initial residual stresses were incorporated along with the welding induced residual stresses. In the finite element simulation, the initial residual stresses were implemented as the initial state for the welding induced residual stress analysis. Figure 22 shows the residual stress distribution along the length of the beam up to 500 mm for specimen MC1 considering both cases with and without initial residual stresses. After

analyzing the residual stress distribution, it was observed that the inclusion of initial residual stresses did not increase the peak residual stress values close to the weld toe.

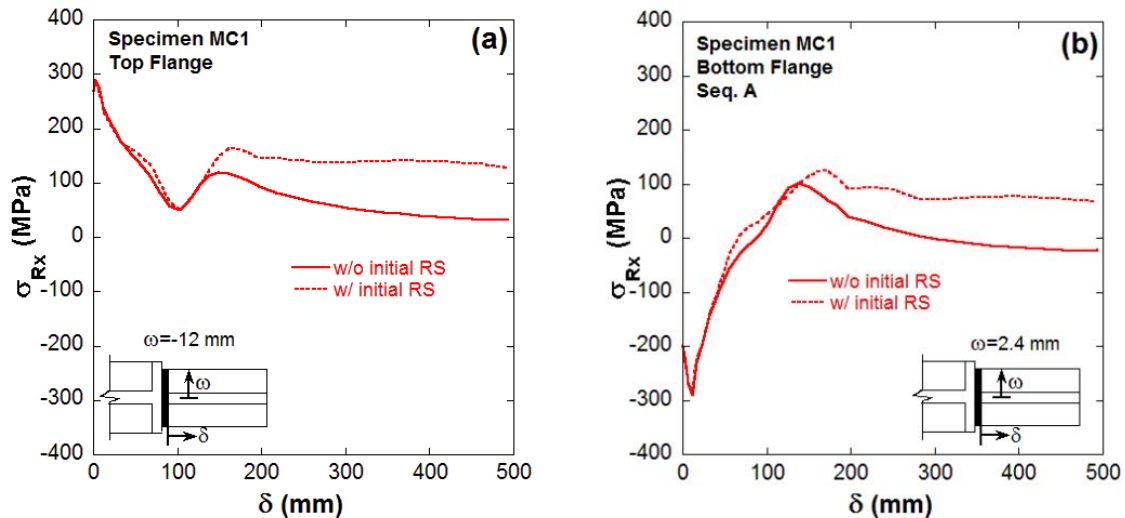


Figure 22 Residual stress distribution along the length of the beam for specimen MC1 showing the influence of initial residual stresses. (a) Beam top flange, (b) beam bottom flange.

The distribution of the residual stresses was not influenced by the initial residual stresses for a length of about 150 mm from the weld toe. This is due to the fact that initial residual stress values were insignificant at the ends of the beam [48]. However, initial residual stresses affected the stress values as the distance from the weld toe increased, especially after a distance of about 150 mm from the weld toe. After 150 mm, the total residual stresses became constant, which was predominantly contributed by the initial residual stresses. Although the initial residual stresses of the beam section did not change the distribution of the overall residual stresses near weld toe, it may not have significant influence on the low-cycle fatigue failure of the connection. However, in this study both the initial residual stresses (for the beam section) and weld residual stresses were considered for investigating the seismic response of the WUF-W connections to represent the actual physics of residual stress development in the connections.

6. Effect of Residual Stresses on the Seismic Performance of WSMCs

Since structural behavior under seismic events is usually characterized by small number of cycles, only a few of which involve large excursions in the plastic range, the failure under such conditions is conventionally referred as low-cycle fatigue failure [66]. Fatigue failure of a structure usually results from localized crack initiation, subsequent crack propagation and final fracture. However, fatigue design methods generally use global approaches. These global approaches are based on nominal stresses on critical cross-sections and corresponding fatigue lives obtained from experiments. The mechanisms of localized fatigue damage accumulation and crack initiation in the presence of residual stresses are not considered in the design approaches. Residual stresses which arise during welding processes are an important factor in fatigue failure of welded structures [28, 30]. In the low-cycle fatigue range, the influence of residual stresses is usually ignored because of the assumption that the residual stresses relax to zero after only a few cycles. The finite element analysis results in this study demonstrated that both tensile and compressive residual stresses in welded joints can be as high as two-thirds of the yield stress at the weld toe and higher than yield stress at the weld access hole. The development of the residual stresses can act as mean stresses to the fatigue loading cycle and thus lead to degradation and failure of structures due to the accumulation of strain. In order to investigate the influence of residual stresses on the seismic response of WSMCs, the finite element models of the WUF-W connections were subjected to seismic type of loading to investigate the localized failure mechanisms in presence of the residual stresses. For the fatigue failure analysis, the constant amplitude loading history used in the experiments presented in Chapter 4 was prescribed in order to make comparisons with the experimental observations.

Traditionally, cyclic tests are carried out with reference to standard procedures such as [68-70] which use loading histories consisting of groups of cycles at increasing amplitudes (Figure 23a). Such loading histories present the advantage of allowing on a single specimen a satisfactory appraisal of the cyclic performance of the component. However, they appear inadequate for the development of cumulative damage models useful not only for the seismic design of new structures but also for the assessment of safety and reliability of damaged

structures and for the development of adequate repair procedures. Hence it has been proposed by various authors both in Europe and U.S. [69, 71-75] to perform tests with cycles at a constant amplitude. Such a procedure presents the advantage of allowing a clear understanding of the damage accumulation process as well as of the key parameters governing it. The constant amplitude loading history used in the analysis is shown in Figure 23b.

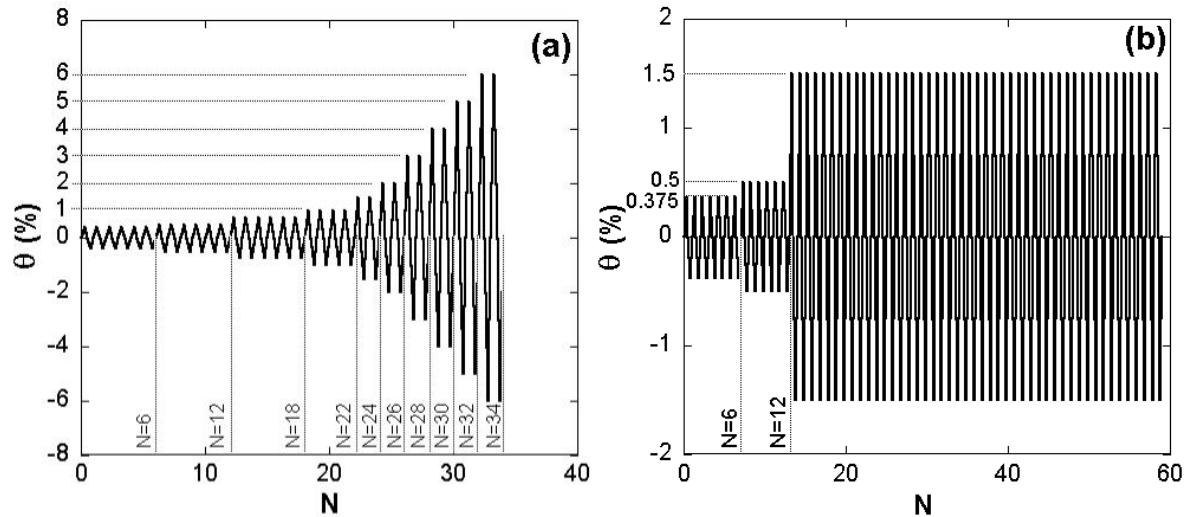


Figure 23 (a) SAC loading protocol [34], (b) non-standard constant amplitude loading history prescribed in this study.

The prediction of experimental responses of moment connections using finite element simulation is highly sensitive to the material models adopted and the parameters of the adopted material models, especially under cyclic loading. In the literature, most of the works related to the finite element modeling and analysis of moment resisting connections used either bilinear or multilinear kinematic hardening material model in the finite element simulation of the cyclic behavior of moment connections. Although both bilinear and multilinear material models obey von-Mises yield criterion and include Bauschinger effect, both the models are incapable of simulating ratcheting or shakedown, which is essential for cyclic response simulation of moment connections. Both multilinear and bilinear material models have a linear kinematic hardening rule and hence, are not sufficient for simulating

ratcheting or shakedown. To simulate ratcheting and shakedown in a FE simulation, a metal plasticity model is required with a nonlinear kinematic hardening rule. Nonlinear kinematic hardening implies a shift (or movement) of the yield surface along a nonlinear path. The Chaboche material model [75], available in ANSYS Mechanical software, offers such a nonlinear kinematic hardening rule. Since this study deals with cyclic response simulation of WUF-W connections, the advanced nonlinear kinematic hardening model of Chaboche [75] has been adopted in this study to define the material characteristics. A brief description of the Chaboche [75] model is given below to demonstrate different features of the model.

The yield criterion:

$$J_2(\underline{\sigma} - \underline{\alpha}) = \left[\frac{3}{2} (\underline{s} - \underline{a}) \cdot (\underline{s} - \underline{a}) \right]^{1/2} = \sigma_0 + R(p, q), \quad (7)$$

where $\underline{\sigma}$ is the stress tensor, $\underline{\alpha}$ is the current center of the yield surface in the total stress space, \underline{s} is the deviatoric stress tensor, \underline{a} is the current yield surface center in the deviatoric space, σ_0 is the initial size of the yield surface, and R represents the isotropic hardening variable as a function of the accumulated plastic strain p and the size of the plastic strain surface q . The rate-independent plastic strain increment will be calculated using the associated flow rule:

$$d\underline{\varepsilon}^p = d\lambda \frac{\partial J_2}{\partial \underline{\sigma}} = \frac{3}{2} dp \frac{\underline{s} - \underline{a}}{\sigma_0 + R} \quad (8)$$

The superimposed kinematic hardening rule is given by:

$$d\underline{a} = \sum_{i=1}^4 d\underline{a}_i \quad (9)$$

$$d\underline{a}_i = \frac{2}{3} C_i d\underline{\varepsilon}^p - \gamma_i \underline{a}_i dp \quad (10)$$

Each of the superposed kinematic hardening rules has a strain hardening term (1st term in Eq. 10) and a dynamic recovery term (2nd term in Eq. 10). These are important modeling features for simulating cyclic responses of materials. Use of Chaboche model to simulate the material responses requires that the stable hysteresis loop of the cyclic stress–strain response be known. In this case, stable hysteresis loops were obtained from single amplitude strain

controlled cyclic test of ASTM A992 steel coupons [30]. Chaboche parameters were determined from the up going strain controlled experiment of ASTM A992 steels. The nonlinear kinematic hardening parameters were determined by using a genetic algorithm based optimization method. Simulations were made at the material level with obtained parameters for validation. As shown in Figure 24, the simulated responses matched very well with the experimental responses obtained from [61]. It is to be noted here that the heterogeneous material models used in the residual stress calculation was not accounted for in the fatigue analysis of the connection. This is attributed to the unavailability of cyclic response data of ASTM A992 steel at different conditioning temperature.

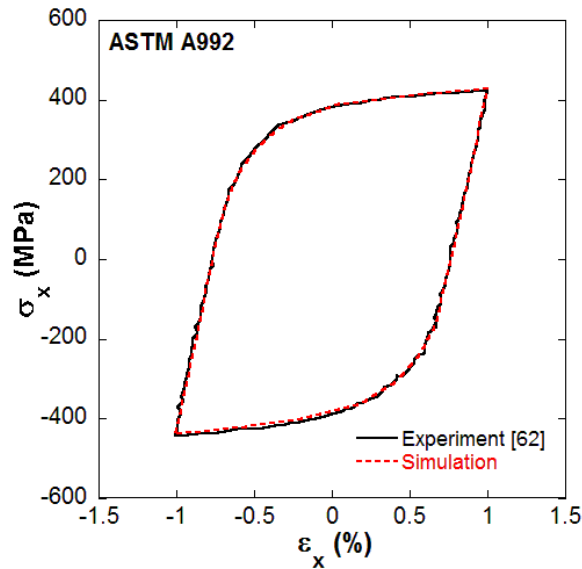


Figure 24 Experimental and simulated response of strain controlled hysteresis loop for ASTM A992 steel with Chaboche parameters.

In the finite element study, firstly, the importance of considering the residual stresses will be discussed by showing comparisons with the experimental results presented in Chapter 4, and later the effect of the welding sequence on the low-cycle fatigue response will be addressed. In the experiments, specimen MC2 showed ductile mode of failure by fracture of

the beam top flange in the mid-way of weld access hole. Visible cracks were observed at the weld toe and around the weld access hole. On the contrary, specimen MC1 showed brittle and sudden failure by rupturing of the beam top flange at a small distance away from the weld toe. No cracks were visible at the weld toe or near weld access hole. However, specimen MC1 showed much lower fatigue life than specimen MC2.

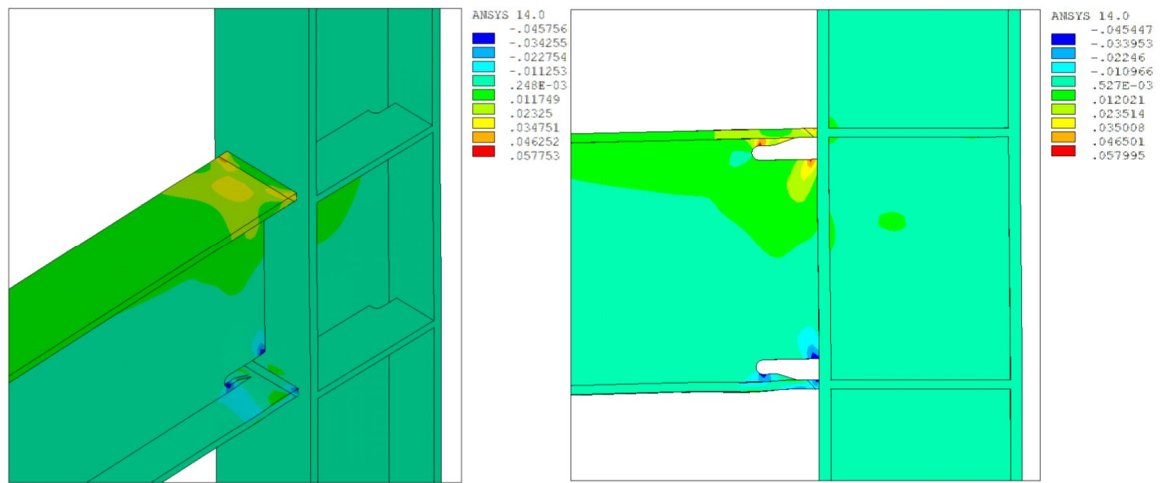


Figure 25 Plastic strain contour in axial direction showing accumulation of strains near weld toe and weld access hole in presence of residual stresses.

Detailed investigation of the experimental results demonstrated accumulation of axial strain (known as ratcheting) at the weld toe, weld access hole and also in the region of top and bottom beam flanges close to the weld toe. Ratcheting is known to be demonstrated by metallic materials under inelastic cyclic loading along the directions of force-controlled loading—steady or fluctuating [24]. Hence, it was anticipated that the occurrence of ratcheting at the welded joint under displacement-controlled loading could be influenced by its residual stresses. Similar to the experimental observations, axial strain accumulation was observed very close to the weld toe and also around the weld access hole in the finite element simulation (Figure 25).

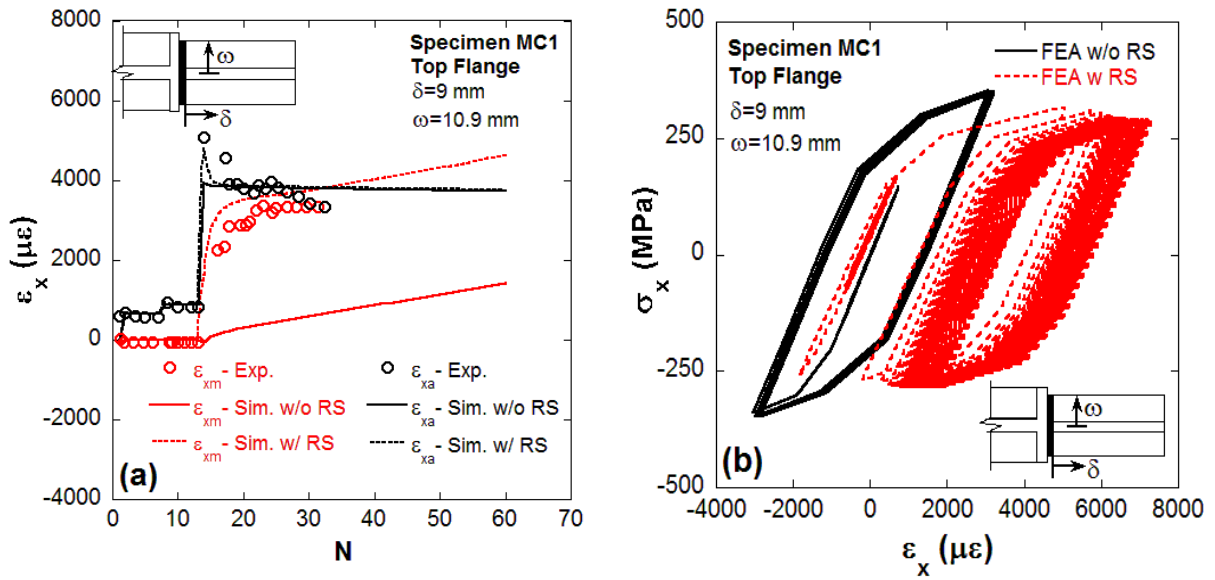


Figure 26 Low-cycle fatigue response of the connection for specimen MC1. (a) Axial mean strain and amplitude plotted against number of loading cycles, (b) axial stress-strain hysteresis cycles showing ratcheting.

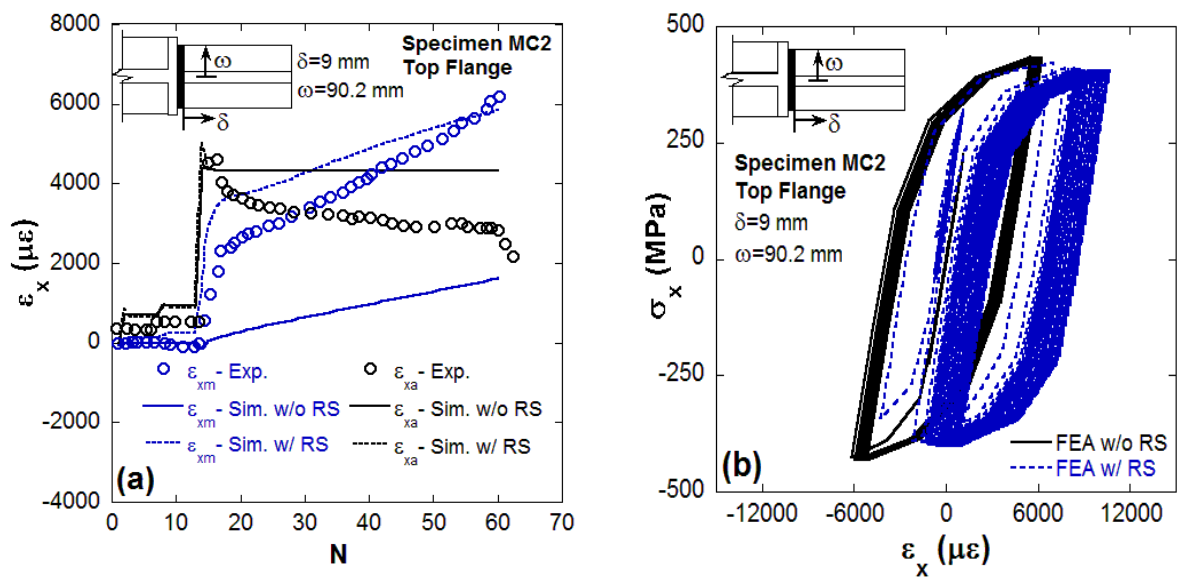


Figure 27 Low-cycle fatigue response of the connection for specimen MC2. (a) Axial mean strain and amplitude plotted against number of loading cycles, (b) axial stress-strain hysteresis cycles showing ratcheting.

A comparison of the axial mean strain and amplitude obtained from the finite element analysis with that of the experimental results is shown in Figure 26a and Figure 27a for specimen MC1 and MC2 respectively. It is interesting to note that finite element simulation results predicted the axial strain ratcheting correctly when residual stresses were considered in the analysis. The results of finite element analysis without residual stress showed very small ratcheting phenomena. This was observed for both the specimens. In the experiments, it was observed that the mean axial strain had a sharp increase when loading changed from elastic to inelastic cycles, which was captured by the FE simulation when residual stresses were considered. Although FE simulation without residual stresses showed small ratcheting, it did not show this trend of sharp increase in the magnitude of axial mean strain. However, the rate of ratcheting for both cases was comparable after the sharp increase in the mean axial strain; still the magnitude of mean axial strain was much higher for the case with residual stress as a result of the strain jump. The discrepancy in the FE simulation between the cases with and without residual stresses as well as the sharp increase in the mean axial strain can be clearly seen in Figure 26b and Figure 27b, where axial stress-strain hysteresis cycles shifted in the direction of axial strain indicating axial strain accumulation when residual stresses were considered in the analysis, whereas with no residual stress, the hysteresis loops were cycling almost in the same location. Based on the experimental and simulated responses, it is apparent that the increase in the axial strain accumulation observed in the experiments was attributed to the presence of high residual stresses near the welded joint of the connection, which can be simulated properly by considering residual stresses in the analysis. The accumulation of axial strain near the connection can be very detrimental to the performance of the connection which may lead to brittle low-cycle fatigue failure. Hence, analysis without considering the residual stresses may not yield the actual failure response of the connection.

In order to investigate the region of influence of the residual stresses on the axial strain accumulation, mean axial strains and strain amplitudes were plotted at different locations across the flange width and length. One set of such plots for specimen MC1 is shown in Figure 28. Accumulation of axial strain was observed across the flange width near weld toe

(Figure 28a). As already discussed, this can be attributed to the high residual stresses induced by welding near the weld toe.

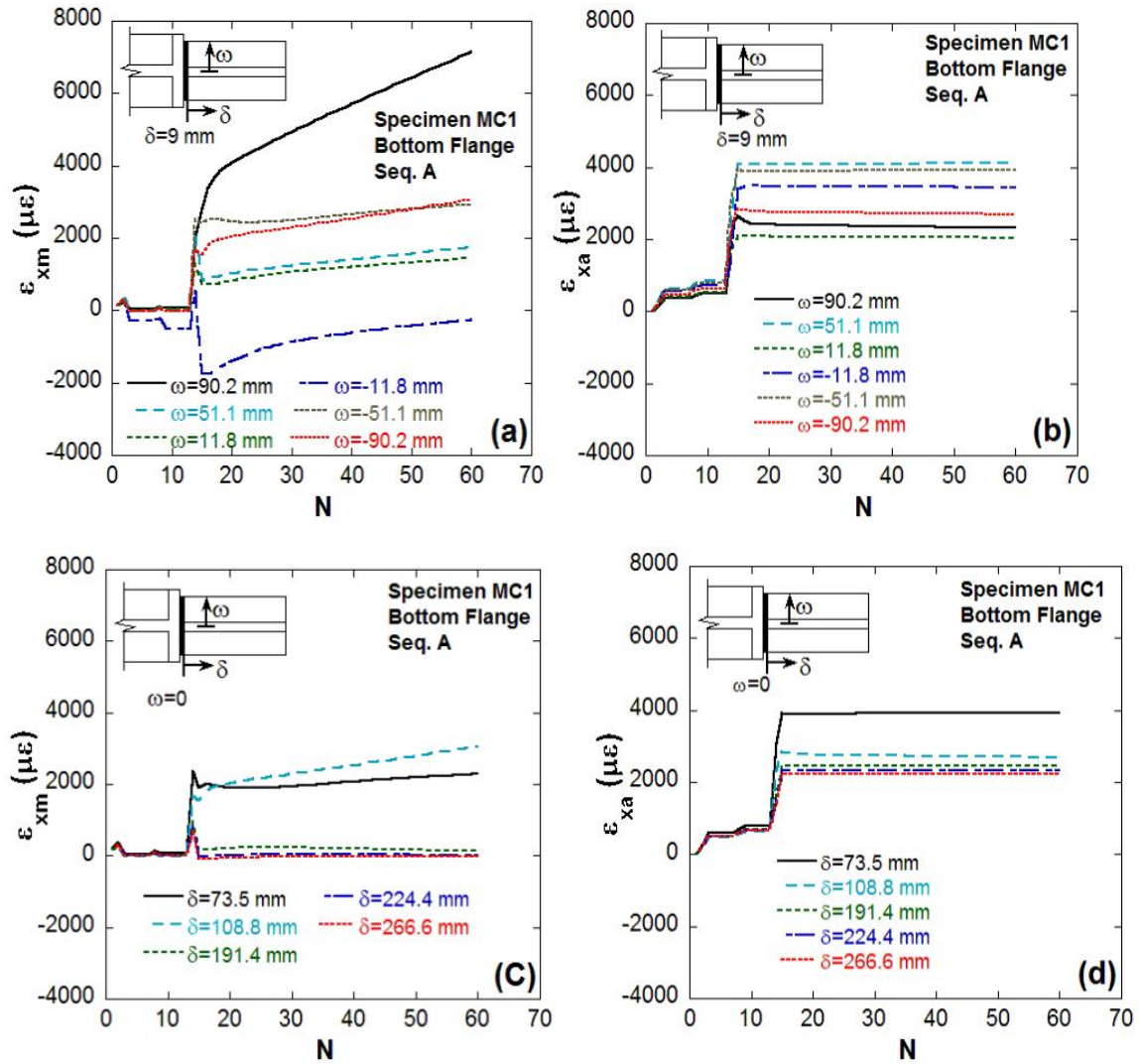


Figure 28 Low-cycle fatigue response of the connection at the beam bottom flange for specimen MC1. (a) Axial mean strain, and (b) strain amplitude plotted against number of loading cycles at different locations across the width near weld toe; (c) axial mean strain and (d) strain amplitude across the length.

Variation in the axial strain amplitudes was observed along the flange width and there was no specific trend in the variation of axial strain amplitude (Figure 28b). However, as the distance from the weld toe increased, there was a decreasing trend in both the axial mean strain and amplitude with almost no ratcheting after a distance of 108.8 mm from the weld toe (Figure 28c,d). This is due to the fact that the magnitude residual stresses decreased as the distance from the weld toe increased. The axial mean strain and amplitude plots near the weld access hole (Figure 29a) shows very high amount of negative strain accumulation which was also observed in the experiments. Without considering the residual stresses, the finite element simulation did not show any axial strain accumulation near the weld access hole. Another interesting phenomenon observed was the mean axial stress relaxation with loading cycles near weld toe (Figure 29b). The mean axial stresses relaxed completely after 15-20 loading cycles, however, the axial strain continued to accumulate with number of loading cycles. This unique feature of strain ratcheting even after relaxation of the mean axial stresses was also observed by Lu [21] and Cheng [29] during experimental and numerical study on cyclic response of welded piping joints. However, the reason for such type of behavior was not explained. To find an explanation of the strain ratcheting phenomena even after relaxation of the mean axial stresses, axial and von-Mises mean stresses were plotted in Figure 30a and Figure 30b at two locations near (25 mm) and away (190 mm) from the weld toe of the top flange for specimen MC1, respectively. The mean axial strains were also plotted in the same figures to compare the responses. It was observed that although the mean axial stresses relaxed with loading cycles, the von-Mises mean stresses did not relax, rather remained constant throughout the loading cycles for simulation considering residual stresses (Figure 30a). The magnitude of von-Mises mean stress was around 250 MPa for a location close to the weld toe, whereas the mean axial stress peak was around 180 MPa (Figure 30a). The mean axial stresses relaxed completely when the loading cycles were changed from elastic to inelastic cycles, at the same time there was a sharp increase in the mean axial strain. On the contrary, for simulation without considering residual stresses, the mean axial stress was zero during the loading cycles, whereas von-Mises mean stress had a small value of 74 MPa at the beginning of the loading cycles. When the loading cycles had a transition from

elastic to inelastic phase, the von-Mises mean stress had a sharp increase and approached a value close to the von-Mises mean stress value with residual stress case, and afterwards remained constant. Similar observations were also made for a location away from the weld toe, nonetheless, the magnitude of the stresses was lower compared to the location near the weld toe (Figure 30b). The beam bottom flange also experienced analogous trend of stress development, and hence not shown here.

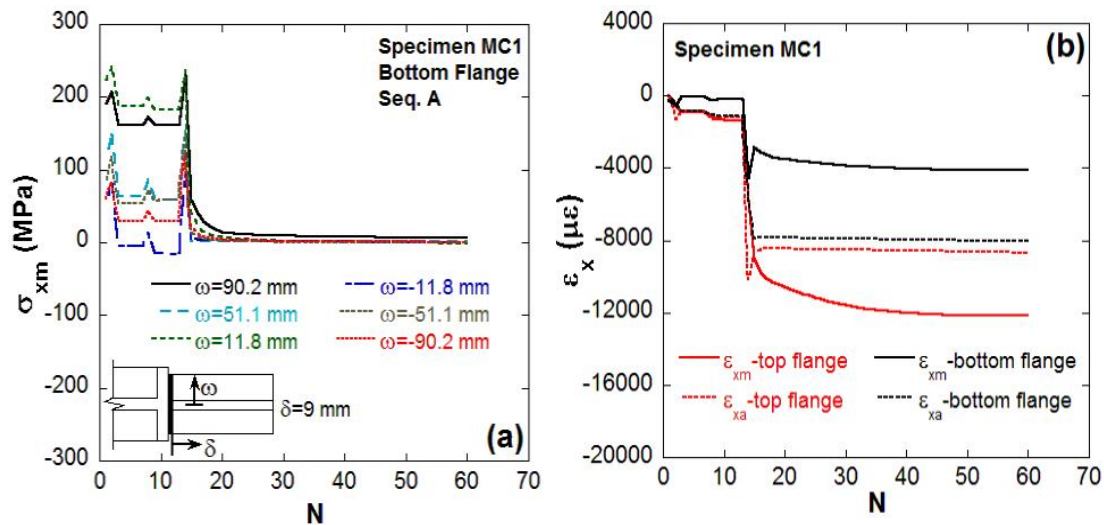


Figure 29 (a) Axial mean stress plotted against number of loading cycles for specimen MC1 at different locations across the width of near weld toe showing stress relaxation, (d) axial mean strain and amplitude near the top and bottom beam flange weld access hole for specimen MC1.

Based on these observations, the ratcheting phenomenon or the sharp increase in the mean axial strain can be attributed to either of the two following reasons or combination of both. Firstly, the magnitude of mean axial stress was high at the beginning of the transition phase between the elastic and inelastic loading cycles, which might have triggered the sharp increase in the mean axial strain. Alternatively, at the transition phase between elastic and inelastic loading cycles, the magnitude of von-Mises mean stress was large which might have

also influenced the sharp increase in the mean axial strain. After the sharp increase in the mean axial strain both the analyses with and without residual stresses showed ratcheting. At this point the mean axial stress had completely relaxed, and hence, it is apparent that at this stage the ratcheting must have been influenced by the von-Mises mean stresses since both the analyses with and without residual stress showed higher values of von-Mises mean stresses, which remained constant after the sharp increase in the mean axial strain. Consequently the ratcheting rate was constant after the sharp increase in the mean axial strain.

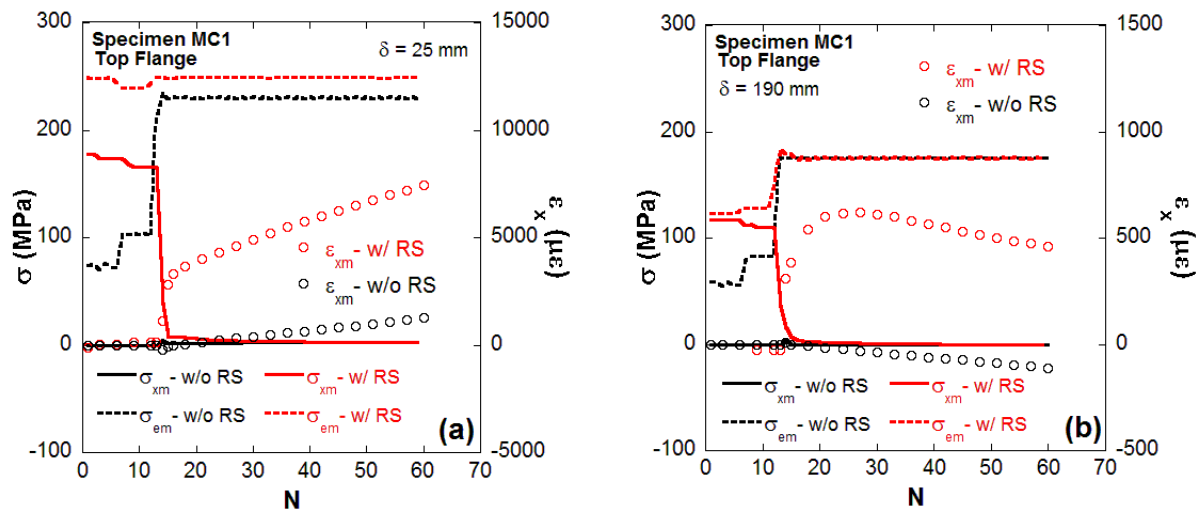


Figure 30 Axial mean stress and strain, and von-Mises mean stress plotted against number of loading cycles at the top flange for specimen MC1. (a) 25 mm from weld toe, (b) 190 mm from weld toe.

Next, results are compared for the two specimens under consideration to show the influence of the welding sequence on the low-cycle fatigue response of the connection. It has been already shown that the two specimens developed different peak residual stresses and different distribution. The mean strain and strain amplitudes as well as the mean stress and stress-strain hysteresis loops are plotted at different locations across the beam top and bottom flanges to study the difference in the response of the connections. Figure 31 and Figure 32 show stress-strain hysteresis cycles along with axial strain mean and amplitude near the weld

toe for top and bottom beam flanges respectively. More plots of axial strain mean and amplitude are presented in Figure 33.

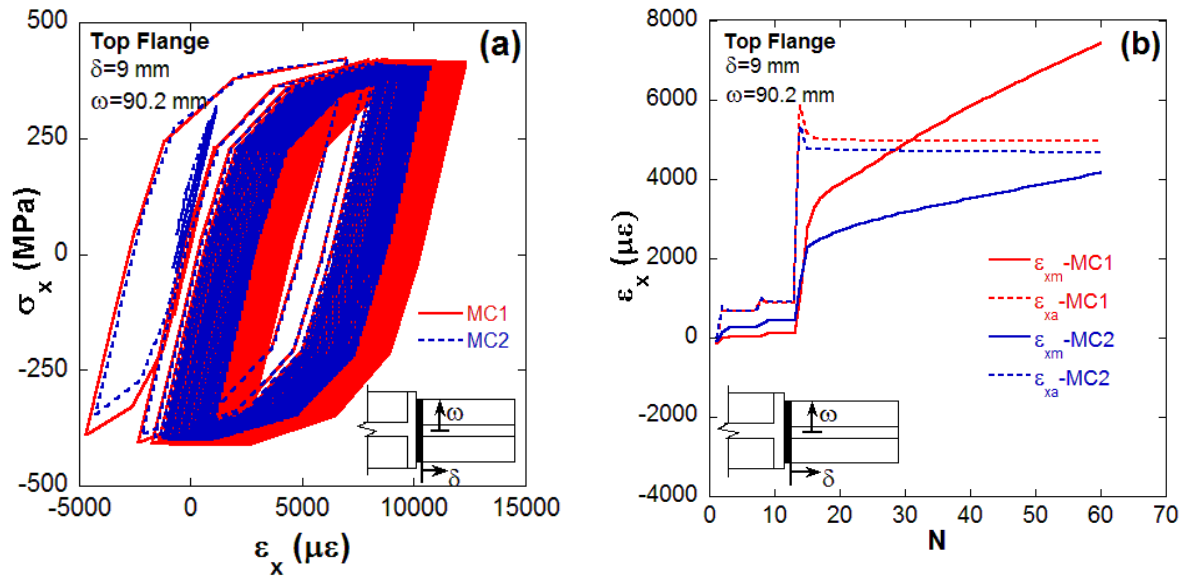


Figure 31 Comparison of stress-strain response at the beam top flange for the two specimens. (a) Stress-strain hysteresis response, (b) axial mean strain and amplitude plotted against number of loading cycles.

It is apparent that the axial strain accumulation rate was completely different for the two specimens with different weld sequences. In most of the locations across the weld toe and weld access hole, specimen MC1 developed significantly higher strain ratcheting compared to specimen MC2 for both beam top and bottom flanges. However, there were very few locations where the axial strain ratcheting for specimen MC2 was either equal or slightly higher than those for specimen MC1. Finally, the axial strain mean plots for the approximate positions of fracture in the experiments (Figure 33d) evidently shows that the mean strain values for specimen MC1 was almost two times higher than those for specimen MC2. This observation clearly justifies the lower fatigue life that was observed for specimen MC1 during the experiments and the influence of weld sequence on the strain ratcheting.

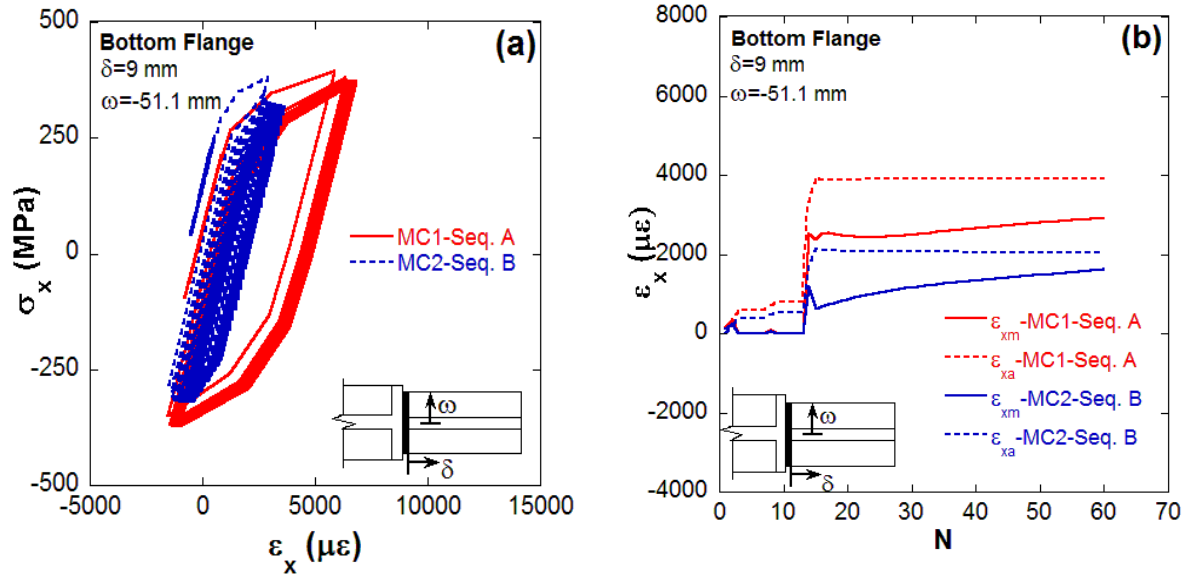


Figure 32 Comparison of stress-strain response at the beam bottom flange for the two specimens with different weld sequences. (a) Stress-strain hysteresis response, (b) axial mean strain and amplitude plotted against number of loading cycles.

However, although the influence of weld sequence on the mean axial strain was significant, the axial strain amplitude responses were not influenced by the weld sequence as much as the mean axial strain. In several locations (Figure 31b, Figure 32b, Figure 33a) specimen MC1 had higher strain amplitudes compared to specimen MC2 as anticipated. Subsequently, there were several locations where specimen MC2 had equal and higher strain amplitudes compared to specimen MC1 (Figure 33b,c,d). Hence, the direct influence of weld sequence on the axial strain amplitude was not as clear as its influence on the mean axial strain or ratcheting. Based on these observations, it can be concluded that the axial mean strain has more influence on the low-cycle fatigue failure of the connections compared to axial strain amplitude. Nonetheless, in both the specimens, the mean stresses relaxed within 10-20 cycles of loading, but still the ratcheting continued to increase with number of loading cycles. High axial strain ratcheting rate was also observed around the weld access hole region for both the specimens. As a result, the weld access holes are more prone to cracking during

low-cycle fatigue loading. The trend of axial strain accumulation near the weld access hole was similar for both the specimens with different welding sequences.

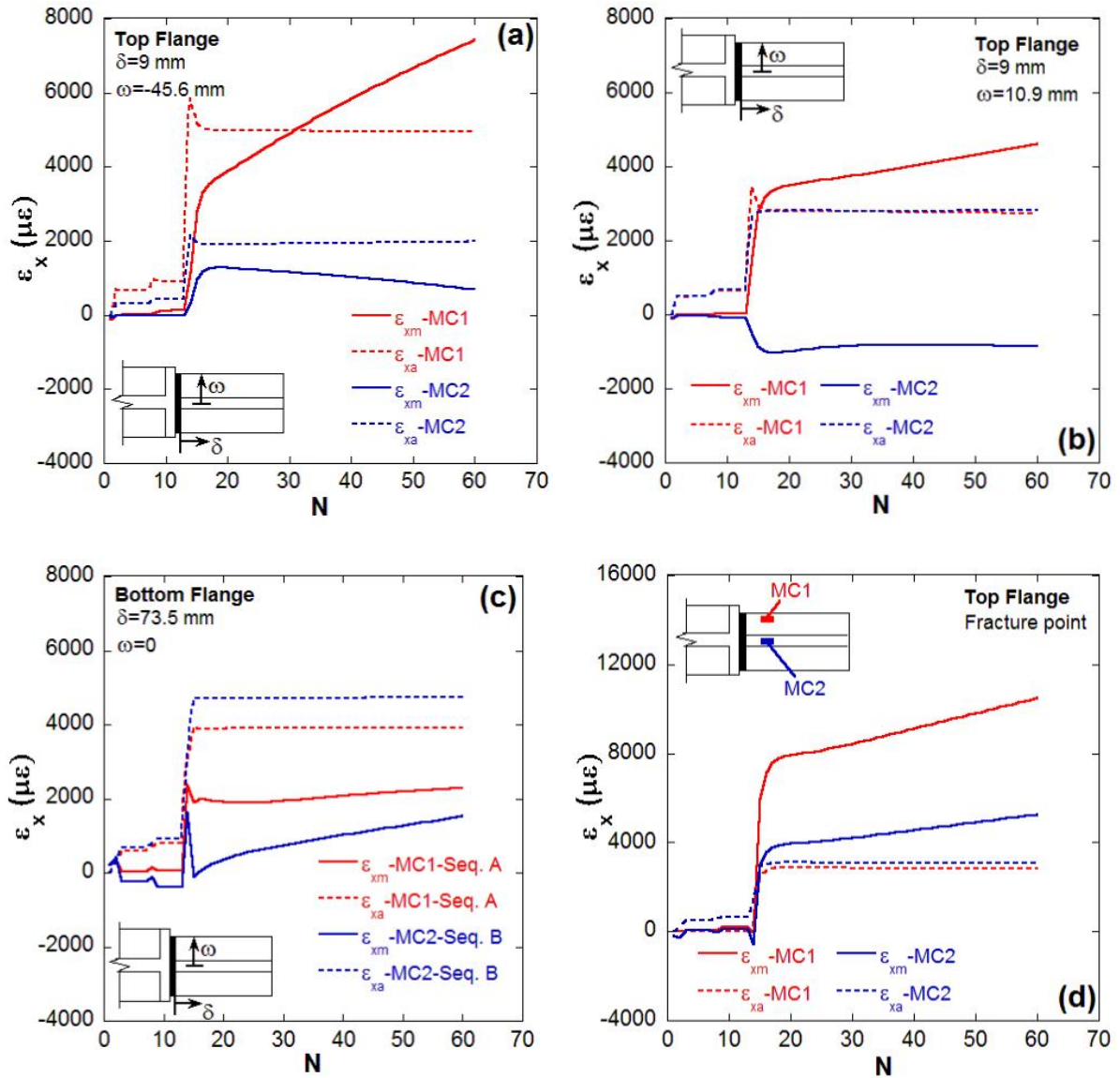


Figure 33 Axial mean strain and amplitude plotted against number of loading cycles at different locations of the beam flanges showing influence of weld sequence.

From the finite element investigation, it is apparent that the residual stress distribution can be significantly influenced by the sequence of welding which inevitably may lead to

significantly different stress-strain response at different locations of WSMCs, especially near the weld toe region of the beam flanges. It is believed that an optimized sequence of welding can be obtained with a broad set of finite element analyses as presented in this study to reduce the residual stresses near the weld toe and access hole region and thereby, increase the fatigue life of the connections. Alternatively, the as-welded beam-column connection can be heat treated based on the post weld heat treatment technique recommended by AWS D1.1 [78] to reduce the magnitude of residual stresses. This study dealt with the post weld heat treatment technique to reduce the residual stresses which is presented later. Therefore, based on the responses from the seismic analysis of WUF-W connections, it is apparent that the residual stresses can be one of the contributing factors of the low-cycle fatigue failures that have been observed in the cyclic testing of post-Northridge connections. The global approaches of connection design ignore the influence of residual stresses on the seismic performance of the connection because of the stress relaxation observed after few cycles of loading. However, this study clearly showed that although the mean stresses relaxed after few cycles of loading, the mean stresses worked as a driving force for axial strain accumulation near the weld toe region and the weld access hole. Moreover, based on the welding sequences, the axial strain accumulation rate was different at different locations near the welded joint. This study manifests the necessity of incorporating welding induced residual stresses in the analysis and design of moment connections during seismic loading, where the connection may develop low-cycle fatigue damage leading to brittle failure of the entire connection.

7. Post Weld Heat Treatment of WSMCs

The influence of post weld heat treatment (PWHT) on the residual stress relaxation at the welded joints has been studied both experimentally and numerically and it has been observed that the residual stresses can be significantly relieved with systematic post weld heat treatment [22, 80-86]. This is the process commonly referred to as stress relief, so called because it is carried out at temperatures at which the yield strength has fallen to a low value. If the structure is heated uniformly, the yield strength of the material around the weld is

unable to support the initial level of the residual stresses, which are relieved by plastic deformation [86]. Creep occurs at elevated temperatures and strain occurs by a diffusion mechanism, relaxing the residual stresses even further. The extent to which the residual stresses are relaxed depends on temperature and time for any given material and on material for any given temperature.

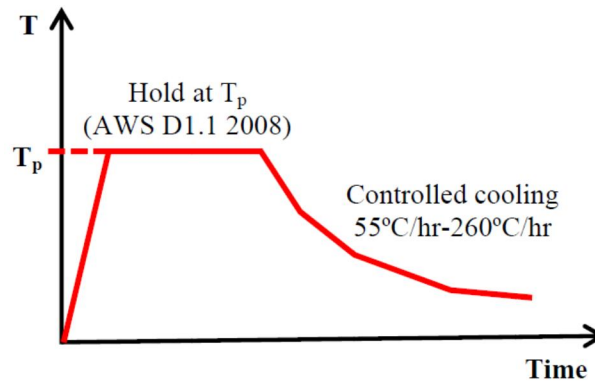


Figure 34 A schematic of the time-temperature curve for the post weld heat treatment specified by AWS D1.1 [78].

The stress distribution at the higher temperatures becomes more uniform and stress reduces to a low level. After cooling, provided that it is carried out in a controlled manner, the improved stress distribution is retained. Stress relieving heat treatments are generally avoided unless specified as mandatory by Codes and/or Standards, because of the high cost involved and potential adverse consequence of incorrect PWHT procedure [82]. However, the influence of PWHT on relieving the residual stresses at the welded joint of moment resisting connections has never been studied. Hence, in this study an attempt was made to investigate the feasibility of the PWHT for moment resisting connections in increasing the fatigue life by relieving the residual stresses.

AWS D1.1 [78] provides guidelines for post weld heat treatment of welded joints. According to AWS D1.1 the welded assembly needs to be heated in the temperature range of 600-650°C with a rate of heating as high as 220°C/hr for heating temperatures above 315°C.

Once the peak temperature is reached, it is kept constant for a certain amount of time based on thickness of the connecting parts which may vary from 15 minutes to several hours. Then the assembly is allowed to cool down in a controlled way with the rate of cooling being as low as 55°C/hr and as high as 260°C/hr. A schematic of the time-temperature curve for the post weld heat treatment proposed by AWS D1.1 is shown in Figure 34.

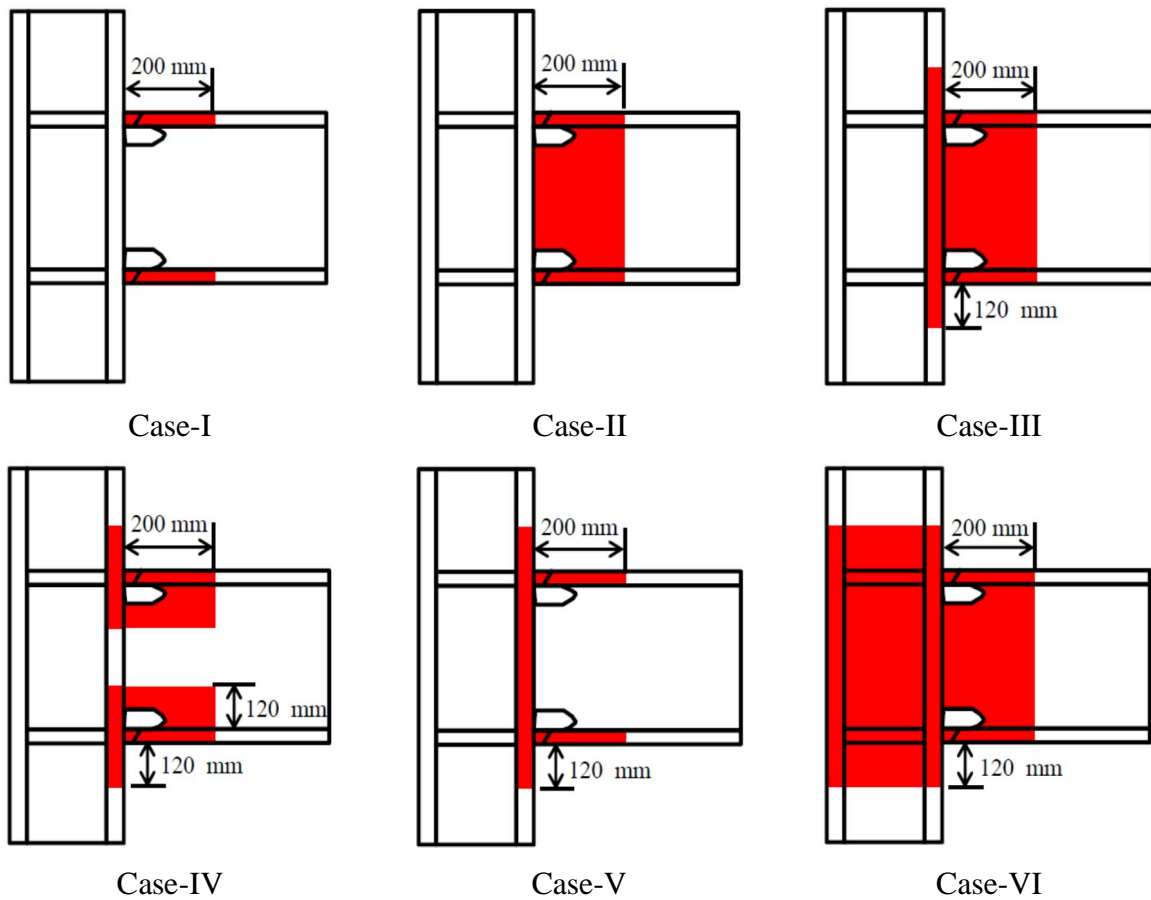


Figure 35 Post weld heat treatment cases investigated in the study.

In order to incorporate the post weld heat treatment in the finite element simulation, sequentially coupled transient thermo-mechanical analysis was performed similar to the procedure described for weld residual stress simulation. First a heat transfer analysis was performed on the WUF-W connection with six different cases of post weld heat treatment as

shown in Figure 35. These six different cases of PWHT were determined based on residual stress distribution observed after the initial and welding process simulation. Since the residual stress values were high up to a distance of 200 mm away from the weld toe, it was decided to heat treat only 200 mm distance of the beam. In case-I of PWHT only beam flanges were heat treated, whereas case-II involves heat treating both beam flanges and web. Case-III, IV, V consist of heating the beam flanges, web and column flange close to the welded joint, while case-VI involved heating the whole connection region. For the PWHT, the peak temperature chosen was 600°C with a heating rate of 200°C/hr. Then the peak temperature was hold constant for a time interval of 1 hour which was followed by slow cooling at 55°C/hr until the assembly reached the ambient temperature. The thermal analysis of the six cases of PWHT provided the real time temperature distribution during the heating and cooling phases which were then used as input in the residual stress calculation. However, for the simulation of residual stresses after post weld heat treatment, both the initial and weld residual stresses were fed as the initial state. The distribution of residual stresses after post weld heat treatment for the six cases under investigation is shown in Figure 36 for specimen MC1.

For cases I through V, the residual stresses were relieved reasonably, but the redistribution of residual stresses as a result of post weld heat treatment led to development of residual stresses higher or very close to the yield stress of the base material at several locations near the weld toe and around the weld access hole. Since for cases I through V, the entire connection region was not heated, the cooler adjacent areas led to the nonuniform cooling rate at different parts of the heated welded joint. This different cooling rate eventually led to the generation of residual stresses at the welded joints after PWHT. However, case-VI where the whole connection region was heat treated showed significant reduction in the residual stresses with no sign of higher stresses anywhere in the welded joint. This was attributed to the uniform cooling of the welded joint as a result of heating the entire connection region. The peak tensile and compressive residual stresses observed after post weld heat treatment were 203 MPa and 186 MPa respectively which are less than half the yield stress of the base material.

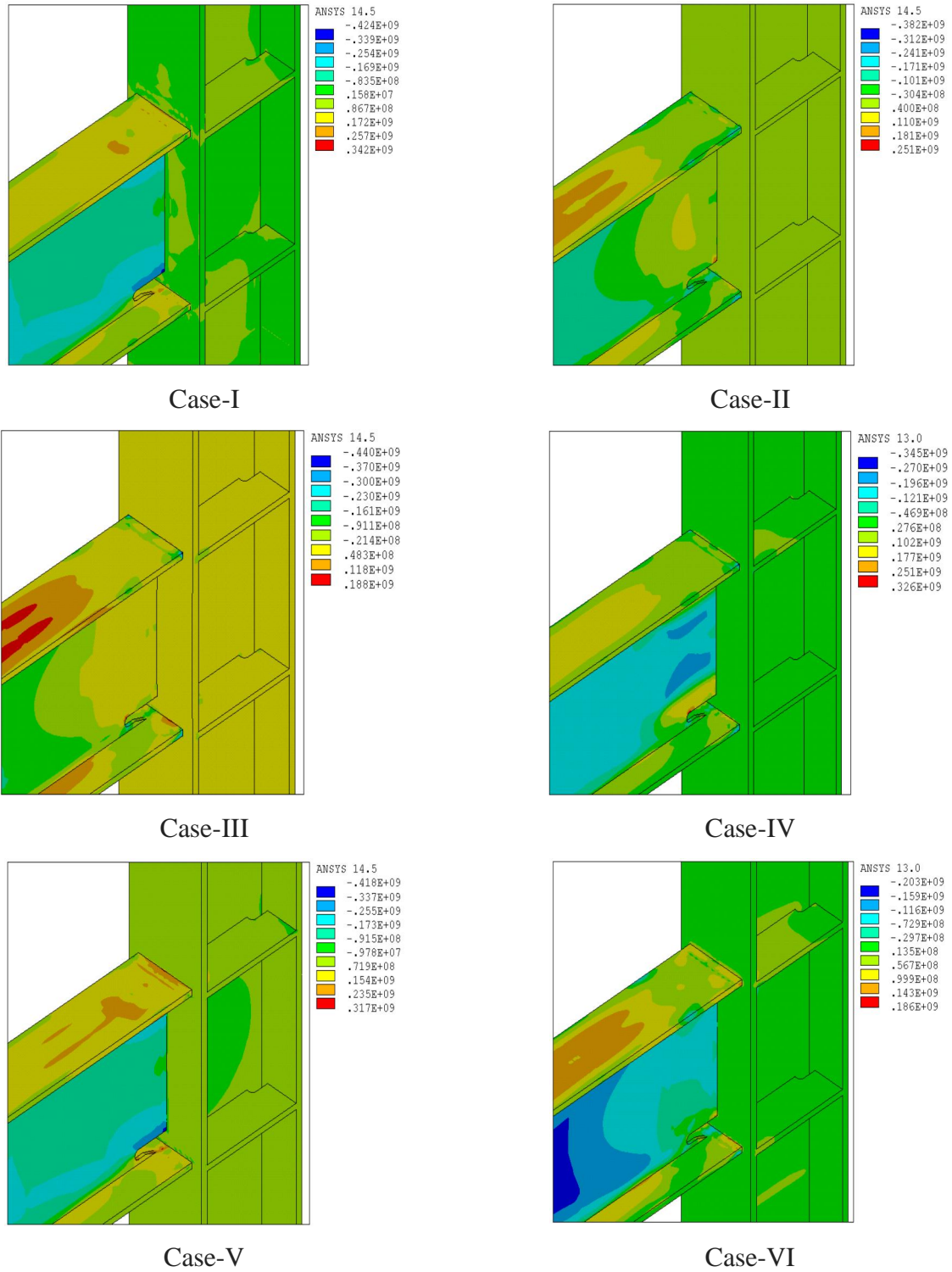


Figure 36 Residual stress contours showing distribution of residual stresses after PWHT for the six cases under investigation for specimen MC1.

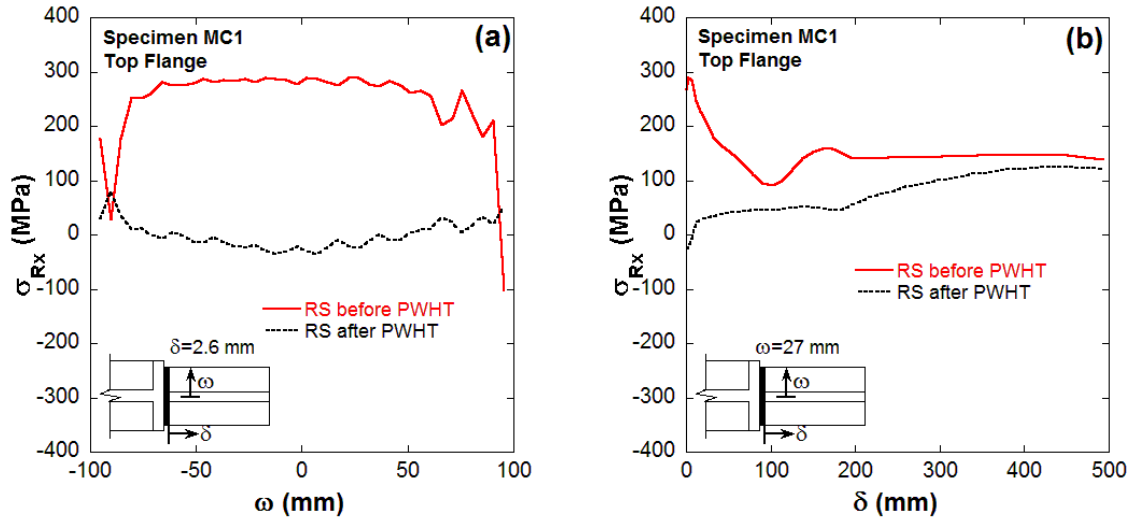


Figure 37 Residual stress distribution in the beam top flange for specimen MC1 showing effect of post weld heat treatment (Case-VI). (a) Across the width of the flange near the weld toe, (b) along the length of the beam.

In order to investigate the residual stress redistribution at different locations in the connection after post weld heat treatment for case-VI, residual stress distribution was plotted at different locations of the connection as shown in Figure 37 and Figure 38. For specimen MC1, the peak tensile residual stress at the weld toe across the width of the top flange was around 300 MPa with compressive peaks at the edges of the flange as shown in Figure 37a. After post weld heat treatment, the tensile stresses transformed to compressive stresses across the width of the flange with a peak value less than 50 MPa indicating more than 83% reduction in the peak value of the residual stresses. On the other hand, the compressive stresses at the edges of the flange converted to tensile stresses with a peak value less than 75 MPa indicating 62% reduction in the peak value of residual stresses. The reduction of residual stresses were significant around 200 mm length of the beam from the weld toe, which was heat treated, however, the influence of heat treatment was visible up to 500 mm distance along the length of the beam as seen in Figure 37b. Unlike beam top flange, the residual stress distribution after welding was not uniform for beam bottom flange because of the several start and stop locations of welding beads across the width of the flange. The

residual stress distribution at the weld toe across the width of the beam bottom flange is shown Figure 38a, where there were several locations experiencing peak tensile (100 MPa) and compressive residual stresses (300 MPa). However, after post weld heat treatment significant reduction in the residual stresses was observed. Interestingly, the residual stresses became completely compressive with almost a uniform distribution across the width of the beam bottom flange.

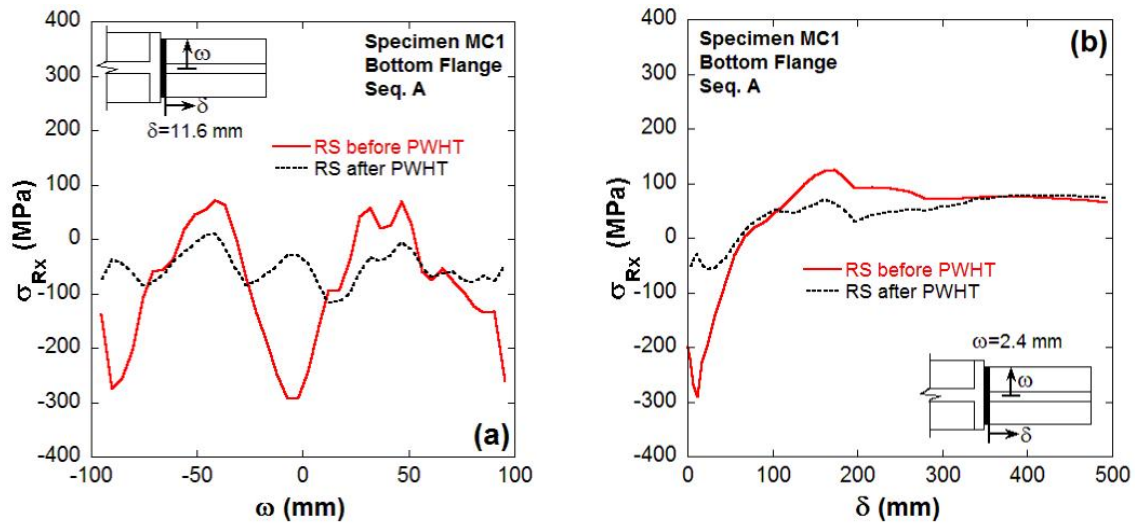


Figure 38 Residual stress distribution in the beam bottom flange for specimen MC1 with weld sequence A showing effect of post weld heat treatment (Case-VI). (a) Across the width of the flange near the weld toe, (b) along the length of the beam.

The peak value of the residual stress observed after post weld heat treatment was around 100 MPa which indicates a 65% reduction in the peak value. Similar to the top flange of the beam, the residual stress reduction was significant near the weld toe and the extent of reduction decreased as the distance from the weld toe increased. However, unlike beam top flange, there was no influence of post weld heat treatment in reducing the residual stresses after 300 mm distance from the weld toe. One thing that must have been noted in both beam top and bottom flanges is that after post weld heat treatment the distribution of residual

stresses near the weld region became almost uniform across the width of the flange and the residual stresses developed were predominantly compressive. It has been concluded by many studies that compressive residual stress is beneficial while tensile residual stress is detrimental to fatigue strength [21, 27, 88-90].

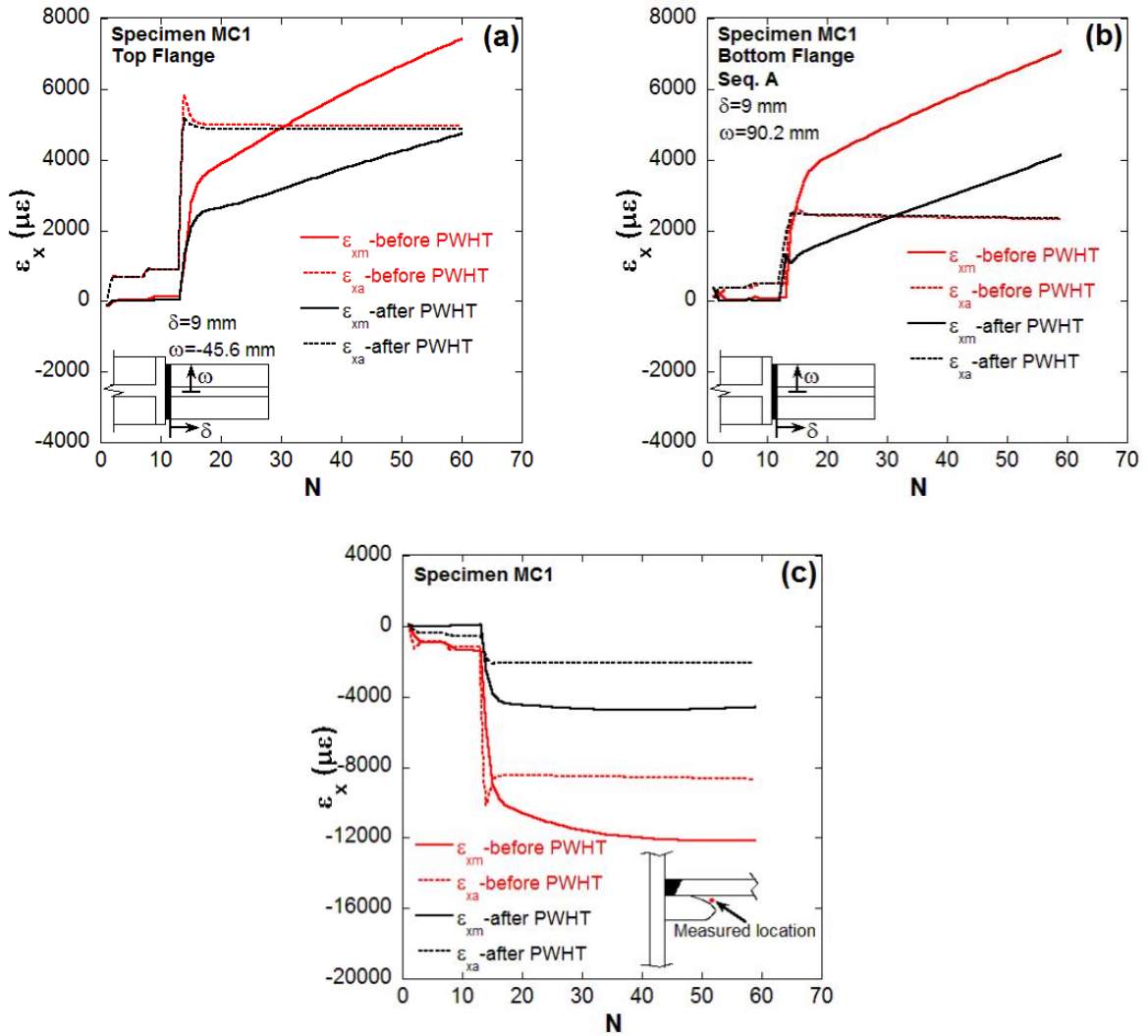


Figure 39 Axial strain mean and amplitude plotted against number of loading cycles at (a) beam top flange near weld toe, (b) bottom flange near weld toe, (c) around weld access hole near beam top flange of the connection for specimen MC1 showing influence of PWHT (Case-VI).

Hence, it is evident that systematic post weld heat treatment has a great potential in increasing the fatigue life of moment resisting connections by relieving the residual stresses near the weld region of the connection. The influence of case-VI of post weld heat treatment on the low-cycle fatigue response of the WUF-W connections was investigated by performing finite element analysis of the connections with PWHT under seismic type of loading that was used in the previous analyses as shown in Figure 23b. As anticipated, the axial mean strain accumulation was significantly reduced by the post weld heat treatment (Figure 39) since the residual stresses were relieved significantly. As can be seen in Figure 39a and Figure 39b, the magnitude of axial mean strain in each loading cycle with PWHT near the weld toe of beam top and bottom flanges was around half in magnitude compared to the cases without PWHT.

On the contrary, around the weld access hole, the magnitude of axial mean strain without PWHT was three times higher compared to the case with PWHT (Figure 39c). Hence, it is evident that the axial strain ratcheting can be significantly reduced by incorporating post weld heat treatment. Although the magnitude of ratcheting was lower with PWHT, the rate of ratcheting was similar for both the cases with and without PWHT. The responses also revealed that near the weld toe of the top and bottom beam flanges, the post weld heat treatment did not have any influence on the axial strain amplitude (Figure 39a and Figure 39), however, around the weld access hole the axial strain amplitude showed significant decrease similar to what was observed for axial mean strain (Figure 39c). The explanation for such type of behavior in the axial strain amplitude was not very clear, and hence, the influence of residual stresses and the post weld heat treatment on the axial strain amplitude response needs further investigation. Moreover, further research is necessary to study the influence of axial strain amplitude on the low-cycle fatigue response of moment connections.

8. Conclusions

This study demonstrated the development of initial and welding induced residual stresses in moment resisting connections by using advanced numerical techniques which exhibited good correlation with the experimental observations. Two WUF-W moment connections

with different welding sequences were simulated to investigate the influence of welding sequence on the residual stress distribution, and subsequently on the low-cycle fatigue response of moment resisting connections under seismic type of loading. The observations of the study led to the following conclusions:

- The development of initial and welding residual stresses can be properly simulated by using advanced numerical techniques as described in this study, and three dimensional modeling of the welding process is required in order to model the weld sequence effect.
- Significant amount of residual stresses develop close to the weld toe and weld access hole of the connection because of the welding procedure, which gradually diminishes with increase in the distance from the weld toe. The peak value of residual stresses can be higher than the yield stress of the base material and it can be either tensile or compressive or a combination of both.
- Initial residual stress values are negligible around the edges of the beam, and it increases with an increase in the distance from the edge with a peak value at the centerline along the beam length. As a result, the residual stresses close to the weld region are predominantly welding induced residual stresses.
- The presence of residual stresses may lead to axial strain ratcheting near the weld toe and weld access hole, and subsequently may lead to low-cycle fatigue failure of the connection. Hence, the low-cycle fatigue failures that have been observed in the cyclic testing of the post-Northridge connections can be attributed to the development of damage accumulation near the weld toe and weld access hole as a result of the axial strain ratcheting.
- Different weld sequences induce different distribution and magnitude of residual stresses around the welded joint, and hence, the ratcheting phenomenon would be different for different weld sequences which subsequently influence the fatigue life of the connections.

- Post weld heat treatment as specified by AWS D1.1 [78] can be used systematically to reduce the magnitude of residual stresses which is expected to increase the fatigue life of moment resisting connections.

9. References

- [1] FEMA-350. Recommendation and seismic design criteria for new steel moment-frame buildings. prepared by the SAC Joint Venture for the Federal Emergency Management Agency, Washington, DC, 2000.
- [2] FEMA-353. Recommended specifications and quality assurance guidelines for steel moment- frame construction for seismic applications. prepared by the SAC Joint Venture for the Federal Emergency Management Agency, Washington, DC, 2000.
- [3] FEMA-355D. State of the art report on connection performance. prepared by the SAC Joint Venture for the Federal Emergency Management Agency, Washington, DC, 2000.
- [4] SAC/BD-99/23. Failure analysis of welded beam to column connections. by Barsom, JM, Pellegrino JV.
- [5] Stojadinovic B, Goel SC, Lee KH, Margarian AG, Choi JH. Parametric tests on unreinforced steel moment connections. Journal of Structural Engineering 2000;126:40-49.
- [6] SAC/BD-00/01. Parametric tests on unreinforced connections. by Lee KH, Stojadinovic B, Goel SC, Margarian AG, Choi J, Wongkaew A, Reyher BP, Lee DY.
- [7] SAC/BD-00/24. Development and evaluation of improved details for ductile welded unreinforced flange connections. by Ricles JM, Mao C, Lu LW, Fisher JW.

- [8] Lee D, Cotton SC, Hajjar JF, Dexter RJ. Cyclic behavior of steel moment-resisting connections reinforced by alternative column stiffener details, I. Connection performance and continuity plate detailing. *Engineering Journal* 2005;4th Quarter:189-213.
- [9] Suita K, Nakashima M, Morisako K. Tests of welded beam-column subassemblies II: Detailed behavior. *Journal of Structural Engineering* 1998;124(11):1245-1252.
- [10] Nakashima M, Suita K, Marisako K, Maruoka Y. Tests of welded beam-column subassemblies. I. Global behavior. *Journal of Structural Engineering* 1998;124:1236-1244.
- [11] Mazzolani FM. (Editor). *Moment resistant connections of steel frames in seismic areas: design and reliability*. E&FN Spon, 2000.
- [12] SAC/BD-00/22. Cyclic response of RBS moment connections: loading sequence and lateral bracing effects.” by Yu S, Gilton C, Uang CM.
- [13] Uang CM, Yu QS, Noel S, Gross J. Cyclic testing of steel moment connections rehabilitated with rbs or welded haunch. *Journal of Structural Engineering* 2000;126:57-68.
- [14] SAC/BD-99/04. Effects of strength/toughness mismatch on structural and fracture behaviors in weldments. by Dong P, Kilinski T, Zhang J, Brust FW.
- [15] Smith JK. Vibrational fatigue failures in short cantilevered piping with socket-welded fittings. *ASME PVP-Vol. 338, Pressure Vessels and Piping Codes and Standards* 1996;1:21-24.
- [16] Vecchio RS. Fatigue evaluation of socket welded piping in a nuclear power plant. *ASME PVP-Vol. 338, Pressure Vessels and Piping Codes and Standards* 1996;1:25-41.

- [17] Brust FW, Zhang J, Dong P. Pipe and pressure vessel cracking: the role of weld induced residual stresses and creep damage during repair. Trans. of the 14th Int. Conf. on Struct. Mech. in Reactor Technol. (SMiRT 14), Lyon, France, 1, 297–306, 1997a.
- [18] Brust FW, Dong P, Zhang J. Influence of residual stresses and weld repairs on pipe fracture. Approximate Methods in the Design and Analysis of Pressure Vessels and Piping Components, W. J. Bees, ed., PVP, **347**, 173–191, 1997b.
- [19] Zhang J, Dong P, Brust FW. Analysis of residual stress in a girth weld of a bwr core shroud. Approximate Methods in the design and Analysis of Pressure Vessels and Piping Components, W. J. Bees, ed., PVP, **347**, 141–156, 1997.
- [20] Brickstad B, Josefson BL. A parametric study of residual stresses in multi-pass butt-welded stainless steel pipes. International Journal of Pressure Vessels and Piping 1998;75(1):11-25.
- [21] Higuchi M, Nakagawa A, Iida K, Hayashi M, Yamauchi T, Saito M, Sato M. Experimental study on fatigue strength of small-diameter socket-welded pipe joints. Journal of Pressure Vessel Technology 1998;120:149-156.
- [22] Riccardella PC, Pan SH, Sullivan M, Schletz J, Gosselin SR. vibration fatigue testing of socket welds. Pressure Vessel and Piping Codes and Standards 1998;360:453-463.
- [23] Durantou P, Devaus J, Robin V, Gilles P, Bergheau JM. 3D modelling of multipass welding of a 316L stainless steel pipe. Journal of Materials Processing Technology 2004;153-154:457-463.
- [24] Joseph A, Rai SK, Jayakumar T, Murugan N. Evaluation of residual stresses in dissimilar weld joints. International Journal of Pressure Vessels and Piping 2005;82:700-705.

- [25] Gosselin S. Fatigue in operating nuclear power plants components after 60 years. Workshop on U.S. nuclear power plant life extension research and development issues, 2008.
- [26] Zhang YH, Maddox SJ. Fatigue testing of full scale girth welded pipes under variable amplitude loading. *Journal of Offshore Mechanics and Arctic Engineering* 2014;136:021401-1- 021401-10.
- [27] Mochizuki M, Hattori T, Nakakado K. Residual stress reduction and fatigue strength improvement by controlling welding pass sequences. *Journal of Engineering Materials and Technology* 2000;122:108-112.
- [28] Lu X. Influence of residual stress on fatigue failure of welded joints. Ph.D. Dissertation, North Carolina State University, Raleigh, NC, 2002.
- [29] Humphreys AE. Influence of residual stress on the initiation of fatigue cracks at welded piping joints. MS Thesis, North Carolina State University, Raleigh, NC, 2004.
- [30] Cheng PY. Influence of residual stress and heat affected zone on fatigue failure of welded piping joints. Ph.D. Dissertation, North Carolina State University, Raleigh, NC, 2009.
- [31] Deng D, Kiyoshima S. FEM prediction of welding residual stresses in a SUS304 girth-welded pipe with emphasis on stress distribution near weld start/end location. *Computational Materials Science* 2010;50(2):612-621.
- [32] Jiang W, Yahiaoui K. Effect of welding sequence on residual stress distribution in a multipass welded piping branch junction. *International Journal of Pressure Vessels and Piping* 2012;95:39-47.
- [33] Teng TL, Chang PH, Tseng WC. Effect of welding sequences on residual stresses. *Computers & structures* 2003;81(5):273-286.

- [34] Ji SD, Fang HY, Liu XS, Meng QG. Influence of a welding sequence on the welding residual stress of a thick plate. *Modelling and Simulation in Materials Science and Engineering* 2005;13(4):553.
- [35] Machold W, Staron P, Bayraktar FS, Riekehr S, Koçak M, Schreyer A. Influence of the welding sequence on residual stresses in laser welded t-joints of an airframe aluminium alloy. *Materials Science Forum* 2008;571:375-380.
- [36] Brust FW, Raju IS, Cheston D. Residual stresses and critical initial flaw size analyses of welds. 50th AIAA/ASME/ASCE/AHS/ASC Structures, Structural Dynamics, and Materials Conference, Palm Springs, California, 2009.
- [37] Gannon L, Liu Y, Pegg N, Smith M. Effect of welding sequence on residual stress and distortion in flat-bar stiffened plates. *Marine Structures* 2010;23(3):385-404.
- [38] Deng D. Influence of deposition sequence on welding residual stress and deformation in an austenitic stainless steel j-groove welded joint. *Materials & Design* 2013;49:1022-1033.
- [39] Keivani R, Jahazi M, Pham T, Khodabandeh AR, Afshar MR. Predicting residual stresses and distortion during multisequence welding of large size structures using fem. *The International Journal of Advanced Manufacturing Technology* 2014;1-11.
- [40] SAC/BD-97/05. Finite element fracture mechanics investigation of welded beam-to-column connections. by Chi WM, Deierlein GG, Ingraffea A.
- [41] SAC/BD-99/24. Weld acceptance criteria for seismically-loaded welded connections. by Mohr W.
- [42] Chi WM, Deierlein GG, Ingraffea A. Fracture toughness demands in welded beam-column moment connections. *Journal of structural engineering* 2000;126(1):88-97.

- [43] Matos CG, Dodds Jr RH. Modeling the effects of residual stresses on defects in welds of steel frame connections. *Engineering Structures* 2000;22(9):1103-1120.
- [44] Matos CG, Dodds Jr RH. Probabilistic modeling of weld fracture in steel frame connections part i: quasi-static loading. *Engineering structures* 2001;23(8):1011-1030.
- [45] Matos CG, Dodds Jr RH. Probabilistic modeling of weld fracture in steel frame connections part ii: seismic loading. *Engineering structures* 2002;24(6):687-705.
- [46] Righiniotis TD, Omer E, Elghazouli AY. A simplified crack model for weld fracture in steel moment connections. *Engineering structures* 2002;24(9):1133-1140.
- [47] Zhang J, Dong P. Residual stresses in welded moment frames and implications for structural performance. *Journal of Structural Engineering* 2000;126(3):306-315.
- [48] Lindgren LE. Finite element modeling and simulation of welding part 1: increased complexity. *Journal of Thermal Stresses* 2001;24(2):141-192.
- [49] Quayyum S., Hassan T. Simulation of initial residual stresses in hot-rolled wide flange shapes. To be submitted to *Journal of Constructional Steel Research*, 2014.
- [50] Fourier J. *Analytical theory of heat*. Dover Publications, New York, 1955.
- [51] Shamsundar N, Sparrow EM. Analysis of multidimensional conduction phase change via the enthalpy model. *Journal of heat transfer* 1975;97(3):333-340.
- [52] Comini G, Guidice D. Finite element solutions of non-linear heat conduction problems with special reference to phase change. *International Journal of Numerical Methods in Engineering* 1979;8:613-624.
- [53] Radaj D. *Heat effects of welding*. Springer-Verlag, 1992, ISBN 3-540-54820-3.

- [54] Hong JK, Tsai CL, Dong P. Assessment of numerical procedures for residual stress analysis of multipass welds. *Welding Research Supplement* 1998;372s-382s.
- [55] European Committee for Standardization EN1993-1-2. Eurocode 3: Design of steel structures, part 1.2, general rules, structural fire design. European Committee for Standardization, 2005.
- [56] Wickström U. TASEF-2: A computer program for temperature analysis of structures exposed to fire. Report No. 79-2, Lund Institute of Technology, Lund, Sweden, Department of Structural Mechanics, 1979.
- [57] Hu G, Morovat MA, Lee J, Eschell E, Engelhardt M. Elevated temperature properties of astm a992 steel. In: *Proceedings of ASCE structure congress 09*, Austin, TX, USA, 2009.
- [58] AISC. Specification for structural steel buildings. Chicago, IL, American Institute of Steel Construction, 2005.
- [59] Wikander L, Karlsson L, Nasstrom M, Webster P. Finite element simulation and measurement of welding residual stresses.” *Modelling and Simulation in Materials Science and Engineering* 1994;2(4):845.
- [60] AISC. Manual of steel construction: load and resistance factor design—Volume I: Structural members, specifications and codes. 2nd Ed., American Institute of Steel Construction, 1994.
- [61] SAC/BD-00/13. Preliminary evaluation of heat affected zone toughness in structural shapes used in the construction of seismic moment frames. by Johnson MQ, Ramirez JE.
- [62] Morrison M. An innovative seismic performance enhancement techniques for welded steel moment connections. PhD Dissertation Research, North Carolina State University, Raleigh, NC, 2014.

- [63] Ketter RL, Kaminsky FL, Beedle LS. Plastic deformation of wide-flange beam columns. ASCE Trans. 1955;120:1019, Reprint No. 91 and 101.
- [64] Huber AW. Residual stresses in wide flange beams and columns. Fritz Engineering Laboratory Report No. 220A.25, Lehigh University, Bethlehem, PA, 1958.
- [65] Ketter RL. The influence of residual stresses on the strength of structural members. Welding Research Council Bulletin 44, (November 1958), Reprint No. 132 (58-6).
- [66] Alpsten GA. Thermal residual stresses in hot-rolled steel members. Fritz Engineering Laboratory Report No. 337.3, Lehigh University, Bethlehem, PA, 1968.
- [67] Bernuzzi C, Calado L, Castiglioni CA. Ductility and load carrying capacity prediction of steel beam-to-column connections under cyclic reversal loading. Journal of Earthquake Engineering 1997;1(2):401–432.
- [68] European Convention for Constructional Steelworks, ECCS. Recommended testing procedure for assessing the behavior of structural elements under cyclic loads. TWG 1.3—Seismic Design, ECCS Publication No. 45, Technical Committee 1, 1986.
- [69] ATC. Guidelines for cyclic seismic testing of components of steel structures. ATC-24, Redwood City, Calif., 1992.
- [70] SAC/BD-97/02. Protocol for fabrication, inspection, testing and documentation of beam-column connection tests and other experimental specimens. by Clark P, Frank K, Krawinkler H, Shaw R.
- [71] Krawinkler H, Zohrei M. Cumulative damage in steel structures subjected to earthquake ground motions. Computers and Structures 1983;16:531–541.
- [72] Ballio G, Castiglioni CA. Seismic behavior of steel sections. Journal of Constructional Steel Research 1994;29:21–54.

- [73] Mander JB, Chen SS, Pekan G. Low-cycle variable amplitude fatigue modelling of top-and-seat angle connections. *Engineering Journal* 1994a;2:54–62.
- [74] Mander JB, Chen SS, Pekan G. Low-cycle fatigue behavior of semi-rigid top-and-seat angle connections. *Engineering Journal* 1994b;3:111–122.
- [75] Castiglioni CA. Effects of the loading history on the local buckling behavior and failure mode of welded beam-to-column joints in moment-resisting steel frames. *Journal of Engineering Mechanics* 2005;131:568-585.
- [76] Chaboche JL. Constitutive equations for cyclic plasticity and cyclic viscoplasticity. *International Journal of Plasticity* 1989;5(3):247-302.
- [77] Royster PB. Localized low cycle fatigue failure of welded steel moment connections. MS Thesis, North Carolina State University, Raleigh, NC, 2007.
- [78] Hassan T, Kyriakides S. Ratcheting of cyclically hardening and softening materials: I. Uniaxial behavior. *International Journal of Plasticity* 1994;10:149-184.
- [79] ANSI/AWS D1.1. Structural welding code-steel. The American Welding Society, 2008.
- [80] Josefsson BL. Residual stresses and their redistribution during annealing of a girth-butt welded thin walled pipe. *Journal of Pressure Vessel Technology* 1982;104:245–250.
- [81] Berglund D, Alberg H, Runnemalm H. Simulation of welding and stress relief heat treatment of an aero engine component. *Finite elements in analysis and design* 2003;39(9):865-881.
- [82] Sedek P, Brozda J, Wang L, Withers PJ. Residual stress relief in MAG welded joints of dissimilar steels. *International Journal of Pressure Vessels and Piping* 2003;80:705-713.

- [83] Paradowska A, Price JWH, Dayawansa P, Kerezsi B, Zhao XL, Ibrahim R. Measurement of residual stress distribution in tubular joints considering post weld heat treatment. *Materials Forum* 2006;30:30-38.
- [84] Yaghi AH, Hyde TH, Becker AA, Sun W. Finite element simulation of welding and residual stresses in a p91 steel pipe incorporating solid-state phase transformation and post-weld heat treatment. *The Journal of Strain Analysis for Engineering Design* 2008;43(5):275-293.
- [85] Wen Y, Geng L, Gong J, Wang Y, Tu S. Finite element analysis of welding residual stress of the ultra-thick 13MnNiMoR steel cylinder of a large EO reactor made in China. *In ASME 2013 Pressure Vessels and Piping Conference*, pp. V06BT06A071-V06BT06A071. American Society of Mechanical Engineers, 2013.
- [86] Akbarzadeh I, Attarha MJ, Salehi M, Sattari-Far I. Numerical and experimental study on the effect of post-weld heat treatment parameters on the relaxation of welding residual stresses. *The Journal of Strain Analysis for Engineering Design* 2011;46(2):79-86.
- [87] Hosford WF. *Mechanical behavior of materials*. Cambridge University Press, New York, 2005.
- [88] Chiarelli M, Lanciotti A, Sacchi M. Fatigue resistance of MAG welded steel elements. *International Journal of Fatigue* 1999;21:1099-1110.
- [89] Iida K, Yamamoto S, Takanashi M. Residual stress relaxation by reversed loading. *Welding in the World* 1997;39(3):138-144.
- [90] Teodosio JR, Fonseca MC, Pedrosa PD. Relaxation of residual stresses during fatigue cycles in steels. *Materials Science Forum* 2003;426-432:3981-3988.

CHAPTER 7: SEISMIC PERFORMANCE OF A FIRE DAMAGED MOMENT RESISTING FRAME

Abstract

If a steel building skeleton does not deform severely by a fire event, it is usually rehabilitated for continued service. Material properties of structural steel undergo significant change when exposed to high temperatures and subsequently cooled to room temperature. During fire, a steel structure is exposed to very high temperatures with varying peak temperatures at different locations of the structure. Hence, it is anticipated that the material properties of the structural steel will be heterogeneous throughout the structure after the fire event. It is not known how such a fire exposed steel building will perform under a seismic event, if the extent of fire damage is low enough to rehabilitate for continued operation. In this study, finite element analyses were performed on such type of fire damaged steel moment resisting frames to investigate their seismic performance by considering the heterogeneity of the material due to fire exposure. A seismic analysis was also performed on a fire damaged isolated beam-column connection to characterize the influence of material heterogeneity on the connection's performance. The results of the study demonstrate the vulnerability of fire damaged steel structures.

Keywords: Seismic analysis, Moment frame, Fire damage, Material heterogeneity, High temperature

1. Introduction

Steel building structures may suffer various degrees of damages from fire exposure and extinguishing, which can range from minor structural damage to complete collapse of the building. To name few of the past major fires which exhibited severe damage to steel structures but no collapse are the 1980 First Interstate Bank fire in Los Angeles, USA, the 1990 Broadgate Phase 8 fire in London, UK, the 1991 Credit Insurance Building fire in

Churchill, UK, the 1991 One Meridian Plaza fire in Philadelphia, USA, and the 2004 Parque Central fire in Caracas, Venezuela [1-6]. All of these buildings, with the exception of One Meridian Plaza, were repaired and returned to service. After extensive investigations and studies, One Meridian Plaza was dismantled for economic reasons [6]. On the other hand, the 1970 One New York Plaza fire in New York, USA, the 1986 Alexis Nihon Plaza fire in Montreal, Canada, the 2001 World Trade Center fire in New York, USA and the 2005 Windsor Building fire in Madrid, Spain are examples of catastrophic fire damage to steel structures which led to complete collapse of the building [6-9]. The damages induced by fire can be further exacerbated by another hazardous event, such as an earthquake. It is well recognized that immediately after most major earthquakes in urban areas, a cluster of building fires occurs. The post-earthquake fire losses can at times be similar to those made by the ground movement alone. Under these circumstances, there is an expanded danger of fire sources, diminished or strained firefighting capacities, the presence of structural damage, and damage to the buildings' fire protection systems. The 1906 San Francisco earthquake, the 1923 Tokyo earthquake, the 1989 Loma Prieta earthquake, the 1994 Northridge earthquake, 1995 Kobe earthquake are some of the examples of post-earthquake fire disasters. As reported by Scawthorn *et al.* [10], 80% of 28000 buildings that were destroyed during the 1906 San Francisco earthquake and 77% of the 447000 houses that were destroyed by the 1923 Tokyo earthquake were caused by fire following the earthquakes. During the 1989 Loma Prieta Earthquake, San Francisco experienced 22 structural fires and over 500 reported incidents during the seven hours after the earthquake began [6]. During the 1994 Northridge earthquake, the Los Angeles Fire Department reported 476 fire incidents during almost a 20-hour period following the earthquake [6, 11]. During the 1995 Kobe Earthquake approximately 100 fires started within minutes of the quake, primarily in the densely populated, low-rise residential areas of Kobe, Japan. It was reported that several large conflagrations had developed within 1 to 2 hours, with a total of 142 fires and numerous collapses and destruction [6, 11]. Accessible authentic records do not clearly demonstrate any particular multi-story building failures because of post-earthquake fires. This may be the consequence of an absence of fiasco information and exact representing the resultant building

damages or collapses between the seismic tremor and blaze causes. Nevertheless, post-earthquake fires represent a serious danger to different varieties of development in their conceivably harmed post-seismic tremor state, both regarding their diminished structural and fire safety. While past experience does not give any immediate confirmation of such events in multi-story structures, the likelihood for this consolidated extreme hazard from both seismic tremor and fire exposures does exist.

Although significant loss to properties and human lives resulted during these fires, still the knowledge-base on structural steel building during and after fire is relatively unknown; especially when the structure involved in a fire survives. When a steel structure survives a fire, the safety and reparability of the structure depends on the extent of structural damage and the mechanical properties of structural steel of the connecting members [12-13]. On many occasions fire affected steelwork shows little or no distortion resulting in considerable uncertainty regarding its re-usability. An often quoted general rule for fire affected hot rolled structural steels is that if the steel is straight and there are no visible distortions then it is probably still fit for use. At 600°C the yield strength and stiffness of steel is equal to about 40% and 30% respectively of their room temperature values; it follows therefore that any steel still remaining straight after the fire and which had been carrying an appreciable load was probably not heated beyond 600°C, will not have undergone any metallurgical changes and will probably be fit for re-use [12, 14-18].

During post-fire structural damage evaluation, the structural members can be categorized into three types [12]- firstly, members that appear to be straight including slightly distorted members, which is not easily detected by visual observations (within 4-5 times of ASTM A6 [19] rolling tolerances), secondly, members noticeably deformed but could be heat straightened if economically justified, and finally, members severely deformed that only under extreme circumstances would repair be given any consideration. When the member is straight, it is generally assumed that the member has experienced temperatures less than 600°C, and hence, the member can be accepted unconditionally for re-use assuming no metallurgical change has occurred, whereas members with distortion may need to be investigated properly to elucidate whether they can be accepted unconditionally, or there is

need for any rehabilitation measures such as heat straightening, strengthening with steel plates or braces. On the other hand, for members with severe distortion, it is anticipated that there is major metallurgical change which may affect the load carrying capacity of the members. As a result, these types of members are usually replaced unless it is inappropriate or impossible to remove the member. Only in those cases, repair or strengthening is allowed.

Test data on the fire performance of structural steel members led to the notion that over 600°C the members start to deform noticeably, which become significant with increasing temperature based on the size of the members. Studies by Saul [14], Dill [20], Smith [16], Wright [21], Kirby *et al.* [22] showed that buckling and large deflection can occur at temperatures well below 650°C, whereas Kirby [23] and Li and Guo [24] observed substantial distortion in a temperature range of 700°C-900°C. Another study by Wald *et al.* [25] showed development of large buckle at temperatures over 1000°C, and they showed that the distortion of structural members not only depends on the peak temperature, but also on the fire exposure time. However, in the literature, the experimental test data pertaining to the fire performance evaluation of structural members consist of smaller beam and column sections, and hence, most of the beam-column specimens distorted considerably at relatively lower temperature range (600°C-800°C). Structures with large beam and column sections was not investigated under fire scenario, and hence, there is a possibility that they may be able to sustain very high temperatures (~1000°C) without severe distortion. As a result, the member will appear as if no or little distortion has taken place, nonetheless, there would be significant degradation in the material strength as a result of very high temperature exposure and subsequent cooling, which will be discussed later in this paper. Moreover, the peak temperatures will vary along the length and depth of the members leading to material heterogeneity in the fire exposed part of the structure. From the rehabilitation point of view, the members might have been accepted unconditionally or with minor repairs since they look nearly straight. Nobody knows how such type of fire damaged structure will perform if the structure faces an earthquake after being exposed to fire, which is the subject of this study.

Although the post-fire material strength degradation has been addressed in few studies [26-29], its influence on the seismic response of the structure has never been investigated. In

this study, seismic responses of special moment frames were investigated by performing finite element analysis to account for the influence of material strength degradation and heterogeneity due to fire exposure. A thermal analysis was performed to get the temperature distribution in beam-column members during and after fire exposure. Once the temperature distribution is obtained for each of the element in the finite element models, the material properties or model parameters were determined. Subsequently, seismic performance of the frames was investigated under simulated seismic loading history [30]. The results of the finite element analysis were evaluated to explore the seismic responses of fire damaged steel buildings.

2. Post-Fire Mechanical Properties of Steel

Since the objective of this study is to investigate the influence of post-fire change in the mechanical properties of structural steel on the seismic response of moment frames, hence it is essential to shed some light on the change in the mechanical properties of structural steel due to fire exposure and subsequent cooling to room temperature. Limited past studies have addressed the post-fire mechanical properties of structural steel [26-27]. However, the available experimental data pertinent to post-fire evaluation of structural steel is limited. Further, a review of the literature suggests that there is very little data available on the effects of heating and cooling on the mechanical properties of ASTM A992 steel, which is currently the most common structural steel used for rolled wide flange shapes in the U.S. Morrison [29] studied the change in the mechanical properties of ASTM A992 steel due to heating at elevated temperatures and subsequent cooling, where monotonic tension tests were performed on ASTM A992 steel coupons. The coupons were conditioned at different peak temperatures varying from 600-1200°C; hold the peak temperature for 15 minutes followed by air cooling until it reaches the room temperature. The stress-strain response of one set of monotonic tension tests is shown in Figure . It was observed that as the maximum temperature increased both the yield and ultimate stresses of the steel gradually decreased by downward shift of the stress-strain curves. The influence of temperature on the reduction of the yield stress was more noticeable in the temperature range of 800-1200°C, since steel

undergoes a phase change near 730°C from ferrite (α -Fe) to austenite (γ -Fe). As seen in Figure , up to 600°C, the yield stress was close to the room temperature value, and a 40% reduction in yield stress was observed for maximum temperature of 1200°C. Based on the observations from the experiments it can be concluded that if ASTM A992 steel is heated over 600°C followed by air cooling, the yield stress never goes back to the room temperature value upon removal of temperature, rather it reduces from that of the room temperature value. Another important observation made in this study was that the elastic modulus does not change with the peak temperature. A contemporary study by Lee and Engelhardt [28] observed similar responses for ASTM A992 steel, where they performed monotonic tension tests on ASTM A992 steel heated up to 1000°C followed by three different cooling conditions - air cooling, blanket cooling and water cooling. About 25% reduction in the yield stress was observed under blanket and air cooling conditions, whereas water cooling condition showed decrease in yield stress only at 800°C after which the yield stress started to increase. Moreover, the tensile strength increased with temperature under water cooling condition, while for blanket and air cooling conditions, the tensile strength decreased with temperature. It is obvious that the behavior of ASTM A992 steel is dependent on the peak temperature exposure and the corresponding cooling condition.

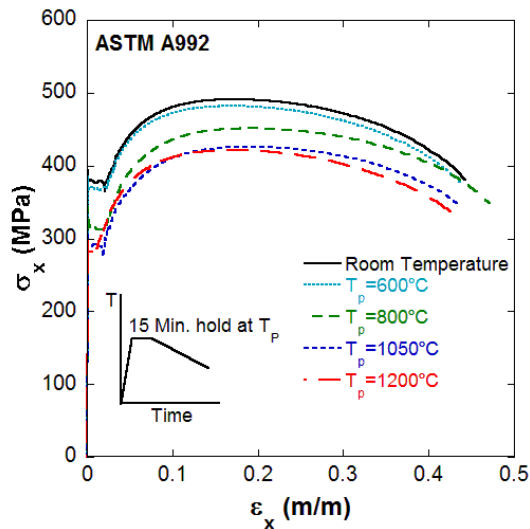


Figure 1 Monotonic stress-strain response of ASTM A992 steel heated at different peak temperatures followed by air cooling [29].

This study accounts for the post-fire change in the mechanical properties of structural steel to investigate its influence on the seismic response of steel structures by performing finite element analyses on steel moment resisting frames. The experimental data of Morrison [29] was used to characterize the post-fire material properties of ASTM A992 steel.

3. Seismic Analysis of Moment Resisting Frames with Fire Damage

The study reported herein dealt with finite element investigation of special moment frames under simulated earthquake loading history with and without fire exposure. The influence of material heterogeneity on the seismic performance of moment frames was investigated by performing nonlinear finite element analysis of a three story special moment resisting frame. A three story special moment frame was adapted from the study by Adan [31] to study the influence of post-fire material properties on the seismic response of the frame. The special moment frame was designed and detailed in accordance with the recommendations of AISC [32-33]. A schematic of the special moment frame adapted in this study is shown in Figure 2.

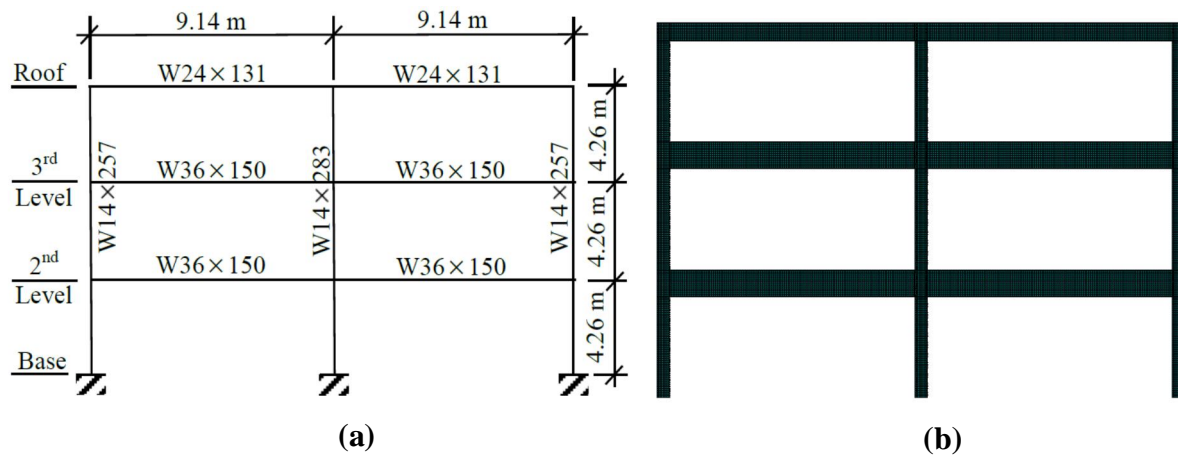


Figure 2 (a) A schematic of the special moment frame used in this study (adapted from Adan [31]), (b) finite element mesh developed for the frame analysis.

The frame consisted of two bays of 9.14 m length each and three stories with a height of 4.26 m. The frame comprised of W36x150 beams in the 2nd and 3rd levels with W24x131

beams in the roof level. The exterior column size was W14×257, while interior column size was W14×283. The connection between beam-to-column was designed as welded unreinforced flange welded web (WUF-W) connection. The factored uniformly distributed load on the beam was assumed to be 14.6 kN/m, whereas the factored axial load on the column was assumed to be 444 kN as adopted by Adan [31].

3.1. Finite Element Modeling

Three dimensional finite element models were developed for the special moment frame as shown in Figure 2a by using the finite element analysis software ANSYS. The frame was discretized by 8-noded solid elements, and both geometric and material nonlinearities were considered. The FE mesh developed for the special moment frame is shown in Figure 2b. The frame assembly was assumed to be made of ASTM A992 steel, and both the room temperature and post-fire material properties of ASTM A992 steel was obtained from the study by Morrison [29]. The multilinear kinematic hardening model was used in the finite element simulation to characterize the material behavior and the material model parameters were obtained by fitting the stress-strain response of ASTM A992 at different temperatures as shown in Figure . For the simplification of the analysis and to reduce the computational time and cost, the weld access hole and the shear tab was excluded in the frame analysis. Since the purpose of the study was to investigate the global performance of the frame, the exclusion of weld access hole or shear tab would not be much influential. The finite element frame models were investigated under a displacement-based artificial loading protocol offered by SAC/BD-97/02 [30]. The displacement based time history was based on the SAC Test Protocol and consisted of imposing a series of prescribed quasi-static cyclic displacements to the top of the building frame. The prescribed displacements included six cycles of 0.375, 0.5 and 0.75% interstory drift, followed by four cycles of 1% interstory drift and two cycles each of 1.5, 2, 3, 4, 5, 6% and so forth interstory drift. A schematic of the loading protocol is shown in Figure 3. The frame was analyzed for room temperature condition followed by four fire case studies based on fire in different compartments. The four fire cases are defined as follows:

Fire Case-I: Fire in left compartment at 1st story

Fire Case-II: Fire in both compartments at 1st story

Fire Case-III: Fire in left compartment at 2nd story

Fire Case-IV: Fire in both compartments at 2nd story

Before performing detail finite element investigation of the special moment frame under different fire scenarios, it is important to define a time-temperature history to characterize the fire event and a distortion analysis need to be performed on the moment frame using the defined time-temperature history to ensure selection of a peak temperature which will not cause severe deformation in the frame members.

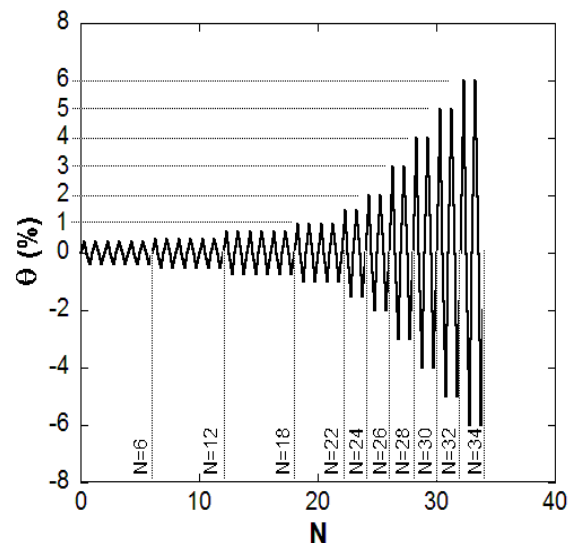


Figure 3 Displacement based simulated earthquake loading history [30].

3.2. Distortion Analysis of a Single Story Moment Resisting Frame during Fire

In order to study the influence of material heterogeneity induced by fire exposure, the distribution of temperature across the members need to be determined during a fire scenario by performing a thermal heat-transfer analysis. Based on the peak temperature of each of the elements in the FE model from the thermal analysis, the relevant mechanical properties of structural steel will be assigned to each of the element in the seismic analysis. However, the thermal analysis requires a specific time-temperature history to adequately represent a real

fire event. In this study a realistic fire time-temperature curve, which includes a cooling phase, is used instead of the more traditional standard fire curves such as those presented in ASTM E-119 [34] and ASTM E-1529 [35]. The selected curve is taken from a study by Quiel and Garlock [36] and provides an accurate representation of a typical compartment fire seen in office buildings. The realistic time-temperature curve used for this study can be seen in Figure 4a compared to the standard fire curves presented in ASTM E-119 and ASTM E-1529. It can be observed that the peak temperature of the prescribed time-temperature curve in this study was around 1000°C, and it is not known whether the beam and column sections in the current study will be significantly distorted at this peak temperature level. Since the main focus of this study is to investigate the influence of post-fire mechanical properties of steel on the seismic performance of moment frames, it is assumed that the damage of the frame members from fire exposure will be accepted unconditionally or with minor repairs before being re-used. Hence, a coupled thermo-mechanical analysis was performed for a single story of the special moment frame shown in Figure 2a, to investigate whether there is any substantial distortion in the connecting members during fire exposure. The thermo-mechanical analysis will enable to establish the peak temperature for the fire time-temperature curve. The thermo-mechanical analysis was performed under gravity loading, where a factored uniformly distributed load of 14.6 kN/m was assumed on the beam, whereas a factored axial load of 444 kN was assumed on the column. Supports were provided in the out-of-plane direction at every 1.83 m distance along the length of the beam to avoid the out-of-plane bending of the beam section. Figure 5 shows the finite element mesh of the single story two bay moment frame used for the thermo-mechanical analysis, where the frame was discretized by 8-noded solid elements. To reduce the computational time and cost, a coarser mesh was used. The distortion analysis was performed considering two fire scenarios-fire in a single compartment, and fire in both compartments.

Thermal analysis was performed on the moment frame in order to get the real time temperature distribution during the fire event and subsequent cooling. For the thermal finite element analysis, temperature was given as input with time as presented in Figure 4a (red line). The temperature was assigned to the bottom surface of the beam bottom flange and

inside surface of the column flanges in order to simulate the real compartment fire scenario. The fire temperature initially increases with time up to 20 minutes when it reaches the peak temperature of 1000°C, where it is held constant for 30 minutes before the start of the air cooling process. The air cooling was simulated in thermal finite element analysis by allowing free heat transfer in all directions. Heat loss occurred from the material surface through both convection and radiation, which were related to the heat transfer coefficient. The temperature-dependent material properties (specific heat, thermal conductivity, enthalpy, heat transfer coefficient) of structural steel were used in the heat transfer analysis, where the material parameters were defined as a function of temperature. Latent heat/phase transformation was accounted for by defining enthalpy of the material as a function of temperature.

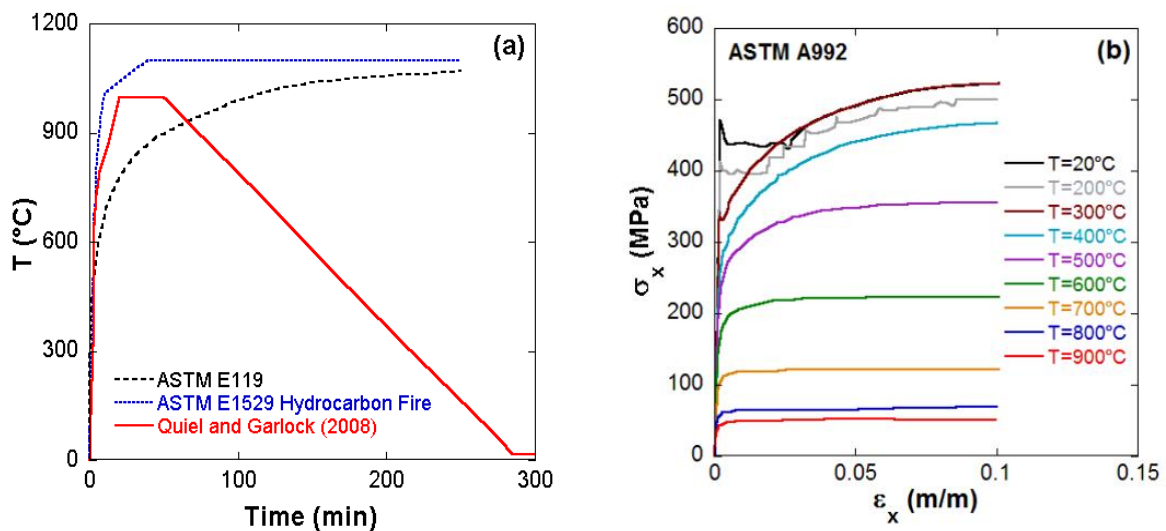


Figure 4 (a) Time-temperature curves to represent a fire scenario, (b) monotonic stress-strain response of ASTM A992 steel at elevated temperatures [37].

Figure 6a shows the distribution of temperature in the moment frame after 50 minutes of fire exposure in the left compartment only. It is observed that the temperature at beam bottom flange and column inside flange was 1000°C. However, the temperature at the web of the beam located close to the bottom flange reached a temperature of 800-900°C, and as the

distance increased along the depth of the beam there was a decrease in the temperature. It was noted that after about one-third distance away from the beam bottom flange, the temperature of the beam web was almost close to the room temperature. As a result, the material properties of structural steel will be heterogeneous along the depth of the beam. The beam bottom flange and the beam web close to the bottom flange will experience major change in the material properties because of very high temperature exposure (800-1000°C), whereas the beam web one-third distance away from the bottom flange and the beam top flange will experience no change in the material properties. Similar type of temperature variation along the depth of the column was observed, where the inside flange of the column experienced 1000°C while the outside flange was at room temperature. The temperature distribution in the column web was variable where the temperature reached room temperature value about two-third distance away from the inside flange. This will induce material heterogeneity along the depth of the columns as well. Similar observations were made in the temperature distribution in the moment frame when both the compartments were subjected to fire (Figure 7a). The beam and the exterior columns showed the same trend in the temperature distribution as was observed for single compartment fire, however, unlike exterior column, in the interior column both the flanges experience 1000°C, and the temperature varied from 800°C-360°C along the depth of the web.

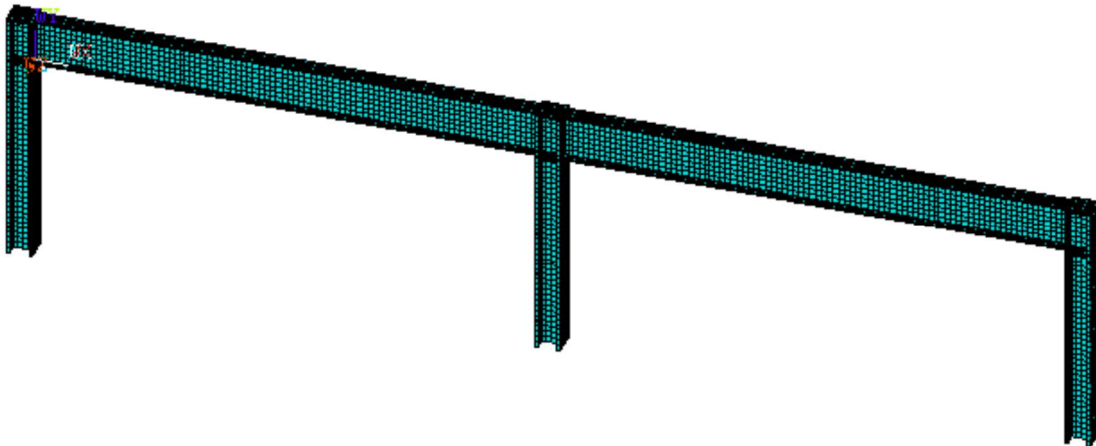


Figure 5 Finite element mesh developed for thermo-mechanical analysis of a single story two bay moment frame.

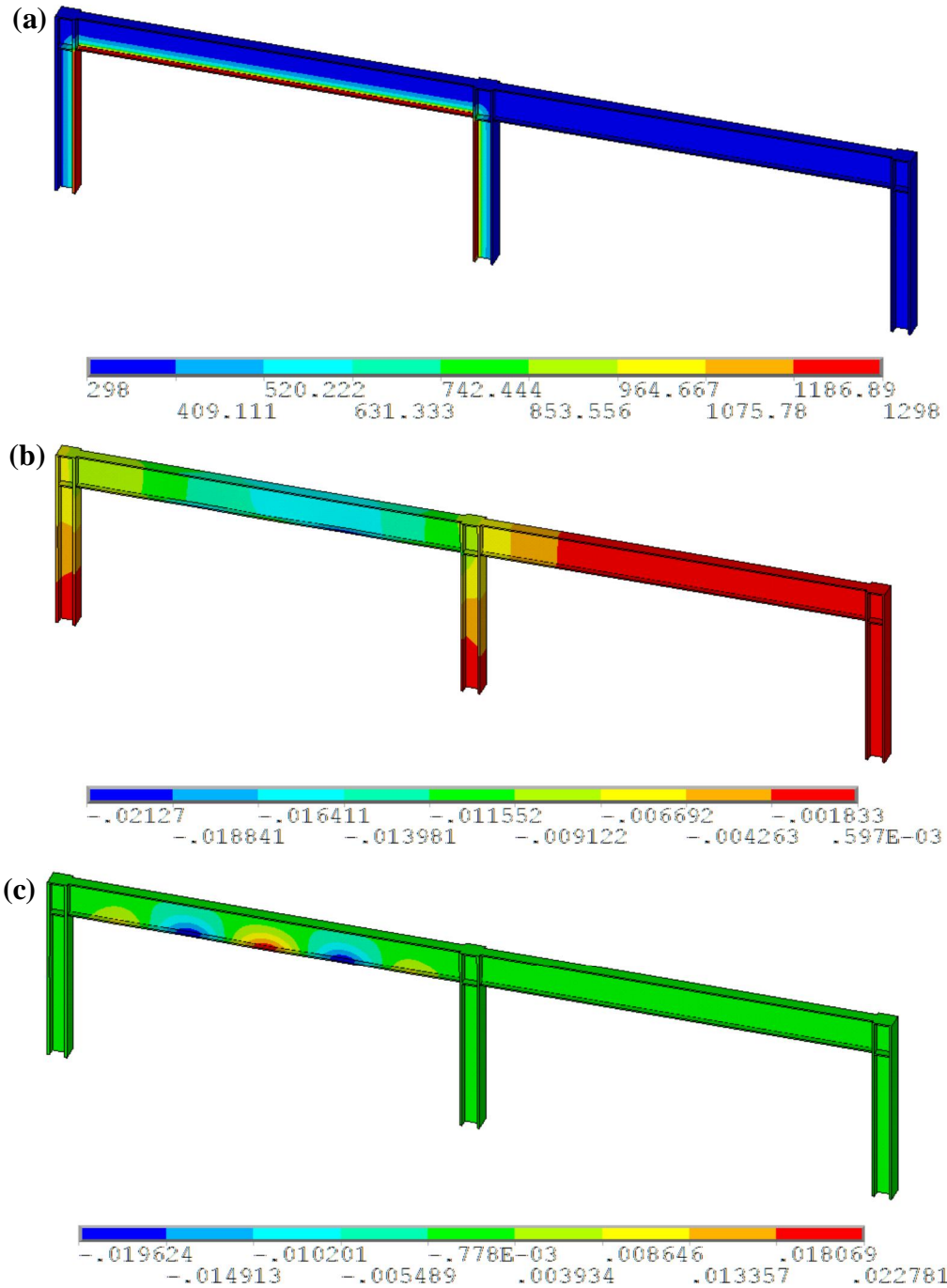


Figure 6 Response of a single story frame with fire in a single compartment. (a) Temperature distribution (in Kelvin) at the end of peak temperature exposure (50 minutes), (b) vertical deflection (in meter), and (c) out-of-plane deflection (in meter) at the end of the cooling phase.

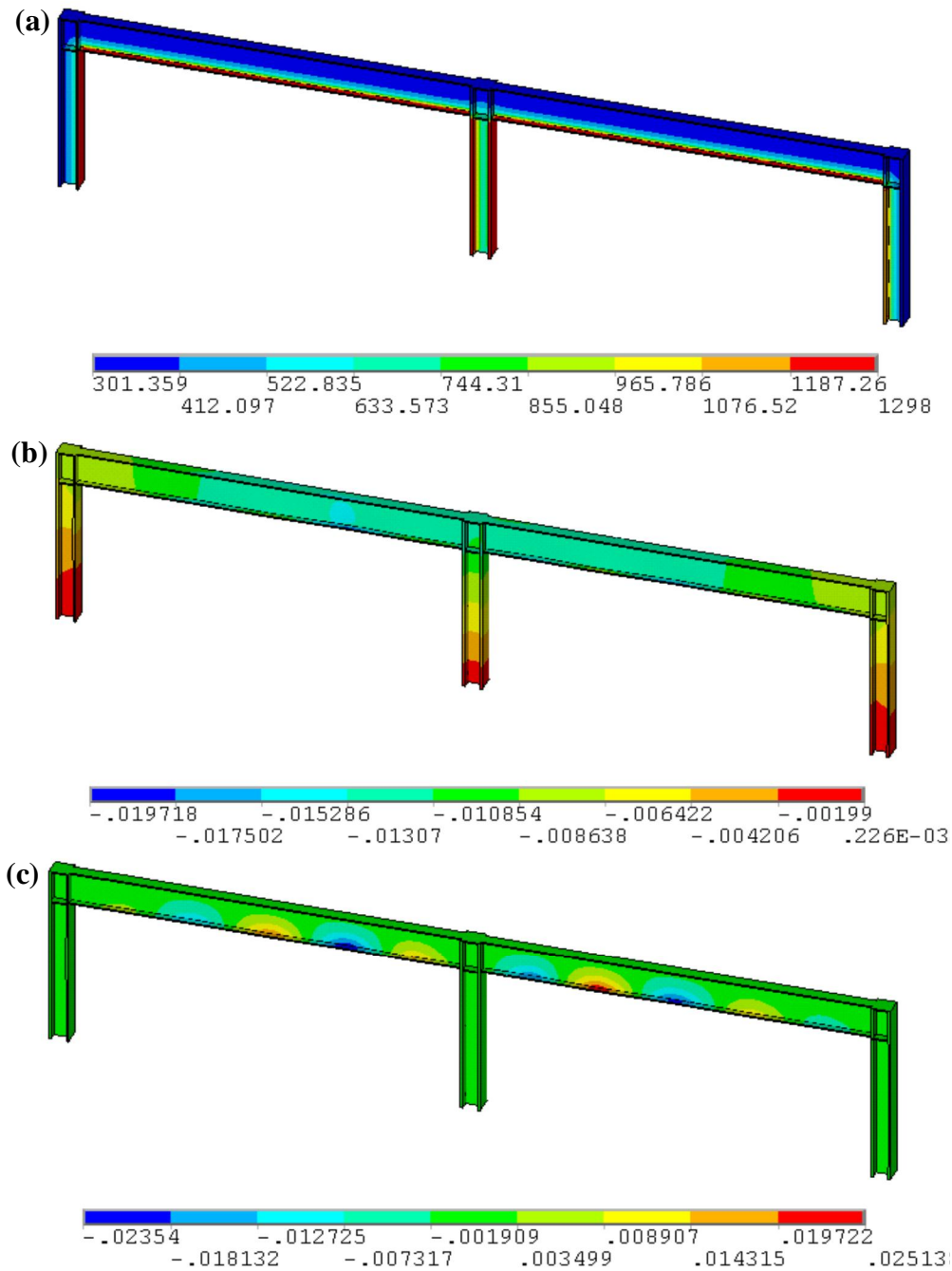


Figure 7 Response of a single story frame with fire in both compartments. (a) Temperature distribution (in Kelvin) at the end of peak temperature exposure (50 minutes), (b) vertical deflection (in meter), and (c) out-of-plane deflection (in meter) at the end of the cooling phase.

Once the heat-transfer analysis was finished, structural analysis was performed under gravity loading by changing the thermal solid elements to structural solid elements, where the results from the solution of the thermal environment was coupled to the information provided in the structural environment. In the structural analysis of the frame, temperature dependent mechanical properties of ASTM A992 steel were used with relevant constitutive equations. The mechanical properties used in the structural analysis were density, elastic modulus, initial yield stress, Poisson's ratio and coefficient of thermal expansion. The elevated temperature stress-strain response of ASTM A992 steel under monotonic tension loading was obtained from Hu *et al.* [37] as shown in Figure 4b. The elevated temperature stress-strain response of ASTM A992 steel was implemented in the finite element simulation by using multilinear kinematic hardening model available in ANSYS which incorporates von-Mises yield criterion and associative flow rule. The multilinear kinematic hardening model parameters were obtained through fitting the stress-strain response of A992 steel. Note that there was no material data available for temperatures over 900°C, for which linear interpolation method was used to obtain the model parameters. Figure 6b and Figure 6c show the deformation in the vertical and out-of-plane direction of the frame at the end of the cooling phase after fire exposure in a single compartment. It can be observed that the maximum vertical and out-of-plane deflections were 21.7 mm and 22.7 mm at the end of the cooling phase, which is only twice the values permitted by ASTM A6 [19] for variation in straightness of W shapes. Similarly when both the compartments were subjected to fire (Figure 7b and Figure 7c), the maximum vertical and out-of-plane deformations observed were 19.7 mm and 25.1 mm respectively, which are not significantly large compared to the values permitted by ASTM A6 [19] for variation in straightness of W shapes. Hence, based on the observed deformation values it is quite obvious that the frame did not incur major structural distortion, which can be accepted unconditionally, or recovered by minor heat straightening if necessary. Therefore, the members of the special moment frame adapted in this study should not distort significantly under the prescribed fire condition, and hence, could be used further to investigate the influence of material heterogeneity on the seismic response.

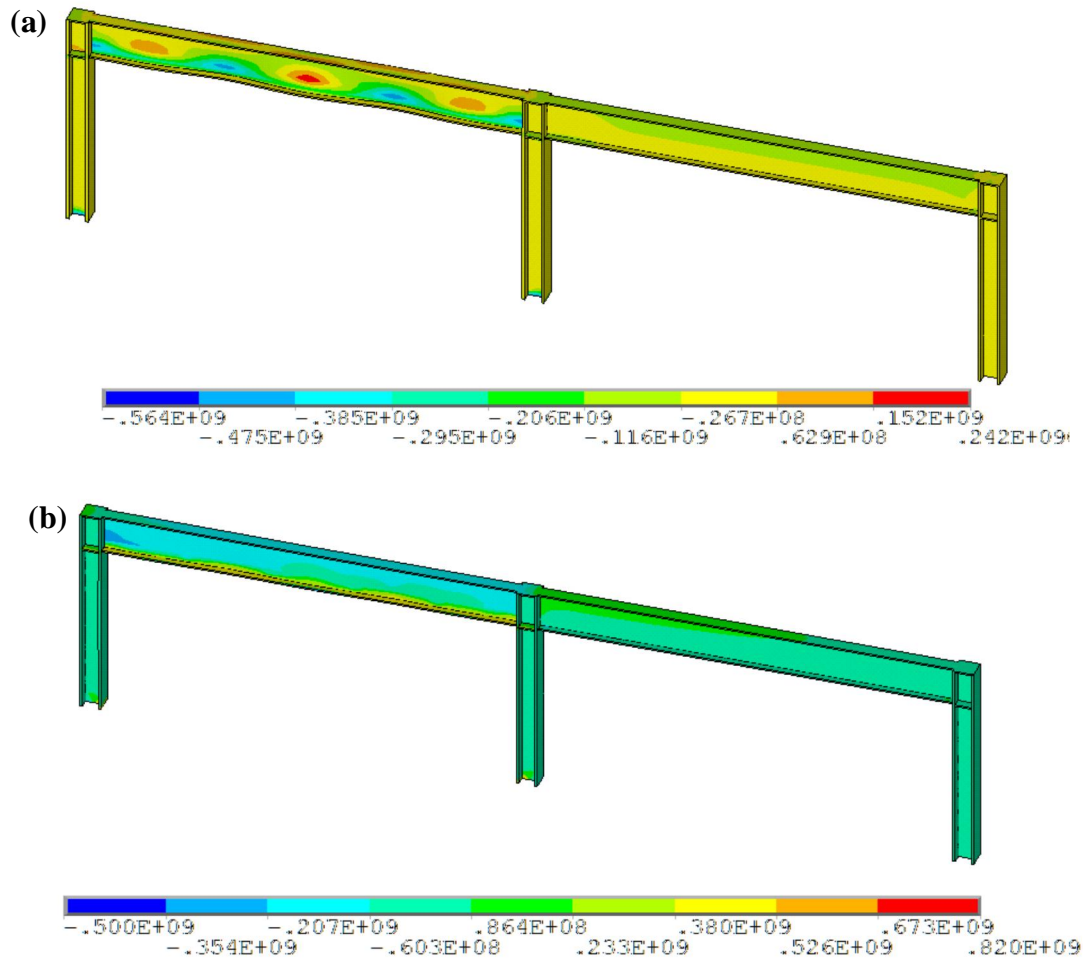


Figure 8 Stress (in Pa) in longitudinal direction of a single story frame with fire in a single compartment. (a) At the end of peak temperature exposure (50 minutes), (b) at the end of the cooling phase.

It is important to note here that the out-of-plane deformation was predicted by the global finite element models despite the fact that initial imperfections were not assigned to the geometry of the model. Typically, finite element models require the inclusion of initial imperfections to predict out-of-plane deformation; however, for the models considered in this study out-of-plane deformation was predicted even though the initial prescribed geometry was perfect. The out-of-plane deformation observed in the moment frame for both the cases

with single and two compartment fire was due to the thermal contraction and expansion of the beam as a result of the fire exposure and subsequent cooling. The thermal expansion during the fire exposure led to high compressive stresses in the bottom flange of the beam and the lower part of the beam web, whereas tensile stresses developed at the top flange of the beam and upper part of the beam web (Figure 8a). As a result, noticeable buckling was observed at the beam bottom flange and beam web. During the cooling phase, due to thermal contraction, the compressive stresses developed at the bottom flange and lower part of the beam web transmitted to tensile stresses, whereas the tensile stresses developed at the top flange and upper part of the beam web became compressive (Figure 8b). As a result, the deformation on the beam bottom flange and lower part of the beam web decreased. This decreased the out-of-plane deformation of the frame. This is clearly seen in Figure 9a where the axial stresses at three different locations of beam cross-section is plotted against time at the centerline along the beam length. The out-of-plane deformation at the same locations are also plotted in Figure 9b.

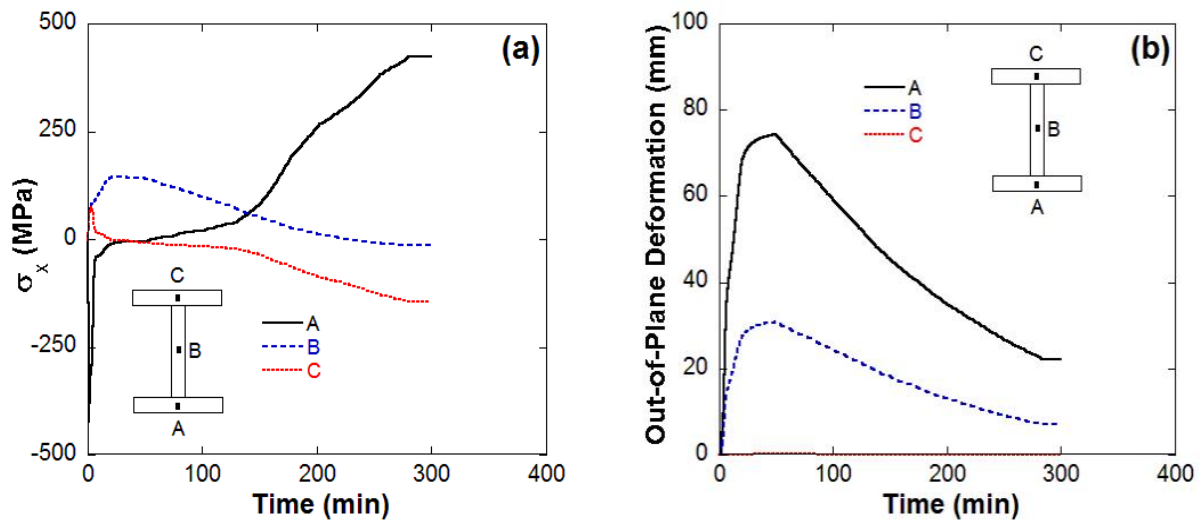


Figure 9 (a) Stress in longitudinal direction, and (b) out-of-plane deformation at three different locations across the beam cross section along the centerline of the beam length.

3.3. Seismic Response of Fire Damaged Moment Resisting Frames

As already mentioned, the special moment frame shown in Figure 2 was investigated for room temperature and four different fire scenarios. In Fire Cases-I and III, a single compartment was subjected to fire in 1st and 2nd story of the frame respectively, whereas in Fire Cases-II and IV, both the compartments were subjected to fire in 1st and 2nd story of the frame respectively. The temperature distribution in the frame for Fire Cases-I and III were obtained from the thermal analysis of single story frame with one compartment fire used in the distortion analysis of the frame (Figure 6a). Similarly, the temperature distribution in the frame for Fire Cases-II and IV were obtained from the thermal analysis of single story frame with fire in both compartments used in the distortion analysis of the frame (Figure 7a). The material properties of ASTM A992 steel were defined at different locations of the moment frame based on the temperature distribution obtained from the thermal analysis.

To study the seismic behavior of the special moment frame at room temperature the simulated earthquake loading history was applied at the roof level of the frame up to 6% interstory drift angle. The frame was designed based on the strong column-weak beam philosophy, and hence, all the connections in the frame showed development of plastic hinges in the beam flanges as shown in Figure 10a, where the equivalent plastic strain contour is plotted for the entire frame. Zoomed views of the exterior (left) and interior connections at the 3rd level of the frame are also shown in Figure 10c and Figure 10d respectively. The base shear-interstory drift angle response of the frame (Figure 10b) shows that the frame started to loose strength at 4% interstory drift angle with a gradual decrease in the strength of the frame with loading cycles. The reduction in the strength at 6% interstory drift angle was 17% which indicates very stable response of the frame. The lateral and out-of-plane displacement contours of the frame are plotted in Figure 11a, and b respectively. The lateral displacement profile of the frame showed that in each story the drift was about the same, and hence, the energy was dissipated over the entire height of the building which resulted in lower maximum drift demands. On the other hand, the out-of-plane displacement contour shows that the beam-column assemblies developed significant buckles in the beam flanges and web, which resulted in out-of-plane deformation of the beam, and the maximum

value of the out-of-plane deformation obtained was around 92.5 mm for loading up to 6% interstory drift angle. When fire damage was included in the finite element analysis by incorporating post-fire material heterogeneity, it was observed that the strength of the frame decreased regardless of the fire case.

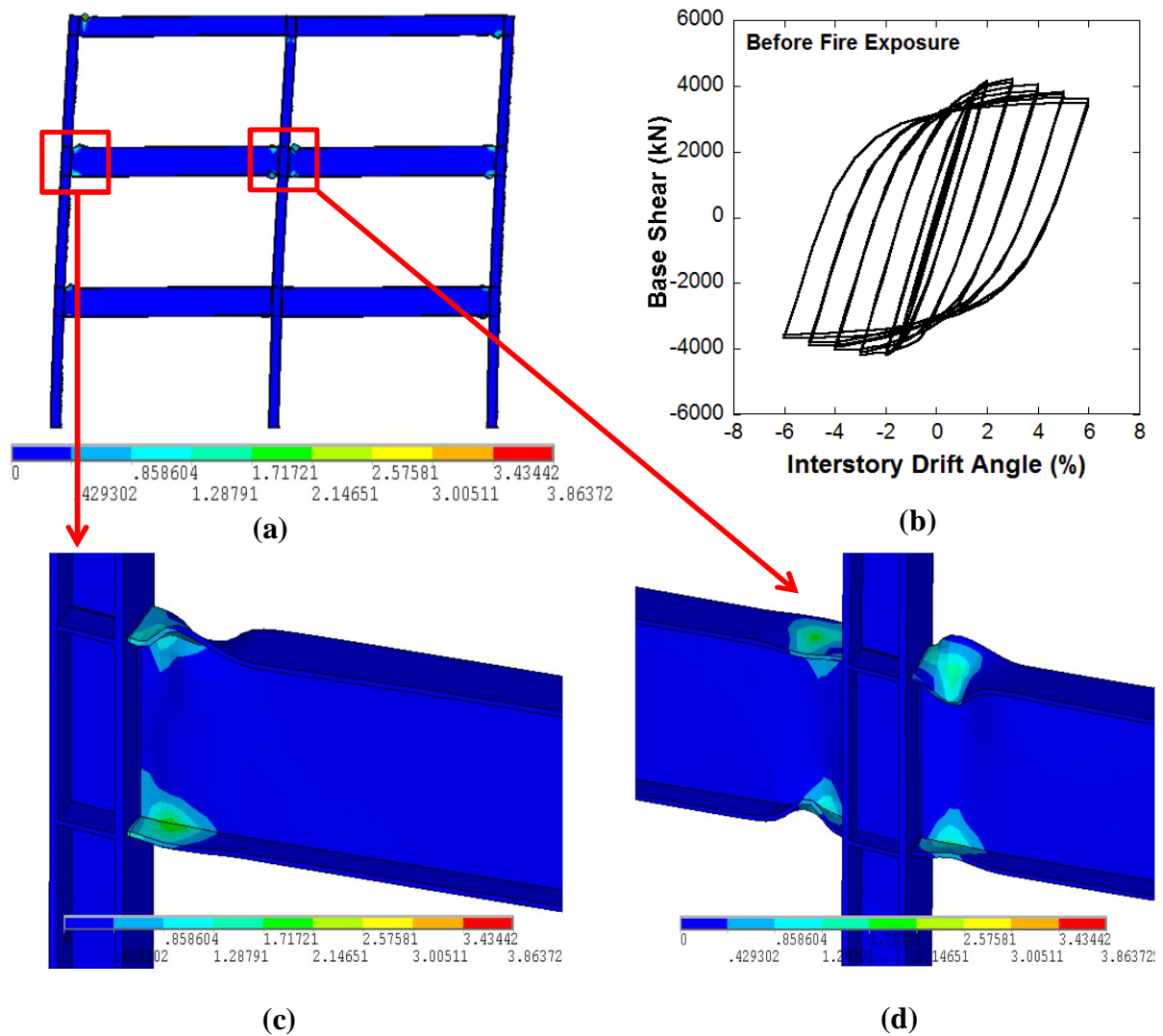


Figure 10 Cyclic response of the frame at room temperature. (a) Equivalent plastic strain contour of the frame at 6% interstory drift angle, (b) base shear plotted against interstory drift angle showing hysteresis response of the frame, (c) equivalent plastic strain contour of the exterior (left), and (d) interior connection at the 3rd level at 6% interstory drift angle.

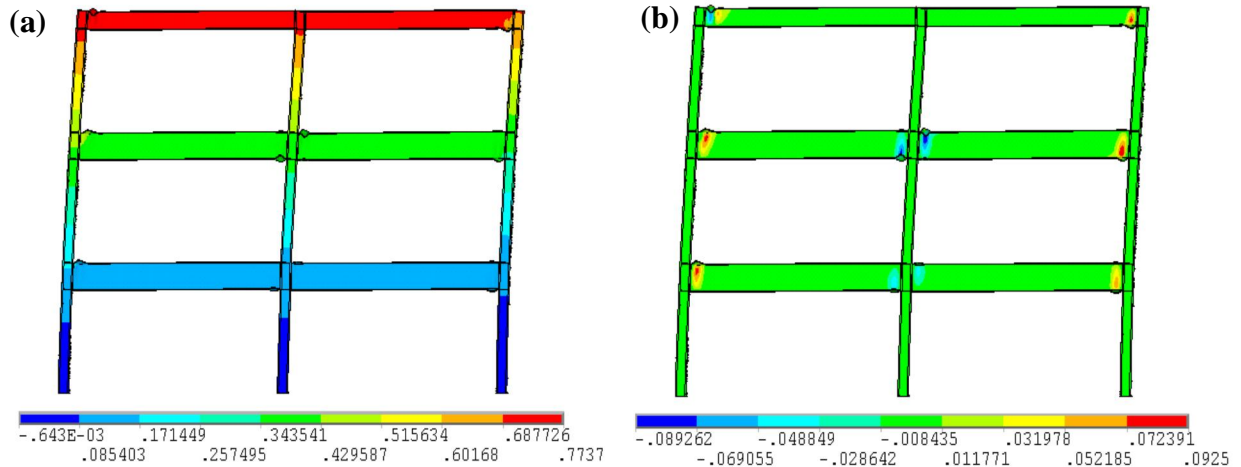


Figure 11 Displacement contours (in meter) of the frame at room temperature at 6% interstory drift angle. (a) Lateral displacement, (b) out-of-plane displacement.

For Fire Cases-II and IV where both compartments were exposed to fire in a story, the reduction in strength was more compared to Fire Cases-I and III, where only one compartment was exposed to fire. The hysteresis responses of the frame for different fire cases are shown in Figure 12, where it can be observed that the basic pattern of the hysteresis response with fire damage was similar to the room temperature hysteresis response with reduced peak forces at each loading cycles. The envelope of the positive and negative peak lateral forces are compared in Figure 13a for different fire cases with room temperature response. For Fire Case-I only 4% reduction in strength of the frame was observed, whereas Fire Cases-II and III yielded 5% reduction in strength. On the other hand, Fire Case-IV showed 8% decrease in the lateral strength. It was observed that the hysteresis responses were symmetric for all the fire cases. However, although the material strength degradation in the fire exposed members was not influential in the overall strength of the frame, the interstory drift demands of the frame was significantly affected by the material strength degradation and heterogeneity. For Fire Case-I, only the left compartment on 1st story was involved in fire. As a result, the beams and columns in the compartment experienced high temperature and degradation in material strength. Consequently, the 1st story possessed lower

lateral strength compared to the adjacent stories and hence, more lateral deformation took place at the 2nd level indicating higher maximum drift demands at the 2nd story level. As shown in Figure 13b, nearly all of the lateral displacement occurred at the 2nd story level, and the upper stories did not show much movement relative to the adjacent stories. Similar observations were made for Fire Case-II where both the compartments at 1st story were involved in fire.

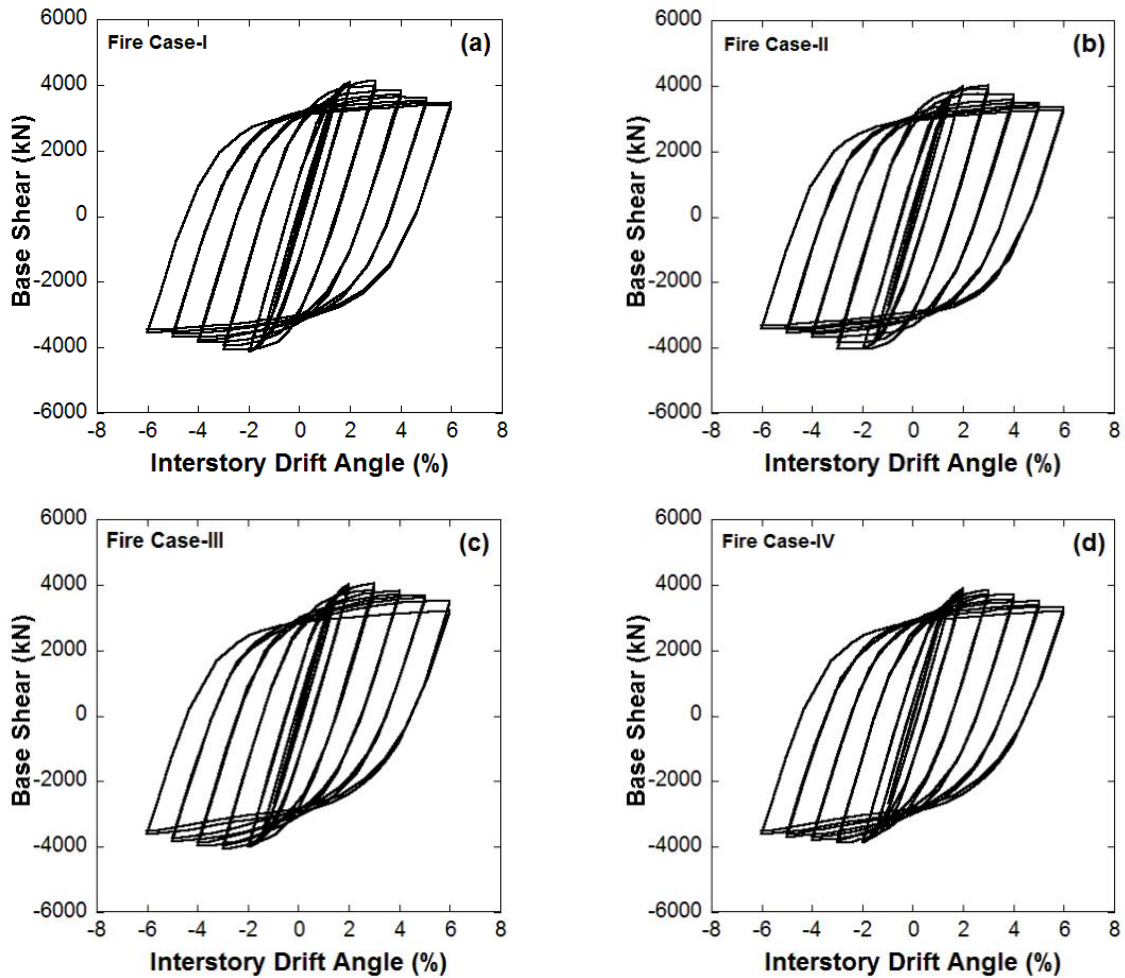


Figure 12 Hysteresis response of the frame for different fire cases.

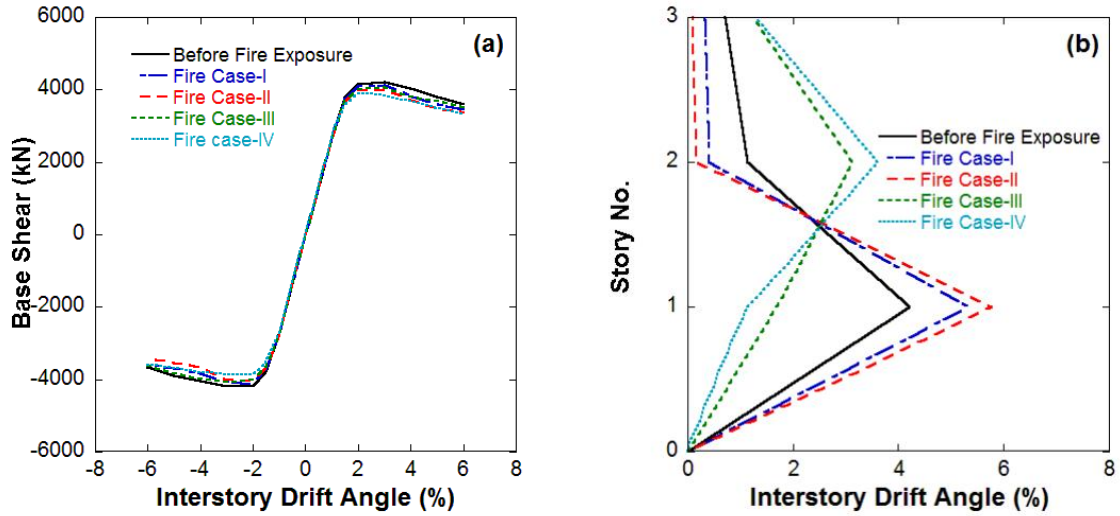


Figure 13 Comparison of frame responses at room temperature and different fire cases. (a) Peak positive and negative lateral forces at each loading cycle plotted against interstory drift angle, (b) interstory drift angles at each story level.

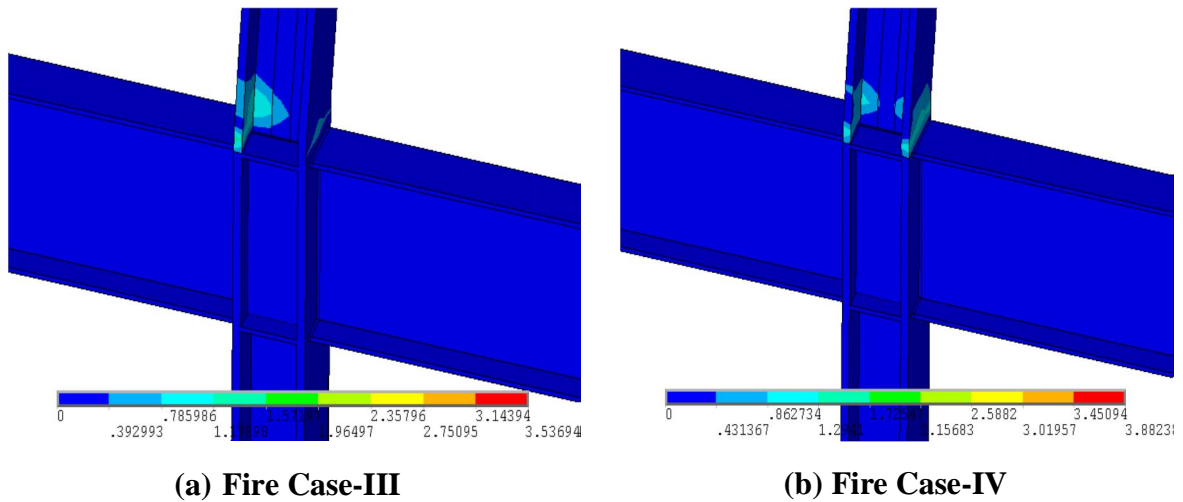


Figure 14 Formation of plastic hinge in the interior column at the 2nd level. (a) Fire Case-III, (b) Fire Case-IV.

Since two compartments were exposed to fire, the lateral strength at the 1st story was even less than Fire Case-I and as a result, the maximum drift demands at the 2nd level was even higher compared to Fire Case-I. On the other hand, for Fire Cases-III and IV, compartments at 2nd story were exposed to fire. Similar to Fire Cases-I and II, the maximum drift demands now increased at the 3rd level indicating significant reduction in lateral strength at the 2nd story. As shown in Figure 13b, for Fire Case-III, at the 2nd level, the interstory drift angle was around 1.7%, whereas, at the 3rd level, the interstory drift angle was around 3.1% indicating more than 50% of the total drift occurring at the 3rd level. For Fire Case-IV, where two compartments at the 2nd story were exposed to fire, the maximum drift demands at the 3rd level increased even more compared to Fire Case-III, In this case, 67% of the total story drift was occurring at the 3rd story level. It was interesting to note here that for Fire Cases-III and IV, where compartments at the 2nd story were exposed to fire, the interior connection at 2nd level did not exhibit development of plastic hinges in the beam flanges, rather plastic hinges started to develop at the column as shown in Figure 14. Since the 2nd story was weaker in the lateral direction compared to 1st and 3rd stories, an inflection point developed between the relatively stiff 1st story and weak 2nd story. This indicates a weak column-strong beam mechanism, which is essentially undesirable mode for seismic applications. Based on the responses, it is quite obvious that when compartments at any specific story are exposed to fire, the story becomes weaker or more flexible than the other stories. Consequently, there is significant reduction in the lateral strength at that story level which leads to very high drift demands. This is a sign of development of single story mechanism commonly known as soft story which may lead to catastrophic failure of the whole structure. The post-fire change in the material properties not only influenced the lateral deformation of the frame, but also the out-of-plane deformation. The out-of-plane displacement contours for the fire cases are shown in Figure 15. The same plot for the frame at room temperature was shown in Figure 11b. It can be observed that for all fire cases as well as at room temperature, severe buckling occurred in the beam flanges and web close to the connection region, except Fire Cases-III and IV where the interior connection at the 2nd level did not show buckling in the beam.

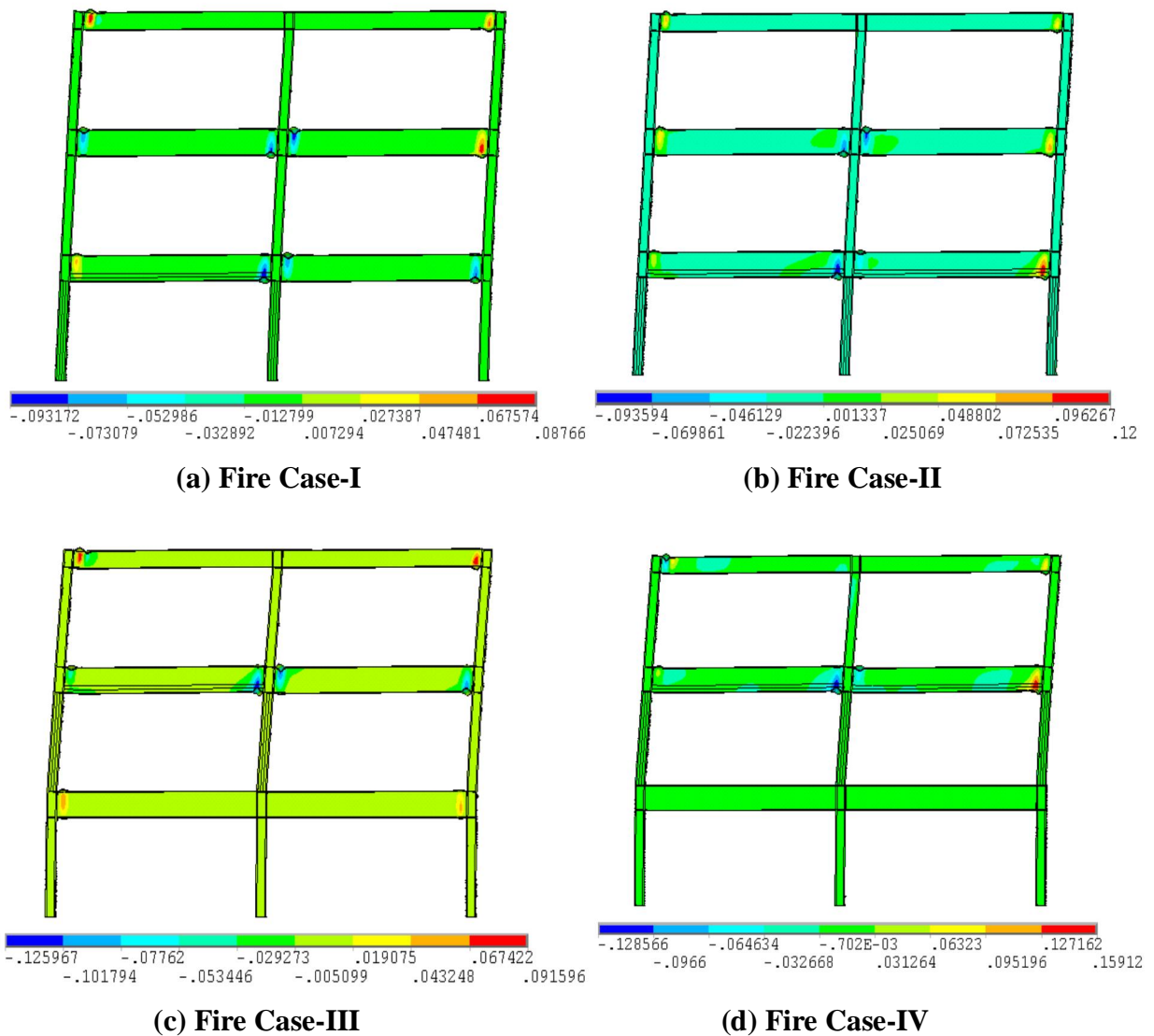


Figure 15 Out-of-plane displacement contours (in meter) of the frame for different fire cases.

This is a common phenomenon observed in large inelastic loading cycles during the cyclic testing of beam-column assemblies which initiates instability in the connection assemblies. Comparing the contour plots of Figure 11b and Figure 15, it can be observed that post-fire material strength degradation increased the out-of-plane deformation in the beam corresponding to the fire exposed compartment. However, for Fire Case-I, the out-of-plane

deformation was insensitive to the post-fire material strength, whereas for fire cases-II, III and IV, the increase in the out-of-plane deformation were 20%, 37%, 72% respectively. This manifests that the fire damaged structures will be susceptible to early instable behavior compared to the structures without fire damage. Therefore, based on the responses from the analyses performed in this study it is apparent that if a steel building does not experience severe distortion during a fire event and is rehabilitated for continued service, it may be vulnerable to earthquake loading due to the post-fire material strength degradation and heterogeneity. Hence, it is essential that the post-fire material strength be investigated regardless of the distortion level before making a decision on the re-usability or reparability of the structure.

3.4. Seismic Response of an Exterior WUF-W Connection with Fire Damage

To characterize the influence of post fire material properties of the structural steel on the seismic response of moment connections, an exterior welded unreinforced flange welded web (WUF-W) moment connection was chosen from the reference special moment frame as shown in Figure 16a. The finite element model developed for the exterior WUF-W connection is shown in Figure 16b, where the beam and column were modeled and discretized by 8-noded solid brick elements and the presence of weld access hole and shear tab was included. A finer mesh was considered along the beam and column length in the vicinity of the beam-to-column connection, and also in the column panel zone where majority of the inelastic action occurs. The other regions of the connection will remain elastic and hence, coarser mesh was used in those places to reduce the computational time and cost. Initially the connection was investigated at room temperature under the simulated seismic loading history. In the finite element simulation, the support conditions of the specimens were chosen to represent the theoretical inflection points of the beam and the column in a typical frame building. The specimen supports were designed to mimic the support conditions of hinge support. The specimen was treated as a cantilever beam connected to the column flange and the far end of the beam was subjected to the simulated earthquake loading history. The equivalent plastic strain contour and the moment-rotation hysteresis responses

for the WUF-W connection under simulated seismic loading history at room temperature are shown in Figure 17. It was observed that the connection developed plastic hinges in the beam flanges away from the welded joint (Figure 17a) with a symmetric moment-rotation hysteresis response. The moment-rotation plot (Figure 17b) showed that the connection started to loose strength after 2% interstory drift angle, and there was gradual decrease in the strength of the connection with loading cycles at higher interstory drift angles. The decrease in the strength of the connection at 3%, 4%, 5% and 6% interstory drift angles were 13%, 24%, 31% and 40%, respectively under both positive and negative bending, which indicates that considerable amount of energy can be dissipated by the WUF-W connection at room temperature.

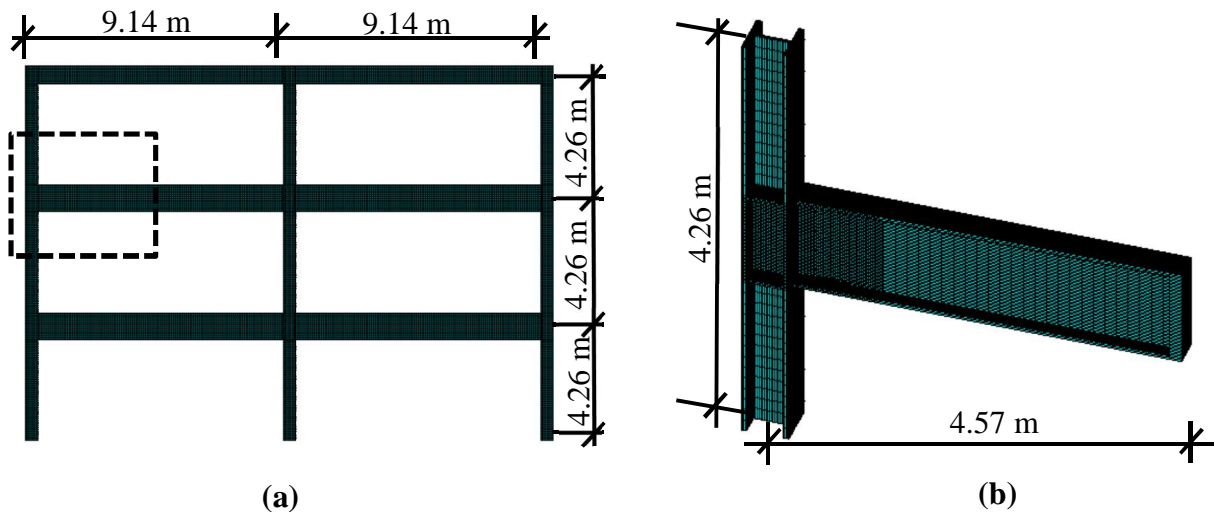


Figure 16 (a) Reference special moment frame showing an exterior WUF-W connection taken for the study, (b) finite element mesh of the external WUF-W connection.

To study the post-fire seismic performance of this connection, a thermal analysis was performed on the connection to get the temperature distribution during and after the fire event. Once the temperature history was obtained for each of the element from the thermal analysis, the material parameters for each of the element was obtained by considering the peak temperature of the element during the temperature history. The post-fire material

properties of ASTM A992 steel was obtained from the experimental tests performed by Morrison [29] and implemented in ANSYS by using multilinear material model. Figure 18a shows the temperature distribution in the connection after being exposed to the peak temperature level in the prescribed time-temperature curve (Figure 4a). The distribution is similar to the one that has been observed in the single story moment frame distortion analysis where only one compartment was subjected to fire, and hence won't be discussed here to avoid repetition. However, the contour plot clearly shows the variation of temperature along the depth of the beam and columns with temperatures as high as 1000°C, and as low as room temperature.

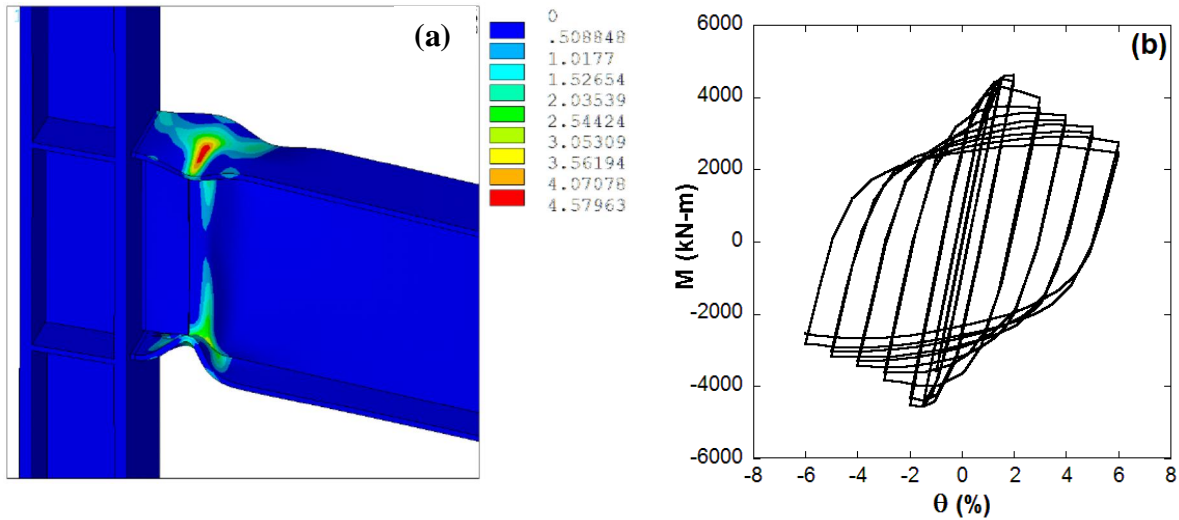


Figure 17 Response of WUF-W connection at room temperature under simulated seismic loading history. (a) Equivalent plastic strain contour showing formation of plastic hinges, (b) moment-rotation hysteresis response.

Once the temperature distribution was obtained from the thermal analysis, structural analysis was performed on the connection under simulated seismic loading history. The equivalent plastic strain contour of the connection is shown in Figure 18b. Similar to the response of WUF-W connection at room temperature, the WUF-W connection with fire damage developed plastic hinges away from the welded region, but the beam bottom flange

exhibited more deformation compared to the top flange. This was anticipated since the bottom flange was exposed to higher temperature (1000°C) compared to the top flange which led to material strength degradation at the bottom flange, whereas the top flange maintained the room temperature material strength. This led to an unsymmetrical moment-rotation hysteresis response (Figure 19a), where the degradation under negative bending was significantly higher than that under positive bending. Under positive bending, the connection showed increase in strength up to 2% interstory drift angle, and afterwards the strength started to degrade gradually. The reduction in the strength at 3%, 4%, 5% and 6% interstory drift angles were around 5%, 13%, 20% and 28% respectively.

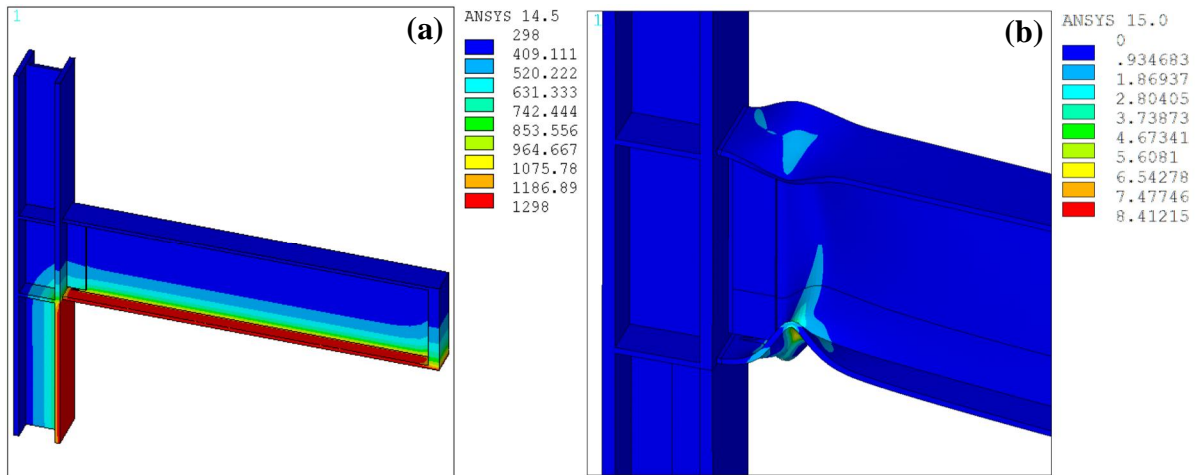


Figure 18 (a) Temperature distribution (in Kelvin) at the peak temperature level of fire exposure in the WUF-W connection, (b) equivalent plastic strain contour of fire damaged WUF-W connection showing formation of plastic hinges.

On the other hand, under negative bending, the connection showed increase in strength up to 1.5% interstory drift angle followed by a 12% decrease at 2% interstory drift angle. At higher interstory drift angles such as 3%, 4%, 5% and 6%, the strength decreased by 28%, 43%, 55% and 64% respectively. The decrease in the strength of the fire damaged connection at 4% interstory drift angle under negative bending was higher than the degradation observed at 6% interstory drift angle at room temperature. As a result of significant strength

deterioration of the connection under negative bending, the moment-rotation hysteresis loop exhibited hysteresis pinching which led to reduced energy dissipation capacity as observed in Figure 19a. A comparison plot of the moment-rotation envelope of the peak negative and positive moments at each loading cycle is shown in Figure 19b, where the moment-rotation envelopes were plotted for the WUF-W connections with and without fire damage.

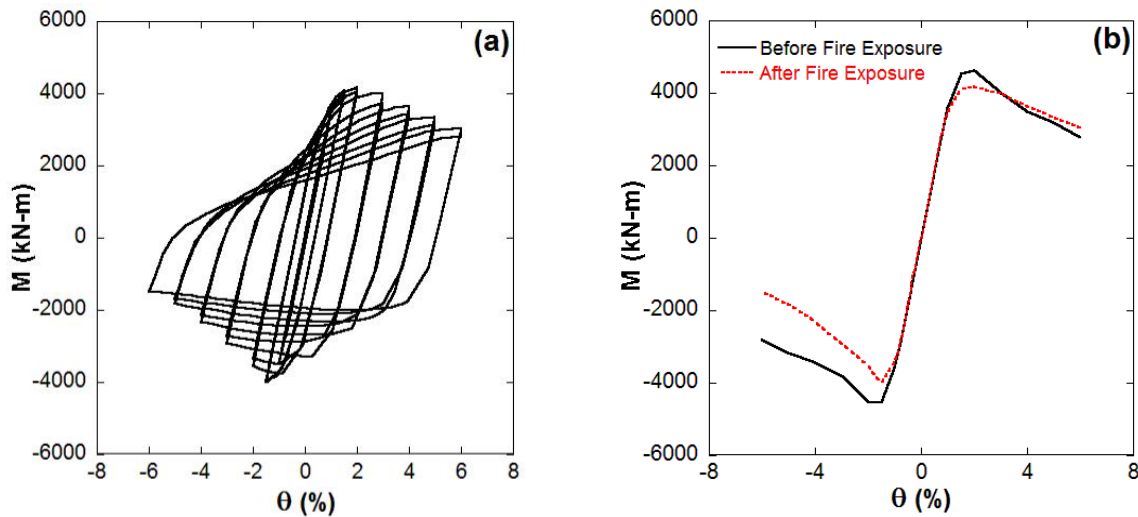


Figure 19 (a) Moment-rotation hysteresis response of WUF-W connection with fire damage under simulated seismic loading history, (b) comparison of moment-rotation envelopes showing peak positive and negative moments at each loading cycle.

It can be observed that for the fire damaged connection, the overall strength of the connection reduced compared to the connection without fire damage regardless of positive and negative bending. The reduction in the peak moments under positive and negative bending were around 10% and 14% respectively. This was attributed to the post-fire degraded strength of the material. However, as already mentioned, for fire damaged connection, the strength under positive bending degraded gradually, whereas the strength deteriorated sharply under negative bending. Moreover, under negative bending the strength degradation initiated earlier than that under positive bending. This type of hysteresis behavior was not observed in the overall response of the frame because of the strength contribution of the members unaffected by fire. However, while considering the response of each individual

connection in the frame, this type of hysteresis behavior poses severe risk for the connections that are directly exposed to fire.

4. Conclusions

This study demonstrated the influence of post-fire material strength degradation and heterogeneity on the seismic response of steel structures by performing finite element analyses on special moment resisting frames. The responses obtained from the analyses led to the following conclusions:

- Structural members of special moment frames designed for seismic application with large beam and column sections can withstand higher temperatures (~1000°C) without significant distortion during fire, and hence, visibly they may seem to be unaffected by the high temperature exposure. However, at such high temperature range structural steel undergoes significant change in the mechanical properties which essentially changes the structural behavior. Hence, it is anticipated that even though there is no significant distortion in the structure, the post-fire degradation of structural steel may adversely influence its seismic performance.
- The seismic analysis of special moment resisting frames by considering fire damage demonstrated that the strength degradation of fire exposed structural members is not very influential to the overall strength of the structure, rather the lateral drift demands were significantly influenced by the post-fire strength degradation and heterogeneity of structural steel. It was observed that nearly all of the earthquake-induced lateral displacement occurs at the story level where the fire exposed compartments are located. This may lead to single story mechanism commonly known as soft story at the fire exposed story level which can lead to catastrophic failure of the structure. In addition, it was observed that with increase in the number of fire exposed compartments in a story, there is decrease in the lateral strength and increase in the drift demands at that story level.
- Seismic analysis of an isolated WUF-W moment connection revealed that after fire exposure, the temperature across the depth of a beam is unevenly distributed which

leads to material heterogeneity. As a result, the strength of the connection under negative bending drops steeply compared to the strength under positive bending which induces hysteresis pinching. Although this type of hysteretic behavior is not seen in the overall hysteresis response of the frame, it can increase the possibility of failure of the connection in the fire exposed compartments.

Hence based on the observations from this study, it is obvious that the fire damaged steel structures are vulnerable to earthquake loading, if the fire exposure temperature is over 800°C and the structure is rehabilitated for continued service. The notion that there is no metallurgical change when there is no distortion might not be applicable to moment resisting frames with large beam and column sections. Therefore, it is essential that even if no distortion is noticeable, the fire damaged structures should be investigated thoroughly to make decision about the reparability of the structure based on the post-fire mechanical properties of the structural steel.

5. References

- [1] Klem TJ. First Interstate Bank Building Fire, Los Angeles, CA, May 4, 1988. NFPA Fire Investigation Report, Quincy, MA, 1988.
- [2] Klem TJ. One Meridian Plaza, Philadelphia, PA, three firefighter casualties, February 23, 1991. NFPA Fire Investigation Report, Quincy, MA, 1991.
- [3] Newman GM. Structural fire engineering investigation of Broadgate Phase 8 fire. Steel Construction Institute, Ascot., 1991
- [4] Routley JG, Jennings C, Chubb M. High-Rise office building fire, One Meridian Plaza, Philadelphia, Pennsylvania. Federal Emergency Management Agency (FEMA), 1991.
- [5] Moncada, J.A. Fire unchecked. NFPA Journal 2005.

- [6] Beitel J, Nestor I. Analysis of needs and existing capabilities for full-scale fire resistance testing. US Department of Commerce, National Institute of Standards and Technology, 2008.
- [7] NIST NCSTAR 1-3D. Mechanical properties of structural steel, federal building and fire safety investigation of the of the work trade center disaster. National Institute of Standards and Technology, Gaithersburg, MD, 2005.
- [8] Niwa H. Investigation of Windsor building fire in Spain. Report of Obayashi Corporation Technical Research Institute (CD-ROM) 70:11-2, 2006.
- [9] Isner MS. High-rise office building fire, Alexis Nihon Plaza, Montreal Canada, October 26, 1986. NFPA Fire Investigation Report, Quincy, MA, 1986.
- [10] Scawthorn C, Eidinger JM, Schiff AJ, eds. Fire following earthquake. ASCE Publications, 2005.
- [11] Scawthorn C. Fires following the Northridge and Kobe earthquakes. Thirteenth Meeting of the UJNR Panel on Fire Research and Safety 2 1996;337-345.
- [12] Tide RH. Integrity of structural steel after exposure to fire. AISC Engineering Journal 1998;35:26-38.
- [13] Gosain N, Drexler F, Choudhuri D. Evaluation and repair of fire-damaged buildings. Structure Magazine, 2008.
- [14] Saul FW. Structural steel bounces back. AISC Steel Construction Digest 1956;13(3),3rd Qtr., Chicago, IL.
- [15] Hapgood KB. Metallurgical analysis of bridge samples. U.S. Department of Transportation, Federal Railroad Administration, Washington, DC, 1979.

- [16] Smith CI, Kirby BR, Lapwood DG, Cole KJ, Cunningham AP. The reinstatement of fire damaged steel framed structures. British Steel Corporation, Teesside Laboratories, United Kingdom, 1980.
- [17] Hineman MA. Metallurgical testing of three beams subjected to a fire test at underwriter's laboratories. Report No. 51610, Taussig Associates, Inc., Skokie, IL, 1983.
- [18] Kirby BR. Evaluation of the temperature attained by five bolts during a fire in the Broadgate Phase 8 development—London. British Steel Corporation, Swinden Laboratories, Moorgate, Rotherham, United Kingdom, 1991.
- [19] ASTM, A. 6/A 6M. Standard specification for general requirements for rolled structural steel bars, plates, shapes, and sheet piling. American Society for Testing and Materials, West Conshohocken, PA, 2010.
- [20] Dill FH. Structural steel after a fire. Proceedings of National Steel Construction Conference, Denver, CO, American Institute of Steel Construction, Chicago, IL, 1960.
- [21] Wright W, Cayes L. Route I-78 viaduct over Waverly Yards Bridge fire, material test of damaged girders. Federal Highway Administration, Turner-Fairbank Highway Research Center, McLean, VA, 1990.
- [22] Kirby BR, Lapwood DG, Thomason G. The reinstatement of fire damaged steel and iron framed structures. British Steel Corporation, Swinden Laboratories, Moorgate, Rotherham, United Kingdom, 1993.
- [23] Kirby B.R. Large scale fire tests: the British steel European collaborative research programme on the BRE 8-storey frame. In Proceedings of the 5th International Symposium on Fire Safety Science (IAFSS), 1129-1140, 1997.

- [24] Li GQ, Guo SX. Experiment on restrained steel beams subjected to heating and cooling. *Journal of Constructional Steel Research* 2008;64(3):268-274.
- [25] Wald FA, Simões da Silva L, Moore DB, Lennon T, Chladná M, Santiago A, Borges L. Experimental behavior of a steel structure under natural fire. *Fire Safety Journal* 2006;41(7):509-522.
- [26] Smith CI, Kirby BR, Lapwood DG, Cole KJ, Cunningham AP, Preston RR. The reinstatement of fire damaged steel framed structures. *Fire Safety Journal* 1981;4:21-62.
- [27] Outinen J, Makelainen P. Mechanical properties of structural steel at elevated temperatures and after cooling down. *Fire and Materials* 2004;28(2-4):237-251.
- [28] Lee J, Engelhardt MD. Mechanical properties of ASTM A992 steel after fire. *Engineering Journal* 2012;49(1):33-44.
- [29] Morrison M. Innovative seismic performance enhancements of welded steel building beam-column moment resisting connection. PhD Dissertation Research, North Carolina State University, Raleigh, NC, 2014.
- [30] SAC/BD-97/02. Protocol for fabrication, inspection, testing and documentation of beam-column connection tests and other experimental specimens. by Clark P, Frank K, Krawinkler H, Shaw R.
- [31] Adan SM. Design parameters for steel special moment frame connections. Proceedings 2011 SEAOC convention, Las Vegas, Nevada, Structural Engineers Association of California, 2011.
- [32] AISC. Prequalified connections for special and intermediate steel moment frames for seismic applications. *American Institute of Steel Construction* 358, 2010a.

- [33] AISC. Seismic provisions for structural steel buildings. American Institute of Steel Construction 341, 2010b.
- [34] ASTM E119. Standard test method for fire tests of building construction and materials. American Society for Testing and Materials, West Conshohocken, PA, 2012.
- [35] ASTM E1529. Standard test method for determining effects of large hydrocarbon pool fires on structural members and assemblies. American Society for Testing and Materials, West Conshohocken, PA, 2013.
- [36] Quiel SE, Garlock ME. Modeling high-rise steel framed buildings under fire. In Proceedings of the 2008 ASCE/SEI structures congress, 2008.
- [37] Hu G, Morovat MA, Lee J, Eschell E, Engelhardt M. Elevated temperature properties of ASTM A992 steel. In: Proceedings of ASCE structure congress 09, Austin, TX, USA, 2009.

CHAPTER 8: CONCLUSIONS AND RECOMMENDATIONS

1. Conclusions

This dissertation dealt with experimental and finite element investigation of the localized failure mechanism of welded steel moment connections as well as moment resisting frames. The objective of the study was to study the influence of several important parameters on the seismic response of the connections, address the extent of influence and wherever possible propose modifications to improve the performance of the connections. The parameters that were investigated in the course of the study are influence of end plate stiffeners and bolt arrangement on the seismic performance of extended end plate connection, influence of initial and weld induced residual stresses and weld sequence on the localized failure mechanism of the WUF-W and WUF-B connections, and finally the effect of fire damage (material strength degradation and heterogeneity) on the seismic performance of the moment resisting frames.

In Chapters 2 and 3, a modified design of extended end plate connection was proposed and validated. In order to eliminate the stress concentration caused by the end plate stiffener in AISC qualified eight bolt stiffened extended end plate connection, different arrangements of bolts were studied by using finite element analysis and an optimized bolt arrangement was obtained which led to equal distribution of bolt forces. However, this introduced a different failure mechanism through higher strain demands on the weld. Hence, the beam flanges were heat treated to predefine the plastic hinge location and if failure occurs it will occur in the heat treated location of the beam flanges and the required ductility capacity of the connection will be achieved. This again introduced another failure mechanism through lateral or lateral torsional buckling of the beam due to reduced strength of the material in the heat treated region. As a result, a stiffener was welded to the beam web near the connection region. The modified connection showed significant improvement in ductility and energy dissipation capacity, and the connection showed no strength degradation upto 5% interstory drift angle. The modified connection design was validated by an experiment on full

scale beam-column connection and showed excellent performance under simulated seismic loading history.

Chapters 4, 5 and 6 dealt with experimental and finite element study of the localized failure mechanism of welded steel moment resisting connections by considering the initial and weld induced residual stresses. In the experimental study, two WUF-B connections were tested under fatigue loading in order to investigate the effect of weld sequence on the performance of the connection. The results from the experimental investigation demonstrated accumulation of axial strain near the weld toe and weld access hole, and different welding procedure induced different amount of axial strain accumulation, which consequently led to different fatigue life of the two specimens. In order to simulate the influence of weld sequence on the low-cycle fatigue failure mechanism of the connections, advanced numerical techniques were developed for simulating the initial and weld induced residual stresses and the simulation responses were validated against responses from the experimental study and literature.

The simulation responses showed that significant amount of residual stresses develop close to the weld toe and weld access hole of the connection because of the welding procedure, which gradually diminishes with increase in the distance from the weld toe. The peak value of residual stresses can be higher than the yield stress of the base material and it can be either tensile or compressive or a combination of both. Initial residual stress values are negligible around the edges of the beam, and it increases with an increase in the distance from the edge with a peak value at the centerline along the beam length. As a result, the residual stresses close to the weld region are predominantly welding induced residual stresses. The presence of residual stresses may lead to axial strain ratcheting near the weld toe and weld access hole, and subsequently may lead to low-cycle fatigue failure of the connection. Hence, the low-cycle fatigue failures that have been observed in the cyclic testing of the post-Northridge connections can be attributed to the development of damage accumulation near the weld toe and weld access hole as a result of the axial strain ratcheting. Different weld sequences induce different distribution and magnitude of residual stresses around the welded joint, and hence, the strain ratcheting would be different for different weld

sequences. Post-weld heat treatment can be used to reduce the magnitude of residual stresses which is expected to increase the fatigue life of moment resisting connections.

Chapter 6 dealt with the seismic response of fire damaged steel buildings where the influence of post-fire material properties and heterogeneity of structural steel on the seismic performance of moment resisting frames was investigated. The results of the analysis revealed that the strength degradation of fire exposed structural members is not very influential to the overall strength of the structure, rather the lateral drift demands were significantly influenced by the post-fire strength degradation and heterogeneity of structural steel. It was observed that nearly all of the earthquake-induced lateral displacement occurs at the story level where the fire exposed compartments are located. This may lead to single story mechanism commonly known as soft story at the fire exposed story level which can lead to catastrophic failure of the structure. In addition, it was observed that with increase in the number of fire exposed compartments in a story, there is decrease in the lateral strength and increase in the drift demands at that story level. Seismic analysis of an isolated WUF-W moment connection revealed that after fire exposure, the temperature across the depth of a beam is unevenly distributed which leads to material heterogeneity. As a result, the strength of the connection under negative bending drops steeply compared to the strength under positive bending which induces hysteresis pinching. Although this type of hysteretic behavior is not seen in the overall hysteresis response of the frame, it can increase the possibility of failure of the connection in the fire exposed compartments.

2. Recommendation for Future Works

Although the present research showed its effectiveness in studying the local failure mechanism of welded steel moment connections, but it was not possible to address all the factors that influence the localized failure. There are new ideas of research arising from this dissertation research. Based on the the responses obtained from this study, following are some of the recommendations for future research works.

2.1 Modified Extended End Plate Connection with Extended Shear Tab

In the seismic performance enhancement of AISC prequalified eight bolt stiffened extended end plate connection, heat treatment was implemented at the flanges of the beam to ensure formation of plastic hinge away from the connection region. This was based on the weakening mechanism of the beam similar to what is used for reduced beam section moment connection. Alternatively, the formation of plastic hinge in the beam flanges can be ensured by strengthening the beam in the connection region using an extended shear tab. The extended shear tab will delay the strength degradation by strengthening the connection region, and also push the plastic hinge away from the welded joint. This type of the configuration of the connection was not investigated in this study and there may be a possibility that with the modified bolt arrangement and extended shear tab, the connection can show similar response as observed for the modified connection proposed in this study.

2.2 Further Study on Seismic Analysis of WSMCs with Residual Stresses

In the seismic analysis of moment resisting connection with residual stresses, there are several issues that need further investigation. In this study only two weld sequences were considered for the analysis of WUF-W connection. Using the same procedure used in this study, several weld sequences can be studied to get an optimized weld sequence that will produce the least amount of residual stresses in the connection region. Moreover, in this study the effect of the weld between the beam web and column flange was not considered. The same analysis used in this study can be performed by including a fillet weld between the beam web and column flange to investigate its influence on the overall residual stress distribution. In addition, the presence of void or inclusion in the weld may affect the peak value of the residual stress and its distribution. The weld residual stress analysis can be performed with the inclusion or void in the weld in order to study its influence on the overall residual stress distribution as well as on the low cycle fatigue response of the moment resisting connections.

Although in the residual stress calculation, the effect of material heterogeneity based on the peak temperature was included, however, in the fatigue analysis of moment resisting

connections, the heterogeneity of the material was not accounted for because of the unavailability of cyclic response of ASTM A992 material at high temperatures. Further investigation is required on the seismic analysis of moment resisting connections by considering the heterogeneity in the material to study the influence of material softening on the local strain responses of the connections. There were no experimental measurements of residual stresses induced by welding at the weld region of the connection for which the simulated residual stress response could not be validated. Similarly, no initial residual stress measurements were available for wide flange members consisting of ASTM A992 steel. These residual stress data is required from experimental measurements to validate the simulated responses. Finally, the implemented residual stress simulation technique can be further used to study the influence of residual stresses as well as welding procedure on the local failure mechanism of other types of moment resisting connections such as reduced beam section (RBS) connection, extended end plate connection.

2.3 Fire Damage Analysis with Water Quenched Structural Steel

In the seismic analysis of fire damaged moment resisting frames, it was assumed that the fire exposed structural steel is cooled down slowly to room temperature as the fire slowly extinguished over a long time. Further study is required to investigate the performance of the fire damaged steel buildings under seismic loading history by considering water quenched material properties of structural steel to consider quick extinguishing of fire with firefighter sprayed water.

2.4 Simulation with Advanced Constitutive Models

Although all the simulation results presented in this study showed good conformity with the experimental responses, for more complex analysis where creep, stress relaxation and time dependent behavior is important, it is highly recommended that more advanced constitutive model is used to get a better prediction of the responses. This type of advanced constitutive model will require additional terms such as time sensitivity, influence of dwell time, temperature dependence and finally, multiaxial parameters.